The Long and the Short of it - Ruthenium Alkynyl Complexes

by

Benjamin George Ellis

B.Sc. (Hons)

A Thesis Submitted Towards the Degree of Doctor of Philosophy

THE UNIVERSITY
OF ADELAIDE
AUSTRALIA

Department of Chemistry

December 2003

Contents

CHAPTER FOUR: Syntheses, Characterisation and Reactions of the Diyndiyl Complexes Ru(C≡CC≡CR)(dppe)Cp* (R = TMS, H)

CHAPTER FIVE: Syntheses, Structures and Electronic Properties of Mixed Iron-Ruthenium Diyndiyl Complexes

Abstract

This Thesis continues the study into the syntheses and reactivity of transition metal yndiyl and polyyndiyl complexes. These molecules show promise as models for molecular wires.

Chapter One gives a general overview of modern electronics and introduces the need for molecule based technology. The three most promising classes of molecular wires are described before the four available methods of evaluation are individually addressed.

Chapter Two describes the syntheses of the diyndiyl complexes $\{Ru(PP)Cp^*\}_2(C{\equiv}CC{\equiv}C)$ (PP = dppm, dppe), prepared by four-step procedures. Starting from the chloro-ruthenium precursors RuCl(PP)Cp*, treatment with TMSC≡CH gave the vinylidenes $[Ru(=C=CH_2)(PP)Cp^*]^+$, which were deprotonated to the ethynyls Ru(C≡CH)(PP)Cp*, before being oxidatively coupled ($[FeCp_2][PF_6]$) to give the bis-vinylidenes $[\{Ru(PP)Cp^*\}_2(=C=CHCH=C=)]^{2+}$. Deprotonation of these with dbu or $KOBu^t$ gave the corresponding diyndiyls in excellent yield (90%). Electrochemistry of the diyndiyl complexes revealed the expected sequence of four one-electron redox steps, which occurred at significantly lower $E_{½}$ values than found for the $Ru(PPh_3)_2Cp$ analogue. Single-crystal X-ray structure determinations are reported for all complexes, together with the structures of the mono- and dications of the diyndiyl complex in the dppe series.

Chapter Three summarises a collection of reactions that detail the reactivity of bis-vinylidenes $[\{Ru(dppm)Cp^*\}_2(=C=CRCR=C=)]^{2+}$ (R = H, Me) towards the strong base, $KOBu^t$. Under these conditions, deprotonation of a single dppm ligand and cyclisation, followed by the removal of one of the pendant R groups occurred, giving complexes of the general formula $\{Cp^*(dppm)Ru\}$-C≡CC(R)=C-$\{Ru(Ph_2PCHPPh_2)Cp^*\}$. This Chapter also describes the protonation (HOTf) of the diyndiyl complex $\{Ru(dppe)Cp^*\}_2(C{\equiv}CC{\equiv}C)$ to give the corresponding bis-vinylidene, a reaction that previously has not been reported in the M(PP)Cp' (M = Fe, Ru, Os) series.

Chapter Four includes a large number of reactions that demonstrate the reactivities of the diynyl complexes Ru(C≡CC≡CR)(dppe)Cp* (R = TMS, H). Together with the syntheses of these very versatile reagents, a number of other complexes are also reported that result from the reaction of the intermediate butatrienylidene $[Ru(=C=C=C=CH_2)(dppe)Cp^*]^+$ with a variety of nucleophiles (NH_3, H_2O and MeOH). Also reported is the synthesis of an

asymmetric ruthenium diyndiyl complex featuring Ru(dppe)Cp* and $Ru(PPh_3)_2Cp$ end-groups. An electrochemical study of this complex revealed the expected sequence of four one-electron redox steps, which occurred at values intermediate to those found for the corresponding symmetric diyndiyls. Other complexes reported include mixed ruthenium-gold diyndiyls and trinuclear copper(I) clusters, $Cu_3(\mu\text{-dppm})_3$, capped by either one or two Ru(C≡CC≡C)(dppe)Cp* units. The redox properties for all the isolated complexes are also reported.

Chapter Five details reactions of Ru(C≡CC≡CH)(dppe)Cp* with FeCl(PP)Cp* in the presence of $Na[BPh_4]$ and dbu in THF/NEt_3 solvents, which gave the mixed ruthenium-iron diyndiyls {Cp*(dppe)Ru}(C≡CC≡C){Fe(PP)Cp*} (PP = dppe, dppp). Cyclic voltammetry shows that these complexes undergo sequential loss of up to three electrons. Guided by these data, subsequent chemical oxidation with $[FeCp_2][PF_6]$ gave the corresponding mono- and dicationic derivatives derived from the dppe series. Detailed studies of the IR, UV/Vis/NIR spectra, coupled with NMR, ESR, magnetic and Mössbauer measurements have enabled some understanding of the electronic configurations of these compounds to be obtained. In particular, the relative stabilities of the singlet and triplet configurations of the dication were shown to be related to the electron-donating power of the two end-groups.

Chapter Six describes the syntheses of a series of electron-rich binuclear ruthenium complexes of the general formula [Ru]-$(C\equiv C)_n$-[Ru] (n = 1, 2, 3, 4, 7 and 11). These complexes were prepared under a number of different reaction conditions, demonstrating how subtle variations can influence the outcome of a reaction. The electrochemical properties of these complexes are analysed and the effect of chain length on the electronic interaction between the two end-groups is examined. Of significant interest is the syntheses of complexes with n = 1 and n = 11 repeating acetylene units. These complexes represent the shortest and longest yndiyl and polyyndiyl complexes isolated as pure complexes to date. Also described are a number of adducts that result from the treatment of the C_6 and C_8 binuclear complexes with the reagents TCNE and $Fe_2(CO)_9$. The products from these reactions crystallise readily, allowing for structural characterisation that was used to confirm the structures of the parent complexes.

Statement of Originality

This thesis contains no material which has been accepted for the award of any other degree or diploma in any university and to the best of my knowledge and belief, contains no material previously published or written by another person, except where due reference is given.

I give consent to this thesis being made available for photocopy or loan.

Benjamin G. Ellis

Acknowledgments

Firstly, I would like to acknowledge the help of my supervisor Professor Michael Bruce throughout my Ph.D. He has given me the opportunity to work within his laboratory and provided me with a project that was not only very interesting, but was also very rewarding. I am also very grateful for his collaborations with Professor Claude Lapinte and Professor Jean-François Halet, which enabled me to spend six-months abroad at the University of Rennes, France. I would also like to thank the following academic staff for their help throughout my project. Thank you to Dr Louis Rendina and Dr Paul Low for their help and support on general chemistry matters, thank you to Professor Brian Nicholson and Dr Paul Humphrey for running mass spectra and a big thankyou to Professor Allan White and Dr Brian Skelton for their crystallography work.

I must also thank my French hosts, Professor Claude Lapinte and Professor Jean-François Halet, who were very hospitable. I also extend my gratitude to Frédéric Paul, Gilles Argouarch, Karine Costuas, Jean-Yves Thépot and Gwenael Colombel for their support and kind friendships.

I would like to thank many of the general staff who have helped throughout my Ph.D. including Barry, Peter, John and Phil. In particular, I would like to thank Graham Bull who has been of immense help with all chemistry and non-chemistry matters.

In the Lab, I would like to acknowledge Ben Hall, Martyn Jevric and Giovanni Melino, you guys have been the best and made coming into the lab a pleasure.

I would like to thank the following people for reading this Thesis, Susan Woodhouse, Professor Michael Bruce and Dr Paul Humphrey (the only person who has read this Thesis as a complete document).

Finally I would like to thank my family and friends who have all supported me in their own unique ways. In particular, I would like to thank my parents for their support throughout high school and university. Susan, I would also like to thank you. Both doing a Ph.D. at the same time is challenging at the very least, but we have made it. I thank you sincerely for all your support and motivation through my Honours and Ph.D.

Abbreviations

General:

[M]	general metal-ligand fragment
°	degrees
°C	degrees Celsius
Å	Angstroms
Ac	acyl, -$COCH_3$
anal.	analysis
ap	2-anilinopyridinate
Ar	aryl group
atm	atmosphere
av.	average
bpy	2,2'-bipyridyl
Bu^n	normal butyl, -$(CH_2)_3CH_3$
Bu^t	tertiary butyl, -$C(CH_3)_3$
ca	circa
calcd	calculated
cm	centimetres
Cp	cyclopentadienyl
Cp*	pentamethylcyclopentadienyl
Cp*H	pentamethylcyclopentadiene
CpH	cyclopentadiene
Cp^{Me}	methylcyclopentadienyl
Cy	cyclohexyl, -C_6H_{11}
dba	*trans*, *trans*-dibenzylideneacetone
dbu	1,8-diazabicyclo[5.4.0]undec-7-ene
DF	density-functional
dippe	1,2-bis(diisopropylphosphino)ethane
DMF	*N, N*-dimethylformamide
dmpe	1,2-bis(dimethylphosphino)ethane
DNA	deoxyribonucleic acid
dpf	*N,N'*-diphenylformamidine
dppe	1,2-bis(diphenylphosphino)ethane
dppm	bis(diphenylphosphino)methane
dppp	1,3-bis(diphenylphosphino)propane
e^-	electron
EH	extended Hückel
eq	equivalents
ESR	electron spin resonance
Et	ethyl, -CH_2CH_3
EtOH	ethanol
eV	electron volts

FET	field-effect transistor
FMO	frontier molecular orbitals
h	hour(s)
HOMO	highest occupied molecular orbital
i.e.	that is
IC	integrated circuit
IR	infrared
J	Joules
K	Kelvin
K_{eq}	equilibrium constant
LDA	lithium diisopropylamide, $LiNPr^{i}_{2}$
LUMO	lowest unoccupied molecular orbital
M	molarity
Me	methyl, $-CH_3$
MeOH	methanol
mg	milligrams
MHz	megahertz
min	minutes
mL	millilitres
mm	millimetres
mmol	millimoles
MO	molecular orbital
MV	mixed-valence
NIR	near-infrared
nm	nanometres
NMR	nuclear magnetic resonance
Nu	nucleophile
OPE	oligo(phenylene ethylene)
ORTEP	Oak Ridge Thermal Ellipsoid Plot Program
OTf	triflate, trifluoromethansulfonate, $CF_3SO_3^-$
OTTLE	optically transparent thin-layer electrochemical
Ph	phenyl, $-C_6H_5$
PP	bis-phosphine
Pr^{i}	isopropyl, $-CH(CH_3)_2$
R	general organic group
r.t.	room temperature
Ref	reference
R_f	retention factor
s	seconds
SAM	self-assembled monolayer
STM	scanning tunnelling microscope
SWCNT	single-walled carbon nanotube
T	temperature (K)

TCNE	tetracyanoethylene
THF	tetrahydrofuran
TLC	thin layer chromatography
TMEDA	tetramethylethylenediamine
TMS	trimethylsilyl, $Si(CH_3)_3$
tol	*para*-tolyl, $-C_6H_4CH_3$
trpy	2,2':6',2"-terpyridine
UV	ultraviolet
Vis	visible
X	halide
ΔG_{th}	thermal activation barrier

NMR:

d	doublet
HMBC	heteronuclear multiple bond connectivity
HSQC	heteronuclear single quantum coherence
Hz	hertz
m	multiplet
$^nJ(ij)$	n bound coupling constant between nuclei i and j
ppm	parts per million
ROESY	rotational Overhauser effect spectroscopy
s	singlet
t	triplet
tms	tetramethylsilane
tt	triplet of triplets
δ	chemical shift

IR:

br	broad
cm^{-1}	wavenumbers (reciprocal centimetres)
m	medium
s	strong
sh	shoulder
w	weak

Mass Spectrometry:

ES	electrospray
FAB	fast atom bombardment
M	molecular ion
m/z	mass per unit charge
MS-MS	mass spectrometry-mass spectrometry

UV/Vis/NIR:

$(\Delta\nu_{1/2})_{theo}$	calculated band-width at half-height
abs	absorbance
IL	intraligand
IVCT	intervalence charge transfer
LMCT	ligand-to-metal charge transfer
MLCT	metal-to-ligand charge transfer
V_{ab}	electronic coupling parameter
$\Delta\nu_{1/2}$	observed band-width at half-height
ε	extinction coefficient
λ	reorganisation parameter

Electrochemistry:

a	amperes
CE	counter electrode
E	potential
E_n	potential of n^{th} redox process
$E_{1/2}$	half-wave potential
E_a	anodic potential
E_c	cathodic potential
I	current
i_a	anodic peak current
i_c	cathodic peak current
irr.	irreversible
K_c	comproportionation constant
RE	reference electrode
V	volts
WE	working electrode
ΔE	potential difference

Mössbauer:

IS	isomeric shift
QS	quadrupole splitting

General Constants:

c	speed of light, 2.997×10^8 m s^{-1}
F	Faraday constant, 9.6485×10^4 C mol^{-1}
h	Planck constant, 6.626×10^{-34} J s
k	Boltzmann constant, 1.38066×10^{-23} J K^{-1}
R	Gas Constant, 8.31451 J K^{-1} mol^{-1}

General Experimental Conditions

All reactions were carried out under dry, high purity argon using standard Schlenk techniques. Solvents were purified as follows: diethyl ether, pentane, THF and toluene were distilled from Na/benzophenone; benzene was distilled from Na; CH_2Cl_2 was distilled from CaH_2; NEt_3 was distilled from KOH; MeOH was distilled from Mg/I_2. Elemental analyses were performed either by the Canadian Microanalytical Service, Delta, B.C., Canada or CMAS, Belmont, Vic., Australia.

Instrumentation

IR spectra were obtained on either a Perkin-Elmer 1720X FT IR spectrometer (4000-400 cm^{-1}) or on a Bruker IFS28 FT IR spectrometer (4000-400 cm^{-1}). Nujol mull spectra were obtained from samples mounted between NaCl discs. Solution spectra were obtained using a 0.5 mm path-length solution cell with NaCl windows.

NMR spectra were recorded on Varian Inova 600 (^1H at 599.87 MHz, ^{13}C at 150.85 MHz) or Bruker AM300WB or ACP300 (^1H at 300.13 MHz, ^{13}C at 75.47 MHz, ^{31}P at 121.50 MHz) instruments. Samples were dissolved in $CDCl_3$ (99.9 atom % D, Aldrich Chemical Co., unless otherwise stated), contained within 5 mm sample tubes. Chemical shifts (δ) are given in ppm relative to internal tms (0 ppm) for ^1H and ^{13}C NMR spectra and external H_3PO_4 (0 ppm) for ^{31}P NMR spectra. In the case of ^{13}C NMR, the following convention will be used to assign the atoms of the carbon chains, [Ru]-C_1-C_2-C_3- etc. In the case of symmetric complexes, numbering will only occur to the centre of inversion, and in the case of asymmetric complexes, numbering will begin at the carbon directly attached to ruthenium.

UV/Vis/NIR spectra were recorded on a Varian Cary 5 UV/Vis/NIR spectrometer. For spectroelectrochemistry, samples (1 mM) were dissolved in CH_2Cl_2 (with 0.5 M $[Bu^n_4N][PF_6]$ supporting electrolyte). The OTTLE cell consists of a 1 mm path length cell with a platinum gauze working electrode, platinum wire counter and pseudo-reference electrodes.

Cyclic voltammograms were recorded using either a PAR model 263 apparatus (using a saturated calomel electrode and platinum working and counter electrodes) or a MacLab/400

supplied by AD Instruments (using a platinum working electrode, platinum wire counter electrode and a pseudo-reference electrode). Solutions were made up in CH_2Cl_2 using a 0.1 M solution of $[Bu^n_4N][PF_6]$ as the supporting electrolyte, at a scan rate of 0.2 V s^{-1}. Ferrocene was used as an internal calibrant, $[FeCp_2]/[FeCp_2]^+ = +0.46$ V.

ES-mass spectra were recorded on either a VG Platform 2 or a Finnigan LCQ spectrometer. Methanol solutions were directly infused into the instrument, using chemical aids to ionisation as required. FAB-mass spectra were recorded with a high resolution MS-MS ZabSpec TOF Micromass spectrometer (8 kV) using *m*-nitrobenzyl alcohol as a matrix.

Mössbauer spectra were recorded with a 2.5 x 10^{-2} C (9.25 x 10^8 Bq) ^{57}Co source using a triangular sweep mode. X-Band ESR spectra were recorded on a Bruker ESP-300E spectrometer.

X-ray crystal structures were determined by Professor Allan White and Dr Brian Skelton, University of Western Australia, Australia. Structural data were received in CIF format and the ORTEP plots of the individual molecules or cations were generated using ORTEP for Windows (Version 3.0), showing 50% ellipsoid probability with non-essential hydrogen atoms omitted for clarity. Throughout this Thesis, ORTEP plots adhere to the following colour scheme: Orange = ruthenium; Purple = iron or chlorine; Green = phosphorus; Pink = silicon; Red = hetero atom (N or O); Brown = gold; Blue = carbon atoms of the bridging or carbon-rich ligand, or cobalt. Atomic numbering will follow the convention used for ^{13}C NMR assignments, with the carbon atoms of the chain labelled in the following order, [Ru]-C(1)-C(2)-C(3)- etc. In the case of a centrosymmetric structure, numbering will occur to the centre of inversion before taking on the following convention, [Ru]-C(1)-C(2)-C(2')-C(1')-[Ru].

CHAPTER ONE

Introduction

1.1. Modern Electronics

Electronics is a branch of the physical sciences concerned with the behaviour of electrons within an electronic circuit. In 1958, the electronics industry was revolutionised with the invention of the integrated circuit (IC) also referred to as a silicon chip. Within an IC, all the electronic devices are built within the layers of a semi-conducting material, usually silicon.

The rapid progress of information technology has driven the fabrication of progressively smaller devices within ICs, ultimately leading to chips with greater processing power. Currently a photographic process known as photolithography is used to manufacture ICs, but it is widely accepted that continued reductions in feature size will become increasingly difficult due to various limiting factors.[1]

In 1965, Gordon Moore, a co-founder of the Intel corporation, was asked to give his thoughts in a special 35th anniversary edition of the journal *Electronics*. Moore predicted that the number of transistors (or the transistor density) that could be fabricated on an IC would double every 18-24 months.[2] While there have been predictions at various times that this trend may end, Moore's law has held strong and has since become a virtual blueprint for the electronics industry. Maintaining this steady increase has required continuous development of new and improved photolithography techniques to enable fabrication of ever-smaller devices within the layers of silicon.

Although Moore's law has shown no signs of tapering off at this stage, various physical limitations such as current leakage that results in poor insulation will pose new obstacles in the near future.[1,3] Also, the economic burden facing manufacturing plants will contribute to slowing down innovative development and an equilibrium between the cost of production and chip performance may soon be reached. As the transistor density is fundamental to Moore's law, companies within the industry will need to consider alternative technologies to continue this trend.

1.2. Molecular Devices

As an alternative to the 'top-down' approach where progressively smaller feature sizes are required to keep up with the requirements of Moore's law, chemists and other material scientists are now working on the opposite 'bottom-up' approach and trying to build electronic circuits from the simplest building blocks, atoms and molecules.

It was first suggested in 1974 that a single organic molecule could function as a unidirectional molecular wire or molecular rectifier.[4] More recently there have been many significant advances towards the realisation of working molecular circuits. Since molecules can be synthesised in large quantities, the potential cost of fabricating electronic circuits based on this technology is anticipated to be far less than current methods. This key point has driven research within the industry and examples of molecular wires,[3,5-7] switches,[8-10] memories[11,12] and rectifiers[13,14] have all been reported, many operating on the same principles as conventional devices.

1.3. Molecular Wires

Wires are the simplest components of any electronic circuit, carrying electrons from a source to a drain. While a large number and variety of compounds have been suggested as potential molecular wires, the three most promising candidates are carbon nanotubes, conjugated organic molecules and redox-active molecular wires. Other compounds that have been suggested include porphyrin oligomers,[15] DNA[16] and doped polymers.[17] While all the proposed compounds vary greatly in their structures, they all possess the ability to be electron- or hole-conducting, providing a pathway for electron transport, enabling a current to flow from one end of the molecules to the other.

Due to their simplicity, the design and fabrication of molecular wires is an obvious starting point for molecular electronics. From this point, by tuning the electronic properties of a molecular wire and controlling physical properties such as resistance, more sophisticated devices such as switches or memory can then be developed.

1.3.1. Carbon Nanotubes

Recently discovered,[18] carbon nanotubes appear as a sheet of graphite with a hexagonal lattice rolled into a seamless cylinder (Figure 1.1). While they are amongst the simplest of any nanomaterials, they are the most diverse in structure and property.[19] Since their discovery, the potential application of carbon nanotubes in molecular electronics has been recognised.[20]

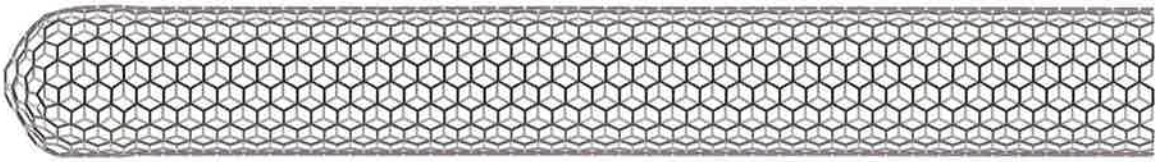

Figure 1.1: *Illustration of a single-walled carbon nanotube (SWCNT).*

An interesting electronic property of carbon nanotubes is that their conductivity is highly dependent on their size and structure. The tube diameter and the wrapping angle can all influence the conductivity, causing changes from a highly conducting (metallic) to a semi-conducting state.[19] There are three forms of carbon nanotubes (shown in Figure 1.2), each with a different wrapping angle. Structure **1a** is the nanotube in the armchair configuration, while **1b** and **1c** are examples of the chiral and zigzag forms, respectively.

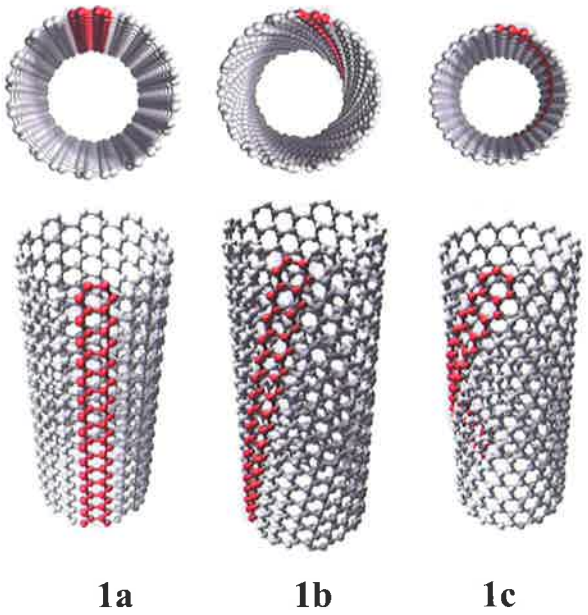

Figure 1.2: *The different helicities of carbon nanotubes, **1a** armchair; **1b** chiral; **1c** zigzag.*

Carbon nanotubes possess many extraordinary properties other than their electrical conductivity, such as high tensile strength, resistance to deformation, high heat transmission and high thermal stability, up to 2,800°C in a vacuum and 750°C in air.[19] This enhanced stability can be attributed to the strong carbon-carbon bonds throughout the molecule.

Various experiments have demonstrated that metallic nanotubes are able to carry extremely large current densities,[21,22] while semi-conducting nanotubes can be switched 'on' and 'off' upon application of a voltage as a field-effect transistor (FET).[23,24] In one experiment, the fabrication of a FET involved a three-terminal switching device consisting of a semi-conducting carbon nanotube connected to two platinum metal electrodes (Figure 1.3). Upon application of a voltage to the gate electrode, the nanotube was switched from a conducting to an insulating state. This development was a significant step towards the fabrication of molecular devices based on semi-conducting nanotubes. While a similar experiment had previously demonstrated that a metallic nanotube could operate as a FET at low temperatures,[20] this experiment represented the first nanotube transistor operating at room temperature, behaviour considered essential if such alternatives are to be applied as replacements for conventional solid-state devices.

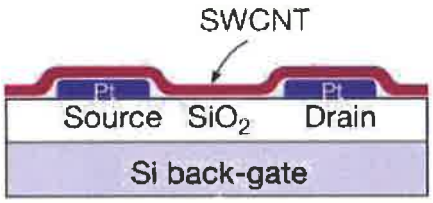

Figure 1.3: *Schematic side view of the FET device. A semi-conducting single-walled carbon nanotube (SWCNT) connecting two platinum electrodes.*[23]

While attention directed towards carbon nanotubes within the field of molecular electronics is warranted, at present no reliable method exists for the selective preparation of purely metallic or semi-conducting nanotubes of desired size and length. This lack of synthetic control is the major obstacle to the realisation of nanotube electronics.

1.3.2. Conjugated Organic Wires

Single conjugated organic molecules containing alternating single and multiple carbon-carbon bonds can conduct electrons through their conjugated π-systems. Discrete oligo(phenylene ethylene)s (OPEs) have been demonstrated to be conductive [linear I(V) curves] and are suitable to act as molecular wires.[25-30] The main advantage of fabricating wires and electronic devices based on conjugated organic molecules is that through the diversity of known organic reactions, OPEs of a precise length and construction can be synthesised.[31] While a number of different methods can be used to prepare OPEs, one very attractive method is the divergent/convergent approach which has been used to synthesise oligomer **1** (Scheme 1.1), an example of an OPE with an impressive length (128 Å) and construction.[32] Advantages of this method include rapid extension of chain length, doubling at every iteration, and straightforward purification.

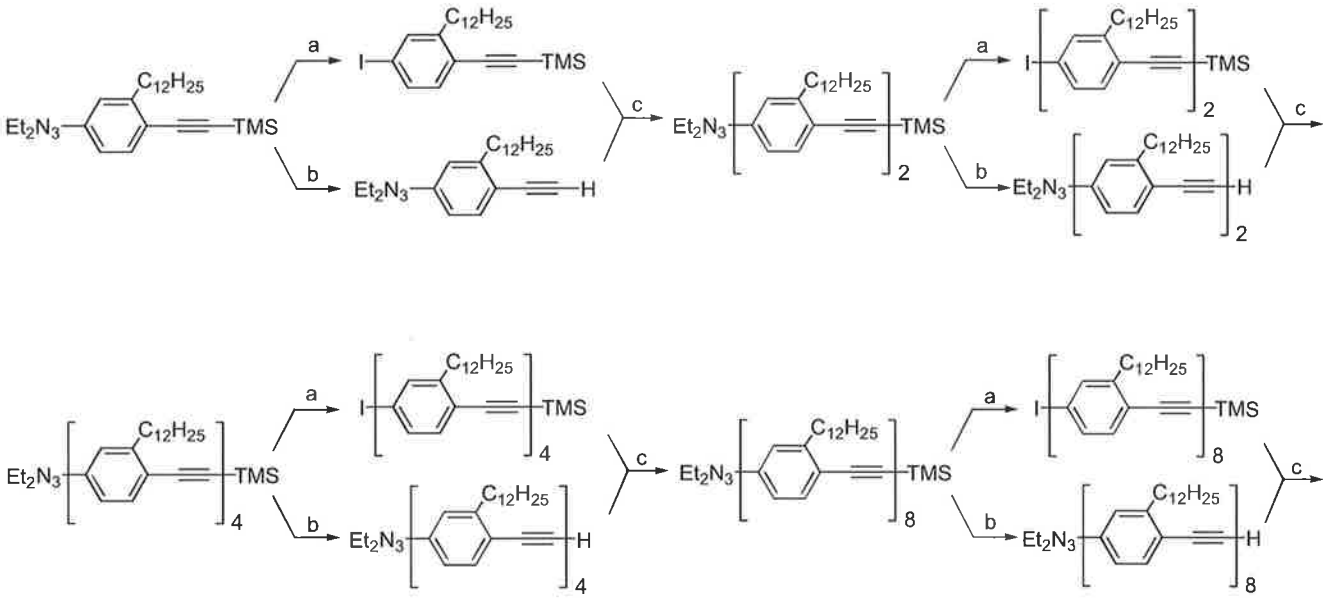

1

Scheme 1.1: *Divergent/convergent synthesis of* ***1****. Reagents: (a) MeI as solvent, 120°C; (b) K_2CO_3, MeOH, 23°C or $[Bu^n_4N]F$, THF, 23°C; (c) $Pd(dba)_2$ (5 mol %), CuI (10 mol %), PPh_3 (20 mol %), $NHPr^i_2$/THF (1:5), 23°C.*[31]

Functionalising OPEs with nitro groups causes them to behave as devices [non-linear I(V) curves] displaying electronic switching and memory behaviour.[11,32] This property results from the ability of the nitro groups to accept electrons, resulting in changes in conformation and conductivity of the molecule.[33]

Once the desired OPE has been synthesised, incorporation of functional groups such as monothioacetate provides a suitable means of attachment to metal surfaces or metal nanoparticles. With this connectivity, the conductance of single molecules can be measured using a number of different experimental techniques. While the conductivity of longer OPEs such as **1** has not been tested, several experiments have been performed on shorter molecules such as oligomer **2** shown in Figure 1.4.[26,34] Using the tip of a scanning tunnelling microscope (STM) it was possible to measure the conductivity of a single molecule of **2** inserted into disordered defects in a preformed self-assembled monolayer (SAM) of alkanethiolates on a gold surface. This experiment demonstrated the relative conductance of oligomer **2** to be greater than that of the surrounding alkanethiolate matrix, suggesting that OPEs are good candidates for molecular wires.

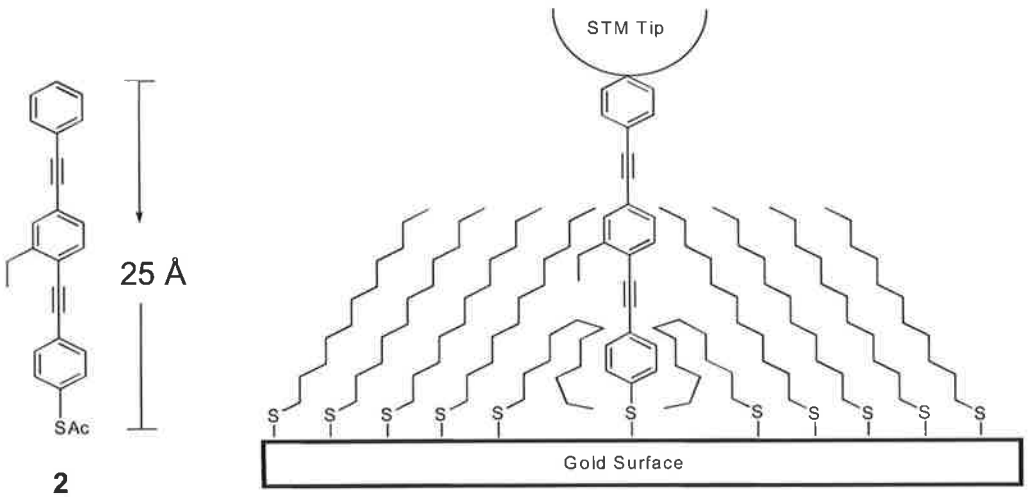

Figure 1.4: *Schematic illustration of the insertion of oligomer 2 into a disordered defect in a self-assembled monolayer of alkanethiolates.*

1.3.3. Molecular Wires Incorporating Transition Metals

Compounds containing a conjugated hydrocarbon ligand bridging two transition metals of the general formula [M]C_b[M] (where [M] represents a general metal-ligand fragment and C_b is the conjugated bridging ligand) have attracted interest as models for molecular wires.[35] Although many of the bridging ligands resemble some of the proposed conjugated organic wires, incorporation of transition metals at either end of the wire offers an opportunity to fine tune the electronic properties of the molecule. The incorporation of redox-active transition metal centres also enables the use of cyclic voltammetry and near-infrared (NIR) spectroscopy to evaluate the electronic interactions between the two redox-active centres across the bridging ligand (see Section 1.3.4). Electronic communication between two redox-active transition metals has been investigated with a range of bridging ligands including pyrazine,[36,37] 4,4'-bipyridines,[38-40] polyenes,[41,42] polyynes,[35,43-46] polyphenylene[47-50] and more.[6,51]

Pioneering work within this area was conducted on the Creutz-Taube ion **3**, which features two equivalent pentaamine ruthenium centres bridged by a pyrazine ligand.[36,37] With an overall 5+ charge, formally one of the ruthenium centres exists in the 2+ oxidation state while the second is in the 3+ state. By definition, this is an example of a mixed-valence (MV) compound, a material that contains an element in more than one oxidation state.

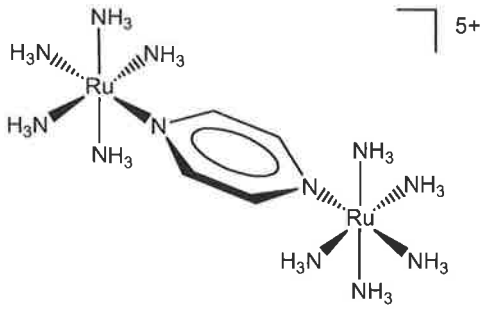

3

Redox-active molecular wires work on the principle that an unpaired electron or hole can be transferred along the entire length of the molecule. The formation of a MV species, either by the one-electron oxidation or reduction allows this exchange to occur between the two terminal end-groups (Figure 1.5).

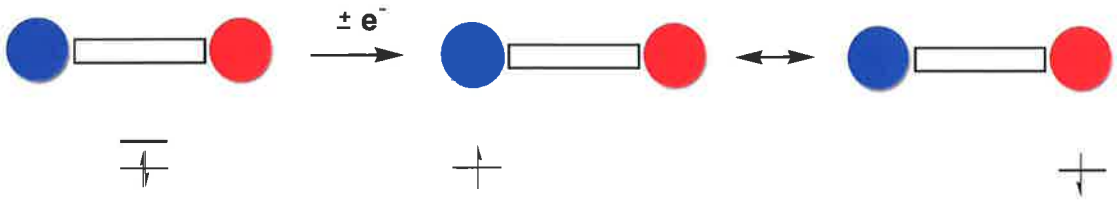

Figure 1.5: *Schematic representation of electron transfer in a redox-active molecular wire.*

The extent to which an unpaired electron is delocalised over a symmetric molecule in its MV state may vary. There are three possibilities which have been classified by Robin and Day:[52]

- A MV compound belongs to Class I if the bridging ligand does not allow any electronic interaction between the two redox centres, therefore acting as an insulator. In this case the charge is totally localised on one of the redox centres and unique properties for each of the redox sites can be observed.

- The intermediate, Class II represents the halfway point between the two extremes. In this state, charge is neither totally localised nor is it totally delocalised and consequently at least one spectroscopic method is able to distinguish between the two redox centres.

- If the bridging ligand acts as a conductor allowing strong interaction between the two redox sites, then the compound is classified as a Class III material. In this case the charge is completely delocalised over the entire length of the molecule and no spectroscopic method can distinguish between the two redox centres.

A key requirement for molecular wires incorporating transition metals is the efficient overlap of the metal d orbitals with the π-orbitals of the bridging ligand. This ensures complete charge delocalisation (i.e. Class III) from one redox centre to the other, an essential property if such compounds are to behave as molecular wires.[53,54]

1.3.4. Evaluation of Molecular Wires

While a considerable number of compounds have been suggested as models for molecular wires, the majority of these have not been tested for their current-carrying ability. Quantification of the electronic properties of a molecular wire has been achieved by four different methods. Often for any given compound, only one of these methods will provide a suitable means to evaluate the electronic properties and in some cases potential candidates will need to be structurally modified to enable the measurement to take place. Despite an impressive amount of research in this area, it must be noted that it is not known if any of these four methods give a reasonable indication of the ability of a molecule to permit transport of electrons across it within a nanoscopic circuit.

1.3.4.1. Direct Measurement

Direct measurement of the current that can flow through a single molecule would provide an ideal method to evaluate the electronic properties of a molecular wire. A number of experiments have demonstrated electrical conductance through single-layer molecular films between two metal electrodes.[11,14,55] The conductance of single molecules or at the most a few molecules imbedded in a non-conducting matrix has been demonstrated by the use of a STM probe (Section 1.3.2).[56,57] In more recent times, a number of experiments have measured the passage of current through a single molecule with connections to two electrodes *via* a chemical bond in a mechanically controlled break junction.[25,58-60]

In 1996, the first quantitative electrical measurement of a single molecule was carried out with a molecule of benzene-1,4-dithiol.[25] In this experiment, molecules were self-assembled onto two facing gold electrodes of a mechanically controllable break junction. After the solvent was removed, the gold electrodes were slowly moved together (in picometre increments) until one molecule bridged the gap between the two electrodes (Figure 1.6). Current/voltage behaviour was quantitatively measured and revealed approximately 0.1 μa of current could be carried through a single molecule, which corresponds to approximately 10^{12}

electrons per second. This result was higher than expected and represents the first fundamental step (conduction through single molecules) in the emerging field of electronics based on single molecules.

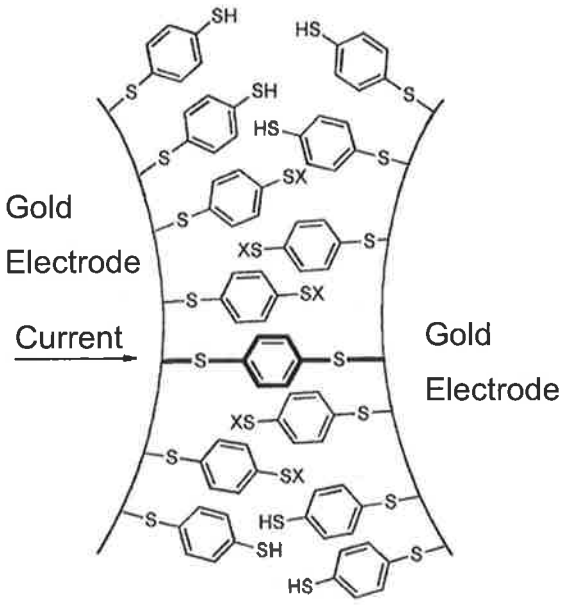

Figure 1.6: *A schematic illustration of a benzene-1,4-dithiolate SAM between two gold electrodes formed within a mechanically controlled break junction. End-groups denoted X can either be H or Au, potentially arising from a previous contact/retraction event.*[25]

1.3.4.2. Bulk Conductivity

Another suitable method for evaluating potential molecular wires is to measure the conductivity of a compound either as an amorphous solid or a crystal. This approach is often used in conductivity measurements of polymers.[61] However in other materials such as crystals, stretched polymers or liquid crystals, physical properties such as strength and optics can be anisotropic, varying in different directions. Likewise, conductivity can be anisotropic, a classic example of which is observed in graphite where conductivity perpendicular to the plane of the sheets of carbon is more than 5000 times lower than the conductivity in the plane.[62]

1.3.4.3. Cyclic Voltammetry

One of the most straightforward and widely used electrochemical techniques is cyclic voltammetry.[63,64] Typically a three-electrode system is used in the cyclic voltammetry experiment, consisting of a working electrode (at which the analyte is oxidised or reduced), a reference electrode, and a counter electrode. The current flows between the working and the counter electrodes and the potential is controlled relative to the reference electrode. Ideally, within the cell the counter and reference electrodes are placed in close proximity to reduce ohmic potential drop.

The experiment involves applying a triangular voltage as shown in Figure 1.7 to a stationary electrode in an unstirred solution. The potential is varied linearly from E_{start} to E_{switch} (*switching potential*), before being swept back to E_{end} to complete the cycle. The current response is then recorded and the resulting trace is displayed as a function of the applied potential. The current response on the forward scan is determined by the concentration, nature of the analyte and the scan rate, while the reverse scan provides additional information regarding the stability of the oxidised or reduced state of the analyte formed at the electrode surface.

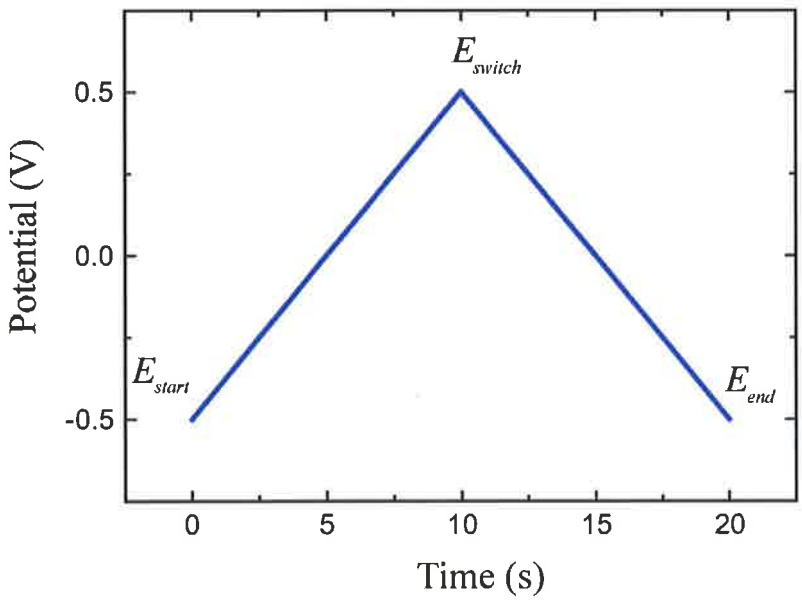

Figure 1.7: *Applied waveform used in a cyclic voltammetry experiment.*

A theoretical trace of a fully reversible one-electron process is shown in Figure 1.8, indicating the various parameters that can be extracted, such as the half-wave potential ($E_{½}$), anodic potential (E_a), cathodic potential (E_c) and the anodic and cathodic peak currents, i_a and i_c, respectively. In an ideal system under standard conditions, $E_{½}$ lies half-way between the oxidation (E_a) and reduction (E_c) peaks, and can be calculated from Equation 1.1.

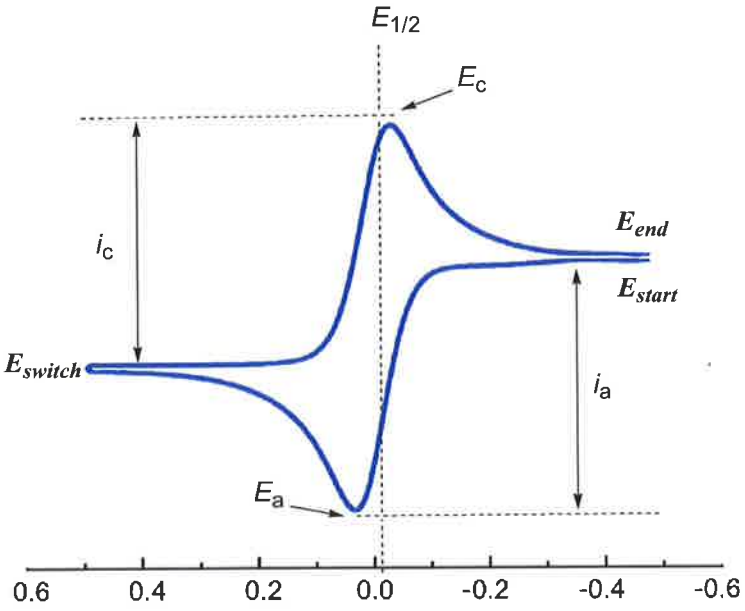

Figure 1.8: *A fully reversible one-electron process revealing the various parameters that can be extracted from the trace.*

$$E_{½} = |E_a - E_c| \qquad \textbf{Equation 1.1}$$

At 25°C, the oxidation and reduction waves should show Nernstian behaviour and can be described by Equation 1.2, where n is the number of electrons transferred.

$$|E_a - E_c| = \frac{0.057}{n} \qquad \textbf{Equation 1.2}$$

At 25°C, the peak current, i_a, is given by the Randles-Sevcik relationship (Equation 1.3),[65] where n is the number of electrons transferred, A is the electrode area (cm^2), D is the diffusion coefficient of the analyte ($cm^2\ s^{-1}$), C_o is the concentration of the analyte ($mol\ cm^{-3}$) and ν is the scan rate ($V\ s^{-1}$).

$$i_a = 2.69 \times 10^5 n^{3/2} A D^{1/2} C_o \nu^{1/2} \qquad \textbf{Equation 1.3}$$

From Equation 1.3, the reversibility of a redox process can be evaluated. If the diffusion coefficients are the same for the bulk analyte and the oxidised or reduced forms (which is quite often the case), then the ratio between the anodic and cathodic currents will be equal ($i_a/i_c = 1$) for a fully reversible system. Furthermore, a plot of the peak current versus the square root of the scan rate will show a linear relationship for a fully reversible system. Therefore, the reversibility of a redox process can be assessed by these two measurements.

The potential difference (ΔE) between the redox waves of two (usually equivalent) redox centres is commonly used to evaluate the extent of electronic interaction between two redox-active sites across a bridging ligand.[6,53,66] Consider a symmetric molecular wire with two redox-active end-groups. If there is no interaction between the two redox centres (Class I) and the spacer acts as an insulator, then the two redox centres will be oxidised or reduced at almost identical potentials, differing only by a small statistical factor [ΔE = 2(RT/F)ln2]. In this case, the cyclic voltammogram will show a single redox process, the height of which corresponds to a two-electron event (Figure 1.9a).[67]

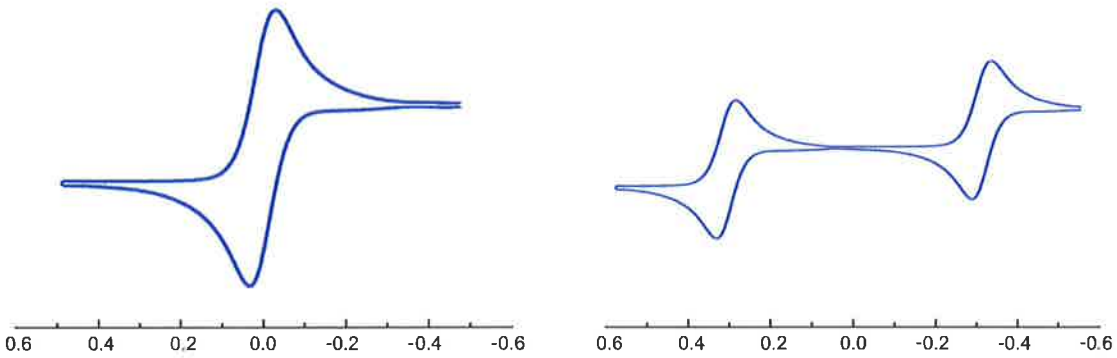

(a) **(b)**

Figure 1.9: *Cyclic voltammogram of (a) Class I and (b) Class III binuclear systems.*

If there are strong interactions between the two metal centres (Class III), the cyclic voltammogram will show two one-electron redox waves (Figure 1.9b). The first oxidation wave represents the formation of the mono-oxidised species, while the second involves the formation of the doubly oxidised state. For Class III materials

displaying strong interactions, the two redox-active sites in the MV state will possess intermediate oxidation states, i.e. Ru(2.5)/Ru(2.5) such as that found the Creutz-Taube ion **3**. For symmetric Class III compounds, ΔE is usually greater than 0.2 V.[6]

The comproportionation constant K_c is the equilibrium constant for the comproportionation reaction (Scheme 1.2) and can be calculated from ΔE between two waves using Equation 1.4 that simplifies to Equation 1.5 where ΔE has units of V (1J = 1C x 1V).[68,69]

$$\text{Ox-Ox} + \text{Red-Red} \overset{K_c}{\rightleftharpoons} 2\ \text{Ox-Red}$$

Scheme 1.2

$$K_c = \frac{[\text{Ox - Red}]^2}{[\text{Ox - Ox}][\text{Red - Red}]} = \exp\left[\frac{\Delta E \times \text{F}}{\text{RT}}\right] \qquad \textbf{\textit{Equation 1.4}}$$

$$K_c = \exp(\Delta E / 0.0257) \qquad \textbf{\textit{Equation 1.5}}$$

In Class II and Class III materials in which two distinct one-electron redox processes can be observed, ΔE gives an indication of the thermodynamic stability of the MV species relative to the doubly oxidised or doubly reduced states. In the case of the Creutz-Taube ion **3**, ΔE = 0.39 V which corresponds to a comproportionation constant $K_c \approx 3 \times 10^6$.[36] This indicates that the equilibrium for the comproportionation reaction lies far enough to the right hand side that the MV species can be prepared and isolated free from contamination from the doubly oxidised or doubly reduced states.

While ΔE is often associated with the degree of electronic interaction between two metal centres, it is also affected by other factors such as solvent,[66,70] counter ions[66,71] and structural rearrangement upon oxidation.[72] Therefore, care needs to be taken when describing the significance of ΔE and comparisons can only be made within related systems measured under similar experimental conditions.

1.3.4.4. NIR Spectroscopy

In the case where a MV compound is stable enough to allow isolation on a preparative or semi-preparative scale, absorption spectroscopy in the NIR region is also a means of evaluating interactions between two redox-active sites. The presence of an intervalence charge transfer (IVCT) band in the NIR region for a MV compound, which is not observed in the doubly oxidised or reduced forms, is an indication of intramolecular electron transfer. Observation of an IVCT band enables the electronic coupling parameter (V_{ab}) to be determined, allowing comparisons with related systems to be made. The parameter V_{ab} depends on the overlap of the electronic wave functions of the donor and acceptor sites and as a consequence the theory used to calculate V_{ab} depends on the classification of the MV compound within the Robin and Day system.[52] A brief explanation of the origin of the IVCT band is given below, with in-depth explanations available elsewhere.[73-75]

Consider a bridged bimetallic complex where the two redox sites are represented by [M] and its one-electron oxidised product [M^+] and separated by a bridging ligand. For simplicity, the two metal centres have the same coordination sphere, but one has been labelled to enable a distinction to be made. Since the coordination spheres are the same, the energy of the odd electron or hole will be identical at either site and the equilibrium constant for the electron transfer reaction (Scheme 1.3) will be K_{eq} = 1, as both the left and right hand sides will be energetically degenerate.

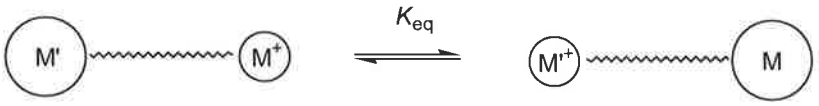

Scheme 1.3

Although there is no overall free energy change, an activation barrier, ΔG_{th}, will exist as a consequence of the differing bond lengths and force constants for [M] and [M^+], along with differences in solvation for the two sites in solution. As a result, electron transfer must be accompanied by nuclear rearrangement and this is the source of ΔG_{th}. According to the Franck-Condon Principle, nuclear motion (10^{-13} s) occurs on a much longer timescale than electronic motion (10^{-15} s). Therefore, prior

to electron transfer, the nuclear configurations of [M] and [M^+] and the surrounding medium must adjust from their equilibrium values to an intermediate value.

If spontaneous electron transfer were to occur between [M] and [M^+] in their equilibrium configurations, the product formed would be in a vibrationally excited state, as [M^+] would have the configuration of [M], and [M] would have the configuration of [M^+]. This is a thermally forbidden electron transfer pathway, illustrated by the upper route in Scheme 1.4. However, thermal electron transfer can occur within an activated complex in which the two redox centres each have the average configuration of [M] and [M^+], illustrated by the lower route in Scheme 1.4.

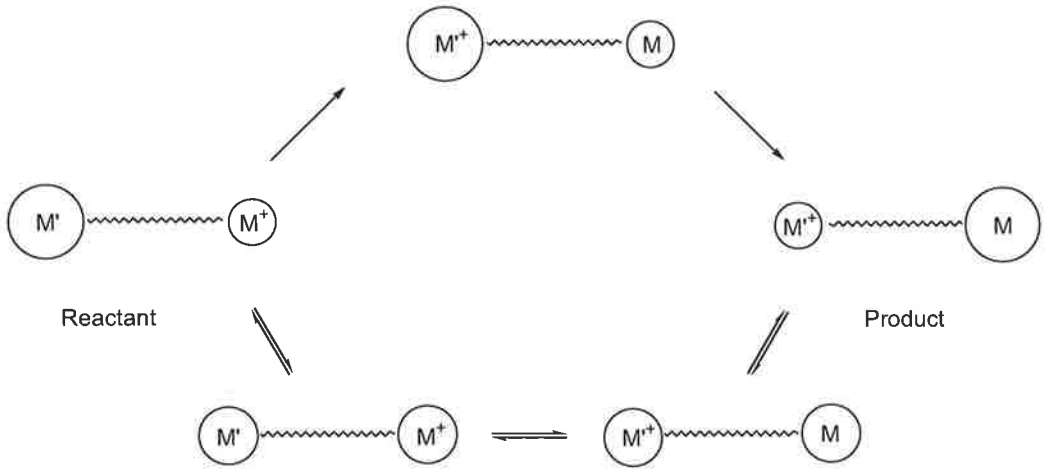

Scheme 1.4: *Thermally forbidden (upper) and thermally allowed (lower) electron transfer processes in a bimetallic complex.*[75]

While spontaneous electron transfer is thermally forbidden, it can occur upon absorption of light of the appropriate frequency to form an excited state. This optically-induced electron transfer process is depicted in the upper pathway in Scheme 1.4, and is the source of the IVCT band found in many MV complexes.

For electron transfer reactions, the potential energy of the system can be plotted as a function of a reaction coordinate, X, defining the changes in the inner and outer coordination spheres. For a zero-order process, two potential energy curves can be constructed for the electronic structures of M-M'^+ and M^+-M'. The reorganisation parameter, λ, is the vertical difference between the free energies of the non-interacting reactants and products at the equilibrium configuration.

In the absence of strong electronic interaction, the curves are displaced horizontally with respect to each other (Figure 1.10a), however with strongly interacting sites, mixing of the two electronic wave functions results in a change in the overall energies (Figure 1.10b).

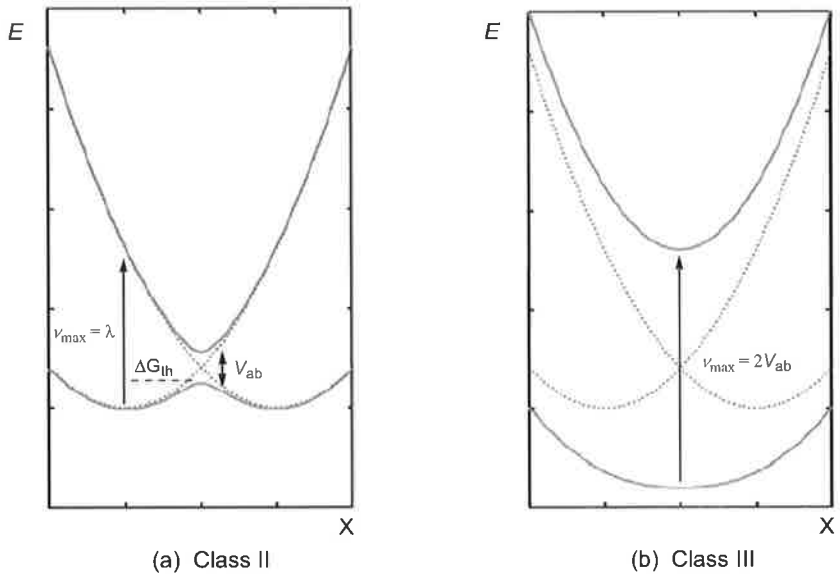

Figure 1.10: *Potential energy curves for (a) Class II and (b) Class III MV compounds. λ is the reorganisation parameter, V_{ab} is the electronic coupling parameter and ν_{max} is the energy of the IVCT transition.*[74]

If electronic coupling is small (Class II), the lowest potential energy surface possesses two minima and two different electronic states can exist (Figure 1.10a). In this case, these two states can interconvert thermally, the rate depending on the height of the energy barrier ΔG_{th}. Although thermal electron transfer does not occur without prior structural rearrangement, optical electron transfer can occur when $\nu_{max} = h\nu$. In the case of strong interactions (Class III), the activation barrier is no longer present as a consequence of the extended mixing of the two electronic wave functions, such that the properties of [M] and [M^+] are absent and only new properties of [M-M']$^+$ can be observed. In this case the compound cannot be regarded as being MV, and is better described by a molecular orbital (MO) approach.

For Class II and Class III MV compounds, the presence of a band in the NIR region typically corresponds to the optically-induced electron transfer process as shown in the upper pathway in Scheme 1.4. For Class I compounds, no IVCT band is observed as a consequence of there being no interaction between the two redox centres across the bridging ligand.

For Class II compounds where the two redox sites are weakly coupled, V_{ab} can be calculated from Equation 1.6, based on the Hush theory,[6,73,76] where ε is the molar extinction coefficient ($M^{-1}cm^{-1}$), ν_{max} is the energy of the IVCT band (cm^{-1}), $\Delta\nu_{½}$ is the half-height width of the IVCT band and $R_{MM'}$ is the through-space internuclear distance between the two redox-active centres (Å).

$$V_{ab} = 2.05 \times 10^{-2} \frac{\sqrt{(\varepsilon \nu_{max} \Delta\nu_{1/2})}}{R_{MM'}} \qquad \textit{Equation 1.6}$$

The theoretical band-width $(\Delta\nu_{½})_{theo}$ for Class II compounds can be calculated from Equation 1.7 and such calculations are often considered to be a diagnostic test enabling a distinction between Class II and Class III compounds.[45,77] Generally, values for $(\Delta\nu_{½})_{theo}$ in Class II materials are either in good agreement with or less than those derived from the experimentally observed IVCT bands.[41,74,75,78]

$$(\Delta\nu_{1/2})_{theo} = \sqrt{2310\nu_{max}} \qquad \textit{Equation 1.7}$$

For Class III complexes, determination of the electronic coupling parameter V_{ab} is somewhat simpler and is related to the energy of the IVCT band, as described by Equation 1.8.

$$V_{ab} = \frac{\nu_{max}}{2} \qquad \textit{Equation 1.8}$$

Calculation of V_{ab} for either Class II or Class III materials allows comparisons with related compounds to be made. Conclusions regarding the effectiveness of the bridging ligand to mediate electron transfer can then be drawn.

1.4. Work Described Within this Thesis

By definition, a molecular wire is a 'one-dimensional molecule allowing a through-bridge exchange of an electron/hole between its remote ends/terminal groups, themselves able to exchange electrons with the outside world'.[79] Considering this definition, complexes in which two redox-active transition metals are bridged by a yndiyl (-C≡C-) or polyyndiyl [-(C≡C)$_n$-] unit, are obvious candidates for molecular wires. Being a sub-set of molecular wires incorporating transition metals, compounds of the type [M]-C$_x$-[M] (where [M] represents a general redox-active metal-ligand end-group and C$_x$ is a linear *sp* carbon chain) have been of interest in recent times for their potential use in molecular electronics.[6,43-45]

Recent work has developed the syntheses and structural characterisation of compounds of this type with increasing numbers of carbon atoms in the straight chain. Cyclic voltammetry has been used to probe the electronic interactions in these systems, and generally confirms that strong interactions through the C$_x$ ligand exist for the lower analogues, which gradually decrease as the chain length is extended.

Work described within this Thesis involves the syntheses and properties of molecular wire models containing the electron-rich ruthenium end-group Ru(dppe)Cp*. Complexes containing even-numbered carbon chains capped by two ruthenium fragments are reported together with various complexes that serve to investigate the influence of other bridging groups towards electronic interactions between two ruthenium centres. The use of the Ru(dppe)Cp* fragment was expected to provide compounds that were oxidatively-sensitive allowing techniques such as cyclic voltammetry and NIR spectroscopy to evaluate the through-bridge exchange of a hole in the MV states. The use of this fragment also allows direct comparisons to be made with an analogous iron series containing the Fe(dppe)Cp* fragment. The Cp* ligand serves to increase the bulk of the end-groups, which was anticipated to have a two-fold effect. Firstly, it was expected that this bulky ligand together with the sterically demanding dppe ligand would facilitate crystallisation. Secondly, it has been demonstrated that the stabilities of polyyne compounds are strongly dependent on the sizes of the end-groups, with bulky end-groups affording

the highest stabilities by preventing thermal chain-chain cross-linking, a process that has extensive precedents with acetylenes,[80,81] diacetylenes[82-84] and triacetylenes.[85]

The influence of chain length on the electronic interaction was investigated by preparing a series of these complexes with varying numbers of carbon atoms. Where possible, the oxidised derivatives were prepared by chemical oxidation and their electronic structures were investigated using a combination of spectroscopic and structural characterisation. Isolation of the MV complexes enabled the electronic coupling parameter V_{ab} to be determined by measuring the NIR spectra, enabling comparisons to be made with related series.

While binuclear complexes containing the trinuclear clusters $Fe_3(CO)_9$ and $Cu_3(\mu\text{-dppm})_3$ have been reported, the influence that these groups have on electronic interactions has not been investigated. It is not clear if these groups will have an insulating or a conducting effect on the interactions, so preliminary studies of the redox behaviour of some of these complexes were carried out.

CHAPTER TWO

Syntheses, Structures and Spectroelectrochemistry of {Cp*(PP)Ru}(C≡CC≡C){Ru(PP)Cp*} (PP = dppm, dppe) and Their Mono- and Dications

2.1. Introduction

Complexes of the general formula [M]-$(CC)_n$-[M] with an even number of carbon atoms bridging two transition metals can be represented by one of the three valence structures below. Structures **2a** and **2c** are based on polyynes and feature alternating single and triple bonds, while structure **2b** is a fully double-bonded cumulenic system. The majority of [M]-$(CC)_n$-[M] complexes reported are best represented by the valence structure **2a**, but examples of both **2b** and **2c** have been found. Ultimately, the nature of the carbon chain in these complexes is a consequence of the interactions between the organic and metallic fragments within the molecule. Subsequently, the choice of metal, together with the oxidation state and ligand environment can all influence the structure of the bridging ligand.

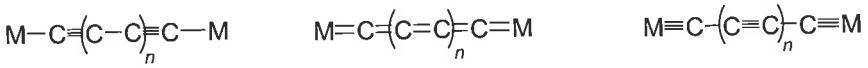

2a **2b** **2c**

2.1.1. Syntheses of Symmetric Diyndiyl Complexes

Diyndiyl complexes have the general formula [M]-C≡CC≡C-[M] and are a sub-set of polyyndiyl compounds that feature a bridging butadiynyl ligand. Generally, these complexes can be prepared by one of four synthetic strategies (Scheme 2.1):

(i) Homo-coupling between two metal ethynyl complexes [M]C≡CH;

(ii) Coupling of an organic C_4 unit with two equivalents of metal fragment;

(iii) Coupling of a monometallic diynyl complex [M]C≡CC≡CR with a single equivalent of metal fragment;

(iv) Alteration of the metal centres in a preformed diyndiyl complex by either a change in their oxidation state or coordination sphere.

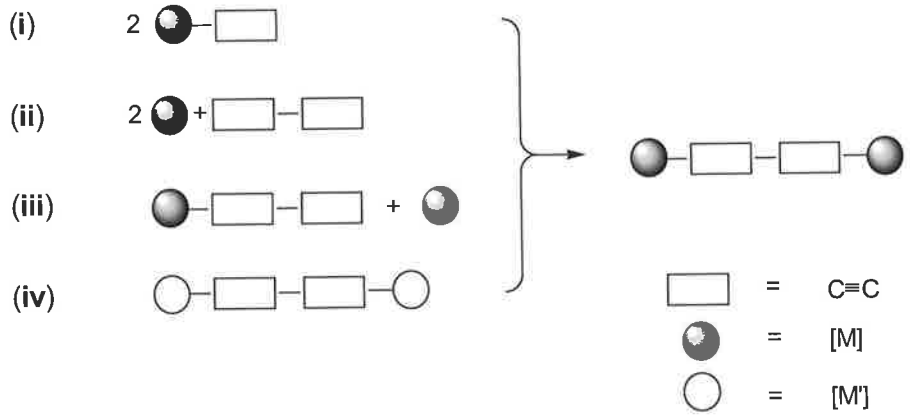

Scheme 2.1: *Synthetic strategies for [M]-C≡CC≡C-[M] complexes.*

Before attempting to synthesise a new diyndiyl complex, the chemistry of the starting materials together with the anticipated chemistry of the desired product or products, must be considered. For example, starting materials may be perfectly stable under one set of conditions, but they may decompose or give side reactions under different conditions. Alternatively, while the desired complex may be readily formed, the presence of a by-product or even the solvent may give further reactions and appreciable loss of yield.

Detailed below are some literature examples that demonstrate the four alternative strategies and the different reaction conditions that have been used to prepare a range of symmetric diyndiyl complexes.

2.1.1.1. Synthetic Strategy (i)

The coupling of two metal ethynyls has been used to synthesise a number of diyndiyl complexes including $\{Re(NO)(PPh_3)Cp^*\}_2(C{\equiv}CC{\equiv}C)$ (**4**)[45] and $\{Fe(dppe)Cp^*\}_2(C{\equiv}CC{\equiv}C)$ (**5**).[44] While both reactions involved oxidative couplings, different conditions were used in each case.

Glaser oxidative coupling conditions [$Cu(OAc)_2$/pyridine] were used to prepare **4** from the ethynyl complex $Re(C{\equiv}CH)(NO)(PPh_3)Cp^*$ (Scheme 2.2). Although this method is quite harsh, requiring the use of high temperatures (80°C), **4** was isolated in an excellent yield (88%).[45] More recently, the tritolylphosphine analogue $\{Re(NO)[P(tol)_3]Cp^*\}_2(C{\equiv}CC{\equiv}C)$ (**6**) has been prepared by the same method.[86]

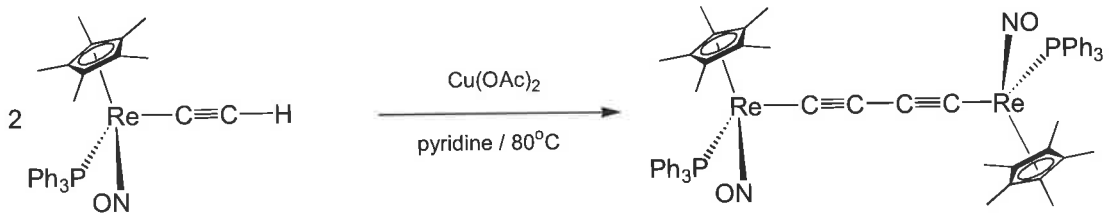

4

Scheme 2.2

Alternative conditions were used in the synthesis of the iron diyndiyl **5**. The one-electron oxidation of $Fe(C{\equiv}CH)(dppe)Cp^*$ with $[FeCp_2][PF_6]$ at -80°C generated a 17-electron radical, which underwent a spontaneous C-C coupling reaction to give an intermediate bis-vinylidene. Subsequent deprotonation with $KOBu^t$ gave **5** in 80% yield (Scheme 2.3).[44]

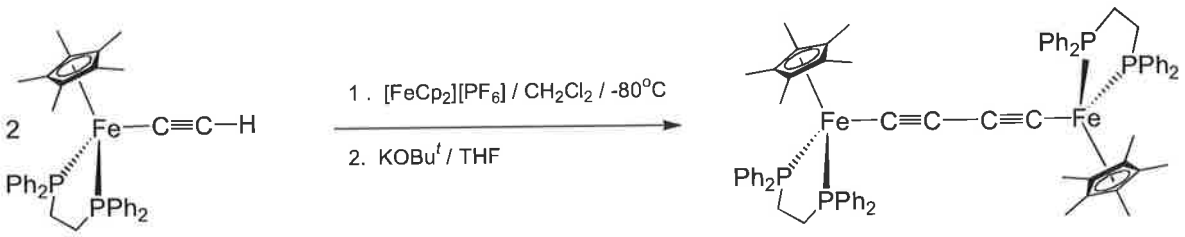

5

Scheme 2.3

The manganese diyndiyl $[\{Mn(dmpe)_2(C{\equiv}CH)\}_2(C{\equiv}CC{\equiv}C)]^+$ ($[\mathbf{7}]^+$) was prepared in a similar manner (Scheme 2.4). Proto-desilylation and subsequent deprotonation of $[Mn(dmpe)_2(C{\equiv}CTMS)_2]^+$ gave the radical $Mn(dmpe)_2(C{\equiv}CH)(C{\equiv}C\cdot)$, which underwent a spontaneous homo-coupling to give $\{Mn(dmpe)_2(C{\equiv}CH)\}_2(C{\equiv}CC{\equiv}C)$

(**7**). Subsequent oxidation of **7** *in situ* by the intermediate $[Mn(dmpe)_2(C{\equiv}CH)_2]^+$ formed in the reaction mixture, gave the final product $[\mathbf{7}]^+$ in an overall 65% yield.[87]

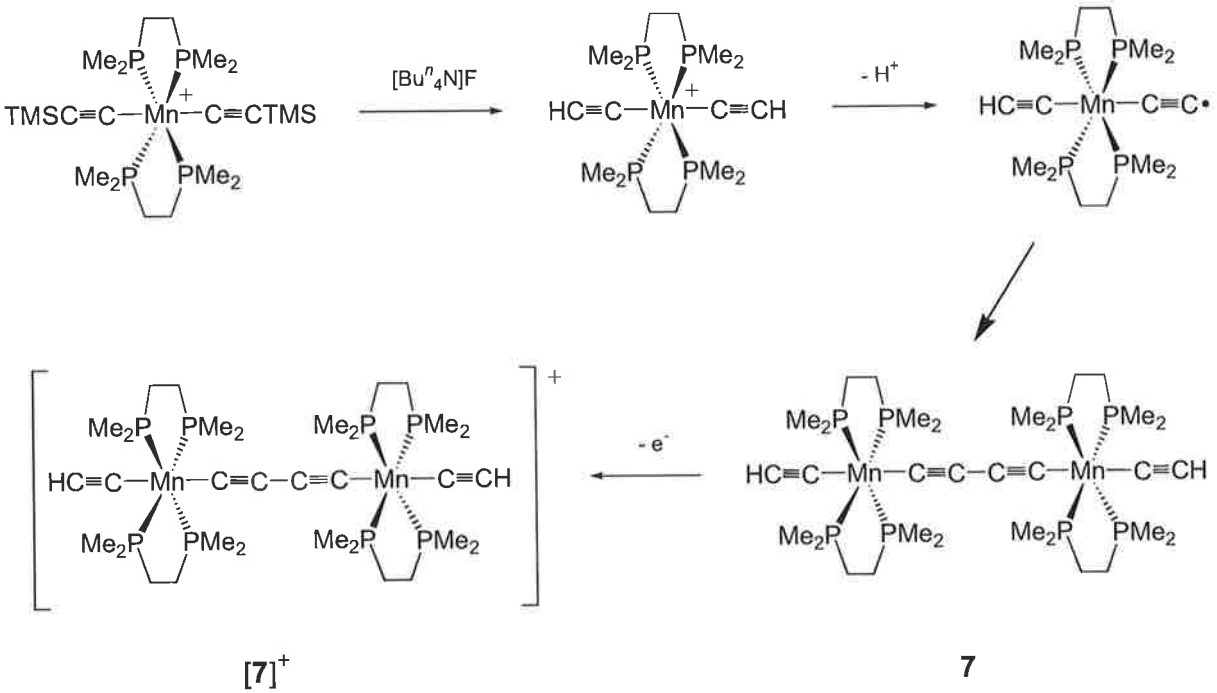

Scheme 2.4

2.1.1.2. Synthetic Strategy (ii)

Strategy (ii) is the most frequently used method to synthesise diyndiyl complexes and involves the coupling of a preformed organic C_4 unit with two equivalents of the desired metal-ligand fragment. The versatility of this method is a consequence of the large number of suitable butadiynyl based starting materials, together with a considerable number of coupling conditions that can be used.

Butadiyne (HC≡CC≡CH) is the simplest diyne molecule and can be prepared by the reaction between 1,4-dichlorobutyne and aqueous KOH, followed by distillation, trapping it in a solvent such as pentane or THF.[88] Kept at low temperatures, it can be stored for periods of up to one week. While manipulations of butadiyne must be treated with care, it has been used to synthesise a number of diyndiyl complexes.

The rhodium and iridium complexes, $\{MHCl(PPr^{i}_{3})_2\}_2(C{\equiv}CC{\equiv}C)$ [M = Rh (**8**), Ir (**9**)], were prepared by the reaction of the Group 9 starting materials with butadiyne in hexane at low temperatures (Scheme 2.5). These relatively unstable diyndiyl complexes were isolated in moderate yields [68% (**8**), 46% (**9**)] and were further reacted with pyridine to give the more stable adducts **10** and **11**, respectively (Scheme 2.5).[89,90]

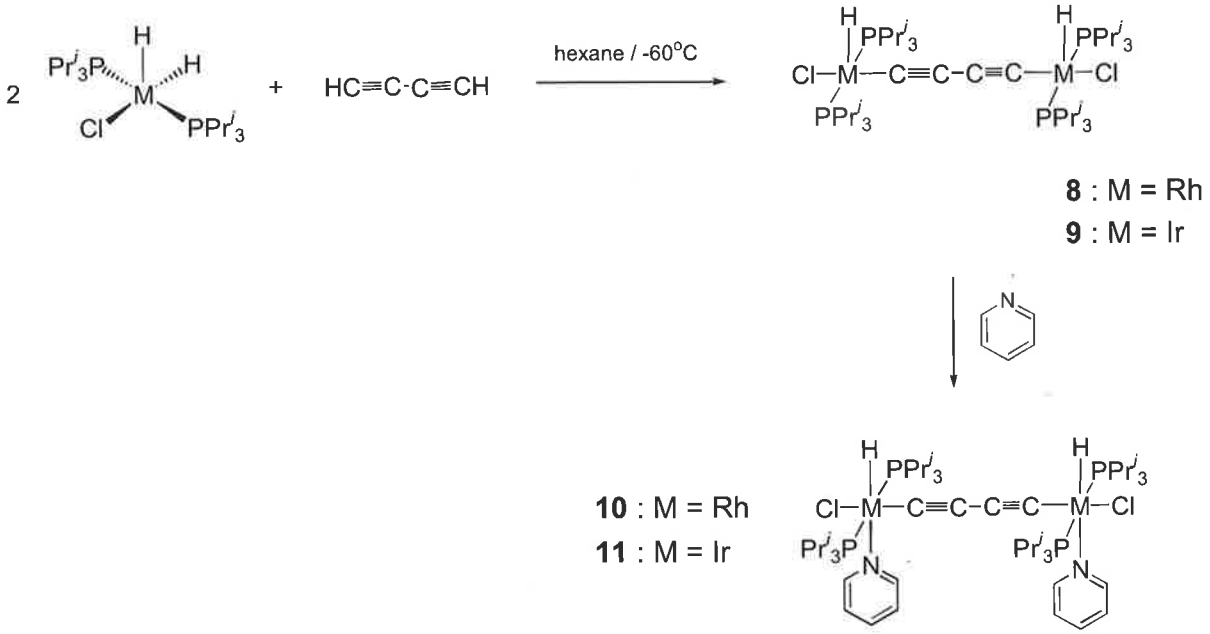

Scheme 2.5

The di-lithio derivative of butadiyne LiC≡CC≡CLi can be prepared by a number of different reactions. Addition of the organo-lithium reagent Bu^{n}Li to solutions of butadiyne[91] or *cis*-HC≡CCH=CH(OMe)[92] at low temperatures, or the treatment of TMSC≡CC≡CTMS[93] with excess MeLi are all suitable methods for its preparation.

The nucleophilic species, LiC≡CC≡CLi reacts with two equivalents of $FeCl(CO)_2Cp$ to give the diyndiyl complex **12** in 40% yield with elimination of LiCl (Scheme 2.6).[94,95]

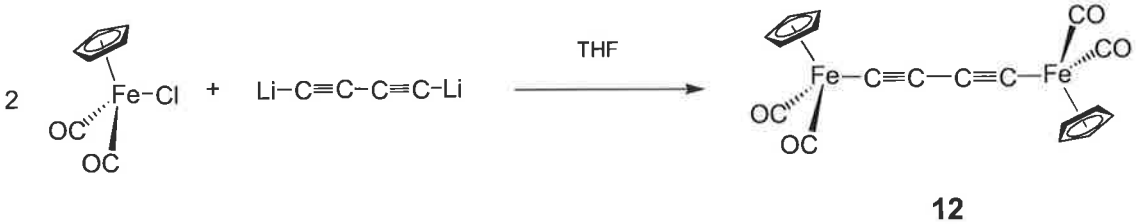

12

Scheme 2.6

In an alternative method, the organostannane $Me_3SnC{\equiv}CC{\equiv}CSnMe_3$, which can be prepared by treating $LiC{\equiv}CC{\equiv}CLi$ with $SnClMe_3$, reacts with two equivalents of $FeI(CO)_2Cp$ in the presence of $PdCl_2(NCMe)_2$ to give **12** in 43% yield (Scheme 2.7).[96]

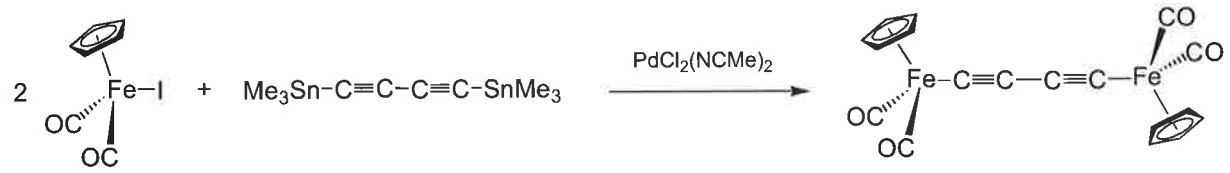

12

Scheme 2.7

1,4-bis(trimethylsilyl)butadiyne ($TMSC{\equiv}CC{\equiv}CTMS$) is a very stable and easy to use derivative of butadiyne. It is a white crystalline solid that can be prepared in large quantities by the oxidative coupling of $TMSC{\equiv}CH$ under Hay coupling conditions ($CuCl/TMEDA/O_2$).[97] It has been used in the preparation of a number of diyndiyl complexes, including $\{Ru(PPh_3)_2Cp\}_2(C{\equiv}CC{\equiv}C)$ (**13**), prepared by a fluoride-catalysed desilylation of $TMSC{\equiv}CC{\equiv}CTMS$ in the presence of excess $RuCl(PPh_3)_2Cp$ in 66% yield (Scheme 2.8).[98]

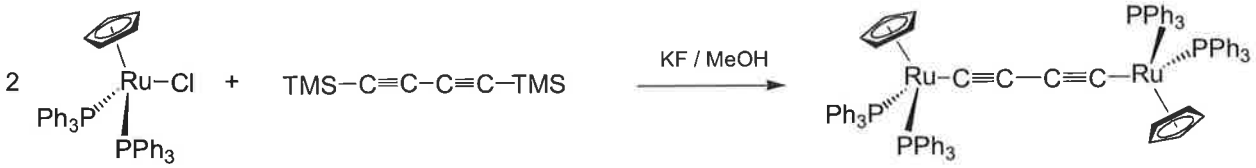

13

Scheme 2.8

Other examples of diyndiyl complexes prepared under similar conditions include those containing $AuPCy_3$[99] and $Rh(CO)(PPr^i_3)_2$[100] end-groups, which both use the hydroxide anion as the desilylating agent.

Using a similar approach, the manganese complex $\{Mn(dmpe)_2I\}_2(C{\equiv}CC{\equiv}C)$ (**14**) was isolated from the reaction between two equivalents of $MnI(dmpe)Cp^{Me}$ and $Me_3SnC{\equiv}CC{\equiv}CSnMe_3$ in the presence of dmpe, in 70% yield (Scheme 2.9).[101]

14

Scheme 2.9

2.1.1.3. Synthetic Strategy (iii)

Preparation of diyndiyl complexes using strategy (iii) has also been a useful method. The iron diyndiyl $\{Fe(dippe)Cp^*\}_2(C{\equiv}CC{\equiv}C)$ (**15**) was synthesised by the reaction of $Fe(C{\equiv}CC{\equiv}CH)(dippe)Cp^*$ with one equivalent of $FeCl(dippe)Cp^*$ in a THF/MeOH mixture and in the presence of KPF_6 and $KOBu^t$, in 70% yield (Scheme 2.10).[102]

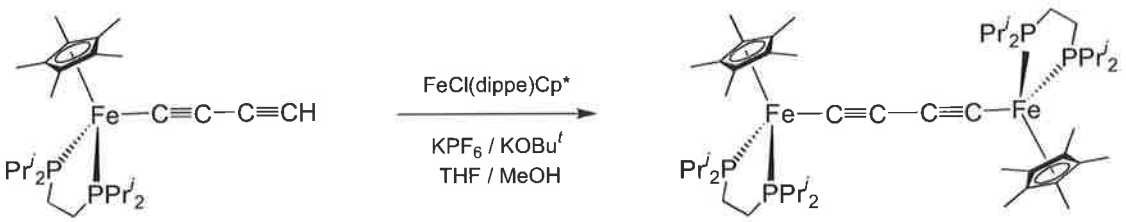

15

Scheme 2.10

Alternative coupling conditions were used in the syntheses of the tungsten diyndiyls $\{W(CO)_3Cp'\}_2(C{\equiv}CC{\equiv}C)$ [Cp' = Cp (**16**), Cp* (**17**)]. In the initial step, the reaction of $WCl(CO)_3Cp'$ with excess $HC{\equiv}CC{\equiv}CH$ in the presence of CuI and an amine solvent gave the butadiynyl complexes $W(C{\equiv}CC{\equiv}CH)(CO)_3Cp'$. These react further under the same conditions with a stoichiometric amount of the tungsten halide

starting material to give **16** and **17** in 71 and 69% yields, respectively (Scheme 2.11).[103-105]

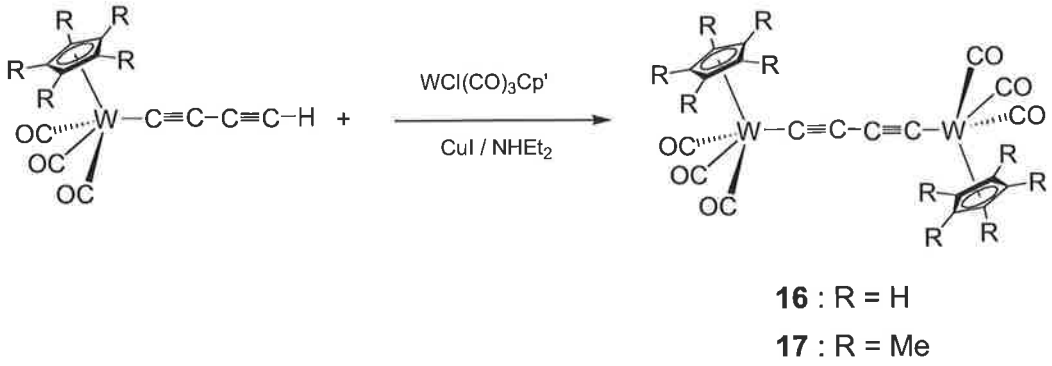

Scheme 2.11

2.1.1.4. Synthetic Strategy (iv)

The final synthetic strategy involves an alteration of the metal centres capping the carbon chain in a preformed diyndiyl complex. This approach has been successfully used to synthesise the mixed phosphine complex, $\{Ru(PPh_3)(PMe_3)Cp\}_2(C{\equiv}CC{\equiv}C)$ (**18**), which was formed upon heating a solution of **13** with excess PMe_3 in refluxing toluene. Trituration of the oily residue gave **18** as an air-sensitive yellow solid in 43% yield (Scheme 2.12).[43]

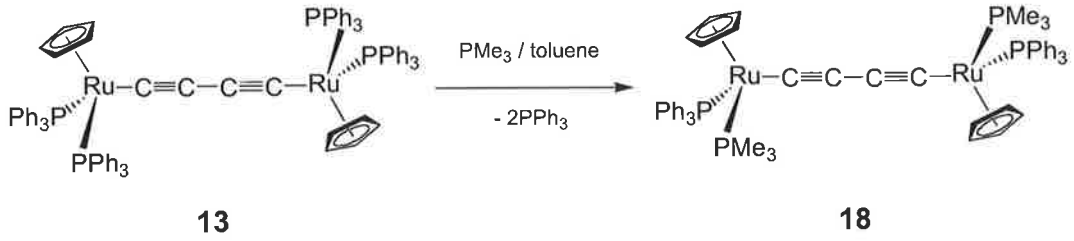

Scheme 2.12

2.1.2. Properties of Diyndiyl Complexes

Bimetallic complexes bridged by diyndiyl ligands have been of interest in recent times due to their potential applications in materials science. Such complexes have

been suggested as components of non-linear optical and liquid crystalline devices.[106,107] For the majority of diyndiyl complexes reported, however, the redox properties have been of particular interest in connection with their potential use as molecular wires.

The cyclic voltammograms of many of these complexes show varying numbers of redox waves depending on the metal centres used. The influence that the auxiliary ligands have on the number and position of these processes can be examined by comparing the redox potentials of diyndiyl complexes within a given metal series. It has been established that substitution with more electron-donating ligands reduces the oxidation potential of the resulting diyndiyl complex.[43,86,102] The cyclic voltammograms of some of these complexes confirm the presence of strong electronic interactions between the two metals across the C_4 ligand. Chemical oxidation of the neutral complexes has allowed the isolation of the stable oxidised forms, which have been structurally characterised in some cases.

Mössbauer spectroscopy, supported by crystallographic analysis of the iron dication [**5**][PF_6]$_2$ suggested that upon oxidation, the diyndiyl nature of the carbon chain (Structure **2a**, page 21) was retained while generating two Fe(III) centres.[44] This is in contrast to the rhenium complex [**4**][PF_6]$_2$, which was shown by crystallographic and spectroscopic evidence to have a reduced C≡C bond order with a simultaneous increase in the C-C bond order relative to the neutral species **4**.[45] The cation in [**4**][PF_6]$_2$ is best described as a cumulene (Structure **2b**).

The cyclic voltammograms of the ruthenium diyndiyls **13** and **18** both displayed four one-electron redox steps as the 0/1+/2+/3+/4+ oxidation states were sequentially generated. While the mono- and dications of **13** have been isolated, suitable crystalline material was not obtained and therefore their single crystal X-ray structures could not be determined. Despite the lack of structural evidence, spectroscopic data and theoretical calculations have suggested that the dication in [**13**][PF_6]$_2$ adopts a cumulenic form **2b** similar to that observed in [**4**][PF_6]$_2$.[43]

2.2. Aims

The primary aim of this work is to synthesise analogues of the previously reported $[\mathbf{13}]^{n+}$ (n = 1, 2) that are more readily crystallised. Substitution by strongly electron-donating ligands, such as Cp* and the bis-phosphines dppm/dppe is anticipated to stabilise the oxidised species. The influence of the strongly electron-donating ligands towards the electronic coupling between the ruthenium centres will also be investigated by comparing the values of K_c and V_{ab} with those previously found for **13** and **18**.

This Chapter reports the syntheses and characterisation of two new ruthenium diyndiyl complexes containing the Ru(PP)Cp* fragments [PP = dppm (series **a**), dppe (series **b**)]. Of significant interest in relation to their electronic structures, X-ray structure determinations of the neutral compound, and of the mono- and dications derived from series **b**, are also reported.

2.3. Results and Discussion

2.3.1. Synthesis of RuCl(PP)Cp [PP = dppm (19a), dppe (19b)]*

While the syntheses of the starting chloro-ruthenium complexes RuCl(dppm)Cp* (**19a**) and RuCl(dppe)Cp* (**19b**) have previously been reported,[108] the synthetic details are quite vague. Outlined below and in Scheme 2.13 is the three step syntheses of **19a/b** together with the details of the slightly modified final step.

The complex $RuCl(PPh_3)_2Cp$ is readily prepared by the reaction of $RuCl_3.3H_2O$ with CpH and PPh_3 in refluxing EtOH.[109] However, if Cp*H is used instead of CpH, $RuCl_2(PPh_3)_4$ is isolated as the sole product.[110] In the absence of phosphine, $RuCl_3.3H_2O$ reacts with Cp*H giving decamethylruthenocene $RuCp^*_2$ (10%), while the major product is a brown crystalline solid with the formula $[RuCl_2Cp^*]_n$ (**20**) (80%).[111] The structure of the latter complex has been suggested to be a chloro-bridged oligomer as illustrated in Scheme 2.13.[112]

The use of freshly distilled Cp*H in degassed MeOH or EtOH was essential for the efficient formation of oligomer **20**. Heating the reaction mixture to reflux for three hours resulted in the product crystallising from solution and it was filtered and washed with portions of MeOH and hexane to ensure complete removal of any free Cp*H or trace quantities of $RuCp^*_2$.

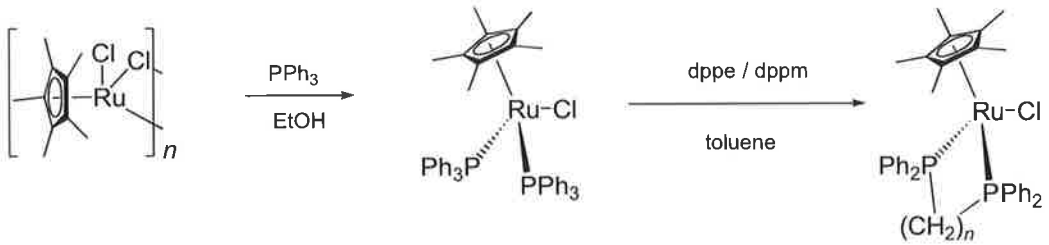

20 **21** **19a** : *n* = 1
19b : *n* = 2

Scheme 2.13

If MeOH was used as the reaction solvent the product obtained was insoluble in $CHCl_3$ or CH_2Cl_2, however if EtOH was used, the product was much more soluble suggesting that the product from the former reaction was a higher oligomer than that obtained in the latter case.[112] Despite this, it was found that either product could be used in the next stage of this reaction sequence.

The second step in the sequence involved the formation of the mono-nuclear species $RuCl(PPh_3)_2Cp^*$ (**21**). This reaction involved heating a suspension of **20** with excess PPh_3 in EtOH for 24 hours.[108] In this reaction, PPh_3 acts both to coordinate ruthenium and to reduce the ruthenium centre from Ru(III) to Ru(II). The orange product was filtered directly from the cooled reaction mixture and washed with hexane to remove any excess phosphine. Complex **21** readily decomposes in chlorinated solvents and was best used without further purification.

The final step in the sequence involved exchange of the two PPh_3 ligands with bidentate ligands dppm or dppe. Heating a solution of **21** and the appropriate bis-phosphine in toluene for three hours, followed by purification, gave the final products **19a/b** in excellent yields. It has previously been demonstrated that this reaction proceeds *via* an intermediate where the bis-phosphine firstly coordinates as a monodentate ligand, before the remaining PPh_3 is displaced by the second arm of the bidentate ligand (Scheme 2.14).[113] A modified procedure for **19a/b** is given in the Section 2.5.[108]

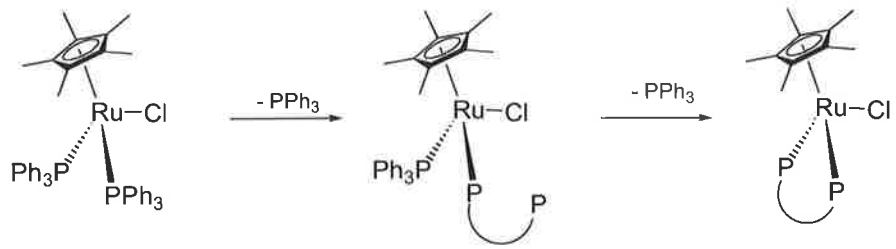

21 PP = dppm / dppe

Scheme 2.14

Single crystals of **19a** from CH_2Cl_2/hexane and **19b** from pentane were grown, and their ORTEP plots are given in Figure 2.1, while selected structural parameters are collected in Table 2.1.

	19a	**19b**
Bond distances (Å)		
Ru-P(1)	2.282(2)	2.2882(5)
Ru-P(2)	2.294(2)	2.2812(5)
Ru-C(Cp*)	2.185(9)-2.22(1)	2.219-2.252(2)
(av.)	2.20(2)	2.24(1)
Ru-Cl	2.434(2)	2.4532(5)
Bond angles (°)		
P(1)-Ru-P(2)	71.53(6)	82.15(2)
P(1)-Ru-Cl	83.25(7)	81.93(2)
P(2)-Ru-Cl	87.59(7)	90.93(2)

Table 2.1: *Selected structural parameters for **19a/b**.*

The coordination around ruthenium in both structures is pseudo-octahedral with the chlorine and bis-phosphine ligands taking up one face of the octahedron while the Cp* ligand occupies the opposite face.

Notable differences between the two structures include the average Ru-C(Cp*) [2.20(2) (**19a**), 2.24(1) Å (**19b**)] and the Ru-Cl distances [2.434(2) (**19a**), 2.4532(5) Å (**19b**)]. The shorter Ru-Cp* and Ru-Cl bond lengths in **19a** are most likely the result of the more compact dppm ligand, which is also reflected in the smaller bite angle of 71.53(6)° for **19a**, than for 82.15(2)° found in **19b**. The Ru-P distances are similar in both complexes [range 2.2812(5)-2.294(2) Å].

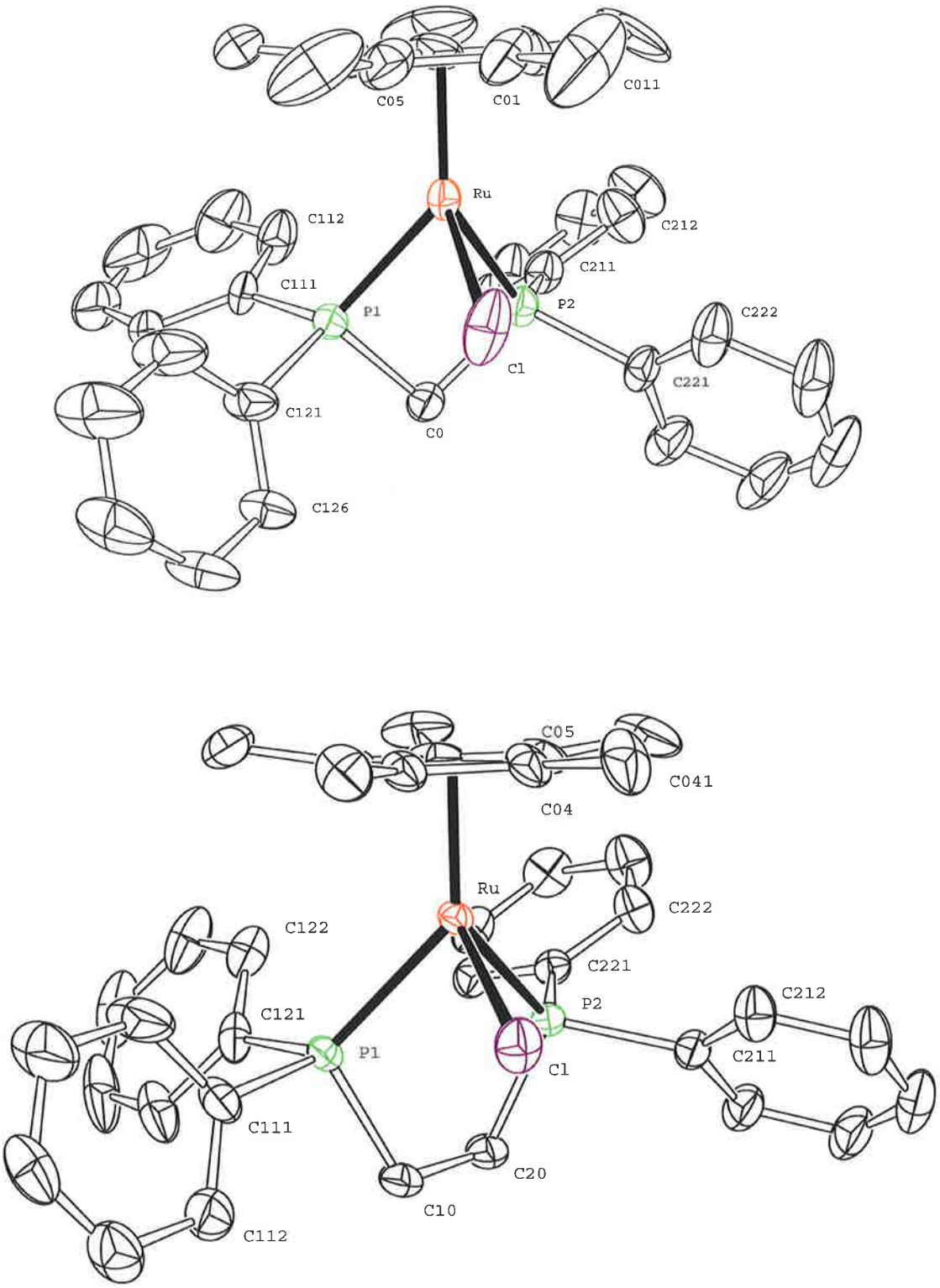

Figure 2.1: *ORTEP views of* ***19a*** *(top) and* ***19b*** *(bottom).*

2.3.2. Synthesis of {Ru(PP)Cp}$_2$(C≡CC≡C) [PP = dppm (25a), dppe (25b)]*

The ruthenium diyndiyl **13** was readily prepared by the fluoride-catalysed desilylation of TMSC≡CC≡CTMS in the presence of $RuCl(PPh_3)_2Cp$.[98] While this reaction has been used to prepare several related complexes within the Ru(dppe)Cp* series (see Chapter 6), it was found the reaction of **19a/b** with TMSC≡CC≡CTMS gave deep blue solutions, which were shown by NMR to contain a mixture of products. The details of these reactions are given in Chapter 4. Consequently, an alternative strategy was required and the reaction sequence used to prepare the analogous iron diyndiyl **5** was successfully adopted (Scheme 2.15).[44]

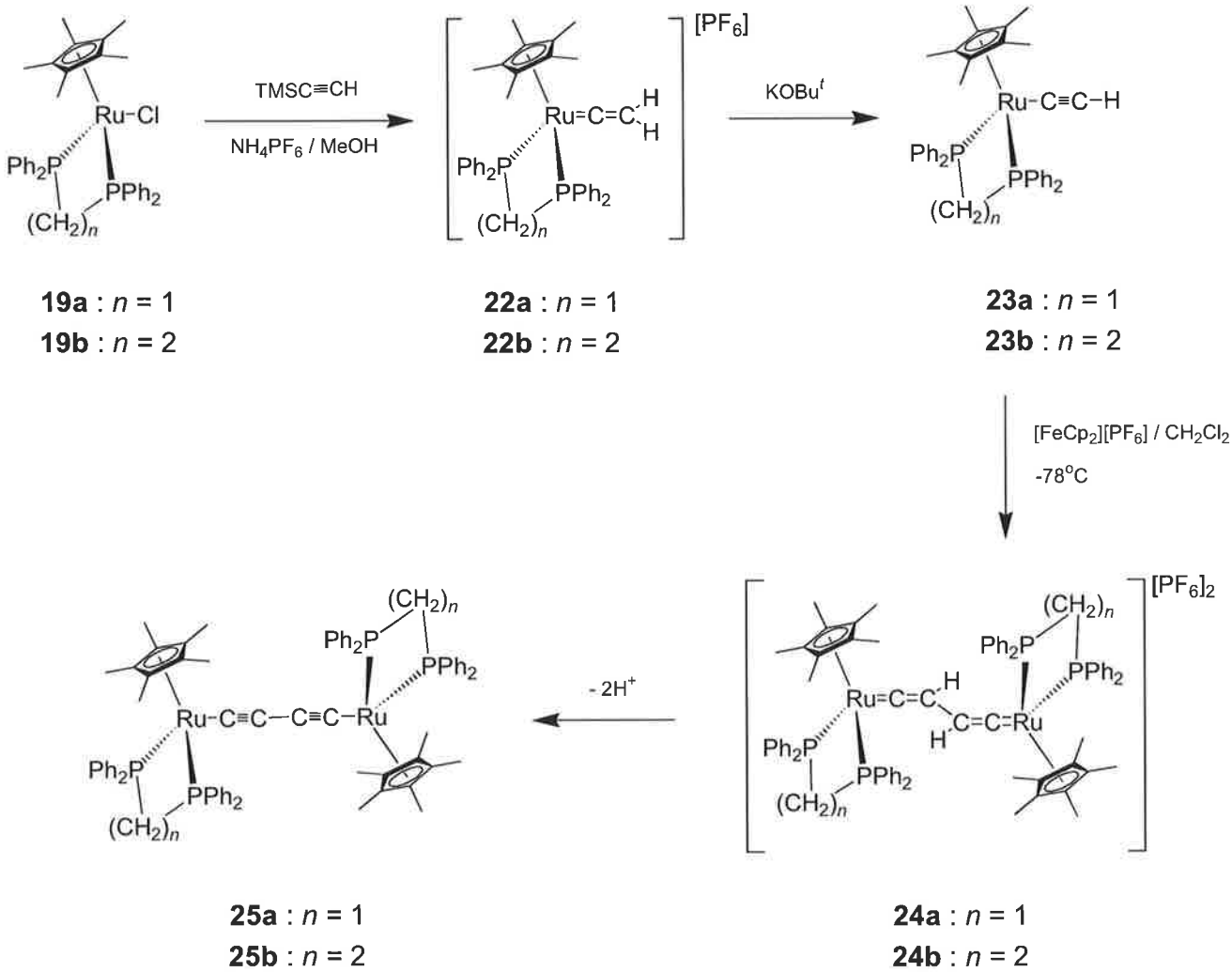

19a : *n* = 1
19b : *n* = 2

22a : *n* = 1
22b : *n* = 2

23a : *n* = 1
23b : *n* = 2

25a : *n* = 1
25b : *n* = 2

24a : *n* = 1
24b : *n* = 2

Scheme 2.15

Accordingly, the chlorides **19a** and **19b** were converted to the bright yellow vinylidenes $[Ru(=C=CH_2)(PP)Cp^*][PF_6]$ (**22a/b**) by reaction with excess TMSC≡CH in MeOH and in the presence of NH_4PF_6 in 96 and 95% yields, respectively. These reactions proceeded very quickly with the product crystallising out from the hot MeOH solutions. The presence of the ammonium salt in this reaction was necessary to assist the ionisation of the Ru-Cl bond and to stabilise the vinylidene as the PF_6^- salt. If CH_2Cl_2 was used as the solvent, reaction times were considerably longer [5 days (**22a**), 24 hours (**22b**)] with lower yields of 62 and 74%, respectively. The significant difference in reactivity between **19a** and **19b** in CH_2Cl_2 may be due to the decreased length and consequent increased strength of the Ru-Cl bond in **19a** compared with **19b** (Table 2.1).

Deprotonation of **22a/b** with $KOBu^t$ in THF afforded the neutral ethynyl derivatives Ru(C≡CH)(PP)Cp* (**23a/b**) in essentially quantitative yields. These complexes were further purified by chromatography on a basic alumina column, but it was found that if solutions were left exposed to air, the colour would slowly change from yellow to green, possibly due to oxidation.

An alternative method for the preparation of **23a/b** was later devised, involving the addition of dbu to a suspension of **22a/b** in a small quantity of acetone. This gave the bright yellow ethynyl complexes in *ca* 90% yields without further purification.

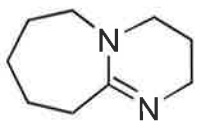

1,8-diazabicyclo[5.4.0]undec-7-ene (dbu)

Oxidative coupling of the ethynyls **23a/b** to give the bis-vinylidene complexes $[\{Ru(PP)Cp^*\}_2(=C=CHCH=C=)][PF_6]_2$ (**24a/b**) occurred upon stirring a CH_2Cl_2 solution with a slight deficiency of $[FeCp_2][PF_6]$ for three hours at -78°C. Slow addition of diethyl ether to the reaction mixture resulted in the products crystallising as brick red solids in 96 and 85% yields, respectively.

Deprotonation (dbu or KOBu^t) of **24a/b** followed by extraction in hot hexane gave the desired diyndiyls {Ru(PP)Cp*}$_2$(C≡CC≡C) (**25a/b**) as bright orange crystalline solids in 90% yield in each case. Although deprotonation of **24a** with dbu gave **25a** as the sole product, a mixture of products were obtained when KOBu^t was used and further details of this reaction are given in Chapter 3. Only one product was found in the case of deprotonation of **24b** with either dbu or KOBu^t.

2.3.3. Spectroscopic Properties of 22-25

All complexes were readily identified from their spectroscopic data and elemental analysis. Most informative in the IR spectra were the bands found near 1625 [vinylidene ν(C=C)], 3265 and 1930 [ethynyl ν(≡CH) and ν(C≡C)], 1600-1635 [vinylidene ν(C=C)] and 1970 cm^{-1} [ethynyl ν(C≡C)] for **22**, **23**, **24** and **25**, respectively. These changes are fully consistent with the expected variations in CC bond order.

In the ^{1}H NMR spectra of **22-25**, single resonances were observed for the Cp* ligands, with its position having no apparent correlation with bis-phosphine or overall charge of the complex. Multiplets for the CH_2 protons of dppm were found downfield between δ 4.08-5.18 while those for dppe were found in the range δ 1.95-2.94. For **22a/b**, the vinylic protons were observed as triplets at *ca* δ 3.0, while in **24a/b**, these were shifted slightly downfield to δ 3.72 and 3.13, respectively. In the ethynyls **23a/b**, triplets at δ 1.52 and 1.57, respectively, were assigned to the acetylenic protons.

In the ^{13}C NMR spectra, interesting changes in the resonances of the carbon chain atoms were observed as the individual steps were realised. As observed in related systems, characteristic resonances for the carbon atoms of the vinylidene ligands in **22a/b** were observed at δ 344.54 and 344.21 (triplets, C_1) and at δ 102.26 and 102.65 (singlets, C_2), respectively. Theoretical studies have shown that such exceptional deshielding of the C_1 resonance in vinylidene complexes is influenced

more by the size of the HOMO-LUMO energy gap rather than the electron-deficient nature of C_1.[114,115]

In the ethynyl derivatives **23a/b**, both carbon atoms C_1 and C_2 resonated as triplets, with C_1 showing the larger ^2J(CP) at δ 120.26 (23 Hz) and 120.58 (23 Hz) for **23a** and **23b**, respectively. In **23a**, C_2 gave a poorly resolved triplet at δ 93.01, whereas in **23b** the C_2 resonance occurred at δ 92.99 with the ^3J(CP) coupling of 2 Hz being fully resolved. The bis-vinylidenes **24a/b** also exhibited the characteristic downfield triplets at δ 348.59 and 348.08, respectively, confirming the presence of the Ru=C double bond, while atoms C_2 resonated as singlets at *ca* δ 103.

In the ^{31}P NMR spectra, resonances between δ 4.76 and 18.0 were found for the dppm complexes, while for the dppe derivatives, resonances were observed between δ 75.92 and 82.53. If the PF_6^- anion was present, a characteristic septet resonance was found at *ca* δ -143.

The ES-mass spectra of the vinylidene and ethynyl complexes were identical within each series, with either $[M]^+$ or $[M + H]^+$ ions found at *m/z* 647 (series **a**) and *m/z* 661 (series **b**). For the dicationic bis-vinylidenes, $[M + PF_6]^+$ ions were found at *m/z* 1436 (**24a**) and at *m/z* 1465 (**24b**).

For complexes **25a/b**, strong IR ν(C≡C) absorptions were observed at 1966 (**25a**) and 1973 cm^{-1} (**25b**), confirming their diyndiyl nature. In the ^{1}H NMR spectra, the Cp* protons were found as singlet resonances at δ 1.89 (**25a**) and 1.95 (**25b**), while the CH_2 protons of the PP ligands resonated as multiplets at δ 4.23 for **25a** and at δ 1.95 and 2.71 for **25b**. In the ^{13}C NMR spectrum of **25a** and **25b**, the C_1 resonances were found as triplets at δ 93.25 and 94.63 [^2J(CP) 27 Hz], while resonances for C_2 were found upfield at δ 100.38 and 99.47 (both singlets), respectively. There are again significant differences in the ^{31}P chemical shifts, with singlets at δ 17.50 (**25a**) or 82.53 (**25b**) observed. The ES-mass spectra recorded in MeOH solutions contained $[M]^+$ ions at *m/z* 1290 and 1318 for **25a/b**, respectively.

2.3.4. Redox Chemistry

The redox potentials for complexes **19a/b** and complexes **22a/b-24a/b** measured under similar conditions are given in Table 2.2. In the case of the chloro-ruthenium complexes **19a/b**, a single reversible and a second irreversible oxidation wave were observed. The dissociation of the Cl^- anion in solution cannot be ruled out and the resulting ruthenium cation may be the source of the irreversible wave found at higher potentials. Single irreversible processes were found for the vinylidene complexes **22a/b**, with the expected high potentials for cations ($E_{½}$ = +1.74/+1.68 V, respectively). In the neutral ethynyl complexes **23a/b**, a single irreversible wave was observed in each case at $E_{½}$ = +0.26/+0.34 V, respectively. This presumably corresponds to the oxidative coupling to give **24a/b**, although no evidence for **24a/b** was found. Two reversible waves were seen for the bis-vinylidenes **24a/b** at $E_{½}$ = +1.00 and +1.26 V in each case.

In general, the neutral complexes **19a** and **23a** (with dppm) are more readily oxidised than their dppe analogues (**19b** and **23b**). As expected, cationic complexes **22a/b** and **24a/b** were oxidised at higher potentials than the neutral species. No reduction processes were found for any of the complexes within the solvent imposed limits.

Complex		E_1	E_2
19a	RuCl(dppm)Cp*	+0.25	+1.15 [a]
19b	RuCl(dppe)Cp*	+0.28	+1.37 [a]
22a	[Ru(=C=CH$_2$)(dppm)Cp*][PF$_6$]	+1.74 [a]	
22b	[Ru(=C=CH$_2$)(dppe)Cp*][PF$_6$]	+1.68 [a]	
23a	Ru(C≡CH)(dppm)Cp*	+0.26 [a]	
23b	Ru(C≡CH)(dppe)Cp*	+0.34 [a]	
24a	[{Ru(dppm)Cp*}$_2$(=C=CHCH=C=)][PF$_6$]$_2$	+1.00	+1.26
24b	[{Ru(dppe)Cp*}$_2$(=C=CHCH=C=)][PF$_6$]$_2$	+1.00	+1.26

Table 2.2: *Redox potentials (V) for **19a/b** and complexes **22a/b-24a/b**, recorded in CH_2Cl_2, 0.1 M $[Bu^n_4N][PF_6]$.* [a] *Peak potential of an irreversible process.*

The rationale for this project was to develop Ru-C_4-Ru systems with lower oxidation potentials than the previously described examples **13** and **18**, with the intention of generating more stable oxidised products. Consequently, the cyclic voltammograms of **25a** and **25b** were recorded (Figure 2.2) and the resulting data are summarised in Table 2.3, together with corresponding data for some related complexes. In the case of **25a** the first two oxidation processes (E_1 and E_2) were fully reversible [i_a/i_c = 1; current proportional to (scan rate)$^{1/2}$]. The E_3 process in **25a** was only partially reversible (i_a/i_c = 0.7), while E_4 was totally irreversible. In **25b**, the first three oxidations were reversible [i_a/i_c = 1; current proportional to (scan rate)$^{1/2}$], while E_4 was only partially reversible (i_a/i_c = 0.7).

The E_1 potentials for **25a/b** at -0.48 and -0.43 V, respectively, are lower than those previously determined for **13** and **18** (Table 2.3).[43] This result is to be expected upon substitution with more electron-donating ligands. Similar comments apply to E_2, which were also found at significantly lower potentials. However, as oxidation proceeds, potentials for the E_3 processes were essentially identical for all four ruthenium diyndiyl complexes, while the E_4 couples of **25a** and **25b** [at +1.44 (irr.), +1.54 V, respectively] were lower than that of **13** [+1.68 V (irr.)] and partially reversible in the case of **25b**. The E_1 potential of the iron complex **5**, measured under similar conditions occurs at an even lower value (-0.67 V).[44] The E_4 couple has not been found in any related iron system to date.[102]

In the cyclic voltammogram of the dppm complex **25a**, an unexpected peak at +0.72 V was observed in the cathodic sweep, the intensity of which was found to decrease at higher scan rates. This redox active species is most likely a product resulting from the decomposition of the higher oxidised species under the experimental conditions and is presently uncharacterised.

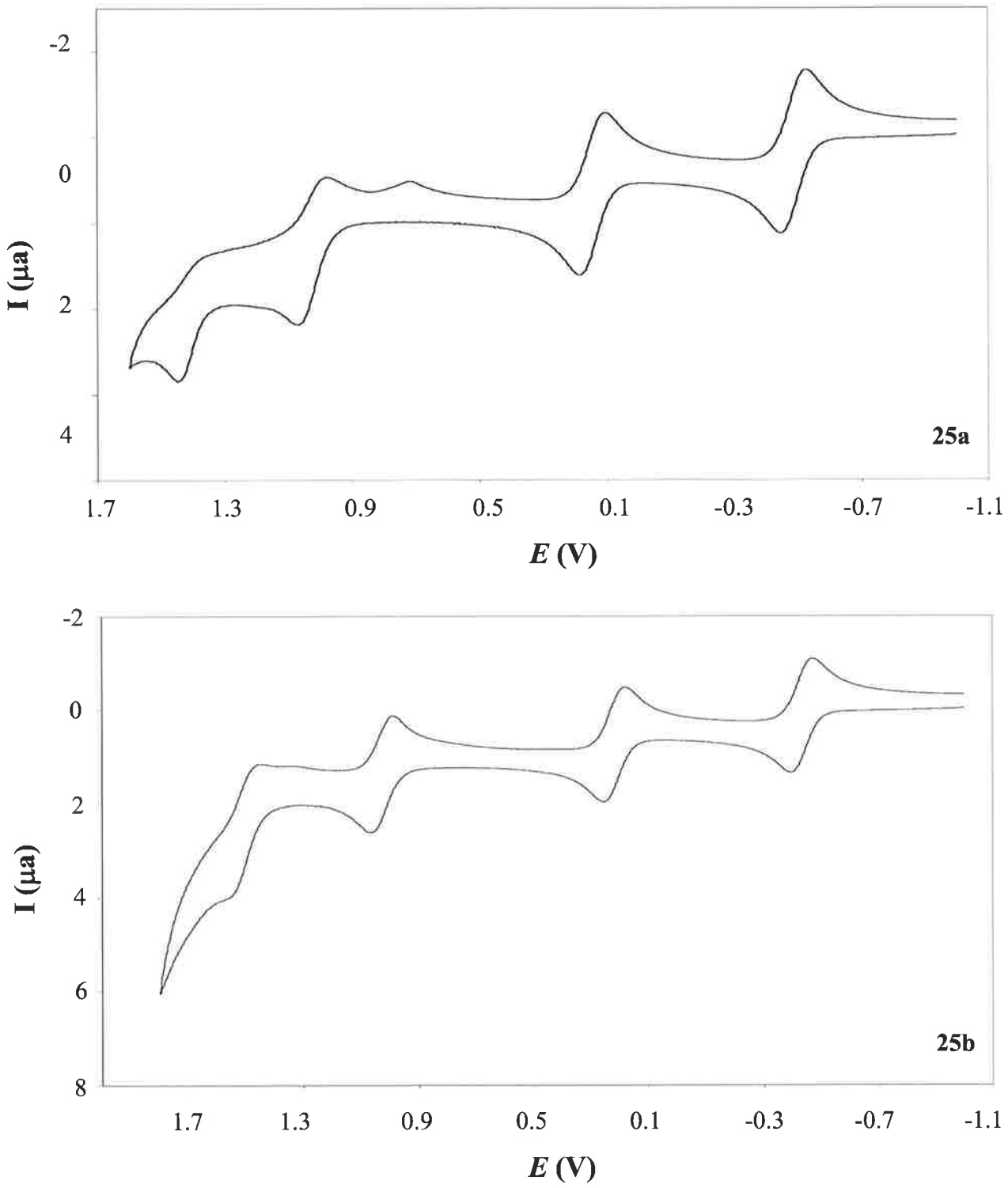

Figure 2.2: *Cyclic voltammograms of* ***25a*** *(top) and* ***25b*** *(bottom), recorded in* CH_2Cl_2, *0.1 M* $[Bu^n_4N][PF_6]$.

The electrochemical data can be further analysed to provide information on the properties of complexes **25a/b** and their oxidised states. The comproportionation reaction involves two molecules of the same complex in different oxidation states undergoing electron transfer to give a single species with an intermediate oxidation state. The equilibrium constant, K_c, for the comproportionation reaction can be calculated from Equation 1.5 (page 14).

The high thermodynamic stabilities of the oxidised species $[\mathbf{25}]^{n+}$ ($n < 4$) is evidenced by the significant separations of each redox process, giving rise to large comproportionation constants (**25a**: n = 1, $K_c = 4.43 \times 10^{10}$; n = 2, $K_c = 1.09 \times 10^{15}$; n = 3, $K_c = 5.75 \times 10^{6}$. **25b**: n = 1, $K_c = 9.64 \times 10^{10}$; n = 2, $K_c = 7.19 \times 10^{13}$; n = 3, $K_c = 2.81 \times 10^{8}$). While these data only provide an estimate of thermodynamic stabilities of the various oxidised species, the oxidised complexes $[\mathbf{25}]^{n+}$ (n = 1, 2, 3) were regarded as viable synthetic targets.

The magnitude of the comproportionation constant is often taken as an indication of the strength of the electronic coupling between two redox centres. In the ruthenium series, K_c is similar for both Cp* derivatives **25a** and **25b** along with their Cp analogues **13** and **18** (Table 2.2). Thus, it appears that despite the increase in electron density resulting from the introduction of the Cp* and PP ligands, there has been no significant increase in the interaction between the two ruthenium centres through the C_4 bridge. This finding is in contrast to the FeCp* series, which was shown to have a significant increase in K_c upon substitution with more electron-donating ligands [9.95×10^{11} (**5**), 2.23×10^{13} (**15**)]. This enhanced interaction was attributed to improved overlap between the organic (C_4) and metallic frontier molecular orbitals (FMO) in **15** compared with **5**.[102]

Complex	[M]	E_1	E_2	$\Delta E_{1/2}$	E_3	E_4	K_c (0/+1/+2) [a]	V_{ab} (eV) [b]	Ref
4	$Re(NO)(PPh_3)Cp^*$	+0.01	+0.54	0.53			9.04×10^8	[c]	[45]
5	$Fe(dppe)Cp^*$	-0.67	+0.04	0.71	+0.95		9.95×10^{11}	0.43	[44]
6	$Re(NO)[P(tol)_3]Cp^*$	-0.22	+0.31	0.53			9.04×10^8		[86]
7	$Mn(C{\equiv}CH)(dmpe)_2$ [d]	-1.46	-0.89	0.57			4.29×10^9		[87]
13	$Ru(PPh_3)_2Cp$	-0.23	+0.41	0.64	+1.03	+1.68 [e]	6.53×10^{10}	0.71	[43]
14	$MnI(dmpe)_2$ [d]	-0.65	-0.02	0.63			4.43×10^{10}		[101]
15	$Fe(dippe)Cp^*$	-0.97	-0.18	0.79	+0.81		2.23×10^{13}		[102]
18	$Ru(PMe_3)(PPh_3)Cp$	-0.26	+0.33	0.59	+0.97	+1.46 [e]	2.34×10^9	0.69	[43]
25a	$Ru(dppm)Cp^*$	-0.48	+0.15	0.63	+1.04 [f]	+1.44 [e]	4.43×10^{10}	0.63	this work
25b	$Ru(dppe)Cp^*$	-0.43	+0.22	0.65	+1.04	+1.54 [f]	9.64×10^{10}	0.63	this work

Table 2.3: *Electrochemical data for [M]-C≡CC≡C-[M] complexes in CH_2Cl_2 unless otherwise stated (V); values referenced to $[FeCp_2]/[FeCp_2]^+ = 0.46$ V. [a] All values recalculated from ΔE and Equation 1.5. [b] For Class III complexes, V_{ab} was calculated from Equation 1.8. [c] Values of 0.69, 0.61, 0.51 eV obtained from three absorption bands in NIR region (ν_{max} = 891, 1020, 1225 nm, respectively). [d] Recorded in MeCN. [e] Peak potential of an irreversible process. [f] Partially reversible.*

2.3.5. Molecular Structures

Single crystals of complexes **22a/b-25a/b** were grown from a variety of solvents, which are given in Section 2.5. The ORTEP plots of each of the complexes or cations are given in Figures 2.3-2.6 and selected structural parameters are collected in Tables 2.4 and 2.5. Similar subtle variations to those found in **19a/b** are found in **22a/b-25a/b** with values for P(1)-Ru-P(2) ranging between 70.71(2) and 71.74(2)° (dppm) and 81.50(3) and 83.33(4)° (dppe). The average Ru-C(Cp*) distances fall in the range 2.234(6)-2.29(1) Å with no apparent correlation with the bis-phosphine or charge. In the cationic derivatives **22a/b** and **24a/b**, the Ru-P distances [range 2.2966(5)-2.331(1) Å] are significantly longer than those found in the neutral complexes **23a/b** and **25a/b** [range 2.2420(8)-2.2813(7) Å], a consequence of reduced back bonding from the cationic ruthenium to the phosphine ligand.

The Ru-C(1) distances vary with the nature of the carbon ligand. For vinylidenes **22a/b** and **24a/b** short Ru-C distances between 1.834(5)-1.85(1) Å are found, suggesting a significant degree of multiple bonding between these atoms. In contrast, the alkynyl ligands in **23a/b** and **25a/b** are found to possess longer Ru-C(1) distances, between 2.001(3)-2.019(2) Å.

The C(1)-C(2) distances of 1.305(4) and 1.31(2) Å in **22a/b** and 1.338(7) and 1.323(5) Å in **24a/b**, are consistent with the presence of C=C double bonds. These values are reduced to between 1.202(3)-1.223(4) Å in **23a/b** and **25a/b**, consistent with the presence of C≡C triple bonds in these complexes. The longer central C-C single bonds in **24a/b** [1.448(7), 1.470(5) Å] and **25a/b** [1.385(3), 1.382(4) Å] are consistent with the conjugated structure of the C_4 ligands. There are slight deviations from linearity along the C_4 chains in **25a/b**, with angles at the individual carbon atoms between 170.6(2)-179.1(2)°. This feature has also been observed in related diyndiyl complexes and results from the facile bending modes of the *sp* carbon atoms.[116-119] In **25a/b**, the Ru-C_4-Ru chains approach a *transoid* configuration, with torsion angles Cp*-Ru....C_4....Ru-Cp* of 69.9° and -46.9°, respectively.

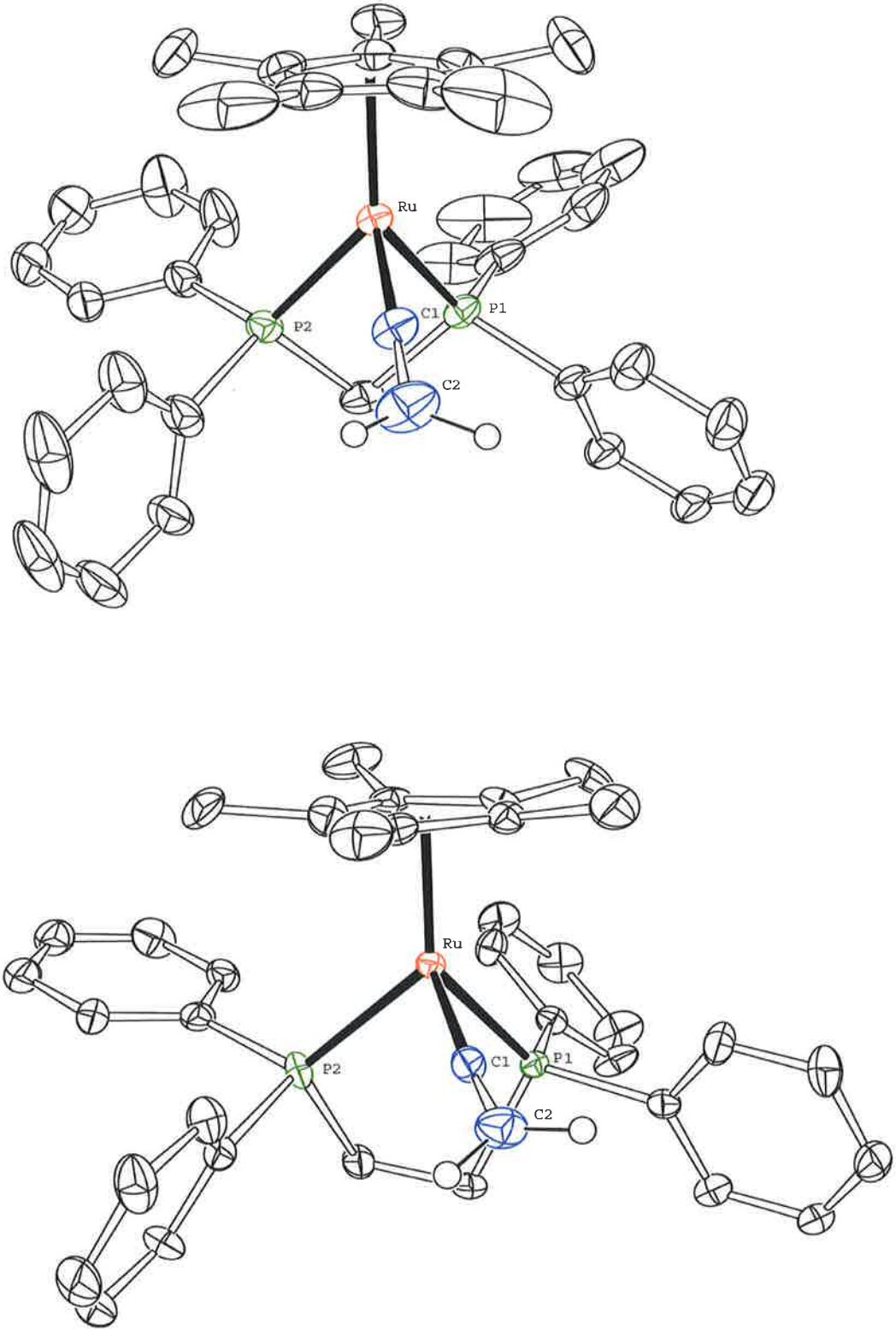

Figure 2.3: *ORTEP views of the cations* ***22a*** *(top) and* ***22b*** *(bottom).*

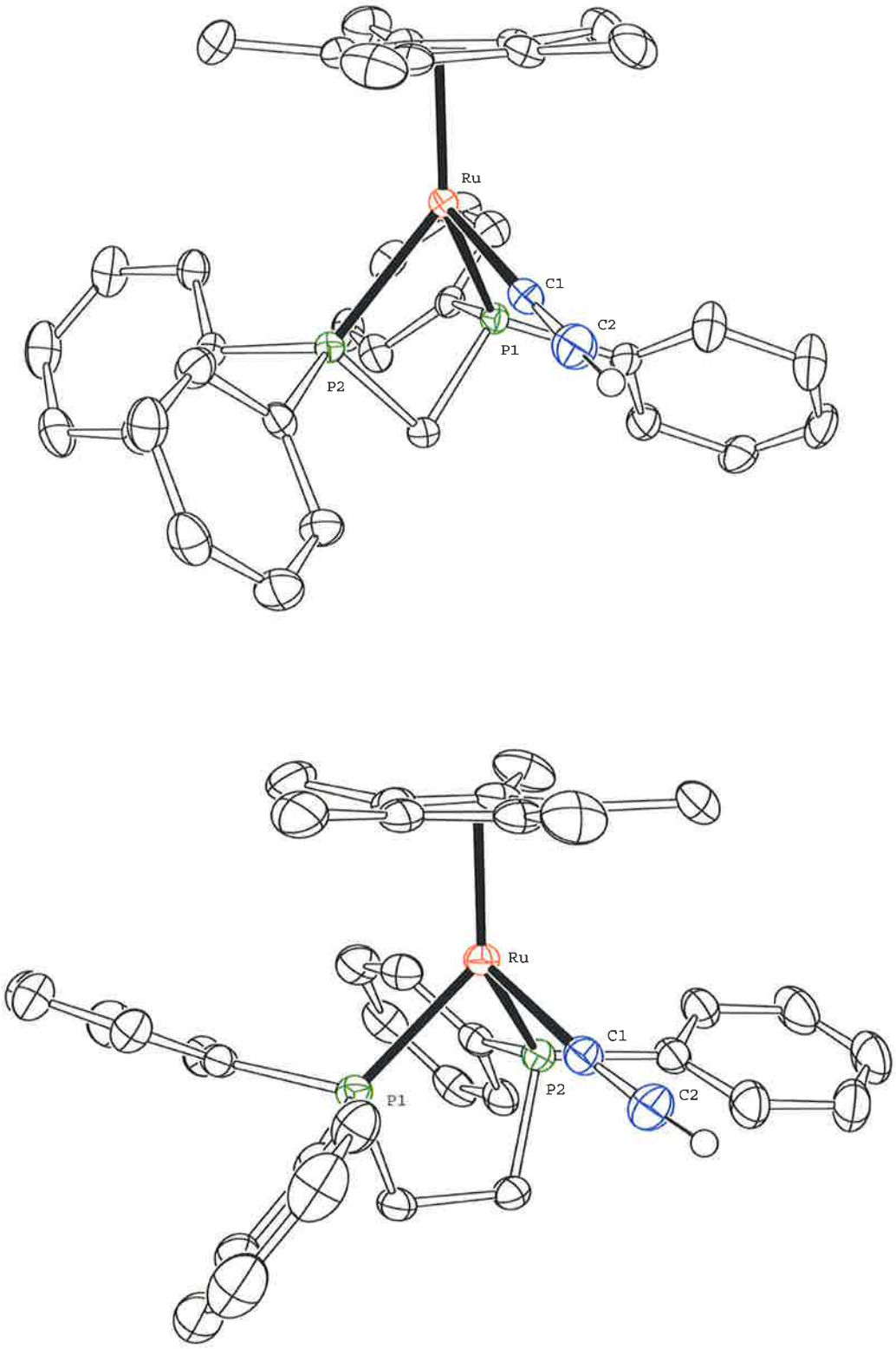

Figure 2.4: *ORTEP views of* ***23a*** *(top) and* ***23b*** *(bottom).*

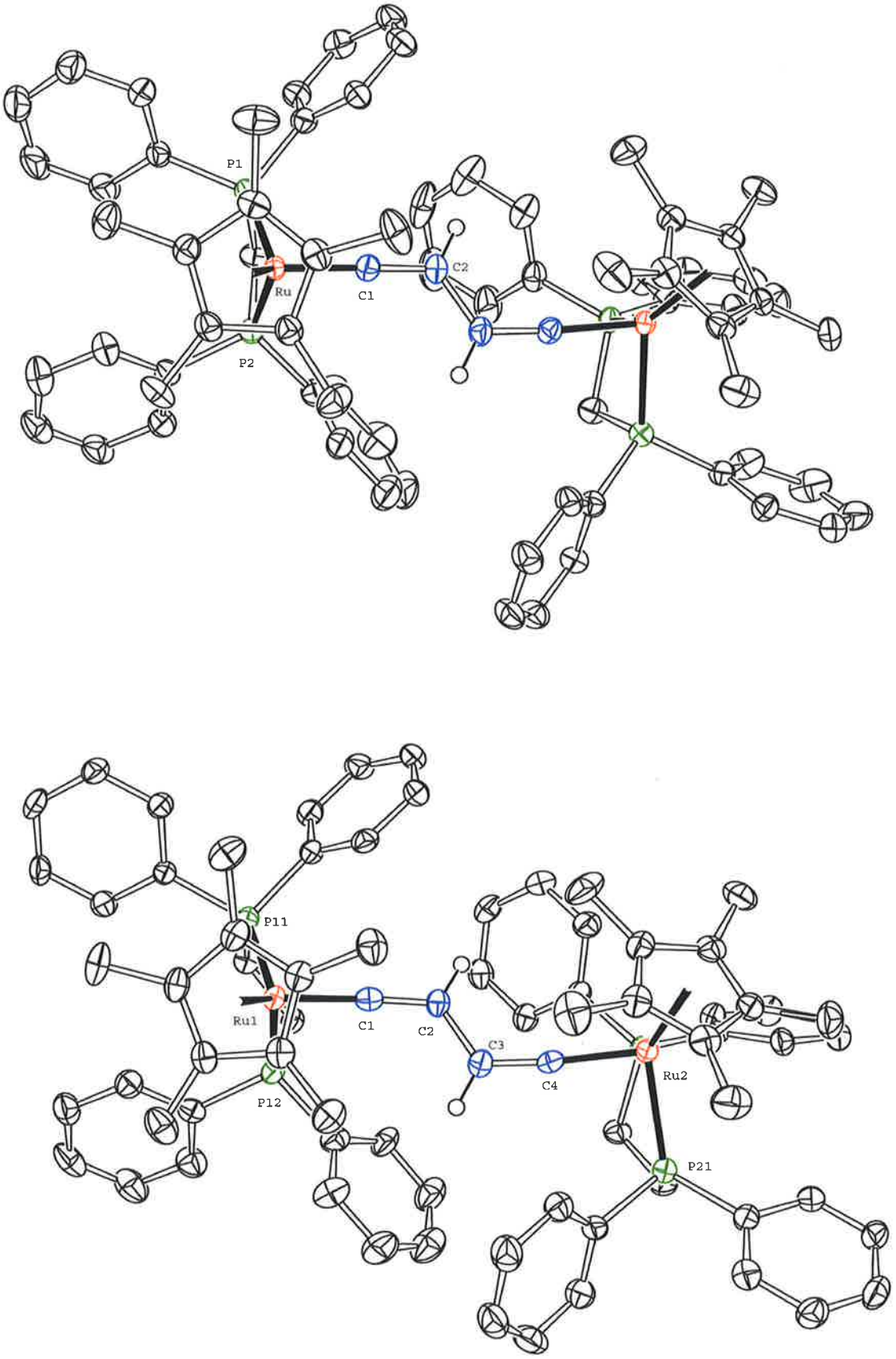

Figure 2.5: *ORTEP views of the cations* ***24a*** *(top) and* ***24b*** *(bottom).*

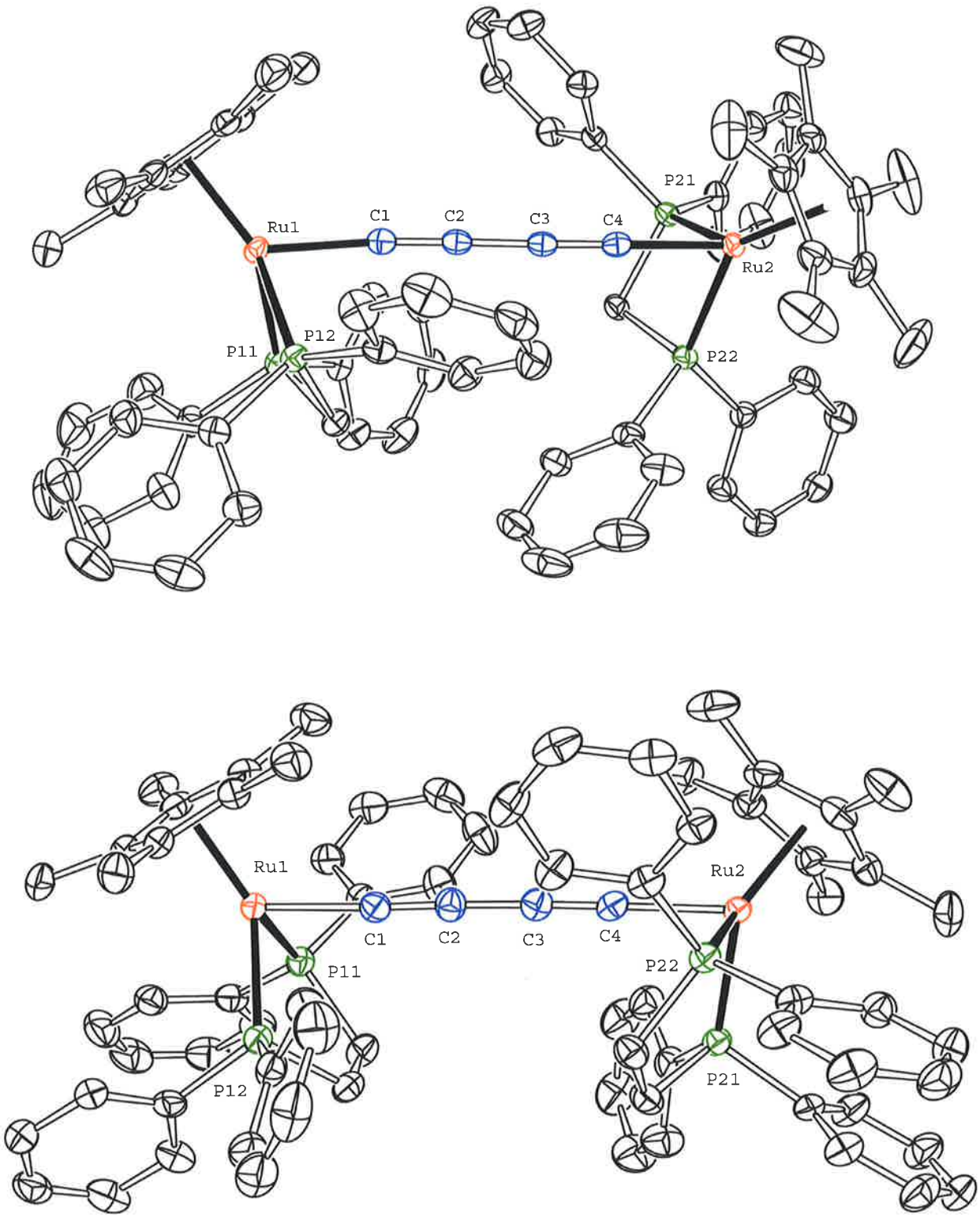

Figure 2.6: *ORTEP views of* ***25a*** *(top) and* ***25b*** *(bottom).*

	22a	22b	23a	23b
Bond distances (Å)				
Ru-P(1)	2.2966(5)	2.320(3)	2.2731(5)	2.2649(5)
Ru-P(2)	2.2975(6)	2.317(3)	2.2756(6)	2.2592(6)
Ru-C(Cp*)	2.248-2.286(2)	2.27-2.30(1)	2.219-2.263(2)	2.215-2.269(2)
(av.)	2.27(2)	2.28(1)	2.24(2)	2.25(2)
Ru-C(1)	1.848(2)	1.85(1)	2.015(2)	2.015(2)
C(1)-C(2)	1.305(4)	1.31 (2)	1.202(3)	1.202(3)
Bond angles (°)				
P(1)-Ru-P(2)	71.74(2)	82.75(9)	70.71(2)	82.71(2)
P(1)-Ru-C(1)	88.18(7)	83.5(3)	87.97(6)	87.50(6)
P(2)-Ru-C(1)	85.54(7)	92.8(3)	80.86(7)	85.27(6)
Ru-C(1)-C(2)	176.2(2)	172.9(9)	171.7(2)	173.7(2)

Table 2.4: *Selected structural data for **22a/b** and **23a/b**.*

	24a [a]	24b	25a	25b
Bond distances (Å)				
Ru(1)-P(11,12)	2.308(1)	2.331, 2.331(1)	2.2633, 2.2697(6)	2.2556, 2.2420(8)
Ru(2)-P(21,22)	2.313(1)	2.310, 2.306(1)	2.2813, 2.2684(7)	2.2465, 2.2531(9)
Ru(1,2)-C(Cp*)	2.262-2.312(5)	2.251-2.324(4), 2.268-2.311(4)	2.226-2.259(2), 2.228-2.243(2)	2.219-2.278(3), 2.223-2.275(3)
(av.)	2.28(2)	2.29, 2.28(1)	2.24(1), 2.234(6)	2.25, 2.25(2)
Ru(1,2)-C(1,4)	1.834(5)	1.837, 1.834(4)	2.017, 2.019(2)	2.001, 2.003(3)
C(1,4)-C(2,3)	1.338(7)	1.323, 1.324(5)	1.216, 1.223(3)	1.223, 1.218(4)
C(2)-C(3)	1.448(7)	1.470(5)	1.385(3)	1.382(4)
Bond angles (°)				
P(11,21)-Ru(1,2)-P(12,22)	71.10(4)	82.38, 83.33 (4)	70.72, 71.20(2)	81.50, 83.09(3)
P(11,21)-Ru(1,2)-C(1,4)	88.1(2)	94.1, 91.0(1)	83.63, 80.14(7)	81.69, 82.54(8)
P(12,22)-Ru(1,2)-C(1,4)	93.4(2)	80.9, 82.0(1)	78.90, 79.57(6)	84.25, 80.70(9)
Ru(1,2)-C(1,4)-C(2,3)	173.7(4)	170.9, 174.2(3)	175.2, 170.6(2)	176.6, 177.1(3)
C(1,4)-C(2,3)-C(3,2)	122.3(5)	123.5, 123.6(4)	179.1(2), 177.7(3)	176.9, 178.0(3)

Table 2.5: *Selected structural data for **24a/b** and **25a/b**.* [a] *centrosymmetric structure, values for C(3) read C(2').*

2.3.6. Synthesis and Properties of [25b]$^{n+}$ (n = 1, 2)

Generally throughout the syntheses of the complexes **22-25**, it was observed that complexes with dppe (series **b**) possessed greater stability than those with dppm (series **a**). Since the primary aim of this work was to isolate and structurally characterise the oxidised derivatives of either **25a** or **25b**, it was decided that all chemical oxidation reactions would be performed solely on the dppe complex **25b**.

Chemical oxidation of **25b** occurred with vivid colour changes. Treatment of orange **25b** with one equivalent of $[FeCp_2][PF_6]$ in CH_2Cl_2 gave the bright green monocation [**25b**][PF_6]. This 35-electron species only displayed broad resonances in its NMR spectra as expected for a paramagnetic complex. In the ^1H NMR spectrum, the Cp* resonance was found at δ 10.72, while resonances for dppe were observed at δ 13.54 (CH_2CH_2) and between δ 6.46-7.92 (aromatic). Although severely broadened, individual assignments were based upon the relative intensities of each peak. No signal was observed in the ^{31}P NMR spectrum for the dppe ligands, however the presence of the PF_6^- anion was confirmed from the characteristic septet at *ca* δ -143. The IR spectrum contained a ν(CC) absorption at 1859 cm^{-1}, together with ν(PF) at 841 cm^{-1}.

The radical-cation nature of [**25b**][PF_6] was confirmed when the X-band ESR spectrum was recorded at 80 K in a CH_2Cl_2/$ClCH_2CH_2Cl$ (1:1 v/v) glass. Three features, corresponding to the three components of the *g*-tensor as expected for a d^5 Ru(III) complex in a pseudo-octahedral geometry, were observed.[120] The values of *g* extracted from the spectra include: $g_1 = 2.2284$; $g_2 = 2.0697$; $g_3 = 1.9910$, with $\Delta g = 0.237$ where $\Delta g = g_1 - g_3$. Further comparison of these data can be seen in Section 5.3.8.

Oxidation of **25b** with two equivalents of $[FeCp_2][PF_6]$ gave the intense dark blue dication [**25b**][PF_6]$_2$ that contained a ν(CC) band at 1769 cm^{-1} in its IR spectrum, consistent with further lowering of the C≡C bond order relative to **25b** and [**25b**][PF_6]. In contrast to the monocation, [**25b**][PF_6]$_2$ displayed relatively sharp

resonances in its NMR spectra, suggesting its diamagnetic nature. In the ^{1}H NMR spectrum, a singlet for Cp* was found at δ 1.94, while a multiplet at δ 3.01 was assigned to the CH_2CH_2 protons of the dppe ligand. The aromatic protons appeared in the expected region between δ 7.15-7.79. In the ^{13}C NMR spectrum, Cp* resonances appeared as singlets at δ 10.38 ($C_5\underline{Me}_5$) and 112.28 ($\underline{C}_5Me_5$), while multiplets at δ 27.79 and between δ 129.80-133.79 were assigned to the CH_2CH_2 and aromatic carbons of the dppe ligands, respectively. Although several attempts were made, the resonances of the C_4 chain were not observed. In the ^{31}P NMR spectrum, a broadened singlet was found at δ 117.89 (dppe), while the PF_6^- anion was observed at δ -143.20. The higher chemical shift of the phosphorus nuclei for dppe in [**25b**][PF_6]$_2$ compared with **25b** (δ 82.53), is consistent with the removal of electron density from the ruthenium atoms and hence the phosphorus nuclei upon oxidation.

According to the electrochemical data, **25b** is oxidised to the trication [**25b**]$^{3+}$ in CH_2Cl_2 at $E_{½}$ = +1.04 V. While oxidising agents with suitable potentials exist (Ag^+, $E_{½}$ = +1.11 V in CH_2Cl_2),[121] all attempts using AgOTf and $AgPF_6$ failed to give [**25b**]$^{3+}$ as a pure complex. The cyclic voltammograms of the products from these reactions showed different traces to that of **25b**, whereas the trace of [**25b**]$^{3+}$ would be expected to be identical to that of [**25b**]$^{n+}$ (n = 0, 1, 2). In a similar result, isolation of iron complex [**5**]$^{3+}$ was also not possible, suggesting the enhanced reactivity of these species. However, the tricationic complex [**15**][OTf]$_3$ featuring the more electron donating dippe ligands has recently been isolated and structurally characterised,[102] suggesting the presence of strongly electron-donating ligands is necessary to stabilise these higher oxidised species.

The gradual decrease in the frequency of the ν(CC) band as oxidation of **25b** to [**25b**]$^{2+}$ proceeds is consistent with the results obtained for **13**.[43] Table 2.6 lists the ν(CC) bands of complexes **25b** and **13** recorded as a Nujol mull, while Figure 2.7 compares the observed ν(CC) absorptions of [**25b**]$^{n+}$ (n = 0, 1, 2) recorded in a CH_2Cl_2 solution. As can be seen, the solution spectrum of **25b** revealed a band at 1963 cm^{-1} (with a shoulder at 1977 cm^{-1}). A single ν(CC) band was observed in

$[\mathbf{25b}]^{+}$ at 1860 cm^{-1}, while in $[\mathbf{25b}]^{2+}$ a further reduction was observed with a band at 1770 cm^{-1}.

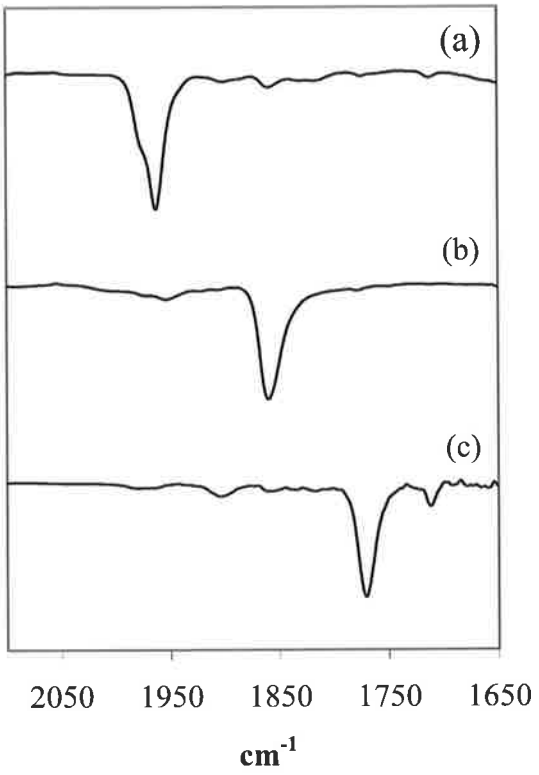

	25b	13
Neutral	1973	1974
Monocation	1859	1861
Dication	1769	1766

Table 2.6: *IR ν(CC) absorptions (in Nujol, cm^{-1}).*

Figure 2.7: *IR ν(CC) bands (in CH_2Cl_2) for $[\mathbf{25b}]^{n+}$ (a) n = 0; (b) n = 1; (c) n = 2.*

The gradual decrease in ν(CC) confirms that upon oxidation, the order of the initial C≡C triple bond in **25b** is decreased. These significant structural changes are represented in Scheme 2.16, which illustrates the anticipated changes in bonding along the Ru-C_4-Ru chain as **25b** is sequentially oxidised from its neutral to the 4+ state.

As confirmed from X-ray structural data, the neutral species **25b** exists as a butadiyndiyl (Structure **2d**) with alternating single and triple bonds. The cumulenic form **2f** is expected upon oxidation to $[\mathbf{25b}]^{2+}$, which is supported by the IR data. While isolation of the tri- and tetracations was not possible, it is anticipated that the same trend will continue and the 4+ cation will exist as the dicarbyne (Structure **2h**), with two Ru≡C bonds and a central C≡C bond.

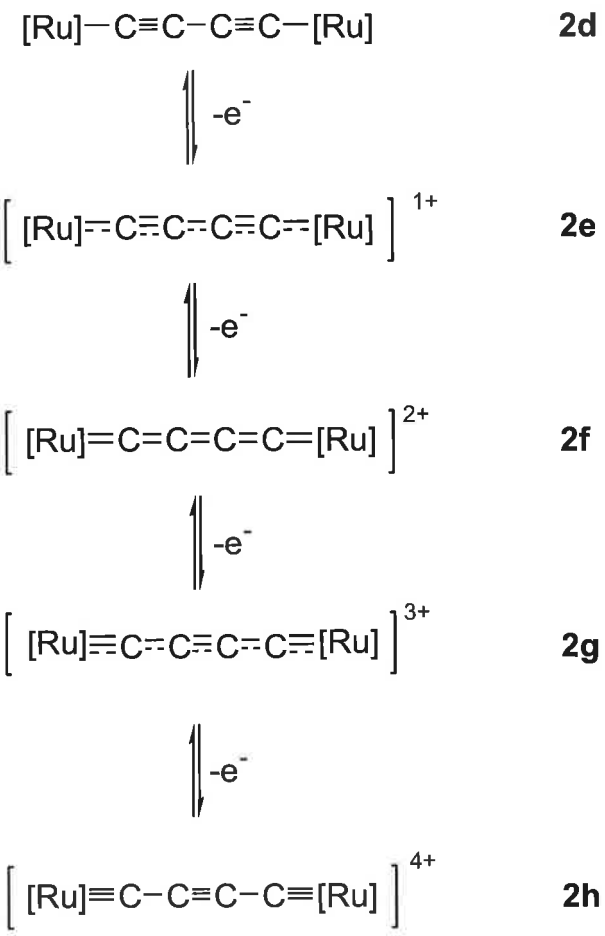

Scheme 2.16

These gradual changes can be rationalised when considering the molecular orbital (MO) diagram of the model complex $\{Ru(PH_3)_2Cp\}_2(C{\equiv}CC{\equiv}C)$, in which the bulky bis-phosphine (PP) and Cp* ligands were replaced with $(PH_3)_2$ and Cp ligands. While the precise details of these calculations have been reported elsewhere,[43] the MO diagram was prepared using extended Hückel (EH) calculations using a fragment analysis resulting from the interaction of the FMOs associated with the $(C_4)^{2-}$ unit with those of the bimetallic fragment $[\{Ru(PH_3)_2Cp\}_2]^{2+}$ (Figure 2.8).

Bonding between the metallic and organic fragments occurs with both σ- and π-type interactions. Strong σ-type interactions exist between the high-lying metallic FMOs $3b_u$ and $3a_g$ and the lower-lying C_4 orbitals $1b_u$ and $2a_g$. These interactions lead to

donation of electron density from the C_4 unit to the metallic fragment. This is complemented by relatively weak π-type back-bonding from occupied metallic FMOs into the high-lying acceptor C_4 FMOs $1a_u$ and $2b_u$. The large energy difference between these orbitals limits their contribution to the overall bonding between the metallic and organic fragments. The predominant π-type interactions are actually filled/filled interactions between the FMOs $1b_g$ and $1a_g$ of the C_4 ligand and the corresponding occupied metallic FMOs of the appropriate symmetry ($1b_g$ and $2a_g$). An important consequence of these interactions is the stabilisation of the C_4 orbitals, while the metallic orbitals are destabilised and become the HOMO and HOMO-1.

At the centre of Figure 2.8 it can be seen that the HOMOs are well separated from the LUMOs (3.37 eV) and the other lower-lying occupied MOs. With this arrangement of MOs, it is expected that a total of four electrons could be removed from the neutral complex, two from each HOMO, giving rise to a total of five potential oxidation states for this compound. The large HOMO/LUMO energy gap suggests that reduction of the neutral complex would not be achievable.

Density-functional (DF) molecular orbital calculations were also made on the model complex with similar results to the EH calculations.[43] Mulliken atomic orbital population calculations show that the HOMO is 27% ruthenium and 59% C_4 in character, while the HOMO-1 is 25% ruthenium and 69% C_4 in character. Relatively minor contributions from the Cp and PH_3 ligands are also made in both cases. As a result of the relatively even contributions from both ruthenium and carbon, the HOMOs are regarded to extend across the entire six-atom chain. An important consequence of this is that any oxidation process cannot be expected to occur solely at the metal centres but rather is delocalised across the entire chain.

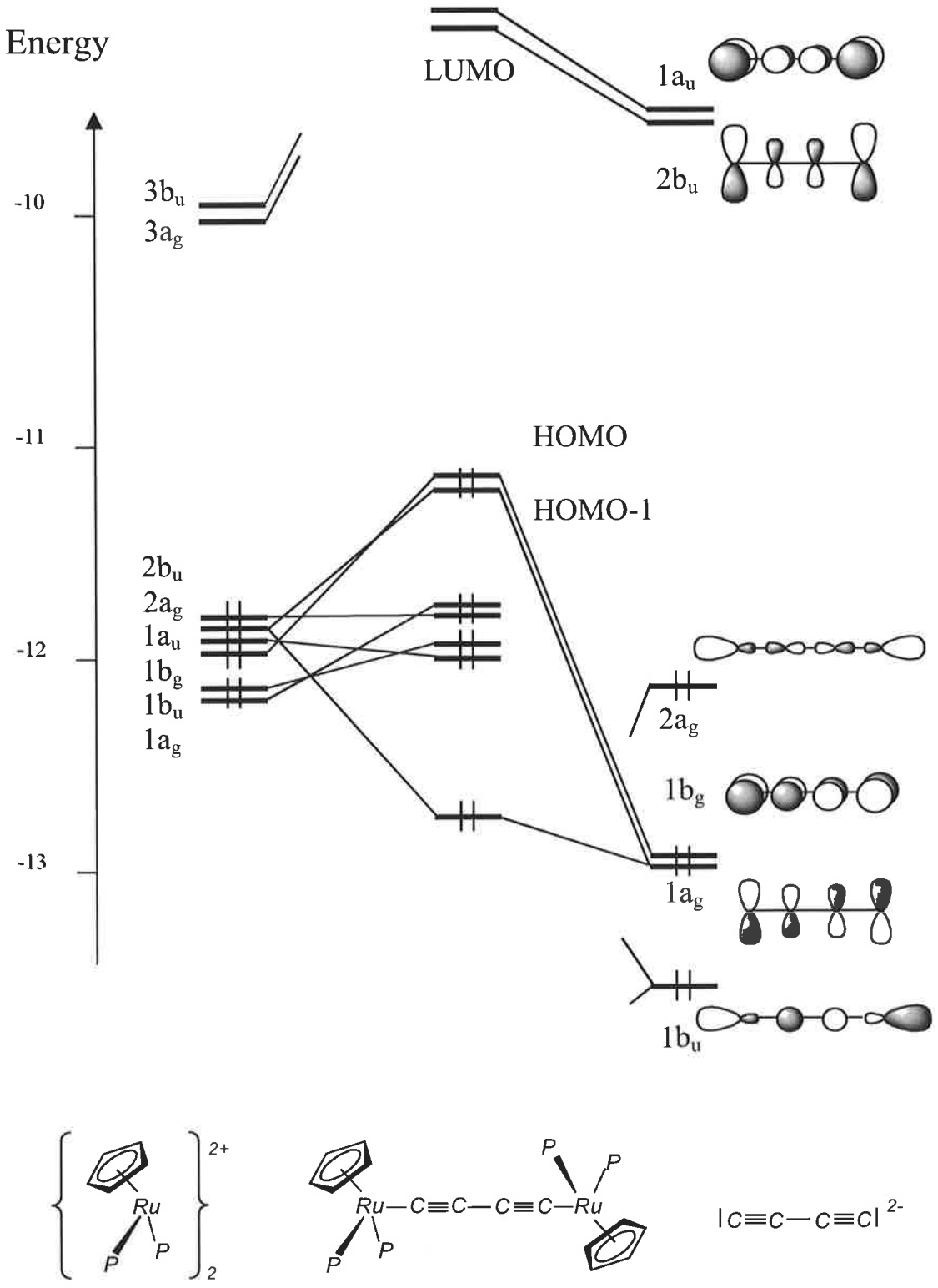

Figure 2.8: *Extended Hückel orbital interaction diagram for {Ru(PH$_3$)$_2$Cp}$_2$(C≡CC≡C).*[43]

Contour plots prepared using DF calculations of the HOMO (a) and the HOMO-1 (b) are shown in Figure 2.9.[43] Nodal planes in both MOs exist between Ru-C(1) and between C(2)-C(2') and both are bonding with respect to C(1)-C(2). Therefore, upon oxidation it can be expected that the Ru-C(1) and C(2)-C(2') bonds will strengthen due to decreased antibonding contributions, while the C(1)-C(2) bonds are expected to weaken due to decreased bonding character. This alternating decrease and increase in bond order along the Ru-C_4-Ru chain as the neutral complex is progressively oxidised results in a significant change in the nature of the carbon chain. These theoretical calculations are consistent with spectroscopic and X-ray structural data and offer a detailed explanation for changes observed upon oxidation as suggested in Scheme 2.16.

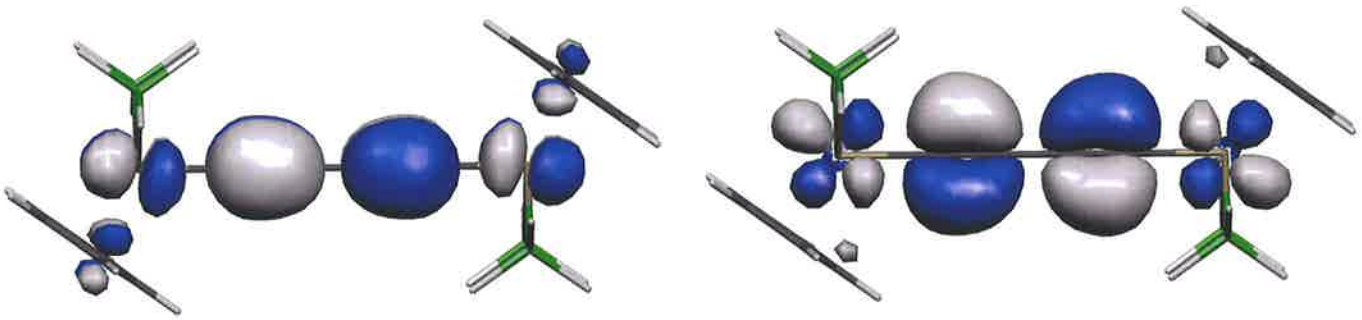

(a) (b)

Figure 2.9: *Contour plots of the (a) HOMO and (b) HOMO-1 of* $\{Ru(PH_3)_2Cp\}_2(C{\equiv}CC{\equiv}C)$.

While the calculations show that the HOMOs are closely related in energy, they are not degenerate. Consequently, in principle, a singlet-triplet equilibrium could exists in the dication of the salt [**25b**][PF_6]$_2$, which is governed by the equilibrium constant for the singlet-triplet transition ΔG_{ST} (Figure 2.10). As both the HOMO and HOMO-1 have the same alternating antibonding bonding antibonding character, it is anticipated that both the singlet and triplet states will exist in the cumulenic form.

The parameter ΔG_{ST} can be determined by magnetic susceptibility measurements of a sample of the dication over a variable temperature range using a SQUID

magnetometer.[122] While this measurement has not been recorded in the case of the [**25b**][PF_6]$_2$, its relatively sharp NMR spectra, especially when compared to that of [**25b**][PF_6] and the finding that [**25b**][PF_6]$_2$ is ESR-silent at both room and liquid nitrogen temperatures suggest that the predominant form is the singlet state.

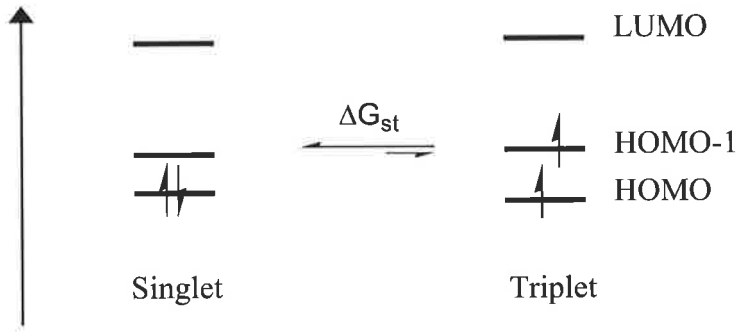

Figure 2.10: *Singlet-triplet transition in [25b][PF_6]$_2$.*

The singlet nature of [**25b**][PF_6]$_2$ is in contrast to [**5**][PF_6]$_2$. Although [**5**][PF_6]$_2$ possesses a singlet ground state, the energy gap is so small (ΔG_{ST} = -18 cm^{-1}) that even at liquid nitrogen temperature the triplet state is still significantly populated.[44]

2.3.7. Molecular Structures of [25b]$^{n+}$ (n = 1, 2)

As the primary aim of this work was to isolate and structurally characterise the oxidised products of **25b**, crystallisations of the PF_6 salts of both the mono- and dication were carried out. It was found however that crystallisations of both oxidised products must be performed in the complete absence of any moisture or O_2 to prevent formation of by-products such as [Ru(CO)(dppe)Cp*][PF_6], the formation of which is detailed in Chapter 3.

Crystals of the oxidised complexes [**25b**][PF_6] (CH_2Cl_2/hexane) and [**25b**][PF_6]$_2$ (EtOH) suitable for X-ray studies were obtained and the ORTEP views of the cations are shown in Figure 2.11, while selected structural parameters are collected

in Table 2.7. The overall structures of the cations are similar to that of **25b**, with the major structural differences existing within the Ru-C_4-Ru chain. In [**25b**][PF_6] the structure of the centrosymmetric six-atom Ru-C_4-Ru chain is intermediate between the diyndiyl structure found in neutral **25b** and the cumulenic structure in [**25b**][PF_6]$_2$. In particular, the bond distances found in [**25b**][PF_6] for Ru-C(1) [1.931(2) Å], C(1)-C(2) [1.248(3) Å] and C(2)-C(3) [1.338(3) Å] are equal to the averages of the corresponding values found in **25b** and [**25b**][PF_6]$_2$. In the case of [**25b**][PF_6]$_2$, the Ru-C(1) distances have decreased substantially to 1.858(5) and 1.856(5) Å, while the C(1)-C(2) distances have increased to 1.280 and 1.269(7) Å, with an associated decrease in the C(2)-C(3) separation to 1.294(7) Å. These data are consistent with a change from the diyndiyl structure **2d** in **25b** to the cumulenic structure **2f** in [**25b**][PF_6]$_2$, as suggested in Scheme 2.16.

Comparison with previous structural studies of [M-C_4-M]$^{n+}$ complexes can be seen in Table 2.8. The dimensions found in [**25b**]$^{2+}$ are similar to those found in the manganese complex [**14**]$^{2+}$, in which the C-C separations along the chain are 1.289, 1.295 and 1.298(5) Å, respectively.[101] Both [**25b**]$^{2+}$ and [**14**]$^{2+}$ provide the closest examples of pure cumulenic systems with the CC separations all being within 3σ. However, in the neutral manganese complex **14**, the C≡C triple bonds are already long at 1.263(17) Å and the central C-C single bond short at 1.33(3) Å.[101]

While significant changes in the bond lengths occurs upon oxidation of **25b** to [**25b**]$^{2+}$, there is little variation in the angles at the carbon atoms, which lie in the range 170.1-176.7(4)°. In [**25b**][PF_6]$_2$ the torsion angle Cp*-Ru....C_4....Ru-Cp* relating the two RuCp* groups is -39.7°. Other changes to the coordination about the ruthenium are minor, with lengthening of the Ru-P distances in the dication [**25b**][PF_6]$_2$ [av. 2.318(1) Å] relative to **25b** [av. 2.2493(9) Å] being comparable with those found in the cations **22a/b** and **24a/b**. Progressive oxidation results in a steady decrease in the Ru....Ru separations from 7.821(1) (**25b**) to 7.6293(8) ([**25b**][PF_6]) and 7.4757(1) Å ([**25b**][PF_6]$_2$).

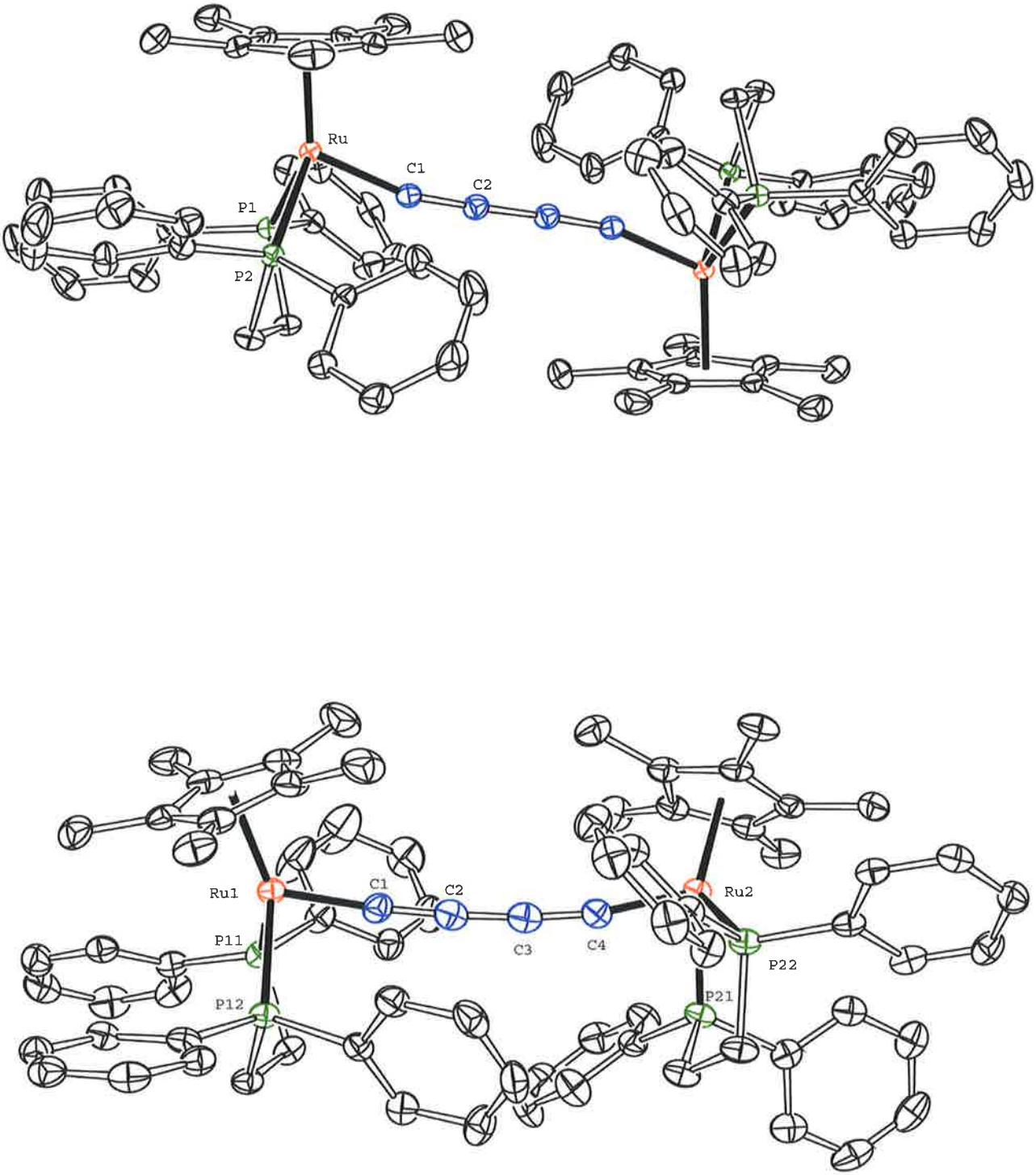

Figure 2.11: *ORTEP views of the cations* $[\mathbf{25b}]^{+}$ *(top) and* $[\mathbf{25b}]^{2+}$ *(bottom).*

	[**25b**][PF_6] [a]	[**25b**][PF_6]$_2$
Bond distances (Å)		
Ru(1)-P(11,12)	2.2756(5)	2.319, 2.312(1)
Ru(2)-P(21,22)	2.3001(5)	2.311, 2.330(1)
Ru(1,2)-C(Cp*)	2.232-2.291(2)	2.260-2.300(4), 2.262-2.309(3)
(av.)	2.26(2)	2.27, 2.28(2)
Ru(1,2)-C(1,4)	1.931(2)	1.858, 1.856(5)
C(1,4)-C(2,3)	1.248(3)	1.280, 1.269(7)
C(2)-C(3)	1.338(3)	1.294(7)
Bond angles (°)		
P(11,21)-Ru(1,2)-P(12,22)	81.89(2)	83.18, 81.93(4)
P(11,21)-Ru(1,2)-C(1,4)	83.38(6)	85.0, 82.8(2)
P(12,22)-Ru(1,2)-C(1,4)	93.45(6)	86.7, 92.5(1)
Ru(1,2)-C(1,4)-C(2,3)	165.6(2)	175.6(5), 170.1(4)
C(1,4)-C(2,3)-C(3,2)	178.9(2)	176.7, 174.2(6)

Table 2.7: *Selected structural data for [**25b**]$^{n+}$ (n = 1, 2).* [a] *centrosymmetric structure, values for C(3) read C(2').*

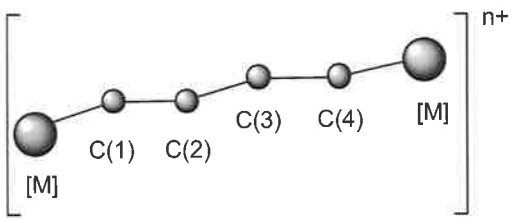

Complex	[M]	n+	M-C(1,4)	C(1,3)-C(2,4)	C(2)-C(3)	M-C(1,4)-C(2,3)	C(1,4)-C(2,3)-C(3,2)	Ref
4	$Re(NO)(PPh_3)Cp^*$	0 [a]	2.037(5)	1.202(7)	1.389(5)	174.4(5)	176.8(6)	[45]
		2	1.909, 1.916(7)	1.263, 1.260(10)	1.305(10)	168.5, 171.4(7)	177.8, 175.4(9)	[45]
5	$Fe(dppe)Cp^*$	0	1.889(9), 1.885(8)	1.22, 1.22(1)	1.37(1)	175, 179(1)	177, 176(1)	[182]
		1 [a]	1.830(8)	1.236(9)	1.36(1)	167.0(6)	177(1)	[44]
14	$MnI(dmpe)_2$	0 [a]	1.798(15)	1.263(17)	1.33(3)	176(1)	177(1)	[101]
		1 [a]	1.763(2)	1.275(3)	1.313(5)	179(1)	179(1)	[101]
		2	1.768, 1.770(4)	1.289, 1.298(5)	1.295(5)	171.9(5), 174.5(4)	173.9(4), 175.9(5)	[101]
25b	$Ru(dppe)Cp^*$	0	2.001, 2.003(3)	1.223, 1.218(4)	1.382(4)	176.6, 177.1(3)	176.9, 178.0(3)	this work
		1 [a]	1.931(2)	1.248(3)	1.338(3)	165.6(2)	178.0(2)	this work
		2	1.858, 1.856(5)	1.280, 1.269(7)	1.294(7)	175.6, 170.1(4)	176.7, 174.2(6)	this work

Table 2.8: *Selected bond distances (Å) and bond angles (°) for structurally characterised $[M\text{-}C_4\text{-}M]^{n+}$ complexes.* [a] *centrosymmetric structure.*

2.3.8. Spectroelectrochemistry of 25a/b

Spectroelectrochemistry is a very useful technique, providing the opportunity for studying chemical species that cannot be synthetically accessed by generating them *in situ* at the electrode surface. In order to follow the oxidation processes, a spectroelectrochemical study of the redox series $[\mathbf{25a/b}]^{n+}$ was undertaken. The oxidised complexes were generated *in situ* using an optically transparent thin-layer electrochemical (OTTLE) cell, the basic layout of which is shown in Figure 2.12. Bulk electrolysis occurs at the platinum gauze working electrode (WE), which is contained within a 0.5 mm path length cuvette. This expands to a cylindrical section that accommodates the platinum wire reference electrode (RE) and platinum wire counter electrode (CE). Both the reference and counter electrodes are separated from the bulk solution by a diffusion-controlled barrier.

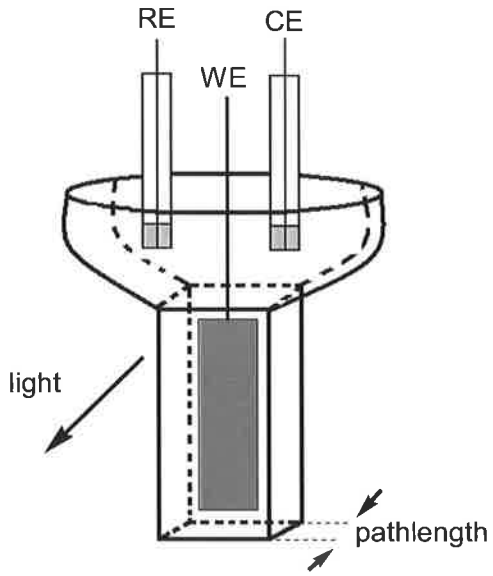

Figure 2.12: *Schematic representation of the OTTLE cell: (RE) reference electrode; (WE) working electrode; (CE) counter electrode.*

The UV/Vis/NIR spectra of $[\mathbf{25a}]^{n+}$ and $[\mathbf{25b}]^{n+}$ are similar and the discussion that follows refers to the species derived from **25a**, but the spectra and interpretation for **25b** are essentially the same (Table 2.9, Figure 2.13). Upon oxidation of **25a** to $[\mathbf{25a}]^{+}$, a set of intense, overlapping bands appear in the NIR region which are assigned to IVCT bands. These bands were deconvoluted by fitting Gaussian plots, allowing the key parameters to be extracted. The observation of multiple bands in the NIR region is uncommon, but has been reported previously for this class of

complex.[45,86] Higher energy shoulders were also observed in the spectra of both $[\mathbf{13}]^+$ and $[\mathbf{18}]^+$ indicating that multiple bands were present in the NIR spectra. However, these overlapping bands were not deconvoluted, which may have resulted in errors in the calculation of the extinction coefficient.

Throughout oxidation of $[\mathbf{25a}]^+$ to $[\mathbf{25a}]^{2+}$ this set of NIR bands collapsed, with concomitant growth of new higher energy bands at *ca* 660, 573 and 463 nm. An isosbestic point was observed near 700 nm. Electrolytic reduction of these 34-electron dications proceeded smoothly with complete chemical reversibility through the corresponding 35-electron monocations to the parent 36-electron complexes.

While the electrochemical studies indicate the high thermodynamic stability of the trications $[\mathbf{25a}]^{3+}$ and $[\mathbf{25b}]^{3+}$ with respect to disproportionation, electrogenerated spectra of neither $[\mathbf{25a}]^{3+}$ nor $[\mathbf{25b}]^{3+}$ could be obtained, even at low temperatures (-30°C).

	ν_{max} (cm^{-1})	ε (M^{-1} cm^{-1})	$\Delta\nu_{½}$ (cm^{-1})	$(\Delta\nu_{½})_{theo}$ (cm^{-1}) [a]	V_{ab} (eV) [b]
$[\mathbf{25a}]^+$	10 165	14 000	2036	4846	0.63
	12 100	9500	2456	5287	
	14 215	3500	3720	5730	
$[\mathbf{25b}]^+$	10 195	9850	2440	4853	0.63
	12 240	6600	2600	5317	
	14 000	2200	3800	5687	
$[\mathbf{25a}]^{2+}$	15385	17 600			
	17 452	5800			
	21 598	4350			
$[\mathbf{25b}]^{2+}$	15 152	24 500			
	17 241	8000			
	21 505	4600			

Table 2.9: *UV/Vis/NIR spectral data.* [a] *Calculated from Equation 1.7.* [b] *Calculated from Equation 1.8.*

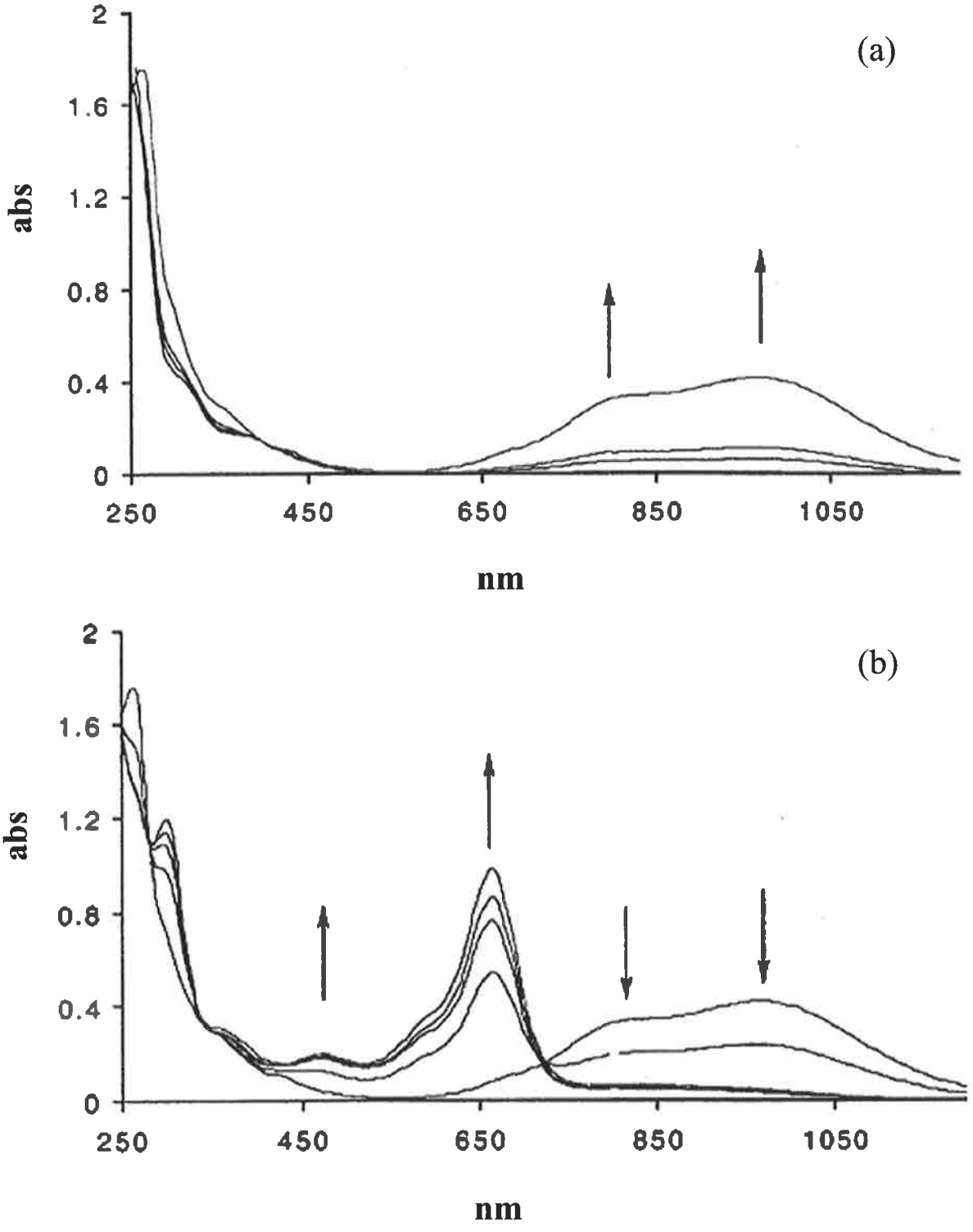

Figure 2.13: *UV/Vis/NIR spectra of {Ru(dppm)Cp*}$_2$(C≡CC≡C) (**25a**) as oxidation proceeds: (a) **25a** to [**25a**]$^+$; (b) [**25a**]$^+$ to [**25a**]$^{2+}$.*

The odd-electron species $[\mathbf{25}]^{+}$ and $[\mathbf{25}]^{3+}$ formally contain Ru(II/III) (or d^6/d^5) and Ru(III/IV) (or d^5/d^4) centres, respectively, and can be classed as MV complexes. Similar complexes have been obtained by oxidation of diyndiyl complexes containing Mn, Re, Fe and Ru metal centres.[43-45,101,102]

For Class III materials in which the odd electron is delocalised over both redox centres, the electronic coupling parameter V_{ab} can be calculated from the energy of the IVCT band (Equation 1.8).[75] Calculation of the parameter V_{ab} is very useful as it allows for comparisons of the electronic interactions between redox sites in one MV compound to be made with other related compounds. At present, standard protocols have not been developed to calculate V_{ab} for compounds such as $[\mathbf{25a/b}]^{+}$ that exhibit multiple overlapping bands in the NIR region so in these cases, V_{ab} was calculated from the lowest energy transition (Table 2.9). Values of V_{ab} for $[\mathbf{25a/b}]^{+}$ are comparable with other Class III MV complexes and comparisons can be seen in Table 2.3. Similar values for all four ruthenium complexes indicate no increase in electronic coupling upon substitution with more electron-donating ligands, a result that is in contrast to the iron series.

A simple test to distinguish Class II and Class III materials involves the comparison of the observed band-width at half-height ($\Delta\nu_{1/2}$) of the lowest energy electronic transition with the value determined from the relation derived by Hush for Class II complexes (Equation 1.7).[75] In $[\mathbf{25a}]^{+}$ and $[\mathbf{25b}]^{+}$, the calculated values, $(\Delta\nu_{1/2})_{theo}$ are approximately double (4846-5730 cm^{-1}) those observed experimentally (2036-3800 cm^{-1}). Therefore both $[\mathbf{25a}]^{+}$ and $[\mathbf{25b}]^{+}$ fail this diagnostic test for Class II complexes. This failure, together with the electrochemical, IR and NMR spectral profiles observed for $[\mathbf{25a}]^{+}$ and $[\mathbf{25b}]^{+}$, strongly suggest that a Class III description is most appropriate for these complexes.

2.4. Conclusions

The syntheses of the new diyndiyl complexes **25a/b** by the four-step procedure (Scheme 2.15) were successfully achieved. Single crystal X-ray structures of the neutral, mono- and dicationic species, **25b**, [**25b**][PF_6] and [**25b**][PF_6]$_2$ have been determined and are of significant interest in relation to the assignments of their electronic structures. As summarised in Table 2.8, the data confirmed the shortening of the Ru-C(1) and C(2)-C(3) bonds and lengthening of the C(1)-C(2) separation as oxidation proceeded. This is fully consistent with changes in Ru-C and CC bond order as electrons are successively removed from the HOMOs, which have Ru-C antibonding character. In general, the dimensions and geometry of the Ru-C_4-Ru moiety in [**25b**][PF_6] are intermediate between the neutral and dicationic species.

Comparison of the V_{ab} values for the four ruthenium diyndiyl complexes in the RuCp* and RuCp series shows no significant increase in electronic coupling between the two redox sites upon increase in electron density at the metal centre. This result is surprising as an increase in electronic coupling was observed in the iron series upon substitution with more electron donating ligands.

In conclusion, the use of strongly electron-donating ligands has given rise to complexes with oxidised derivatives that are more readily accessible. However, the decreased chemical stability of these highly oxidised complexes renders them more difficult to obtain on a preparative or semi-preparative time scale. This work further serves to highlight the influence that subtle variations in electronic structure, which can be engineered through control of the metal-ligand environment, have on the structures of diyndiyl complexes.

2.5. Experimental

General experimental conditions are detailed on page ix.

Reagents: The compounds TMSC≡CH,[123] $RuCl(PPh_3)_2Cp^*$ (**21**)[108] and $[FeCp_2][PF_6]$[121] were all prepared by standard literature methods.

RuCl(dppm)Cp* (19a)

A solution of $RuCl(PPh_3)_2Cp^*$ (100 mg, 0.12 mmol) and dppm (69 mg, 0.18 mmol) was heated in refluxing toluene (20 mL) for 2 h. The solution was cooled to r.t. before being loaded directly onto a silica column (10 x 3 cm). Elution with toluene removed any uncoordinated phosphine before a bright orange band was removed with 1:9 acetone/toluene. After the solvent was evaporated, crystallisation from CH_2Cl_2/hexane gave bright orange crystals of **19a** (68 mg, 83%), identified from its ^{1}H NMR spectrum: δ 1.92 [t, ^4J(HP) 3 Hz, 15H, Cp*], 4.49, 5.16 (2m, 2 x 1H, CH_2), 7.53-7.78 (m, 20H, Ph) [Lit. values were measured in a different solvent (THF-d_8): δ 1.66 (s), 4.18 (m), 4.94 (m), 7.27-7.53 (m)].[113] Further spectroscopic details: ^{13}C NMR: δ 10.78 (s, $C_5\underline{Me}_5$), 49.09 [t, ^1J(CP) 19 Hz, CH_2], 88.61 (s, $\underline{C}_5Me_5$), 128.00-134.80 (m, Ph). ^{31}P NMR: δ 12.48 (s, dppm). ES-mass spectrum (*m/z*): 621, $[Ru(dppm)Cp^*]^+$.

RuCl(dppe)Cp* (19b)

A solution of $RuCl(PPh_3)_2Cp^*$ (100 mg, 0.12 mmol) and dppe (72 mg, 0.18 mmol) was heated in refluxing toluene (20 mL) for 2 h. The solution was cooled to r.t. before being loaded directly onto a silica column (10 x 3 cm). Elution with toluene removed any uncoordinated phosphine before a bright orange band was removed with 1:9 acetone/toluene. After the solvent was evaporated, crystallisation from CH_2Cl_2/hexane gave bright orange crystals of **19b** (76 mg, 95%), identified from its ^{1}H NMR spectrum: δ 1.43 (s, 15H, Cp*), 2.13, 2.65 (2m, 2 x 2H, CH_2CH_2), 7.18-7.68 (m, 20H, Ph) [Lit. values were measured with a different solvent (THF-d_8): δ 1.41 (s), 2.14 (m), 2.66 (m), 7.20-7.69 (m)].[113] Further spectroscopic details: ^{13}C

NMR: δ 9.59 (s, $C_5\underline{Me}_5$), 28.44 [t, ^1J(CP) 32 Hz, CH_2CH_2], 89.00 (s, $\underline{C}_5Me_5$), 127.38-139.03 (m, Ph)]. ^{31}P NMR: δ 76.25 (s, dppe). ES-mass spectrum (*m/z*): 635, $[Ru(dppe)Cp^*]^+$.

$[Ru(=C=CH_2)(dppm)Cp^*][PF_6]$ (22a)

To a suspension of **19a** (1375 mg, 2.12 mmol) and NH_4PF_6 (694 mg, 4.25 mmol) in MeOH (25 mL) was added TMSC≡CH (1030 mg, 10.5 mmol) and the reaction was heated to reflux point for 1 h. The resulting bright yellow suspension was left to cool to r.t. before being filtered on a sintered glass funnel and washed with diethyl ether (2 x 10 mL) to give a yellow crystalline solid that was dried under vacuum and identified as **22a** (1570 mg, 96%). Single crystals suitable for X-ray were grown from CH_2Cl_2/hexane. Anal. Calcd ($C_{37}H_{39}F_6P_3Ru$): C, 56.13; H, 4.96. Found: C, 56.49; H, 4.96. IR (Nujol, cm^{-1}): ν(C=C) 1627 m; ν(PF) 834 s. ^{1}H NMR: δ 1.77 [t, ^4J(HP) 2 Hz, 15H, Cp*], 3.03 [t, ^4J(HP) 3 Hz, 2H, $=CH_2$], 4.63, 5.18 (2m, 2 x 1H, CH_2), 7.13-7.46 (m, 20H, Ph). ^{13}C NMR: δ 10.19 (s, $C_5\underline{Me}_5$), 48.24 [t, ^1J(CP) 28 Hz, CH_2], 95.23 (s, $\underline{C}_5Me_5$), 102.26 (s, C_2), 127.48-135.63 (m, Ph), 344.54 [t, ^2J(CP) 15 Hz, C_1]. ^{31}P NMR: δ -143.6 (septet, PF_6^-), 6.56 (s, dppm). ES-mass spectrum (*m/z*): 647, $[M]^+$; 621, $[Ru(dppm)Cp^*]^+$.

$[Ru(=C=CH_2)(dppe)Cp^*][PF_6]$ (22b)

To a suspension of **19a** (2450 mg, 3.70 mmol) and NH_4PF_6 (1210 mg, 7.42 mmol) in MeOH (25 mL) was added TMSC≡CH (1813 mg, 18.50 mmol) and the reaction was heated to reflux point for 1 h. The resulting bright yellow suspension was left to cool to r.t. before being filtered on a sintered glass funnel and washed with diethyl ether (2 x 10 mL) to give a yellow crystalline solid that was dried under vacuum and identified as **22b** (2333 mg, 95%). Single crystals suitable for X-ray were grown from acetone/hexane. Anal. Calcd ($C_{38}H_{41}F_6P_3Ru$): C, 56.64; H, 5.12. Found: C, 56.74; H, 5.27. IR (Nujol, cm^{-1}): ν(C=C) 1621 m; ν(PF) 835 s. ^{1}H NMR: δ 1.59 [t, ^4J(HP) 1 Hz, 15H, Cp*], 2.58, 2.94 (2m, 2 x 2H, CH_2CH_2), 2.99 [t, ^4J(HP) 2 Hz, 2H, $=CH_2$], 7.09-7.57 (m, 20H, Ph). ^{13}C NMR: δ 9.76 (s, $C_5\underline{Me}_5$), 29.00 (m, CH_2CH_2), 93.11 (s, $\underline{C}_5Me_5$), 102.65 (s, C_2), 128.61-133.75 (m, Ph), 344.21 [t, ^2J(CP) 16 Hz,

C_1]. ^{31}P NMR: δ -143.6 (septet, PF_6^-), 77.28 (s, dppe). ES-mass spectrum (*m/z*): 661, $[M]^+$; 635, $[Ru(dppe)Cp^*]^+$.

Ru(C≡CH)(dppm)Cp* (23a)

To a solution of **22a** (550 mg, 0.69 mmol) in THF (20 mL) was added $KOBu^t$ (78 mg, 0.69 mmol) and the reaction was stirred at r.t. for 30 min. The solvent was removed under vacuum and the solid extracted into the minimum quantity of benzene and loaded onto a short (5 cm) column of basic alumina. Elution with 3:7 acetone/hexane gave a bright yellow band that was collected and concentrated under vacuum to give a bright yellow crystalline solid **23a** (420 mg, 94%). Single crystals suitable for X-ray were grown from CH_2Cl_2/hexane. Anal. Calcd ($C_{37}H_{38}P_2Ru$): C, 68.82; H, 5.93. Found: C, 69.03; H, 5.70. IR (Nujol, cm^{-1}): ν(≡CH) 3279 w; ν(C≡C) 1932 m. ^1H NMR: δ 1.52 [t, ^4J(HP) 3 Hz, 1H, C≡CH], 1.88 [t, ^4J(HP) 2 Hz, 15H, Cp*], 4.35, 4.70 (2m, 2 x 1H, CH_2), 7.26-7.65 (m, 20H, Ph). ^{13}C NMR: δ 10.82 (s, $C_5\underline{Me}_5$), 50.41 [t, ^1J(CP) 20 Hz, CH_2], 91.27 [t, ^3J(CP) 4 Hz, $\underline{C}_5Me_5$], 93.01 (s, C_2), 120.26 [t, ^2J(CP) 23 Hz, C_1], 127.27-132.83 (m, Ph). ^{31}P NMR: δ 17.99 (s, dppm). ES-mass spectrum (*m/z*): 647, $[M + H]^+$; 621, $[Ru(dppm)Cp^*]^+$.

Ru(C≡CH)(dppe)Cp* (23b)

To a solution of **22b** (628 mg, 0.78 mmol) in THF (30 mL) was added $KOBu^t$ (90 mg, 0.78 mmol) and the reaction was stirred at r.t. for 30 min. The solvent was removed under vacuum and the solid extracted into the minimum quantity of benzene and loaded onto a short (5 cm) column of basic alumina. Elution with 3:7 acetone/hexane gave a bright yellow band that was collected and concentrated under vacuum to give a bright yellow crystalline solid **23b** (490 mg, 95%). Single crystals suitable for X-ray were grown from CH_2Cl_2/hexane. Anal. Calcd ($C_{38}H_{40}P_2Ru$): C, 69.18; H, 6.11. Found: C, 68.79; H, 6.63. IR (Nujol, cm^{-1}): ν(≡CH) 3269 w; ν(C≡C) 1925 m. ^1H NMR: δ 1.54 [t, ^4J(HP) 2 Hz, 15H, Cp*], 1.57 [t, ^4J(HP) 3 Hz, 1H, ≡CH], 2.08, 2.76 (2m, 2 x 2H, CH_2CH_2), 7.09-7.83 (m, 20H, Ph). ^{13}C NMR: δ 10.69 (s, $C_5\underline{Me}_5$), 29.90 (m, CH_2CH_2), 92.29 [t, ^3J(CP) 2 Hz, $\underline{C}_5Me_5$], 92.99 [t,

^{3}J(CP) 2 Hz, C_2], 120.58 [t, ^{2}J(CP) 23 Hz, C_1], 127.68-137.97 (m, Ph). ^{31}P NMR: δ 82.15 (s, dppe). ES-mass spectrum (*m/z*): 661, $[M + H]^+$; 635, $[Ru(dppe)Cp^*]^+$.

$[\{Ru(dppm)Cp^*\}_2(=C=CHCH=C=)][PF_6]_2$ (24a)

To a cooled suspension (-78°C) of **23a** (940 mg, 1.44 mmol) in CH_2Cl_2 (30 mL) was added solid $[FeCp_2][PF_6]$ (450 mg, 1.36 mmol). The reaction was stirred at -78°C for 3 h gradually changing from yellow to deep red. The product was crystallised directly from the reaction mixture by slow addition of diethyl ether (50 mL) and collected on a sintered glass funnel and washed with further portions of diethyl ether to ensure any excess ferrocene was removed before being dried under vacuum to give brick red **24a** (1032 mg, 96%). Single crystals suitable for X-ray were grown from CH_2Cl_2/hexane. Anal. Calcd ($C_{74}H_{76}F_{12}P_6Ru_2$): C, 56.20; H, 4.84. Found: C, 56.02; H, 4.71. IR (Nujol, cm^{-1}): ν(C=C) 1634 m; ν(PF) 840 s. ^{1}H NMR: δ 1.78 (s, 30H, Cp*), 3.72 (s, 2H, =CH), 4.08, 5.00 (2m, 2 x 2H, CH_2), 6.99-7.43 (m, 40H, Ph). ^{13}C NMR: δ 10.51 (s, $C_5\underline{Me}_5$), 47.04 [t, ^{1}J(CP) 29 Hz, CH_2], 95.63 (s, $\underline{C}_5Me_5$), 102.87 (s, C_2), 128.63-134.52 (m, Ph), 348.59 [t, ^{2}J(CP) 15 Hz, C_1]. ^{31}P NMR: δ -143.6 (septet, PF_6^-), 4.76 (s, dppm). ES-mass spectrum (*m/z*): 1436, $[M + PF_6]^+$; 621, $[Ru(dppm)Cp^*]^+$.

$[\{Ru(dppe)Cp^*\}_2(=C=CHCH=C=)][PF_6]_2$ (24b)

To a cooled suspension (-78°C) of **23b** (772 mg, 1.17 mmol) in CH_2Cl_2 (30 mL) was added solid $[FeCp_2][PF_6]$ (348 mg, 1.05 mmol). The reaction was stirred at -78°C for 3 h gradually changing from yellow to deep red. The product was crystallised directly from the reaction mixture by slow addition of diethyl ether (50 mL) and collected on a sintered glass funnel and washed with further portions of diethyl ether to ensure any excess ferrocene was removed before being dried under vacuum to give brick red **24b** (685 mg, 85%). Single crystals suitable for X-ray were grown from acetone/hexane. Anal. Calcd ($C_{76}H_{80}F_{12}P_6Ru_2$): C, 56.72; H, 5.01. Found: C, 56.77; H, 5.11. IR (Nujol, cm^{-1}): ν(C=C) 1600 m; ν(PF) 841 s. ^{1}H NMR: δ 1.66 (s, 30H, Cp*), 2.57-2.78 (m, 8H, CH_2CH_2), 3.13 (s, 2H, =CH), 7.00-7.56 (m, 40H, Ph). ^{13}C NMR: δ 10.13 (s, $C_5\underline{Me}_5$), 28.73 (m, CH_2CH_2), 93.95 (s, $\underline{C}_5Me_5$), 103.22 (s, C_2),

128.79-134.41 (m, Ph), 348.08 [t, ^2J(CP) 18 Hz, C_1]. ^{31}P NMR: δ -143.70 (septet, PF_6^-), 75.92 (s, dppe). ES-mass spectrum (*m/z*): 1465, $[M + PF_6]^+$; 635, $[Ru(dppe)Cp^*]^+$.

{Ru(dppm)Cp*}$_2$(C≡CC≡C) (25a)

To a solution of **24a** (640 mg, 0.40 mmol) in CH_2Cl_2 (20 mL) was added dbu (0.6 mL, 4.00 mmol). The solution was stirred for 15 min after which the solvent was removed under vacuum. The oily residue was extracted with hot hexane until no further bright orange complex was removed. The extracts were filtered and the solvent removed to give an orange crystalline solid. Trituration with cold MeOH (5 mL) followed by filtration on a sintered glass funnel and washing with a further portion of cold MeOH gave **25a** (467 mg, 90%). Single crystals suitable for X-ray were grown from acetone, while the analytical sample was obtained from crystallisation from CH_2Cl_2/hexane. Anal. Calcd ($C_{74}H_{74}P_4Ru_2 \cdot CH_2Cl_2$): C, 65.54; H, 5.57. Found: C, 65.51; H, 5.70. IR (Nujol, cm^{-1}): ν(C≡C) 1966 s. ^{1}H NMR (benzene-d_6): δ 1.89 (s, 30H, Cp*), 4.23 (m, 4H, CH_2), 7.01-7.64 (m, 40H, Ph). ^{13}C NMR (benzene-d_6): δ 11.37 (s, $C_5\underline{Me}_5$), 51.20 [t, ^1J(CP) 22 Hz, CH_2], 91.33 (s, $\underline{C}_5Me_5$), 93.25 [t, ^2J(CP) 27 Hz, C_1], 100.38 (s, C_2), 127.46-139.32 (m, Ph). ^{31}P NMR (benzene-d_6): δ 17.50 (s, dppm). ES-mass spectrum (*m/z*): 1290, $[M]^+$; 621, $[Ru(dppm)Cp^*]^+$.

{Ru(dppe)Cp*}$_2$(C≡CC≡C) (25b)

To a solution of **24b** (600 mg, 0.37 mmol) in THF (30 mL) was added KOBu^t (103 mg, 0.92 mmol) and the reaction was stirred at r.t. for 30 min. The solvent was removed and the crude solid extracted with hexane to give a bright orange solution that was filtered through cotton wool and concentrated to give a bright orange crystalline solid. Trituration with cold EtOH (5 mL) and filtration on a sintered glass funnel followed by washings with a further portion of cold EtOH gave **25b** (438 mg, 90%). Single crystals suitable for X-ray were grown from hexane. Anal. Calcd ($C_{76}H_{78}P_4Ru_2 \cdot \frac{1}{2}C_6H_{14}$): C, 69.74; H, 6.29. Found: C, 69.79; H, 6.40. IR (Nujol, cm^{-1}): ν(C≡C) 1973 s. ^{1}H NMR (benzene-d_6): δ 1.68 (s, 30H, Cp*), 1.95, 2.72 (2m, 2 x

4H, CH_2CH_2), 7.04-8.05 (m, 40H, Ph). ^{13}C NMR (benzene-d_6): δ 10.09 (s, $C_5\underline{Me}_5$), 29.11 (s, CH_2CH_2), 92.26 (s, $\underline{C}_5Me_5$), 94.63 [t, ^2J(CP) 27 Hz, C_1], 99.47 (s, C_2), 127.32-140.46 (m, Ph). ^{31}P NMR (benzene-d_6): δ 82.53 (s, dppe). ES-mass spectrum (*m/z*): 1318, $[M]^+$; 635, $[Ru(dppe)Cp^*]^+$.

[{Ru(dppe)Cp*}$_2$C$_4$][PF$_6$] ([25b][PF$_6$])

To a solution of **25b** (50 mg, 0.038 mmol) in CH_2Cl_2 (20 mL) was added $[FeCp_2][PF_6]$ (11.9 mg, 0.036 mmol) causing an immediate colour change from orange to bright green. After the mixture was stirred for 30 min, the solvent was concentrated under vacuum (5 mL) and added dropwise to hexane (250 mL) to give [**25b**][PF$_6$] (48 mg, 91%) as a light green microcrystalline solid. Single crystals suitable for X-ray were grown from CH_2Cl_2/hexane. Anal. Calcd ($C_{76}H_{78}P_5F_6Ru_2 \cdot CH_2Cl_2$): C, 59.70; H, 5.21. Found: C, 59.80; H, 5.21. IR (Nujol, cm^{-1}): ν(CC) 1859 m; ν(PF) 841 s. ^1H NMR: δ 6.46-7.92 (m br, 40H, Ph), 10.72 (br, 30H, Cp*), 13.54 (br, 8H, CH_2CH_2). ES-mass spectrum (*m/z*): 1318, $[M]^+$; 635, $[Ru(dppe)Cp^*]^+$.

[{Ru(dppe)Cp*}$_2$C$_4$][PF$_6$]$_2$ ([25b][PF$_6$]$_2$)

To a solution of **25b** (50 mg, 0.038 mmol) in CH_2Cl_2 (20 mL) was added $[FeCp_2][PF_6]$ (25 mg, 0.076 mmol) resulting in an immediate colour change from orange to deep blue. The mixture was stirred for 30 min and the solvent was concentrated under vacuum (5 mL) and added dropwise to hexane (250 mL) to give [**25b**][PF$_6$]$_2$ (47 mg, 79%) as a dark blue solid. Single crystals suitable for X-ray were grown from EtOH. Anal. Calcd ($C_{76}H_{78}P_6F_{12}Ru_2$): C, 56.79; H, 5.02. Found: C, 57.00; H, 5.02. IR (Nujol, cm^{-1}): ν(CC) 1769 m; ν(PF) 841 s. ^1H NMR (acetone-d_6): δ 1.94 (s, 30H, Cp*), 3.01 (br, 8H, CH_2CH_2), 7.17-7.79 (m, 40H, Ph). ^{13}C NMR (acetone-d_6): δ 10.38 (s, $C_5\underline{Me}_5$), 27.79 (m, CH_2), 112.28 (s, $\underline{C}_5Me_5$), 129.80-133.97 (m, Ph). ^{31}P NMR (acetone-d_6): δ -143.20 (septet, PF_6^-), 117.89 (s br, dppe). ES-mass spectrum (*m/z*): 1463, $[M + PF_6]^+$; 1318, $[M]^+$; 659, $[M]^{2+}$; 635, $[Ru(dppe)Cp^*]^+$.

CHAPTER THREE

Chemistry of bis-vinylidenes $[\{Ru(PP)Cp^*\}_2(=C=CRCR=C=)]^{2+}$ [PP = dppm, dppe; R = H, Me]

3.1. Introduction

The chemistry of transition-metal vinylidene complexes is well understood and has been the subject of theoretical and experimental studies and also the subject of a number of reviews.[114,124] Calculations have shown that the reactivity of these complexes is directed by the electronic properties of the vinylidene ligand.[125] In general, C_1 is electron poor and subject to attack by nucleophiles.[126-128] However, in mono- or unsubstituted vinylidenes, the vinylic proton is acidic and as a consequence competition occurs between nucleophilic attack at C_1 and deprotonation to form the corresponding alkynyl complex (Scheme 3.1).[128]

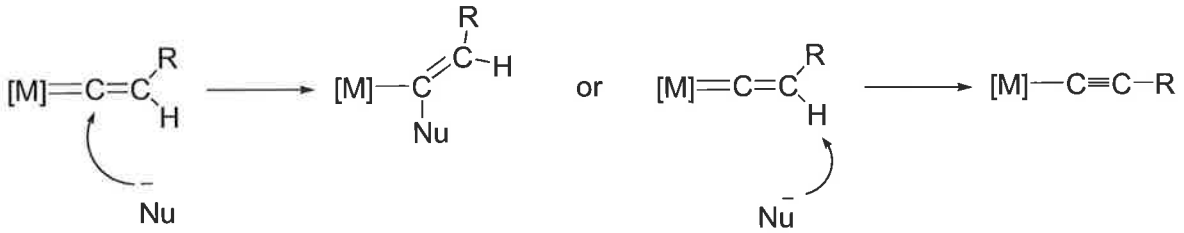

Scheme 3.1

3.2. Results and Discussion

3.2.1. Reaction of [{Ru(dppm)Cp}$_2$(=C=CHCH=C=)][PF$_6$]$_2$ (24a) with KOBu^t*

As described in Chapter 2, addition of dbu to the bis-vinylidene **24a** gave the diyndiyl complex **25a** as the sole product. However, if KOBu^t was used, a mixture of complexes was formed (Scheme 3.2). The ^{31}P NMR spectrum of the reaction mixture of **24a** with KOBu^t revealed four peaks with the two at δ 18.99 and -1.79 of equal intensity, together with minor resonances at δ 16.63 and -3.06 (Figure 3.1).

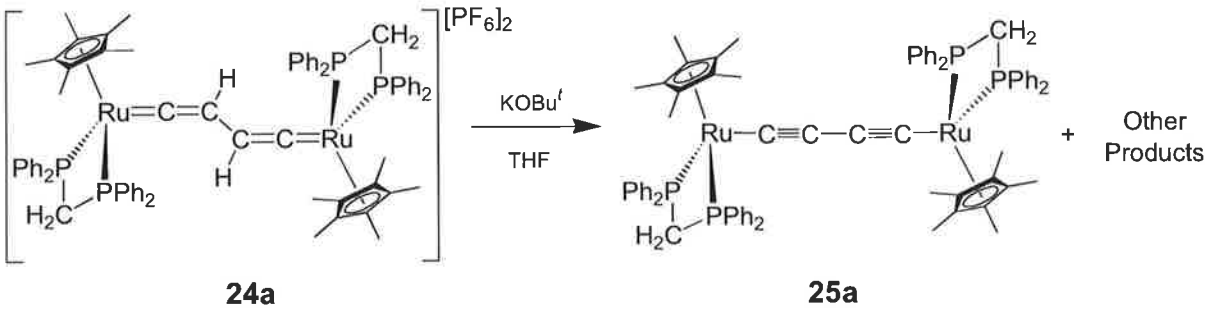

24a **25a**

Scheme 3.2

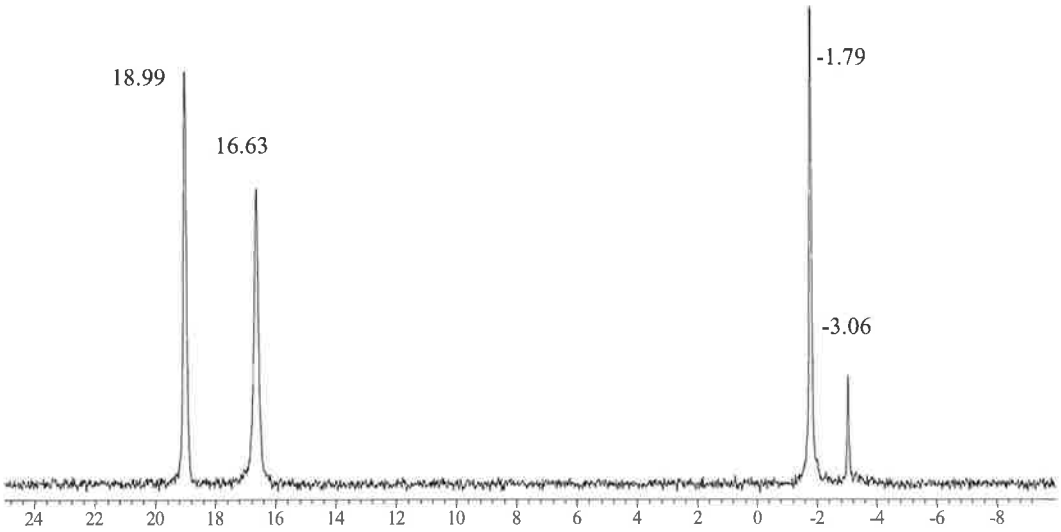

Figure 3.1: *^{31}P NMR spectrum (ppm) of **24a** after the addition of an excess of $KOBu^t$.*

While the separation of the individual components from the mixture was not possible, ^1H and ^{31}P NMR spectroscopy have enabled them to be identified. In the ^{31}P NMR spectrum, the resonance at δ 16.63 was assigned to the diyndiyl complex **25a** by comparison with an authentic sample. The remaining three resonances were assigned to the two metallacyclic derivatives **27** (δ 18.99 and -1.79) and **28** (δ -3.06), based on NMR and structural characterisation. From the relative intensities of the signals, the major product from the reaction was **27**, formed in 60% yield, while only minor quantities of the desired diyndiyl complex **25a** and the metallacycle **28** were isolated in 35 and 5% yields, respectively.

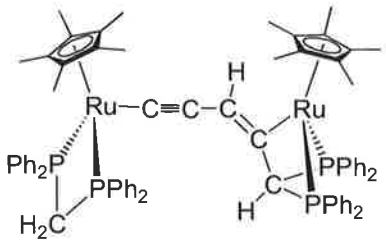

27

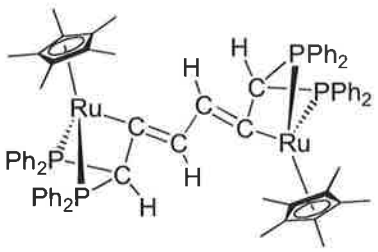

28

The formation of metallacycles **27** and **28** is expected to result from the deprotonation of either one or both of the dppm ligands in **24a** to give zwitterionic intermediates containing the $[(Ph_2P)_2CH]^-$ ligand (Structure **3a** in Scheme 3.3). Subsequent intramolecular nucleophilic attack at the electrophilic atom C_1 of the vinylidene by the substituted methanide anion gives the cyclic structure **3b**. This

observation was unexpected, as similar products were not observed in the reaction of **24b** with KOBu^t. However, related products derived from intramolecular reactions of vinylidenes containing dppm and dppe have previously been reported.[126,128,129]

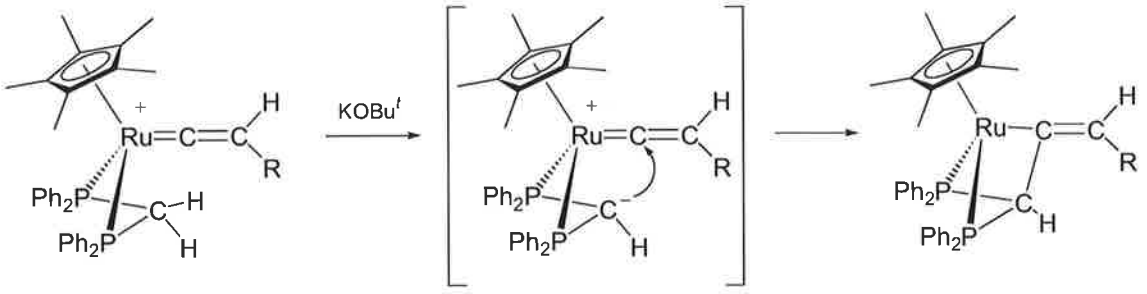

Scheme 3.3

The individual ^{1}H NMR resonances in the spectrum of the mixture could also be assigned. Signals corresponding to **25a** were observed at δ 1.90 and 4.22, assigned to Cp* and the CH_2 protons of dppm ligands, respectively. A pair of equal intensity triplets at δ 1.98 and 2.07 were assigned to the two different Cp* ligands in **27**, with the upfield resonance due to the Cp* bound to ruthenium featuring the dppm ligand based on comparison with **25a**. While the individual aromatic resonances for the dppm and $(Ph_2P)_2CH$ ligands could not be assigned, multiplets at δ 3.85 and 4.12 and a triplet at δ 5.59 were attributed to the CH_2 and CH protons in **27**, respectively. The vinylic proton was found as a singlet at δ 2.11.

Despite complex **28** only being formed in trace quantities, characteristic resonances were also observed. As expected, a single resonance for the two equivalent Cp* ligands was found at δ 2.24, together with a broadened resonance at δ 6.43, assigned to the two equivalent $(Ph_2P)_2C\underline{H}$ protons. The vinylic protons of **28** were not observed.

The proposed structure of **28** was confirmed when single crystals suitable for X-ray diffraction were obtained. Crystallisation of the crude mixture (CH_2Cl_2/hexane) gave thin hair-like crystals of **25a** together with larger cubic shaped blocks that were found to be **28**. Two independent molecules are present in the unit cell and the ORTEP view of a single non-centrosymmetric molecule is shown in Figure 3.2, while selected structural parameters are collected in Table 3.1.

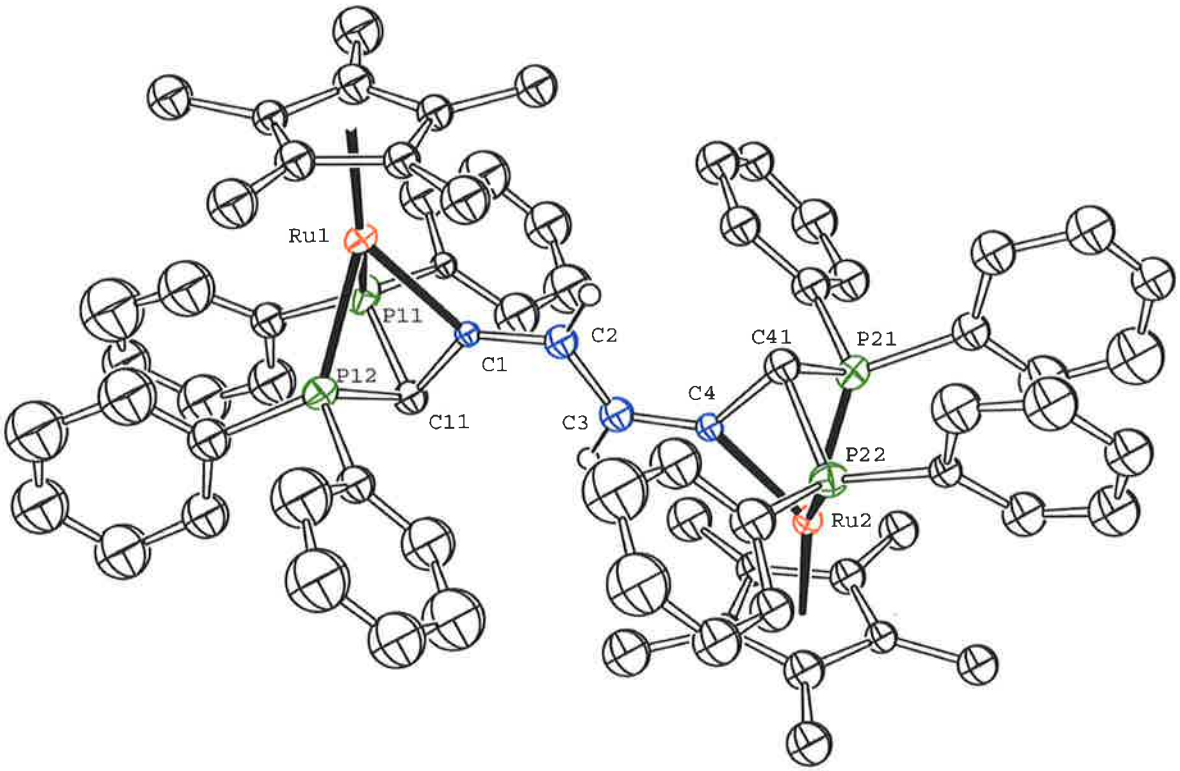

Figure 3.2: *ORTEP view of* ***28****.*

Bond distances (Å)		**Bond angles (°)**	
Ru(1,2)-P(11,21)	2.281, 2.284(4)	P(11)-Ru(1)-P(12)	71.1(1)
Ru(1,2)-P(12,22)	2.271, 2.280(4)	P(21)-Ru(2)-P(22)	70.9(1)
Ru(1,2)-C(Cp*)	2.15-2.26, 2.18-2.23(1)	P(11,21)-Ru(1,2)-C(1,4)	64.0, 63.8(3)
(av.)	2.20, 2.21(1)	P(12,22)-Ru(1,2)-C(1,4)	64.3, 63.6(3)
Ru(1,2)-C(1,4)	2.11, 2.10(1)	Ru(1,2)-C(1,4)-C(2,3)	135.6(9), 135.2(9)
C(11,41)-C(1,4)	1.59, 1.50(2)	C(11,41)-C(1,4)-C(2,3)	129, 127(1)
C(1,4)-C(2,3)	1.37, 1.37(2)	C(1,4)-C(2,3)-C(3,2)	126, 124(1)
C(2)-C(3)	1.44, 1.44(2)		

Table 3.1: *Selected bond distances and angles for* ***28****.*

The structure of **28** confirms that both ruthenium atoms make up part of two individual 1-ruthena-2,4-diphosphabicyclo[1.1.1]pentane rings. The significant deviation from linearity across Ru-C(1)-C(2) (*ca* 135°) is the result of the C(1)-C(2) double bond kinking the C_4 chain. The C(1)-C(2) double bond has a typical length

of 1.37(2) Å and is coplanar with its substituents [Ru(1), C(11), C(3)]. The Ru-C(1) bond [2.11(1) Å] is longer than those found in the related vinylidene **22a** [1.848(2) Å] or diyndiyl **25a** [2.017(2) Å] complexes, but is typical for a Ru-C(sp^2) bond.[126]

All attempts to obtain single crystals of **27** suitable for X-ray diffraction were unsuccessful. Crystallisation of the reaction mixture from acetone gave thin fibres, together with larger crystals that were found to be **25a**.

3.2.2. Synthesis of [{Ru(dppm)Cp}$_2$(=C=CMeCMe=C=)][OTf]$_2$ (29)*

As the individual products from the reaction between **24a** and KOBu^t could not be separated, it was anticipated that deprotonation of the methyl analogue of **24a** would favour deprotonation of the dppm ligands to give the methyl analogue of **28**. The isolation and NMR characterisation of this derivative would further support those assignments made for **28**, and hence **27**.

Addition of 2.2 equivalents of methyl triflate to a CH_2Cl_2 solution of **25a** resulted in a rapid colour change from orange to deep red, before changing further to bright green. The product was crystallised directly by the addition of diethyl ether to the reaction mixture to give [{Ru(dppm)Cp*}$_2$(=C=CMeCMe=C=)][OTf]$_2$ (**29**) in 63% yield (Scheme 3.4).

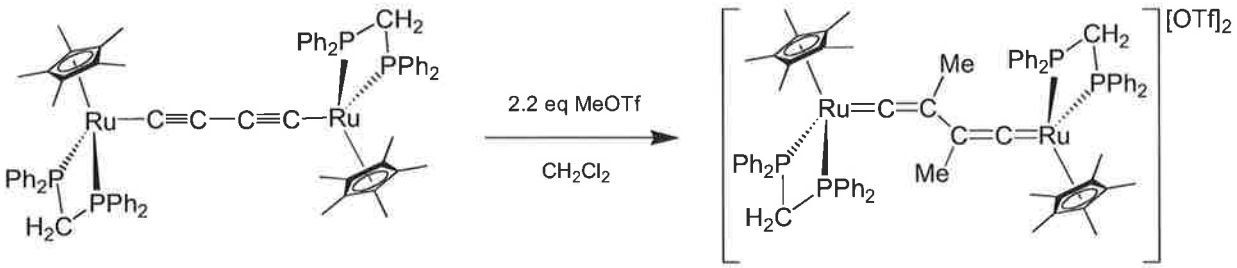

25a **29**

Scheme 3.4

A single band at 1626 cm^{-1} in the IR spectrum of **29** confirmed the bridging C_4 ligand exists as a bis-vinylidene. In the NMR spectra, characteristic resonances for

the Ru(dppm)Cp* fragment were observed and these are summarised in Section 3.4. Interest lies in the upfield signal of the methyl protons, a singlet at δ 0.06. Characteristic resonances for the vinylidene ligand were found in the ^{13}C NMR spectrum at δ 352.20 and 104.61, assigned to atoms C_1 and C_2, respectively. The ES-mass spectrum contained two major ions at *m/z* 1469 and 660, assigned to $[M + OTf]^+$ and $[M]^{2+}$, respectively.

Single crystals of **29** suitable for X-ray diffraction were grown by slow evaporation of a concentrated CH_2Cl_2/hexane solution. The ORTEP view of **29** is shown in Figure 3.3, while selected structural parameters are given in Table 3.2.

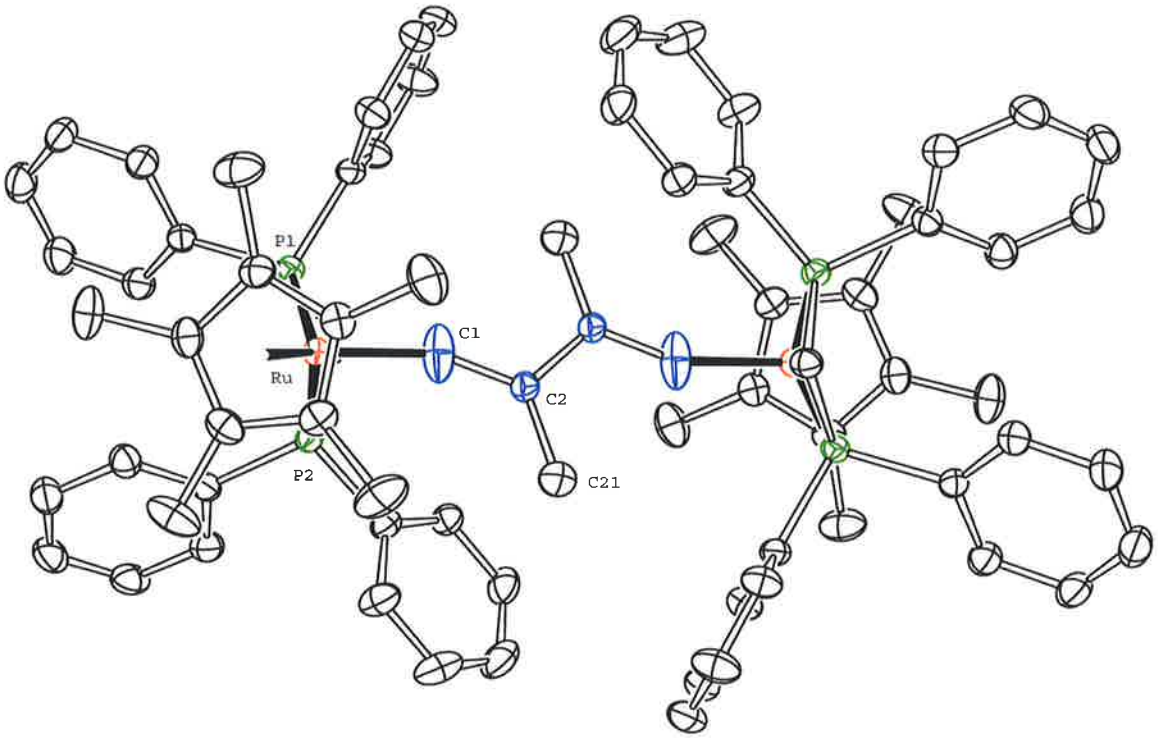

Figure 3.3: *ORTEP view of the cation* ***29****.*

As expected, the structure of the centrosymmetric **29** is very similar to that of **24a** with the two Cp* ligands adopting a *transoid* arrangement. Confirmation of the vinylidene ligand is apparent from the short Ru-C(1) [1.851(3) Å] and C(1)-C(2) [1.376(5) Å] bonds and longer C(2)-C(2') [1.463(5) Å] bond, all of which are very similar to those found in **24a**.

Bond distances (Å)		Bond angles (°)	
Ru-P(1)	2.3189(6)	P(11)-Ru(1)-P(12)	70.18
Ru-P(2)	2.2979(7)	P(11)-Ru(1)-C(1)	90.53
Ru-C(Cp*)	2.243-2.293(3)	P(12)-Ru(1)-C(1)	82.9(1)
(av.)	2.270(2)	Ru(1)-C(1)-C(2)	157.7(3)
Ru-C(1)	1.851(3)	C(1)-C(2)-C(2')	116.8(4)
C(1)-C(2)	1.376(5)	C(1)-C(2)-C(21)	126.6(3)
C(2)-C(2')	1.463(5)		
C(2)-C(21)	1.527(6)		

Table 3.2: *Selected bond distances and angles for* ***29****.*

3.2.3. Deprotonation of [{Ru(dppm)Cp}$_2$(=C=CMeCMe=C=)][OTf]$_2$ (29)*

Treatment of **29** with KOBu^t in THF gave a bright orange solid. NMR and structural data confirmed {Cp*(dppm)Ru}-C≡C-CMe=C-{Ru($Ph_2PCHPPh_2$)Cp*} (**30**) was the sole product from the reaction (Scheme 3.5). Surprisingly, KOBu^t in this case has deprotonated a single dppm ligand allowing for the formation of the metallacycle, as well as removing a methyl group from the vinylidene, forming the alkynyl group in **30**. There was no evidence for the formation of the anticipated methyl analogue of **28**.

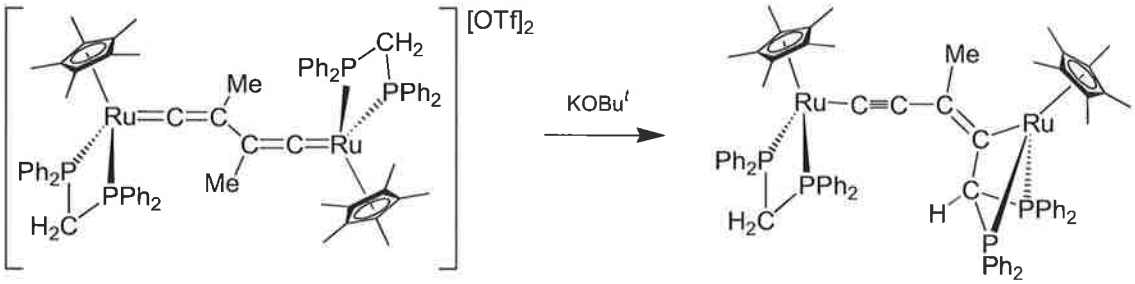

29 **30**

Scheme 3.5

Spectroscopic features shown by **30** were similar to those observed for **27**. Two bands in the IR spectrum at 1713 and 1950 cm^{-1} were consistent with the presence of both C=C double and C≡C triple bonds. The asymmetric nature of **30** was

confirmed by the ^{31}P NMR spectrum, which revealed two equal intensity resonances at δ 0.49 and 19.05. The upfield resonance was assigned to the phosphorus nuclei of the metallacycle, while the resonance at δ 19.05 was due to the dppm ligand.

In the ^{1}H NMR spectrum, two Cp* resonances appeared at δ 1.97 and 2.22, with the upfield signal assigned to the Ru(dppm)Cp* centre. The CH_2 protons of dppm were observed as multiplets at δ 3.94 and 4.25, while the resonance for the $(Ph_2P)_2C\underline{H}$ proton appeared as a triplet at δ 5.43. The methyl group of the vinylidene was observed as a triplet at δ 1.99.

The ^{13}C NMR spectrum of **30** recorded in CD_2Cl_2 is shown in Figure 3.4, together with the assignments and the atomic numbering scheme. As expected, two different Cp* ligands were observed with resonances at δ 11.42 and 13.15 corresponding to the methylene carbons, while resonances at δ 87.85 and 91.28 were due to the ring carbons. A triplet at δ 27.87 was assigned to the $(Ph_2P)_2\underline{C}H$ group while the $(Ph_2P)_2\underline{C}H_2$ carbon of dppm was observed as a triplet at the expected value of δ 49.79. Resonances for the four carbons bridging the two ruthenium centres were also observed. The resonance for C_1 was observed as a well resolved triplet of triplets (insert) with the larger coupling [^{2}J(CP) 25 Hz] due to the phosphorus nuclei of dppm, while the smaller coupling [^{4}J(CP) 5 Hz] results from the two equivalent phosphorus nuclei of the $(Ph_2P)_2CH$ ligand. Coupling to dppm was also observed with C_2, which appeared as a triplet (insert) at δ 113.53 [^{3}J(CP) 11 Hz]. C_3 appeared as a triplet at δ 72.54 [^{1}J(CP) 23 Hz] with the coupling presumably due to the $(Ph_2P)_2CH$ ligand. The ruthenium bound C_4 resonance was shifted significantly downfield to δ 203.24, while the methyl group was found at δ 29.94. In general, NMR data collected for **30** were fully consistent with the assignments made for its hydrogen analogue **27**, further supporting the proposed structure.

ES-mass spectroscopy revealed a strong $[M + H]^+$ ion centred at *m/z* 1305 with no other fragmentation, even at higher cone voltages. If solutions of **30** were left in MeOH for extended periods of time, the colour changed from orange to brown and the ES-mass spectrum of this solution contained a $[M + MeOH]^+$ ion at *m/z* 1336, suggesting the change was due to the addition of MeOH to **30**.

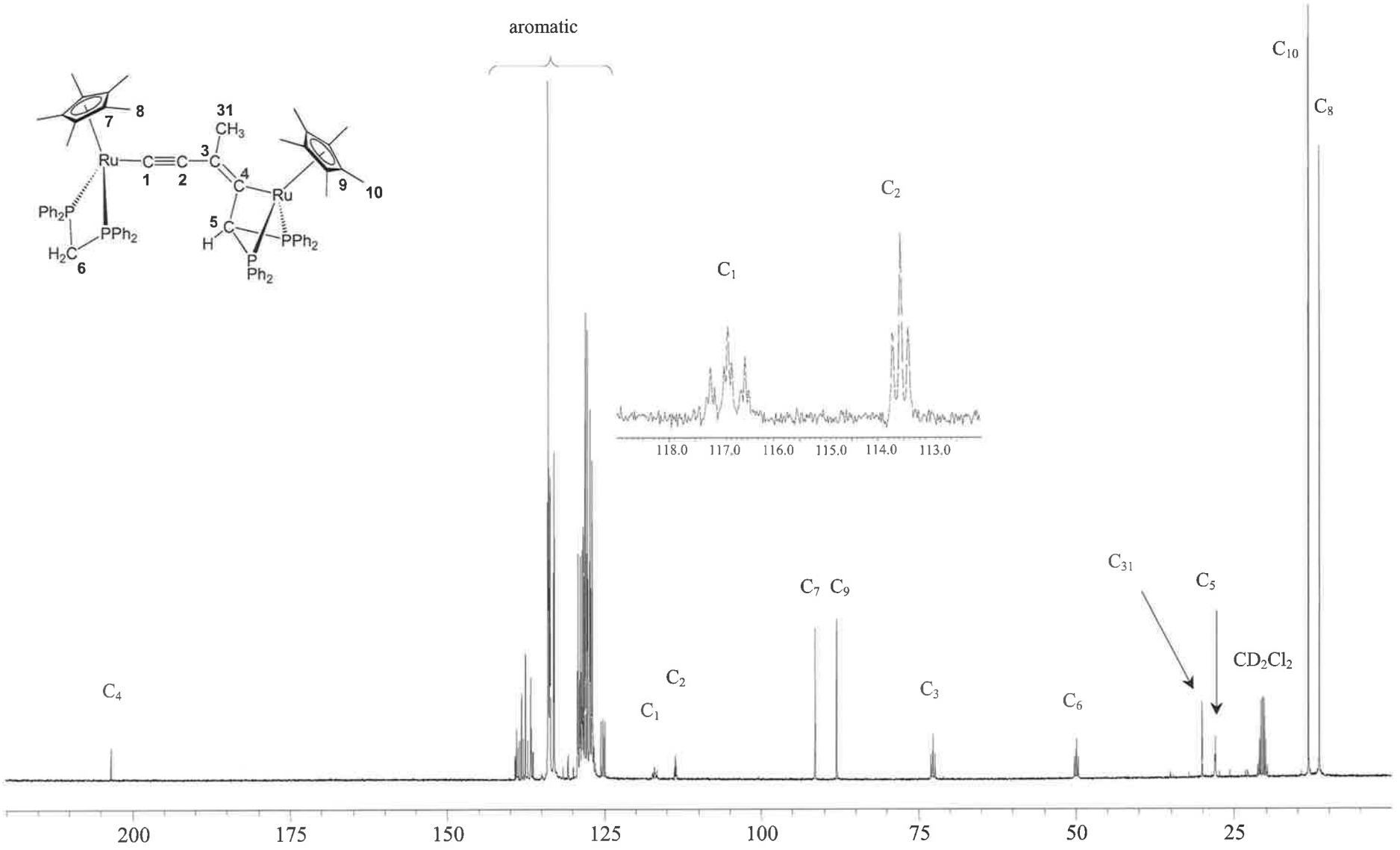

Figure 3.4: *^{13}C NMR spectrum (298 K) of **30** recorded in CD_2Cl_2 (ppm), 300 MHz.*

Crystals of **30** suitable for X-ray diffraction were grown from a benzene/hexane solution and the ORTEP view of a single molecule is shown in Figure 3.5, while selected data are given in Table 3.3. The structure confirms the presence of both ruthenium ethynyl and metallacyclic fragments. Bond lengths for the ethynyl portion resemble those in **23a**, with those for Ru(1)-C(1) [2.0239(8) Å] and C(1)-C(2) [1.224(3) Å] fully consistent with the expected values for Ru-C single and C≡C triple bonds. The metallacyclic portion in **30** features longer Ru(2)-C(4) [2.153(2) Å] and a short C(3)-C(4) bond [1.357(4) Å] consistent with the presence of Ru-C single and C=C double bonds. The C(3)-C(4) double bond adopts the more thermodynamically stable *E* configuration, and is coplanar with its substituents C(31), C(2), C(5) and Ru(2).

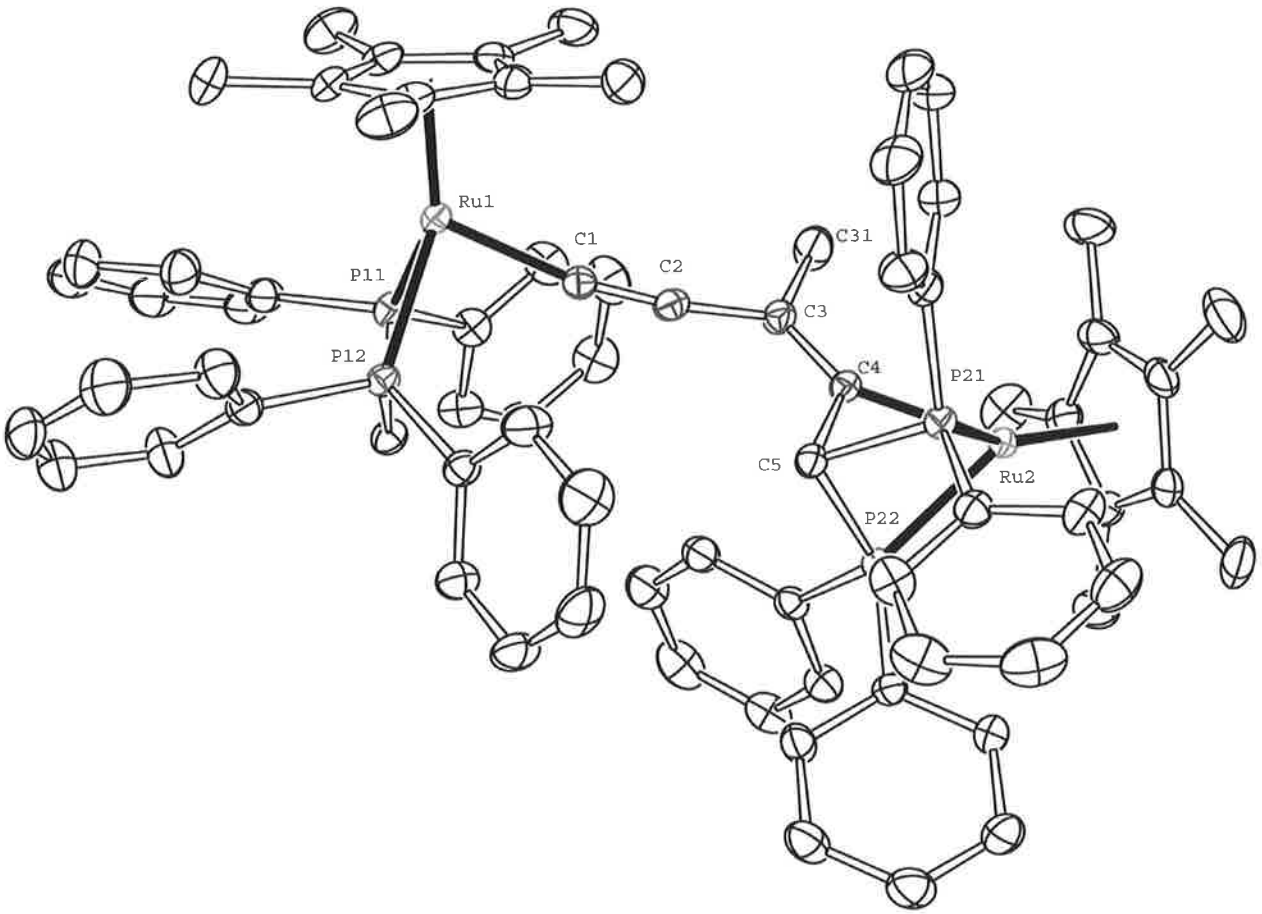

Figure 3.5: *ORTEP view of* ***30****.*

Bond distances (Å)		**Bond angles (°)**	
Ru(1)-P(11)	2.2662(8)	P(11)-Ru(1)-P(12)	71.73(3)
Ru(1)-P(12)	2.2733(8)	P(11)-Ru(1)-C(1)	85.61(8)
Ru(1)-C(Cp*)	2.227(3)-2.259(2)	P(12)-Ru(1)-C(1)	86.07(8)
(av.)	2.243(3)	Ru(1)-C(1)-C(2)	169.3(2)
Ru(1)-C(1)	2.0239(8)	C(1)-C(2)-C(3)	171.3(3)
C(1)-C(2)	1.224(3)	C(2)-C(3)-C(4)	123.3(3)
C(2)-C(3)	1.448(3)	C(3)-C(4)-C(5)	121.7(2)
C(3)-C(31)	1.514(5)	Ru(2)-C(4)-C(3)	142.6(2)
C(3)-C(4)	1.357(4)	P(21)-Ru(2)-P(22)	71.23(3)
C(4)-C(5)	1.547(4)		
Ru(2)-C(4)	2.153(2)		
Ru(2)-P(21)	2.2809(7)	Ru(2)-C(Cp*)	2.217(3)-2.241(2)
Ru(2)-P(22)	2.2723(8)	(av.)	2.228(3)

Table 3.3: *Selected bond distances and angles for* ***30****.*

3.2.4. Protonation of {Ru(dppe)Cp}$_2$(C≡CC≡C) (25b)*

The bis-vinylidenes [{M(dppe)Cp*}$_2$(=C=CHCH=C=)]$^{2+}$ (M = Fe,[44] Os,[130] Ru) can all be deprotonated to give the corresponding diyndiyl complexes. However, the reverse reaction involving the protonation of the diyndiyl complexes to give the bis-vinylidenes has not been demonstrated. The addition of triflic acid to a solution of the iron diyndiyl **5** gave multiple products that presently have not been characterised.[131] So while trivial, protonation of the diyndiyl complex **25b** was attempted.

Addition of a slight excess of triflic acid to a CH_2Cl_2 solution of **25b** resulted in a rapid colour change from orange to deep red. The reaction mixture was stirred for 30 minutes before diethyl ether was added to crystallise the product, shown to be [{Ru(dppe)Cp*}$_2$(=C=CHCH=C=)][OTf]$_2$ (**31**) (Scheme 3.6). The IR spectrum

contained a single ν(C=C) band at 1600 cm^{-1}, while the ^{1}H and ^{31}P NMR spectra were similar to those found for **24b**.

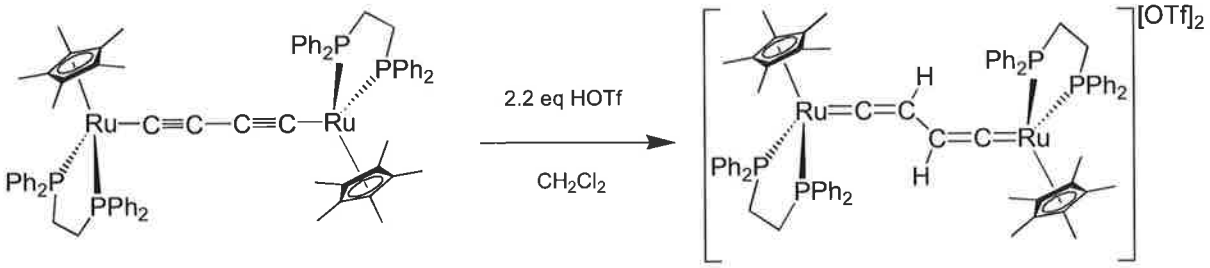

25b **31**

Scheme 3.6

While the bis-vinylidenes **24a/b**, **29** and **31** were all air-stable solids, decomposition was observed if solutions were left exposed to air (1-2 days). In the case of **24b** the carbonyl cation [Ru(CO)(dppe)Cp*][PF_6] (**32**) was isolated as the major decomposition product (Scheme 3.7). Similar oxidations of Ru(II) vinylidenes to give carbonyl cations have previously been reported and in some cases aldehyde by-products isolated.[132-136]

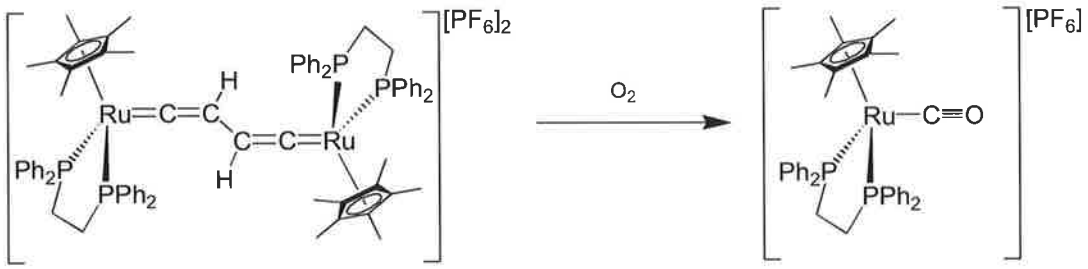

24b **32**

Scheme 3.7

Crystals of **32** were obtained from aerobic MeOH solutions of **24b**. The ORTEP view of the cation is shown in Figure 3.6 and selected structural parameters are collected in Table 3.4. As expected the cation in **32** adopts a pseudo-octahedral geometry around ruthenium. The two Ru-P distances [2.3188(5), 2.3311(4) Å] are slightly longer than in **19b** [2.2882(5), 2.2812(4) Å] and reflect the reduced back-bonding from the cationic ruthenium centre to the phosphorus nuclei. The carbonyl

group has similar Ru-C and C-O bond lengths to those found in related complexes.[133]

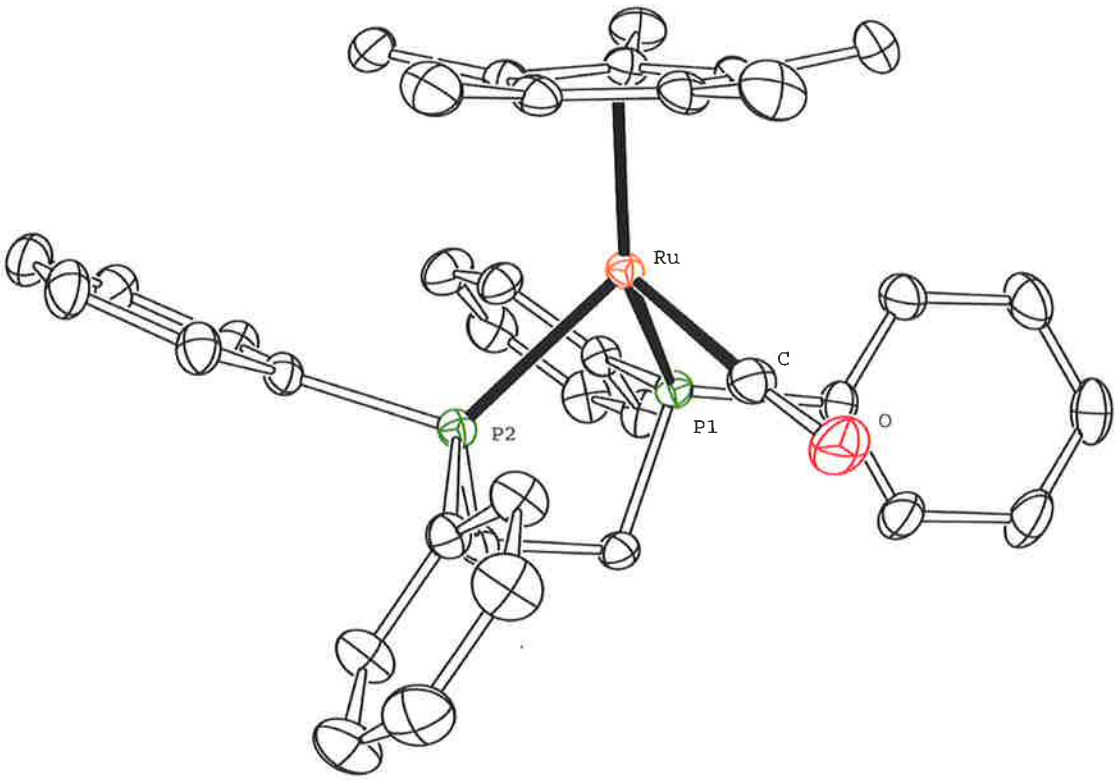

Figure 3.6: *ORTEP view of the cation* ***32****.*

Bond distances (Å)		**Bond angles (°)**	
Ru-P(1)	2.3188(5)	P(1)-Ru-P(2)	83.06(2)
Ru-P(2)	2.3311(4)	P(1)-Ru-C	83.90(7)
Ru-C(Cp*)	2.251-2.298(2)	P(2)-Ru-C	91.32(7)
(av.)	2.233(2)	Ru-C-O	175.8(2)
Ru-C	1.857(2)		
C-O	1.153(3)		

Table 3.4: *Selected bond distances and angles for* ***32****.*

Alternatively, **32** could be synthesised by the reaction of **19b** with NH_4PF_6 in MeOH under an atmosphere of CO (Scheme 3.8). The solution gradually changed colour from bright orange to a very pale yellow upon completion of the reaction. The IR spectrum contained a strong ν(CO) band at 1972 cm^{-1}, while in the ^{13}C NMR spectrum, the carbonyl resonance was observed as a singlet at δ 203.31. Other resonances are summarised in Section 3.4.

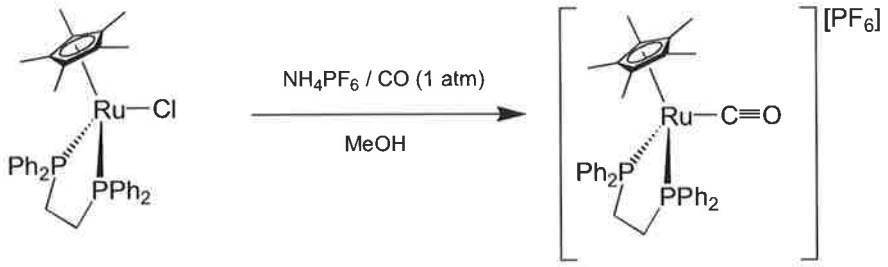

19b **32**

Scheme 3.8

3.2.5. Electrochemistry

The bis-ruthenium complexes **29** and **30** were further investigated by cyclic voltammetry. In the case of the bis-vinylidene **29**, two fully reversible waves were observed at $E_{½}$ = +0.82 and +1.20 (Figure 3.7). Comparisons show that **29** is thermodynamically easier to oxidise than the related hydrogen analogue **24a** ($E_{½}$ = +1.00 and +1.26 V). Additionally, the separation between the two waves (ΔE) is greater in **29** (0.38 V) than in **24a** (0.26 V), suggesting the methyl groups at the C_2 positions in **29** have enhanced the electronic interactions between the two ruthenium centres by donating electron density into the HOMOs which are expected to extend between the two ruthenium centres. The large separation in potentials is also indicated by the large comproportionation constant, $K_c = 2.64 \times 10^6$. This suggests that chemical oxidation with one equivalent of oxidising agent should yield a MV product that could be isolated free from contamination from the doubly oxidised or doubly reduced states.

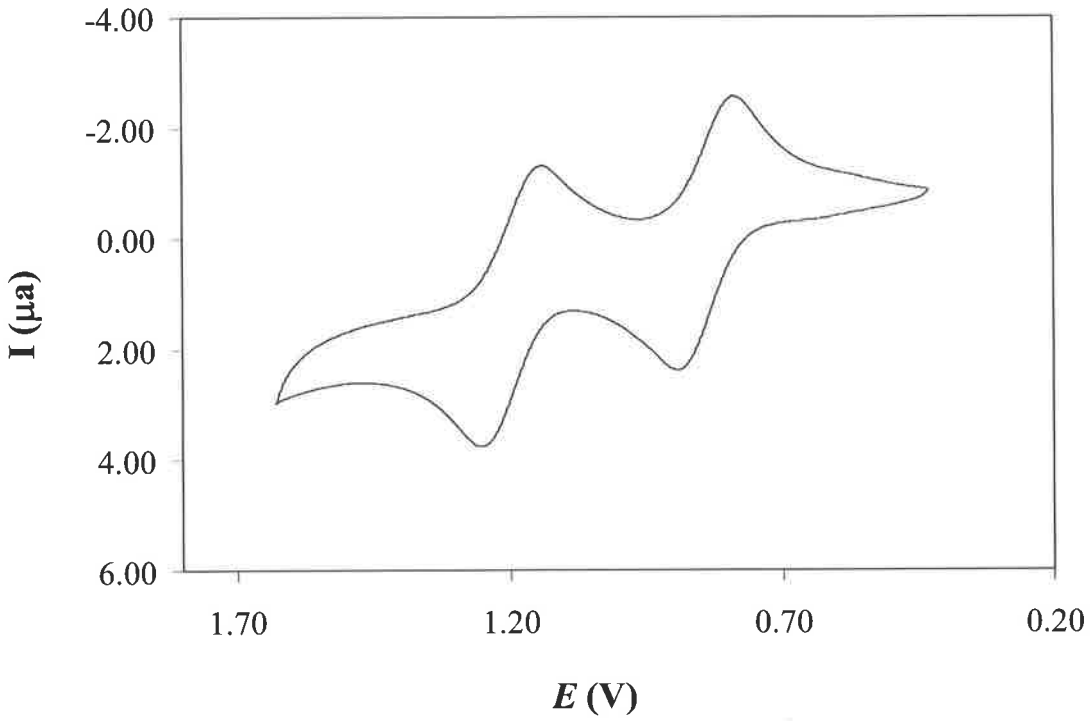

Figure 3.7: *Cyclic voltammogram of* ***29****, recorded in* CH_2Cl_2*, 0.1 M* $[Bu^n_4N][PF_6]$.

The asymmetric complex **30** revealed two reversible well-separated waves at $E_{½}$ = -0.30 and +0.04 V, corresponding to the sequential oxidation of each ruthenium from Ru(II) to Ru(III). Evaluation of the electronic interactions across the bridging ligand in this case is difficult, as comparisons need to be made for the corresponding symmetric derivatives, which for the metallacyclic complex have yet to be prepared.

3.3. Conclusions

In summary, this Chapter has demonstrated that ruthenium(II) vinylidenes containing a coordinated dppm ligand transform to new metallacyclic structures by a reaction sequence which probably involves deprotonation of the dppm ligand followed by intramolecular attack of the resulting anion at C_1. In the case of bis-vinylidene **29**, treatment with $KOBu^t$ resulted in deprotonation of a single dppm ligand and cyclisation followed by the removal of a methyl group to form the metallacyclic and ethynyl portions in **30**, respectively. The single crystal X-ray

structures of **28** and **30** confirm the formation of a 1-ruthena-2,4-diphosphabicyclo[1.1.1]pentane moiety in each case.

Despite the protonation of the iron diyndiyl complex **5** yielding a mixture of inseparable products, the reaction of **25b** with a slight two-fold excess of HOTf gave the expected bis-vinylidene **31** as the sole product. However, care must be taken while handling **31** and related complexes to prevent formation of the corresponding carbonyl cation **32** by oxidation.

3.4. Experimental

General experimental conditions are detailed on page ix.

Treatment of [{Ru(dppm)Cp*}$_2$(=C=CHCH=C=)][PF$_6$]$_2$ with KOBu^t

To a solution of **24a** (50 mg, 0.03 mmol) in THF (20 mL) was added KOBu^t (10.6 mg, 0.09 mmol). The reaction mixture was left to stir at r.t. for 10 min before the solvent was removed. The orange residue was extracted into hexane and the solution filtered and concentrated under vacuum to give a bright orange solid (40 mg), identified by NMR as a mixture of three complexes: **25a** (35%). ^{1}H NMR: 1.90 (s, 30H, Cp*), 4.22 (m, 4H, CH_2). ^{31}P NMR: 16.63 (s, dppm). **27** (60%). ^{1}H NMR: 1.98 [t, ^3J(HP) 2 Hz, 15H, Cp*], 2.07 [t, ^3J(HP) 1 Hz, 15H, Cp*], 2.11 (s, 1H, =CH), 3.85, 4.12 (m, 2H, CH_2), 5.59 [t, ^2J(HP) 4 Hz, 1H, P_2CH]. ^{31}P NMR: -1.80 (s, P_2CH), 18.99 (s, dppm). **28** (5%). ^{1}H NMR: 2.24 (s, 30H, Cp*), 6.43 (br, 2H, P_2CH). ^{31}P NMR: -3.05 (s, P_2CH).

[{Ru(dppm)Cp*}$_2$(=C=CMeCMe=C=)][OTf]$_2$ (29)

To a solution of **25a** (500 mg, 0.38 mmol) in CH_2Cl_2 (25 mL) was added MeOTf (0.096 mL, 0.84 mmol, 2.2 eq). The solution was stirred at r.t. for 3 h, gradually changing in colour from orange to green. Diethyl ether (50 mL) was added and the bright green product crystallised. The solid was filtered and washed with THF and diethyl ether to give **29** (390 mg, 63%). Anal. Calcd ($C_{78}H_{80}F_6O_6P_4Ru_2S_2$): C, 57.92; H, 4.98. Found: C, 58.01; H, 4.86. IR (Nujol, cm^{-1}): ν(C=C) 1626 m. ^{1}H NMR (acetone-d_6): δ 0.06 (s, 6H, 2 x Me), 1.98 (s, 30H, Cp*), 4.82, 5.32 (2m, 2 x 2H, CH_2), 7.22-7.61 (m, 40H, Ph). ^{13}C NMR (acetone-d_6): δ 8.75 (s, Me), 12.37 (s, $C_5\underline{Me}_5$), 45.77 [t, ^1J(CP) 27 Hz, CH_2], 104.61 (s, $\underline{C}_5Me_5$), 117.45 (s, C_2), 129.96-136.81 (m, Ph), 352.20 [t, ^2J(CP) 14 Hz, C_1]. ^{31}P NMR (acetone-d_6): δ 2.00 (s, dppm). ES-mass spectrum (*m/z*): 1469, [M + OTf]$^+$; 660, [M]$^{2+}$.

{Cp*(dppm)Ru}-C≡CCMe=C-{Ru(Ph$_2$PCHPPh$_2$)Cp*} (30)

To a suspension of **29** (70 mg, 0.04 mmol) in THF (10 mL) was added KOBu^t (19.4 mg, 0.17 mmol). The reaction was left to stir at r.t. for 10 min before the solvent was removed and the orange solid extracted into hexane. The solution was filtered and concentrated under vacuum to give bright orange crystals identified as **30** (44 mg, 78%). Anal. Calcd ($C_{75}H_{76}P_4Ru_2$): C, 69.11; H, 5.88. Found: C, 69.14; H, 5.91. IR (Nujol, cm^{-1}): ν(C≡C) 1950 w; ν(C=C) 1713 m. ^{1}H NMR (benzene-d_6): δ 1.97 (s, 15H, Cp*), 1.99 [t, ^5J(HP) 12 Hz, 3H, Me], 2.22 (s, 15H, Cp*), 3.94, 4.25 (2m, 2 x 1H, CH_2), 5.43 [t, ^2J(HP) 4 Hz, 1H, PCHP], 6.78-7.73 (m, 40H, Ph). ^{13}C NMR (toluene-d_8): δ 11.42 (s, C_8), 13.15 (s, C_{10}), 27.87 [t, ^1J(CP) 7 Hz, C_5], 29.94 (s, C_{31}), 49.79 [t, ^1J(CP) 22 Hz, C_6], 72.54 [t, ^1J(CP) 23 Hz, C_3], 87.85 [t, ^2J(CP) 2 Hz, C_9], 91.28 [t, ^2J(CP) 2 Hz, C_7], 113.536 [t, ^3J(CP) 11 Hz, C_2], 116.84 [tt, ^2J(CP) 25 Hz; ^4J(CP) 5 Hz, C_1], 126.30-139.10 (m, Ph), 203.24 (s, C_4). ^{31}P NMR (benzene-d_6): δ 0.49 (s, P_2CH), 19.05 (s, dppm). ES-mass spectrum (*m/z*): 1336, $[M + MeOH]^+$; 1305, $[M + H]^+$.

[{Ru(dppe)Cp*}$_2$(=C=CHCH=C=)][OTf]$_2$ (31)

To a solution of **25b** (100 mg, 0.07 mmol) in CH_2Cl_2 (10 mL) was added HOTf (0.015 mL, 0.17 mmol, 2.2 eq). The reaction was stirred at r.t. for 15 min before diethyl ether (50 mL) was added. The brick red crystals were filtered and washed with further portions of diethyl ether to give **31** (88 mg, 72%). IR (Nujol, cm^{-1}): ν(C=C) 1600 m. ^{1}H NMR: δ 1.66 (s, 30H, Cp*), 2.57-2.78 (m, 8H, CH_2CH_2), 3.13 (s, 2H, =CH), 7.00-7.56 (m, 40H, Ph). ^{31}P NMR: δ 75.92 (s, dppe).

[Ru(CO)(dppe)Cp*][PF$_6$] (32)

A solution of **19b** (100 mg, 0.15 mmol) and NH_4PF_6 (49 mg, 0.30 mmol) in MeOH (20 mL) was stirred at r.t. for 24 h under CO (1 atm). The resulting pale yellow solution was evaporated to dryness and the solid extracted in the minimum quantity of CH_2Cl_2 and the extract filtered dropwise into rapidly stirring diethyl ether (100 mL). The product was collected on a sintered glass funnel and washed with pentane to give **32** as a pale yellow solid (108 mg, 90%). IR (CH_2Cl_2, cm^{-1}): ν(CO) 1972 s;

ν(PF) 841 s. ^{1}H NMR: δ 1.66 (s, 15H, Cp*), 2.62, 2.71 (2m, 2 x 2H, CH_2CH_2), 7.17-7.61 (m, 20H, Ph). ^{13}C NMR: δ 10.20 (s, $C_5\underline{Me}_5$), 30.14 (m, CH_2CH_2), 100.05 (s, $\underline{C}_5Me_5$), 129.48-133.55 (m, Ph), 203.31 (s, CO). ^{31}P NMR: δ -143.05 (septet, PF_6^-), 72.72 (s, dppe). ES-mass spectrum (*m/z*): 663, $[M]^+$.

CHAPTER FOUR

Syntheses, Characterisation and Reactions of the Diynyl Complexes Ru(C≡CC≡CR)(dppe)Cp* (R = TMS, H)

4.1. Introduction

Diynyl complexes of the general formula $[M]\{(C{\equiv}C)_2R\}_n$ (n = 1, 2; R = TMS, H) feature a C_4 unit capped by a metal-ligand fragment at one end and a hydrogen atom or other simple organic group at the other. The syntheses of diynyl complexes are of significant interest as these reagents are very useful starting materials and examples from almost every group within the transition metal series have now been reported.[137] The versatility of these reagents can be attributed to the ability of the C≡CH moiety to behave as a typical organic 1-alkyne, enabling it to take part in numerous well-established alkyne coupling reactions, such as deprotonation to give a nucleophilic anion which can be treated with a second metal-ligand fragment to afford new symmetric or asymmetric diyndiyl complexes. The homo-coupling between two diynyl units under oxidative coupling conditions has been used to synthesise octatetrayndiyl complexes of the general formula $[M](C{\equiv}C)_4[M]$. Furthermore, diynyl complexes may also exhibit numerous reactions specific to the diyne ligand. Addition of electron deficient alkenes such as tetracyanoethylene (TCNE), or electrophiles (H^+, Me^+) to the least sterically hindered C≡C triple bond is well documented.[137]

Diynyl complexes featuring two butadiyne units radiating from a central metal have found a place in the emerging field of 2D and 3D molecular architecture.[138,139] The treatment of square-planar precursors $PtCl_2(PAr_3)_2$ (Ar = aryl) with two equivalents of HC≡CC≡CH gives bis(diynyl)platinum(II) complexes with *cis* or *trans* geometry.[140,141] Those with a *cis* arrangement have been of recent interest due to their application as "molecular tweezers", whereby metals such as copper, silver and gold can bind to the alkyne units upon interaction with the π-electrons (Scheme 4.1).[142-144]

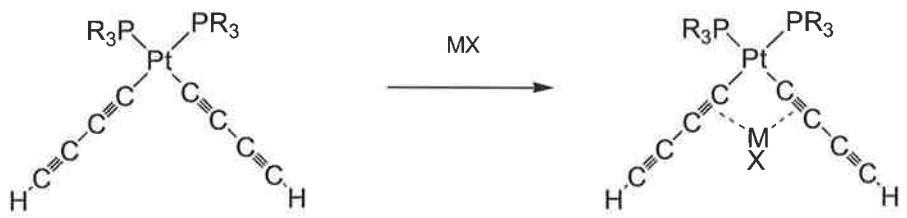

Scheme 4.1

The chemistry of *cis*-bis(diynyl)platinum(II) complexes has also been extended into the syntheses of larger and more impressive molecular architectures. Condensation of *cis*-Pt(C≡CC≡CH)$_2$(dppe) with Pt(OTf)$_2$(dppe) under dilute conditions in the presence of a weak base gave the molecular square *cyclo*-{Pt(C≡CC≡C)(dppe)}$_4$ (**33**) (Scheme 4.2).[116]

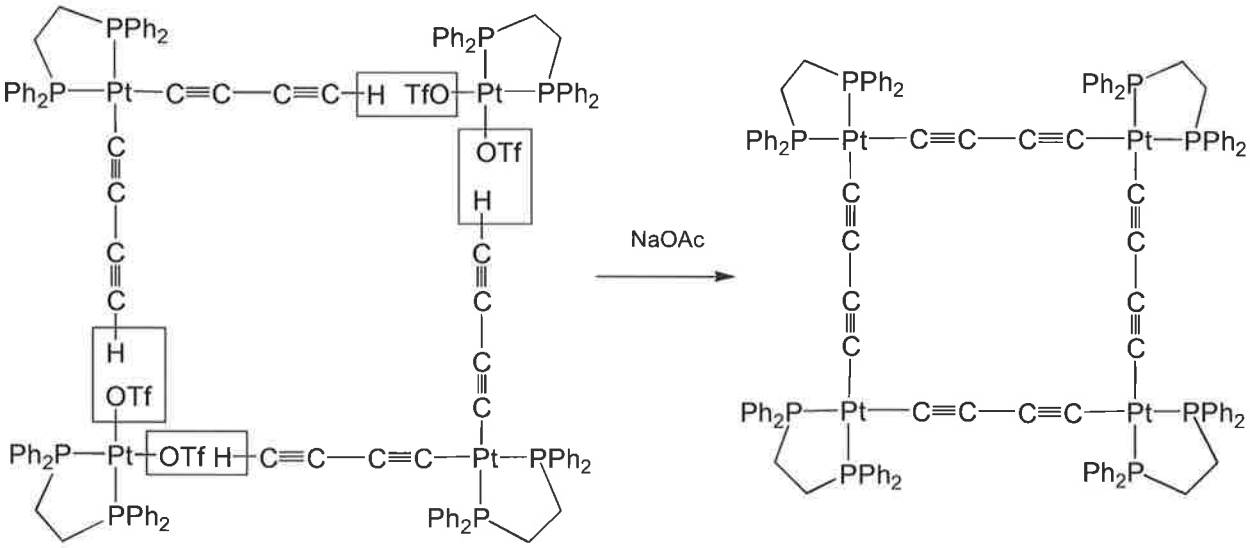

33

Scheme 4.2

4.1.1. Syntheses of Diynyl Complexes

Diynyl complexes are generally prepared by reactions between a suitable metal precursor and 1,3-butadiyne or a derivative. The synthetic strategy employed often depends on the associated chemistry of the starting materials and products.

The three most widely used methods for the preparation of diynyl complexes include:

(i) Reactions of metal-halide precursors with diyne anions;

(ii) Cu(I)-catalysed couplings of 1,3-diynes with metal-halide complexes;

(iii) Metal exchange and couplings of Group 14 diynyl derivatives.

In cases where these methods have not been successful, alternative conditions such as the deprotonation of vinylidene intermediates or the oxidative addition of 1,3-diynes have been used.[137] Detailed below are some literature examples that demonstrate the many different approaches that have been successfully employed to prepare a range of diynyl complexes.

4.1.1.1. Synthetic Strategy (i)

Organolithium reagents have provided a suitable entry into the syntheses of diynyl complexes. Reactions of LiC≡CC≡CTMS with metal-halide precursors generally gives the corresponding diynyl complex with precipitation of the lithium halide driving the reactions to completion (Scheme 4.3). This method has been used to prepare a variety of complexes with $Ru(CO)_2Cp$,[145] $Fe(CO)_2Cp$[94] and $Fe(CO)_2Cp^*$ end-groups.[146,147] The *trans*-bis(diynyl) $Ru(C{\equiv}CC{\equiv}CTMS)_2(CO)_2(PEt_3)_2$ was also prepared in the same manner.[148]

Scheme 4.3

Although the above method works well with the iron precursor $FeI(CO)_2Cp^*$, addition of LiC≡CC≡CTMS to a THF solution of FeCl(dppe)Cp* did not give the desired product, with a mixture of FeX(dppe)Cp* (X = Cl, Br) and the hydride complex FeH(dppe)Cp* isolated.[149] The bromide ligand in FeBr(dppe)Cp* originates from the LiBr present as a complex with the MeLi that was used to prepare the organic diyne anion.

4.1.1.2. Synthetic Strategy (ii)

The Cu(I)-catalysed reaction of 1,3-diynes with metal-halide precursors is the most widely used method for the preparation of diynyl complexes. First utilised in the

syntheses of the *cis* and *trans* isomers of $Pt(C{\equiv}CC{\equiv}CH)_2(PBu^n_3)_2$,[140,141] this method has now been used to prepare diynyl complexes from almost every group in the transition metal series.[150] This reaction is considered to proceed *via* a copper(I) alkynyl intermediate, which undergoes an alkynyl halide exchange with the metal-halide precursor to give the desired diynyl complex (Scheme 4.4). The CuX catalyst is regenerated in the process.

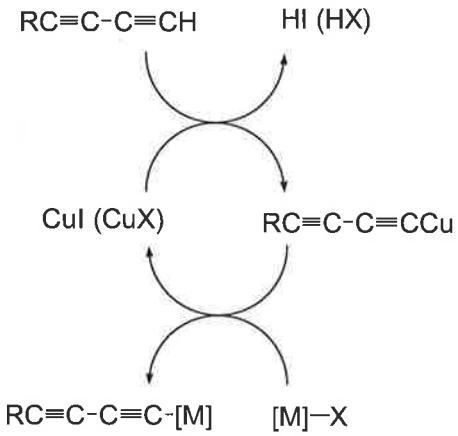

Scheme 4.4

4.1.1.3. Synthetic Strategy (iii)

Group 14 silyl and stannyl reagents have been used to prepare a number of diynyl complexes. Treatment of $ReCl(CO)_3(Bu^t_2\text{-bpy})$ with TMSC≡CC≡CTMS in the presence of KF and AgOTf in refluxing MeOH gave the TMS-protected diynyl **34** (Scheme 4.5).[151] A large excess of the starting organic diyne ensured only the mono-rhenium product was formed.

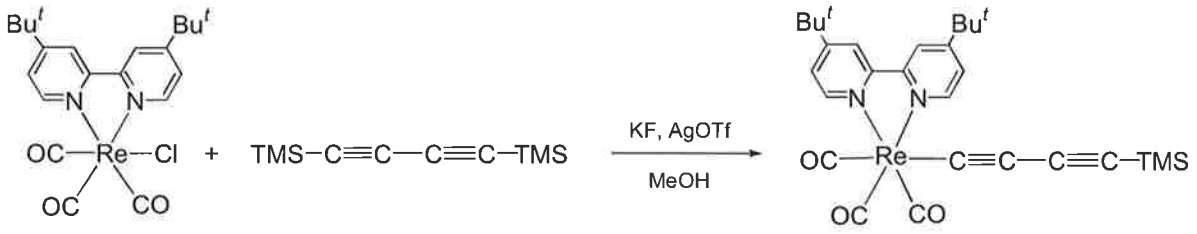

34

Scheme 4.5

The mixed silyl-stannyl diyne $Ph_3SnC{\equiv}CC{\equiv}CTMS$ was used to synthesise the rhodium diynyl $Rh(C{\equiv}CC{\equiv}CTMS)(CO)(PPr^i_3)_2$ (**35**). Treatment of the starting *trans*-$Rh(OH)(CO)(PPr^i_3)_2$ precursor with $Ph_3SnC{\equiv}CC{\equiv}CTMS$ in benzene gave the TMS-protected diynyl **35** in 56% yield (Scheme 4.6).[100] The reaction was driven by the formation of $Sn(OH)Ph_3$, avoiding the use of a Pd catalyst, which is usually required for the coupling of organo-stannanes with metal-halides.

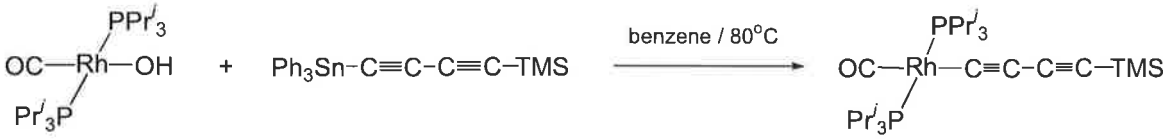

35

Scheme 4.6

4.1.1.4. Alternative Methods

In cases where the above strategies are not appropriate or are unsuccessful, alternative methods may be used. The rhenium diynyl $Re(C{\equiv}CC{\equiv}CTMS)(NO)(PPh_3)Cp^*$ (**36**) was prepared by the reaction of the labile precursor $[Re(ClC_6H_5)(NO)(PPh_3)Cp^*]^+$ with an excess of $HC{\equiv}CC{\equiv}CTMS$, affording the π-bonded intermediate $[Re(HC{\equiv}CC{\equiv}CTMS)(NO)(PPh_3)Cp^*]^+$ (Scheme 4.7). Subsequent deprotonation with $KOBu^t$ gave the neutral diynyl **36** in 95% yield.[152] In this case, the presence of the single TMS group in the starting organic diyne, together with the absence of desilylating agent, prevented the formation of the corresponding bis-rhenium diyndiyl **4**.

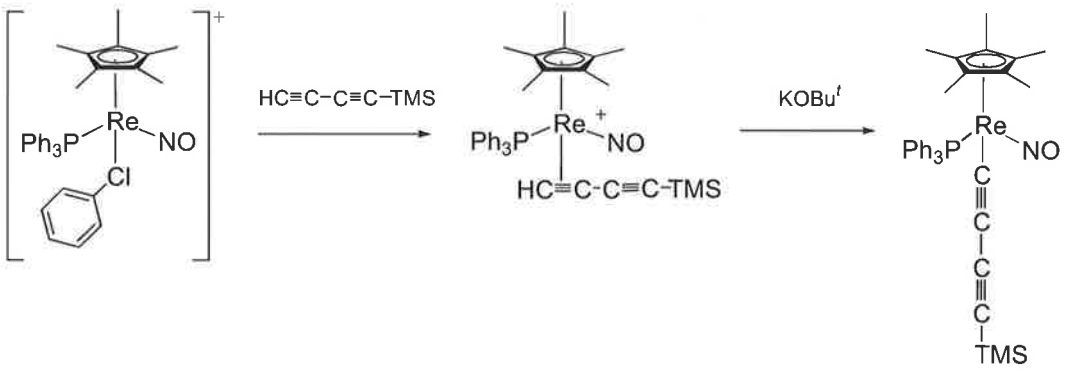

36

Scheme 4.7

Although FeCl(dppe)Cp* does not react with LiC≡CC≡CTMS to give the corresponding diynyl complex, an alternative strategy involved photolysis of Fe(C≡CC≡CTMS)$(CO)_2$Cp* (**37**) in the presence of dppe. Substitution of the two carbonyl groups by the bis-phosphine ligand gave the desired diynyl complex Fe(C≡CC≡CTMS)(dppe)Cp* (**38**) in 40% yield (Scheme 4.8).[147] While this two-step procedure worked reasonably well, a more direct synthesis of **38** was later found. Treatment of FeCl(dppe)Cp* with an excess of HC≡CC≡CTMS in an amine solvent in the presence of Na[BPh_4] gave **38** in a much higher yield (82%) (Scheme 4.8).[149]

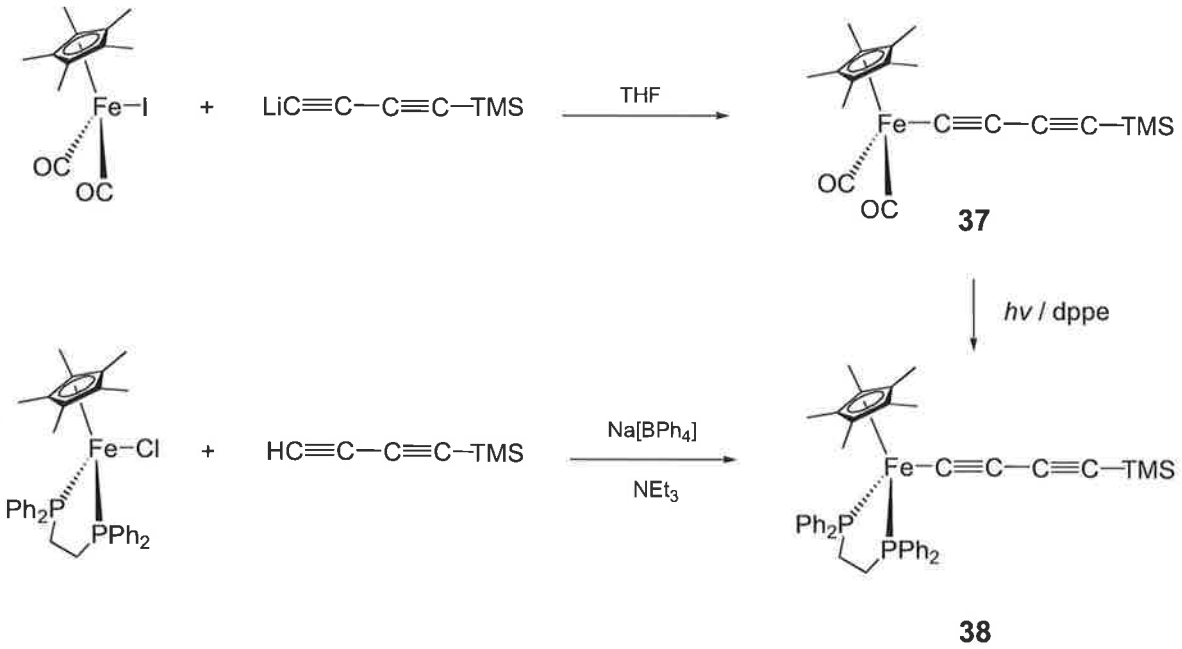

Scheme 4.8

The efficiency of this direct synthesis was due to two key factors. Firstly, the use of the bulky $[BPh_4]^-$ anion assisted with the ionisation of the Fe-Cl bond without acting as a desilylating agent (as is the case with PF_6^-). Secondly, the use of the basic solvent ensured that the intermediate butatrienylidene was deprotonated immediately after formation, preventing further reaction to give unwanted by-products.

4.2. Aims

The syntheses of diynyl complexes featuring the electron-rich synthon Ru(dppe)Cp* is highly desired as these reagents are suitable precursors for the syntheses of new asymmetric diyndiyls. Such complexes, which feature two structurally different metal-ligand fragments, are expected to show some interesting properties in connection with their electrochemical behaviour.

This Chapter details the syntheses and characterisation of Ru(C≡CC≡CR)(dppe)Cp* (R = TMS, H) and a number of adducts formed upon the reaction of the intermediate butatrienylidene with a range of nucleophiles (NH_3, H_2O and MeOH). New asymmetric diyndiyl complexes including a bis-ruthenium and two examples of mixed ruthenium-gold diyndiyls have been prepared. The syntheses of complexes containing the trinuclear copper(I) cluster $Cu_3(\mu\text{-dppm})_3$ capped with either one or two ruthenium diynyl fragments are also reported.

All complexes have been characterised by standard spectroscopic techniques, as well as X-ray structure determinations in some cases. Cyclic voltammetry has revealed some interesting findings concerning the bis-ruthenium complexes, showing that strong electronic interactions are present across the C_4 and C_4-$Cu_3(\mu\text{-dppm})_3$-C_4 bridging ligands.

4.3. Results and Discussion

4.3.1. Synthesis of Ru(C≡CC≡CR)(dppe)Cp [R = TMS (39), H (40)]*

The TMS-protected diynyl Ru(C≡CC≡CTMS)(dppe)Cp* (**39**) was successfully prepared by the reaction of the starting chloro-ruthenium complex **19b** with an excess of HC≡CC≡CTMS in the presence of $Na[BPh_4]$ in a THF/NEt_3 solvent mixture at 50°C over 48 hours (Scheme 4.9). The use of the tetraphenylborate salt was very important in this reaction as it prevented the desilylation of the TMS group and assisted with the ionisation of the Ru-Cl bond. The presence of triethylamine allowed the intermediate butatrienylidene formed upon the reaction of **19b** with the organic diyne to be deprotonated immediately upon formation, thereby preventing any side reactions from occurring. In contrast to the synthesis of the analogous iron complex **38**, which proceeded to completion after stirring at room temperature for 24 hours, no reaction was observed upon stirring **19b** with the organic diyne at room temperature. This difference in reactivity is consistent with the decreased strength of the Fe-Cl bond relative to the Ru-Cl bond.

Desilylation of **39** with $[Bu^n_4N]F$ gave **40** in quantitative yield as an air-stable, but moisture-sensitive yellow crystalline solid (Scheme 4.9). The reaction was monitored by IR, confirming that **39** was completely consumed within three hours.

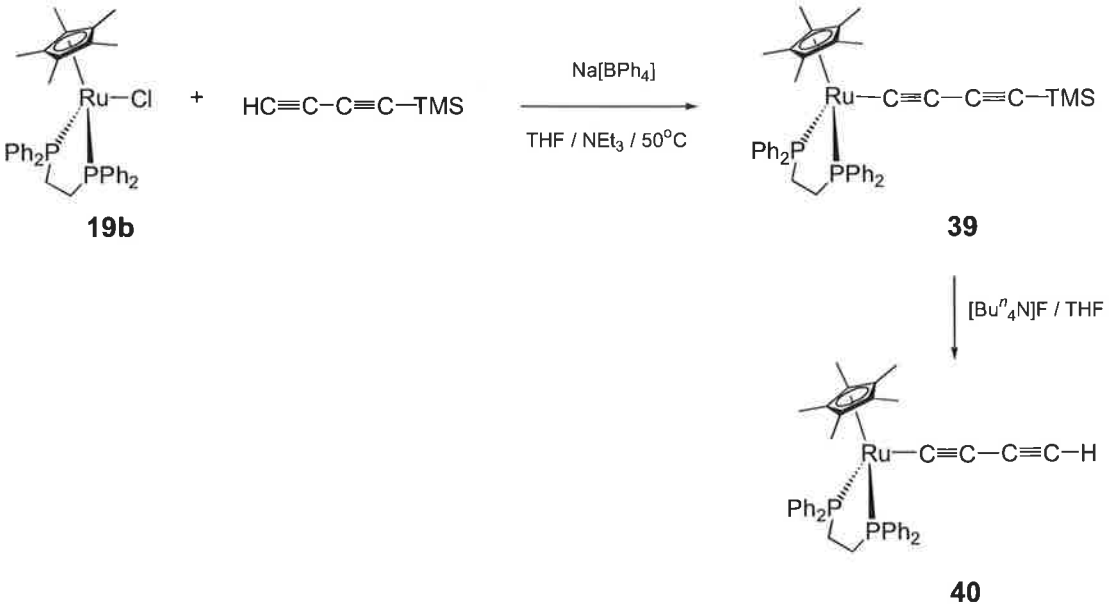

Scheme 4.9

The IR spectrum of **39** contained three ν(C≡C) bands at 2171, 2095 and 1990 cm^{-1}, as found previously with the iron complex **38**, and ascribed to Fermi coupling of one of the modes with another oscillator, such as the TMS group.[147,149] Only two ν(C≡C) bands were present in the IR spectrum of **40** at 2109 and 1971 cm^{-1}, together with a ν(≡CH) band at 3299 cm^{-1}.

Complexes **39** and **40** displayed all expected resonances for the Ru(dppe)Cp* fragment in their ^{1}H , ^{13}C and ^{31}P NMR spectra. The TMS resonance of **39** was observed at δ 0.23 (^{1}H) and at δ 1.17 (^{13}C), while the terminal proton of **40** gave a singlet at δ 1.44. Of interest were the resonances for the carbon atoms of the C_4 chain. In the case of **39**, C_1 was observed as a singlet at δ 120.06, whereas in **40** this resonance was a fully resolved triplet at δ 124.90 [^{2}J(CP) 24 Hz]. The remaining resonances for **39** and **40** were found at δ 115.84 and 91.73, 96.59 and 75.33, and 67.00 and 52.47, and assigned to C_2, C_3 and C_4, respectively.

There are only a limited number of structurally characterised pairs of diynyl and diyndiyl complexes featuring the same metal-ligand fragment.[105] Therefore, a crystallographic study of the ruthenium diynyls **39** and **40** together with the TMS-protected iron analogue **38** was carried out. Figures 4.1 and 4.2 show the ORTEP plots of single molecules of **38-40**, while selected structural data are collected in Table 4.1. The pseudo-octahedral geometry around the metal centres is evident in all three structures, as found in their related diyndiyls **5** and **25b**. The C_4 ligands all show the expected alternating short C(1)-C(2), long C(2)-C(3) and short C(3)-C(4) bonds, confirming their diynyl nature. A comparison between **38** and **39** shows the M-C(1) bond is longer in the case of ruthenium [1.983(2) Å] than in the iron complex **38** [1.875(3) Å], reflecting the different atomic radii (Fe = 1.26, Ru = 1.34 Å).[153] Similarly, the average M-Cp and M-P distances were shorter in the case of iron. Angles at the carbon atoms C(1-4) in all three structures were close to linear in the range of 172.7(5)-179.7(3)°.

Comparison of **40** with **25b** reveals shortening of the Ru-C bond in the latter upon the addition of a second metal-ligand fragment [2.015(4) (**40**) vs. 2.001(3) Å (**25b**)] with an accompanying increase in the C(1)-C(2) distance [1.186(5) (**40**) vs. 1.223(4)

Å (**25b**)]. This can be attributed to the additional set of metal carbon filled-filled orbital interactions towards the HOMOs in **25b**.

Similar variations in C-C bond lengths between related diynyl and diyndiyl complexes have been observed in a number of complexes featuring the capping groups $Fe(CO)_2Cp^*$,[146] $Ru_2(ap)_4$[68] and $W(CO)_3Cp^*$.[105] In the case of the former two complexes, this lengthening of the C(1)-C(2) bond and shortening of the M-C(1) and C(2)-C(3) bonds in the diyndiyls was attributed to increased contributions from the cumulenic resonance structure **4b** in addition to the dominating diyndiyl structure **4a** (Scheme 4.10).

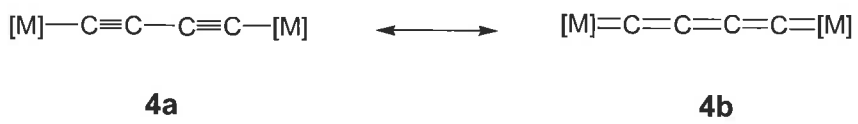

4a **4b**

Scheme 4.10

However, in the case of the $W(CO)_3Cp^*$ diynyl and diyndiyl complexes, it was suggested that these differences arise from an elongation of the conjugated path length as a consequence of interactions between an additional set of d_π orbitals towards the HOMOs in the case of the diyndiyl complex.[105]

Significant structural differences between diynyls **39** and **40** can also be seen. The Ru-C distance is shorter in the TMS-protected **39** than in **40** [1.983(2) (**39**), 2.015(4) Å (**40**)], with an associated extension of the C(1)-C(2) bond in **39** relative to **40** [1.231(2) (**39**), 1.186(5) Å (**40**)]. This difference is attributed to the C≡CC≡CTMS fragment being a better σ-donor than C≡CC≡CH, resulting in a shorter Ru-C distance for the TMS-protected diynyl as observed. The stronger Ru-C bond in this case could allow for better d_π to C_π antibonding orbital mixing through a better matching of energies of these orbitals resulting in the decreased strength and subsequent increased length of the C(1)-C(2) bond. This enhanced σ-donor ability of the C≡CC≡CTMS fragment compared with C≡CC≡CH also explains the lower oxidation potential of **39** over **40** (see Section 4.3.8).

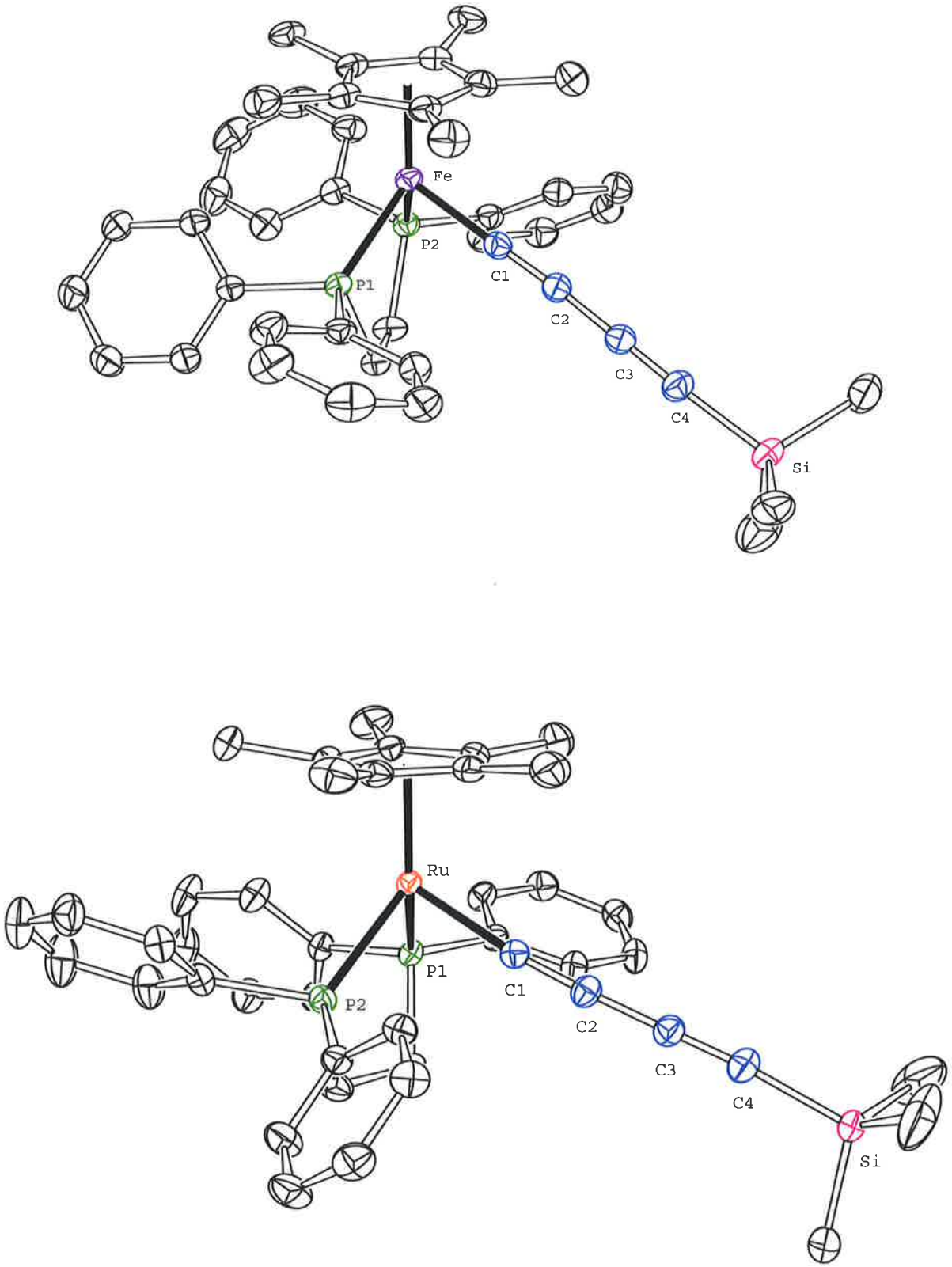

Figure 4.1: *ORTEP views of* ***38*** *(top),* ***39*** *(bottom)*

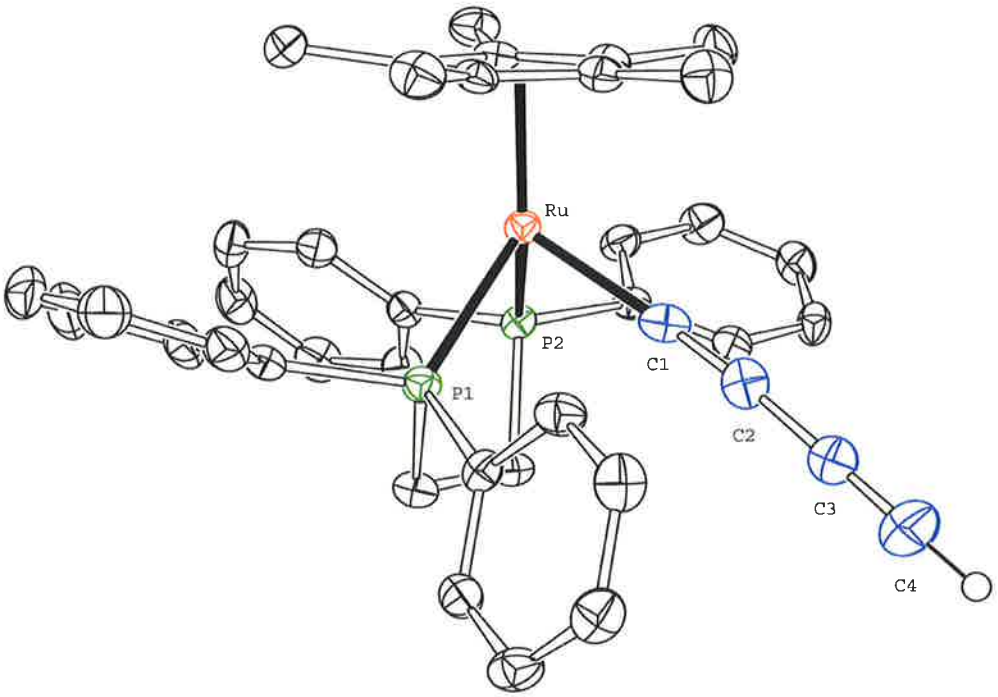

Figure 4.2: *ORTEP view of* ***40****.*

	38	**39**	**40**
Bond Distances (Å)			
M-P(1,2)	2.1801, 2.1875(9)	2.2610(3), 2.2775(4)	2.279, 2.256(1)
M-C(Cp*)	2.101-2.142(3)	2.233-2.275(2)	2.216-2.281(4)
(av.)	2.12(5)	2.25(8)	2.250(4)
M-C(1)	1.875(3)	1.983(2)	2.015(4)
C(1)-C(2)	1.226(4)	1.231(2)	1.186(5)
C(2)-C(3)	1.374(4)	1.371(2)	1.387(6)
C(3)-C(4)	1.221(4)	1.222(3)	1.193(6)
C(4)-Si	1.821(3)	1.822(2)	
Bond Angles (°)			
P(1)-M-P(2)	84.59(3)	81.84(1)	83.43(4)
P(1,2)-M-C(1)	84.67(9), 87.70(9)	85.30, 88.40(4)	84.2, 85.5(1)
M-C(1)-C(2)	176.0(3)	173.8(1)	173.1(4)
C(1)-C(2)-C(3)	175.6(3)	176.7(1)	172.7(5)
C(2)-C(3)-C(4)	179.7(3)	178.9(1)	177.4(5)
C(3)-C(4)-Si	175.2(3)	173.8(1)	

Table 4.1: *Selected structural parameters for* ***38-40****.*

4.3.2. Reaction of RuCl(dppe)Cp (19b) with LiC≡CC≡CTMS*

Initial work towards the syntheses of the diynyl complexes **39** and **40** revealed a number of novel reactions. In an attempt to synthesise the TMS-protected ruthenium diynyl, the starting chloro-ruthenium complex **19b** was treated with an excess of LiC≡CC≡CTMS at -78°C. However, no evidence for the formation of **39** was detected, with only **19b** and the hydride complex RuH(dppe)Cp* isolated. This result is in contrast to the reaction between $RuCl(CO)_2Cp$ and LiC≡CC≡CTMS, which gave $Ru(C{\equiv}CC{\equiv}CTMS)(CO)_2Cp$ in a reasonable yield (72%).[145] This suggests that the $[Ru(CO)_2Cp]^+$ fragment is more susceptible to nucleophilic attack than $[Ru(dppe)Cp^*]^+$. The decreased electrophilicity of the latter is presumably due to two reasons. Firstly, the increased electron density at the ruthenium centre from the enhanced electron-donating abilities of the bis-phosphine and Cp* ligands, as opposed to the electron-withdrawing carbonyl groups and Cp ligand, would decrease the electrophilicity. Secondly, the increased steric hindrance imposed by the bulky phosphine and Cp* ligands relative to the smaller carbonyl and Cp ligands, would also hinder nucleophilic attack.

4.3.3. Reaction of RuCl(dppe)Cp (19b) with TMSC≡CC≡CTMS*

An alternative strategy was therefore required, and it was anticipated that the reaction of **19b** with an excess of TMSC≡CC≡CTMS in the presence of KF and NH_4PF_6 in a MeOH solution would give the desired diynyl. In this reaction, NH_4PF_6 was added to assist the ionisation of the Ru-Cl bond, while KF was used both as a desilylating agent and a source of base to ensure the deprotonation of the expected butatrienylidene intermediate. As the reaction proceeded, the colour quickly changed from the initial orange to a deep blue and then gradually lightened to green. Work-up by preparative TLC revealed that the major product from the reaction was an orange complex identified as $Ru\{C{\equiv}CC(=NH_2)Me\}(dppe)Cp^*$ (**41**) (Scheme 4.11). A number of brightly coloured blue bands were also collected from the preparative TLC plates, but the amounts of these materials were insufficient to allow characterisation.

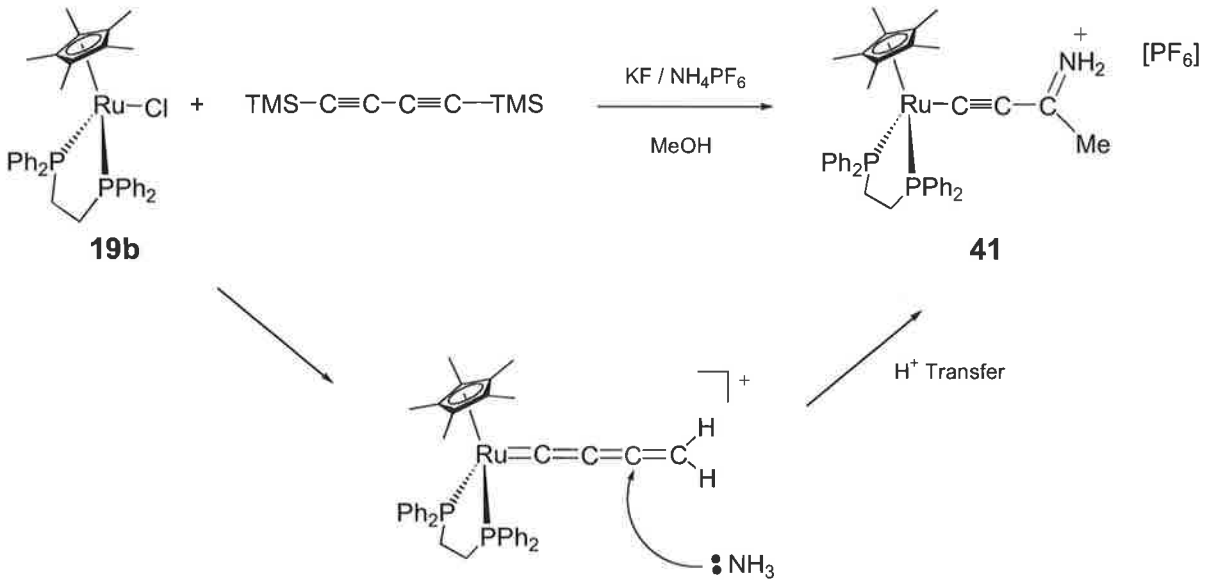

Scheme 4.11

It is considered that under the reaction conditions, desilylation of the protected diyne would generate HC≡CC≡CH *in situ*. Coordination to the $[Ru(dppe)Cp^*]^+$ fragment is expected to occur with either a 1,2-hydrogen shift to give the ethynylvinylidene $[Ru{=}C{=}CH(C{\equiv}CH)]^+$, or with a 1,4-hydrogen shift to generate a butatrienylidene $[Ru{=}C{=}C{=}C{=}CH_2]^+$ intermediate. The chemistry of both systems is well understood from both experimental and theoretical results, which show the carbon atoms have alternating electron-poor and electron-rich character as they extend out from the metal centre.[125,154]

$$[M]{=}C^{\delta+}{=}C^{\delta-}{=}C^{\delta+}{=}C^{\delta-}{=}CH_2$$

With this in mind, it is considered that **41** was generated by the nucleophilic addition of ammonia, formed by the deprotonation of NH_4^+, at the electron-deficient C_3 atom of the butatrienylidene $[Ru(=C=C=C=CH_2)(dppe)Cp^*]^+$ (**42**), followed by proton-shift to C_4 (Scheme 4.11). While both atoms C_1 and C_3 are electrophilic, attack at C_3 is most likely a consequence of the steric hindrance imposed by the bulky ligands around atom C_1.

NMR characterisation of **41** was straightforward with all expected resonances observed in the ^{31}P and ^{1}H NMR spectra for the Ru(dppe)Cp* fragment. In the ^{13}C NMR spectrum, C_1 was observed as a triplet at δ 216.37, while C_2 appeared as a singlet at δ 121.72. The C_3 atom directly attached to nitrogen was found as a singlet at δ 156.74 and assigned upon comparison with related complexes.[155] The IR spectrum of **41** revealed the presence of two bands at 1982 and 1651 cm^{-1} that were assigned to the ν(CC) and ν(C=N) stretching modes, respectively.

Complex **41** was further characterised by X-ray crystallography. Suitable crystals were grown from a CH_2Cl_2/hexane solution and the ORTEP plot of the cation is shown in Figure 4.3, while selected structural data are collected in Table 4.2. The most revealing aspects of the structure are the bond lengths along the RuC_4 chain. The Ru-C(1) bond [1.942(3) Å] is slightly closer to that expected for a ruthenium carbon single bond (2.01 Å) than a Ru=C double bond (1.85 Å), while the C(1)-C(2) bond length of 1.238(4) Å is closer to that of a C≡C triple bond (1.20 Å) than a C=C double bond (1.31 Å).

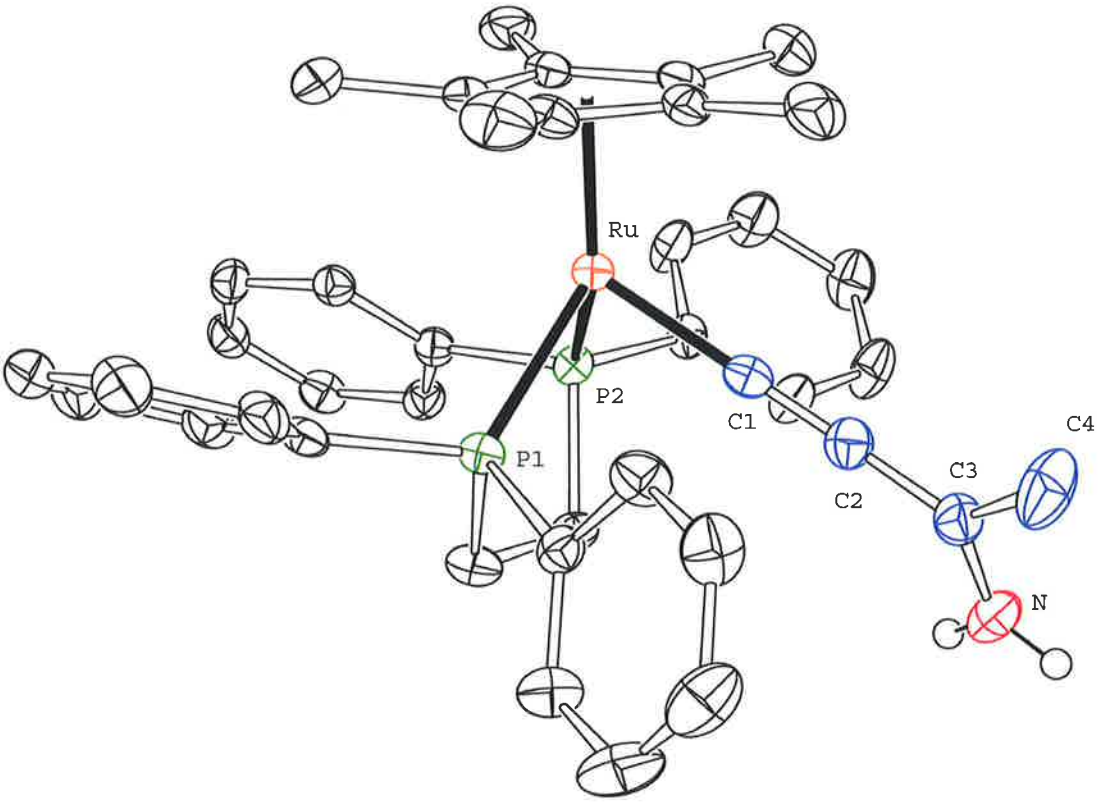

Figure 4.3: *ORTEP view of the cation **41**.*

	41 [a]	**43** [b]
Bond distances (Å)		
Ru-P(1)	2.2910(8)	2.8330(6)
Ru-P(2)	2.2705(8)	2.2684(6)
Ru-C(Cp*)	2.226-2.285(3)	2.217(2)-2.274(3)
(av.)	2.2642(3)	2.251(2)
Ru-C(1)	1.942(3)	1.979(3)
C(1)-C(2)	1.238(4)	1.223(4)
C(2)-C(3)	1.379(5)	1.442(4)
C(3)-R	1.340(4)	1.233(4)
C(3)-C(4)	1.505(6)	1.492(5)
Bond angles (°)		
P(1)-Ru-P(2)	82.70(3)	83.11(2)
P(1)-Ru-C(1)	85.14(9)	84.73(6)
P(2)-Ru-C(1)	85.01(9)	82.79(7)
Ru-C(1)-C(2)	178.4(3)	179.4(2)
C(1)-C(2)-C(3)	167.3(3)	170.1(2)
C(2)-C(3)-R	121.7(3)	121.6(3)
C(2)-C(3)-C(4)	121.1(3)	117.2(3)
R-C(3)- C(4)	117.2(3)	121.1(3)

Table 4.2: *Selected structural data for **41** and **43**.* [a] *R = N.* [b] *R = O.*

Two contributing resonance forms can describe the bonding in **41**, as illustrated in Scheme 4.12. The relative contributions of the alkynyl **4c** and allenylidene **4d** forms in related complexes have been shown to depend on the nature of the heteroatom and its ability to stabilise the positive charge.[156] Generally, when the heteroatom is nitrogen, there are strong contributions from resonance structure **4c**. However, in the case of complex **41**, while structure **4c** will be stabilised by presence of the nitrogen atom, allenylidene form **4d** will also be stabilised by the electron-rich Ru(dppe)Cp* fragment, due to increased back-bonding into the allenylidene ligand.[155]

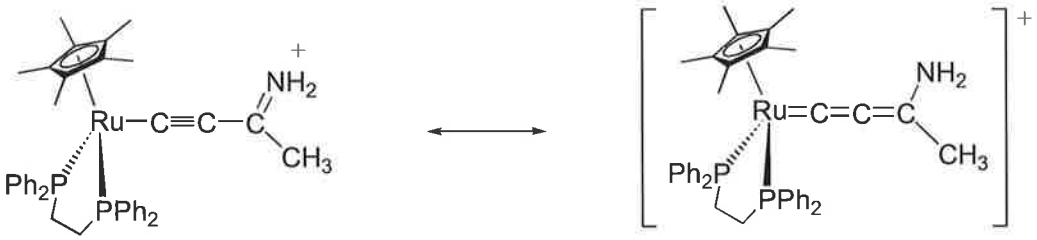

4c **4d**

Scheme 4.12

Considering the spectroscopic data, it appears that the structure of **41** lies somewhere between the two forms. The observation of a ν(C=N) band in the IR spectrum together with the X-ray data that reveals bond lengths close to the values expected for Ru-C single and C≡C triple bonds is evidence for the alkynyl form **4c**. However, the presence of the allenylidene form **4d** can be seen in the ^{13}C NMR spectrum, with resonances for the C_1 and C_2 atoms shifted significantly downfield with respect to those found in ethynyl **23b** [δ 120.58 (C_1), 92.99 (C_2)].

4.3.4. Reaction of RuCl(dppe)Cp (19b) with HC≡CC≡CTMS in MeOH*

A third reaction that failed to give either **39** or **40** involved the treatment of **19b** with an excess of HC≡CC≡CTMS in the presence of NH_4PF_6 in MeOH. As the reaction proceeded, the initial orange suspension quickly changed to a green solution and after three hours at room temperature the solvent was evaporated to give a deep red residue. This was extracted into CH_2Cl_2 and purified on a basic alumina column giving Ru{C≡CC(O)Me}(dppe)Cp* (**43**) as a bright yellow band together with an intense blue band that contained two complexes identified as **44** and **45**.

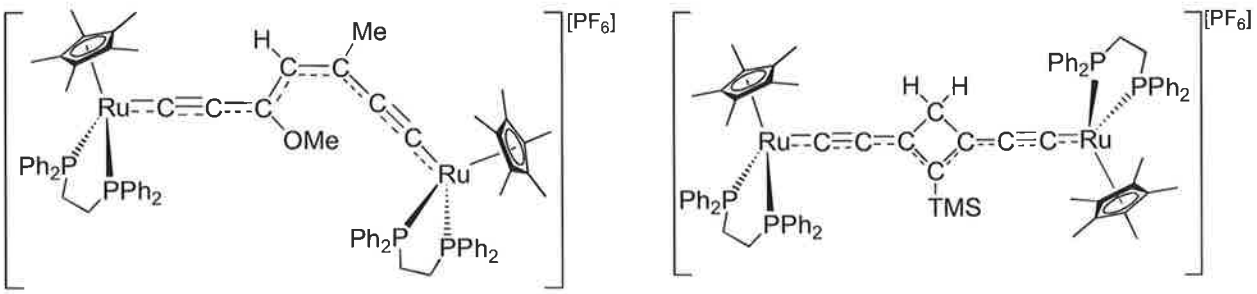

44 **45**

While this reaction was performed in the absence of KF, desilylation of the organic diyne still occurred, presumably from F^- formed by the hydrolysis of the PF_6^- anion.[157] It is proposed that under these reaction conditions, **43** was generated from the intermediate butatrienylidene **42**, which underwent attack at atom C_3 by trace amounts of water to give the hydroxyvinylidene **46**. Subsequent deprotonation generated the neutral complex **43**, isolated in 50% yield (Scheme 4.13).

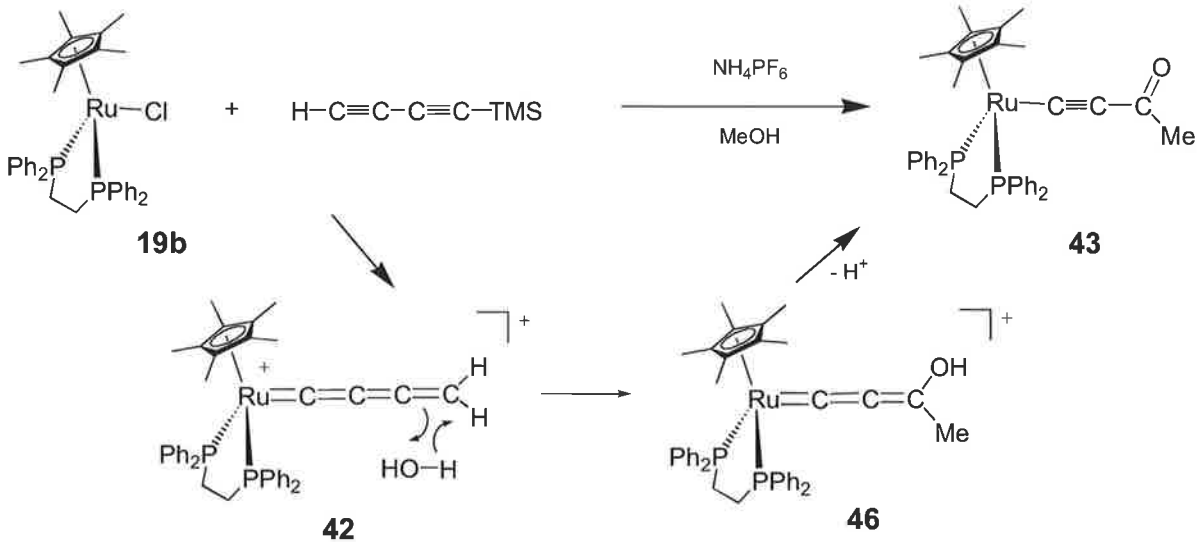

Scheme 4.13

As in the case of **41**, the structure of **43** is best described by two contributing resonance forms **4e** and **4f** (Scheme 4.14). Characterisation of **43** was straightforward with two ν(CC) bands in the IR spectrum at 2024 and 2006 cm^{-1}. These values are lower than those found in the related complex $Ru\{C{\equiv}CC(O)Me\}(PPh_3)_2Cp$ (2048, 2011 cm^{-1})[126] and is consistent with the enhanced electron donating abilities of the Cp* and dppe ligands of **43**, stabilising the resonance form **4f** through increased back-bonding into the allenylidene ligand.

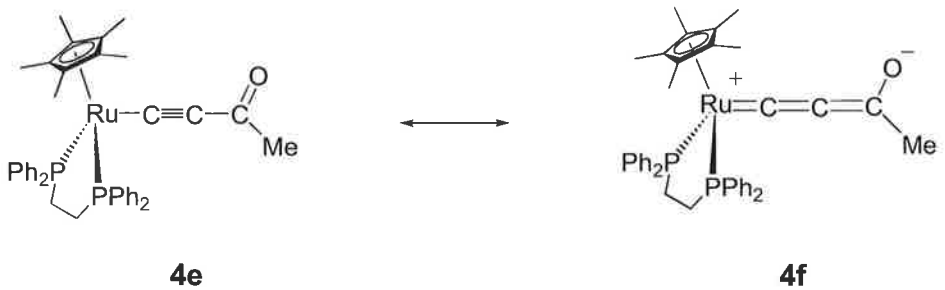

4e **4f**

Scheme 4.14

The NMR spectra of **43** displayed all the expected resonances for the Ru(dppe)Cp* fragment and deserve no further comment here. In the ^{13}C NMR spectrum, atom C_1 was observed as a triplet at δ 159.24, while C_2 appeared as a singlet at δ 118.88. The upfield position of these resonances relative to the corresponding resonances found in **41**, suggests that while there may be some contribution from the resonance form **4f**, resonance structure **4e** appears to be the major contributor to the overall structure of **43**.

Single crystals of **43** suitable for an X-ray study were grown from CH_2Cl_2/hexane and the ORTEP plot of a single molecule is shown in Figure 4.4, while selected bonding parameters are given in Table 4.2. The structural data confirm that the alkynyl form is the major contributor, with values for Ru-C(1) [1.979(3) Å] and C(1)-C(2) [1.223(4) Å] close to those expected for Ru-C single and C≡C triple bonds. The RuC_3 unit adopts an almost linear arrangement with angles at C(1) and C(2) of 179.4(2) and 170.1(2)°, respectively.

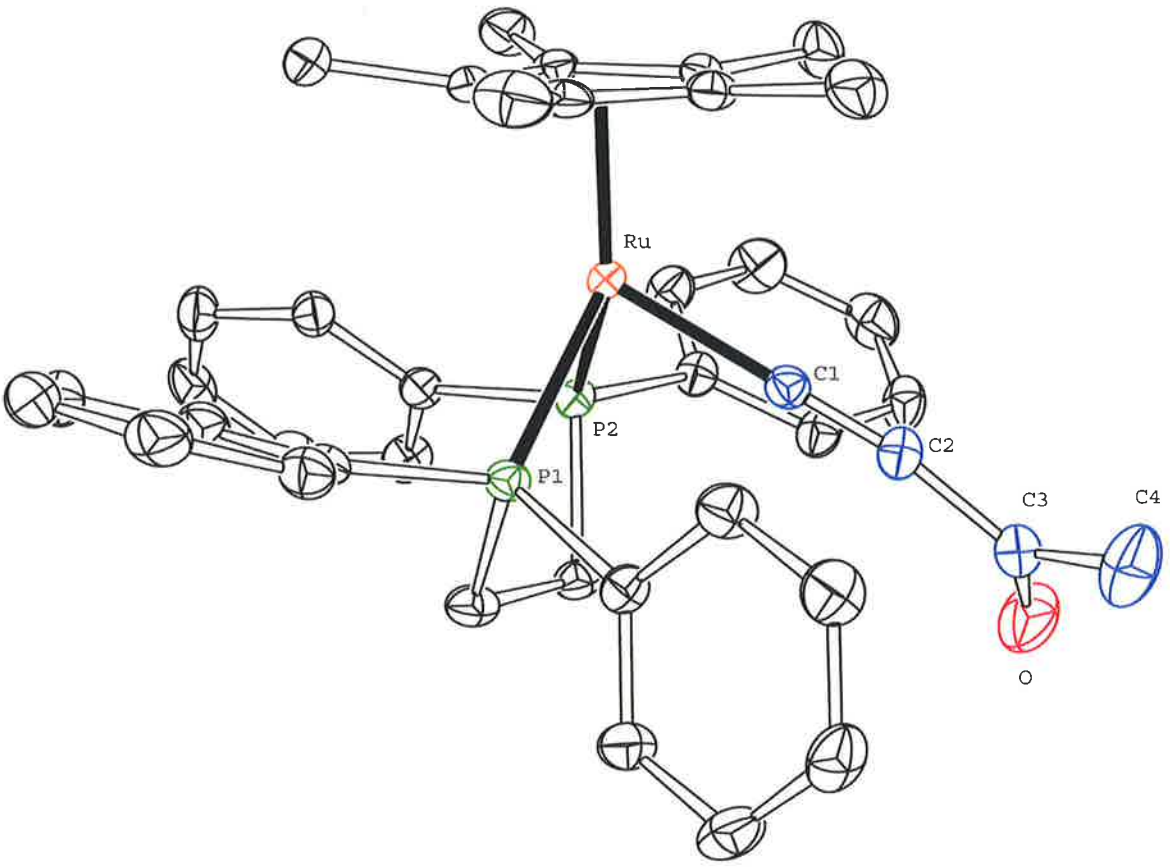

Figure 4.4: *ORTEP plot of 43.*

The majority of the intense blue band removed from the column with diethyl ether was found to be complex **44**, with only trace quantities of **45** detected. An analytically pure sample of **44** was isolated after a second purification on a basic alumina column followed by crystallisation from an acetone/hexane mixture. During crystallisation, it was found important to minimise exposure to atmospheric oxygen to prevent the formation of the corresponding carbonyl cation **32**. The structure of **44** was determined from an X-ray study on crystals obtained by the slow diffusion of hexane into a concentrated acetone solution. The ORTEP plot of the cation is shown in Figure 4.5 and selected structural parameters are given in Table 4.3. The structure confirms both the highly delocalised nature of the C_7 bridging ligand and the presence of the pendant groups OMe, Me and H. The two ruthenium centres adopt a pseudo-octahedral geometry with the Ru-P bond lengths [2.272 and 2.281(1) Å], intermediate between the expected values for a Ru-P single bond in a ruthenium vinylidene and ruthenium ethynyl complex [*ca* 2.32 Å (**22b**), 2.26 Å (**23b**)]. The angle at C_1 is close to linear [176.1(4)°], while the Ru-C(1) bond is shorter and the C(1)-C(2) bond longer than those expected for Ru-C(*sp*) single and C≡C triple bonds, respectively.

Bond distances (Å)		**Bond angles (°)**	
Ru-P(1)	2.272(1)	P(1)-Ru-P(2)	82.95(4)
Ru-P(2)	2.281(1)	P(1)-Ru-C(1)	87.68(4)
Ru-C(Cp*)	2.238-2.271(5)	P(2)-Ru-C(1)	79.5(1)
(av.)	2.257(4)	Ru-C(1)-C(2)	176.1(4)
Ru-C(1)	1.944(4)	C(1)-C(2)-C(3)	144.9(7)
C(1)-C(2)	1.214(6)	C(2)-C(3)-C(4)	127.9(7)
C(2)-C(3)	1.50(1)	C(2)-C(3)-O(3)	112.5(7)
C(3)-C(4)	1.40(1)	C(3)-O(3)-C(31)	116.9(7)
C(3)-O(3)	1.43(1)	C(3)-C(4)-C(5)	129.4(7)
O(3)-C(31)	1.38(1)	C(4)-C(5)-C(51)	121.3(7)
C(4)-C(5)	1.40(1)	C(4)-C(3)-O(3)	111.9(7)
C(5)-C(51)	1.49(1)		

Table 4.3: *Selected structural data for **44**.*

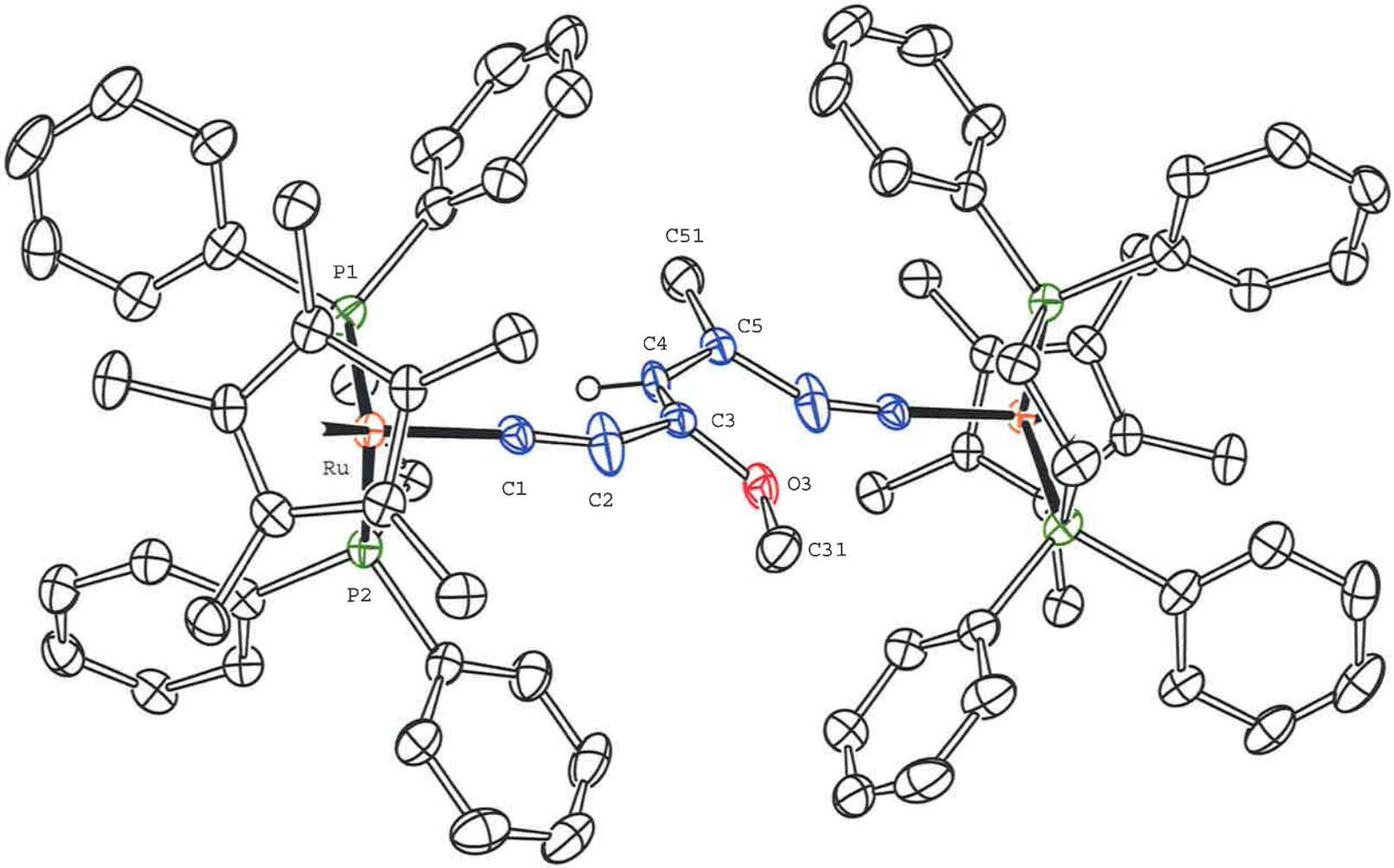

Figure 4.5: *ORTEP view of the cation* ***44****.*

In the ^{1}H NMR spectrum, for each of the H, OMe and Me groups attached to the bridging ligand, two distinct resonances were observed with the relative ratios equal to 56:44 in each case. Furthermore, four Cp* resonances were observed in the ^{1}H and ^{13}C NMR spectra, while in the ^{31}P NMR spectrum, four resonances were also observed, corresponding to two sets of two equal intensity peaks that also reflected the 56:44 ratio. While no changes in the relative ratios were detected by recording the spectrum at low temperature (-80°C), coalescence of the two resonances for the proton attached to C_4 was observed by heating the sample above 55°C.

This observation can be attributed to the presence of two structural isomers of **44** that result from isomerisation around the C(4)-C(5) bond. As the bridging ligand in **44** is highly delocalised, there will be restricted rotation around C(4)-C(5) resulting in two structural isomers having either *E* or *Z* configurations (Figure 4.6). Evidence for this process was found in the 2D ROESY NMR spectrum that confirmed the minor isomer had the *Z* configuration with a ROESY interaction observed between the proton directly attached to atom C_4 and the methyl protons attached to C_{51}. No such interaction was observed with the major isomer, suggesting that it has an *E* configuration around C(4)-C(5). It must be noted that only the *Z* isomer was observed in the crystal structure of **44**.

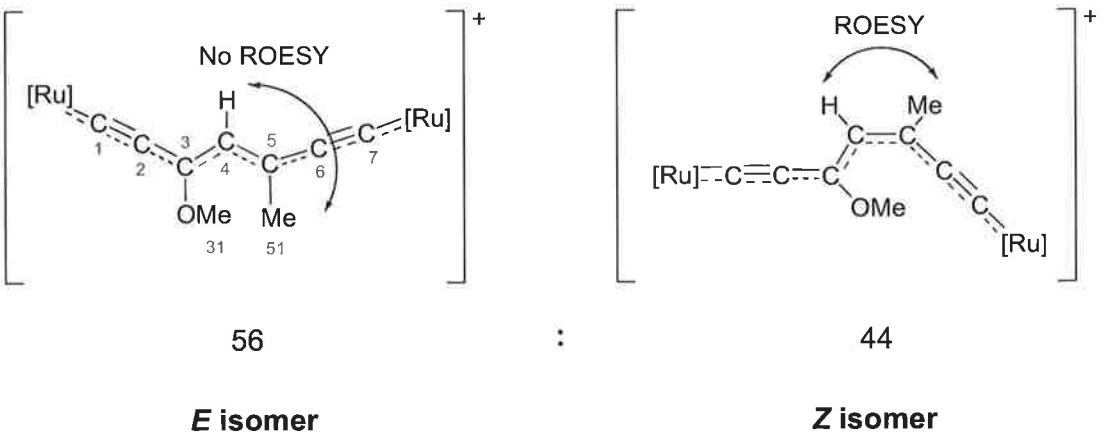

Figure 4.6: *Isomerisation around C(4)-C(5) in 44.*

In the ^{1}H NMR spectrum, the proton attached to C_4 was observed as a singlet at δ 5.44 for the *E* and at δ 5.14 for the *Z* isomer. The methoxy group was observed as singlets at δ 3.24 and 2.87, while resonances for the hydrogen atoms of the methyl group were observed at δ 1.69 and 1.47, for the *E* and *Z* isomers, respectively.

2D HSQC and HMBC NMR experiments supported the X-ray structure, confirming the presence of the H, OMe and Me pendant groups to the C_7 bridging ligand. In the ^{13}C NMR spectrum of **44**, besides the expected resonances for the two Ru(dppe)Cp* fragments, 18 signals were observed, nine for each of the two isomers. Four triplets found between δ 203.40-209.76 were due to the carbon atoms directly attached to ruthenium, however individual assignments of these resonances to either C_1 or C_7 were not possible. The chemical shifts of these resonances lie between the characteristic vinylidene Ru=C (*ca* δ 340.0) and alkynyl (Ru-C≡C *ca* 120.0) carbon resonances, supporting the delocalised structure. HSQC 2D NMR confirmed that resonances at δ 122.42, 58.03 and 26.17 found in the ^{13}C NMR spectrum of the *E* isomer were due to C_4, C_{31} and C_{51}, respectively, with cross peaks being observed between the ^1H and ^{13}C resonances. Other resonances were assigned upon the basis of long-range HMBC 2D NMR experiments and are summarised in Figure 4.6.

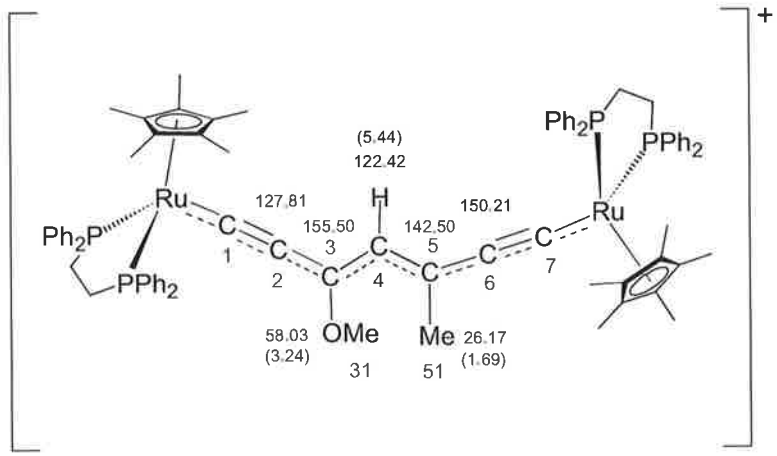

Figure 4.6: *^{13}C (and ^1H) NMR assignments (ppm) for the major E isomer of **44**.*

Scheme 4.15 outlines a plausible mechanism for the formation of **44**. This proposed sequence involves the initial formation of the highly reactive butatrienylidene **42**, which undergoes nucleophilic attack at C_3 to give **47**, for which two tautomers **4g** and **4h** can be written. Attack of the electron-rich CH_2 group in structure **4h** to the electrophilic atom C_3 of a second molecule of **42** to give the binuclear intermediate **48** is followed by allylic hydrogen transfer to give **44**, which exists in equilibrium between the *E* and *Z* configurations.

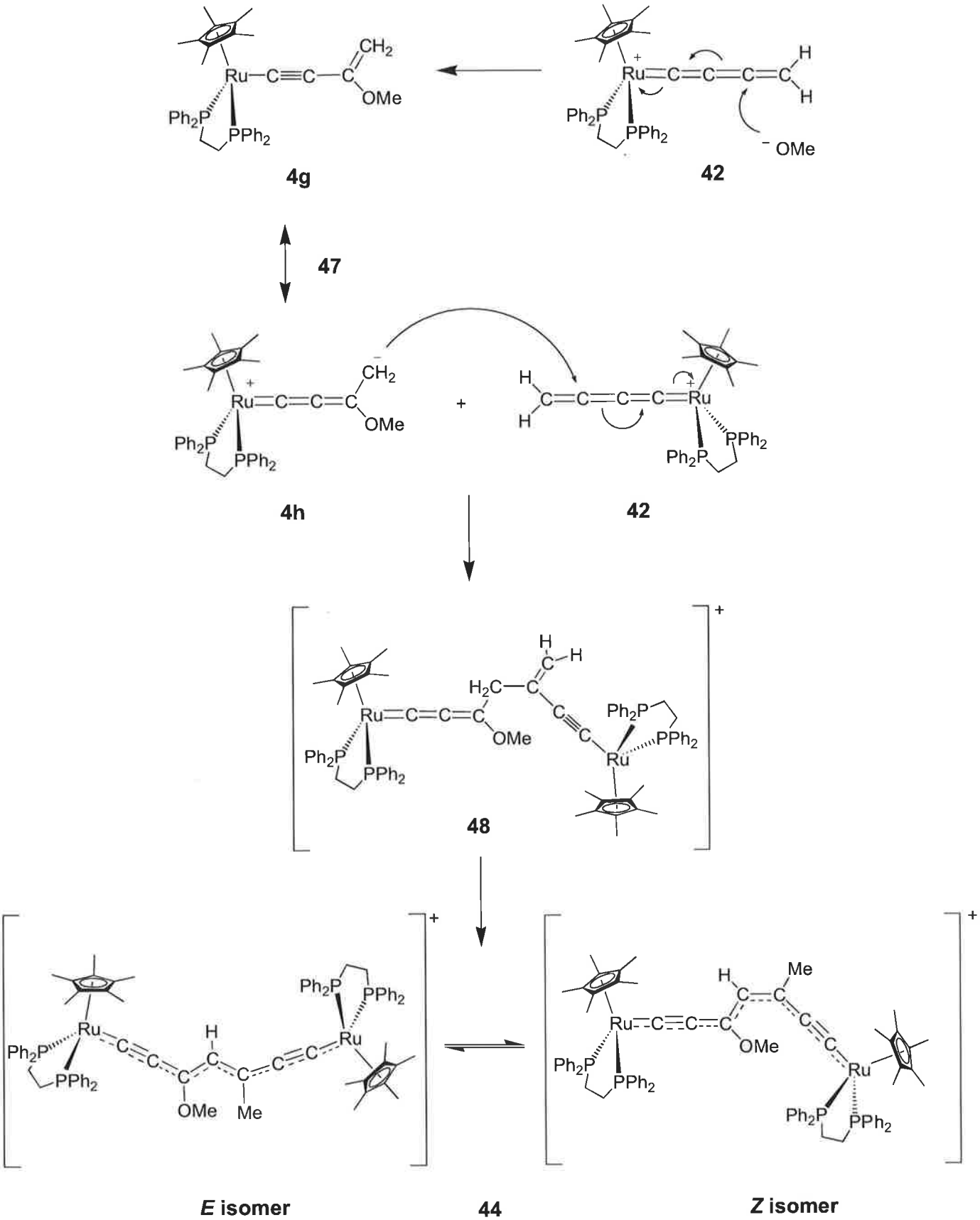

Scheme 4.15

The third product from the reaction of **19b** with HC≡CC≡CTMS in MeOH was the cyclobutenylidene complex **45**. Only formed in trace quantities, it was first characterised whilst attempting to crystallise a crude sample of **44** from CH_2Cl_2/hexane. The ORTEP plot of the cation is shown in Figure 4.7, looking through the cyclobutenylidene ring (top), and down the Ru-Cp* axis (bottom), while selected structural parameters are given in Table 4.4. At this stage, isolation of significant quantities of a pure sample for spectroscopic characterisation have yet to be achieved, due to the low yield. Further characterisation of **45** was obtained from an ES-mass spectrum of a crude sample of **44**, which contained ions corresponding to $[M]^+$ at *m/z* 1401 (**44**) and at *m/z* 1440 (**45**). MS-MS of the ion centred at *m/z* 1440 did not result in fragmentation to give *m/z* 1401.

Bond distances (Å)		**Bond angles (°)**	
Ru-P(1)	2.292(2)	P(1)-Ru-P(2)	83.67(6)
Ru-P(2)	2.284(2)	P(1)-Ru-C(1)	88.8(2)
Ru-C(Cp*)	2.234-2.290(6)	P(2)-Ru-C(1)	81.9(2)
(av.)	2.259(6)	Ru-C(1)-C(2)	176.3(5)
Ru-C(1)	1.929(3)	C(1)-C(2)-C(3)	172.6(7)
C(1)-C(2)	1.229(9)	C(2)-C(3)-C(4)	138.3(6)
C(2)-C(3)	1.352(9)	C(2)-C(3)-C(5)	131.6(6)
C(3)-C(4)	1.44(1)	C(4)-C(3)-C(5)	90.0(5)
C(3)-C(5)	1.50(1)	C(3)-C(4)-C(3')	92.4(7)
C(4)-Si	1.89(1)	C(3)-C(5)-C(3')	87.5(7)

Table 4.4: *Selected structural parameters for 45.*

X-ray analysis confirmed the structure of **45**, with the two Cp* ligands arranged in a *cisoid* geometry. As Figure 4.7 shows, the bridging ligand is linear and the four-membered ring is slightly distorted with the C(3)-C(4) and C(3)-C(5) bonds being marginally different. The centrosymmetric structure confirms that **45** contains a fully delocalised cyclobutenylidene system.

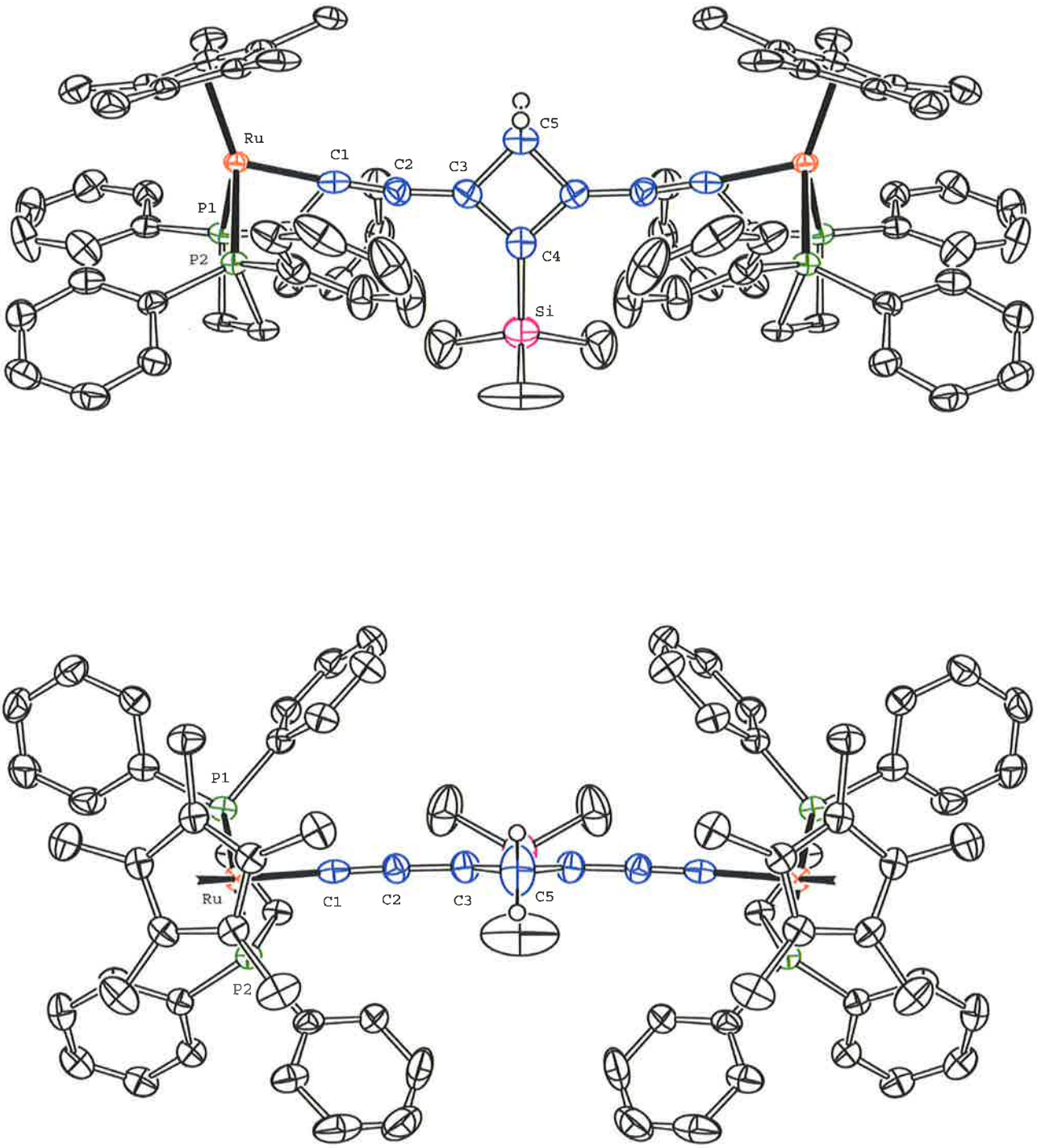

Figure 4.7: *ORTEP views of the cation* ***45****.*

It is considered that **45** was formed by the [2 + 2] cycloaddition of the C(3)-C(4) double bond of the butatrienylidene **42** to the C(3)-C(4) triple bond of the TMS-protected diynyl **39** formed in the reaction mixture (Scheme 4.16). Cycloaddition reactions of this type between vinylidenes and acetylides are well known, generating four-membered cyclic systems.[158-162] However, at the time this work was carried out, no [2 + 2] cycloaddition reactions at the C(3)-C(4) double bond of a butatrienylidene had been reported.

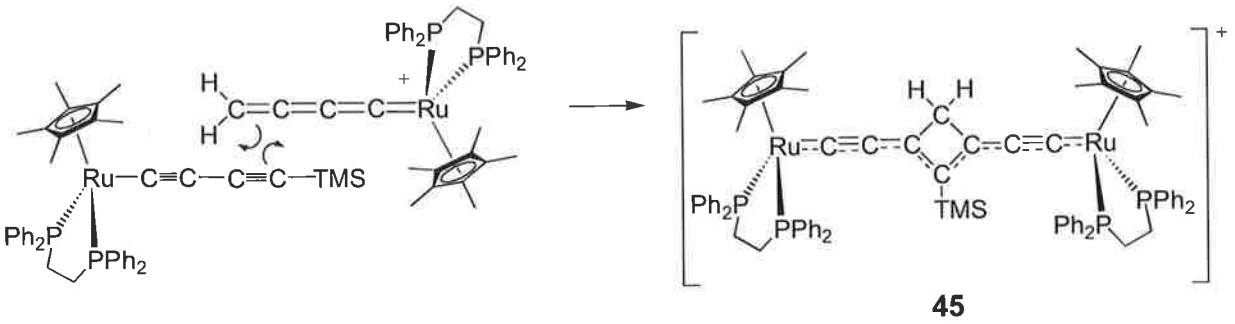

45

Scheme 4.16

More recently, a related binuclear ruthenium complex featuring a C_7 bridging ligand similar to that found in **45** has been reported.[163] Featuring two $RuCl(dppe)_2$ centres, it was prepared by the addition of half an equivalent of the oxidising agent $[FeCp_2][PF_6]$ to a solution of $RuCl(C{\equiv}CC{\equiv}CH)(dppe)_2$ (**49**). It was suggested that this reaction proceeded *via* the formation of a butatrienylidene intermediate, which then underwent a [2 + 2] cycloaddition reaction at the C(3)-C(4) triple bond of the diynyl **49**. Interestingly under similar conditions, neither **39** nor **40** could be coupled to give **45** or any related complexes.

4.3.5. Synthesis of {Cp(dppe)Ru}(C≡CC≡C){Ru(PPh$_3$)$_2$Cp} (50)*

As described in Chapter 2, the symmetric diyndiyls featuring the redox-active end-groups Ru(dppe)Cp* (**25b**) and $Ru(PPh_3)_2Cp$ (**13**) each show the sequential loss of four electrons to give a total of five oxidation states. As expected, the first two oxidation processes of **25b,** which features the more electron-donating Cp* and dppe ligands, appear at significantly lower potentials than those in **13**. As oxidation

proceeds however, the E_3 process in both complexes occurs at virtually identical potentials, while E_4 in **25b** occurs at a lower potential than that found in **13**. The synthesis of the new asymmetric ruthenium complex containing both Ru(dppe)Cp* and $Ru(PPh_3)_2Cp$ fragments is of obvious interest, from both a synthetic and electrochemical point of view.

The reaction between **40** and a single equivalent of $RuCl(PPh_3)_2Cp$ in the presence of $Na[BPh_4]$ and dbu, in a solvent mixture of CH_2Cl_2 and NEt_3 gave the asymmetric diyndiyl $\{Cp^*(dppe)Ru\}(C{\equiv}CC{\equiv}C)\{Ru(PPh_3)_2Cp\}$ (**50**) as an orange crystalline solid in 35% yield (Scheme 4.17). The product was readily crystallised from acetone, but suitable crystals for an X-ray crystallographic study could not be obtained. As in the case of **25b**, complex **50** could not be purified by chromatography, with all attempts generating a bright green complex that was most likely the monocation $[\mathbf{50}]^+$, in accordance with the behaviour of **25b** and **13**.

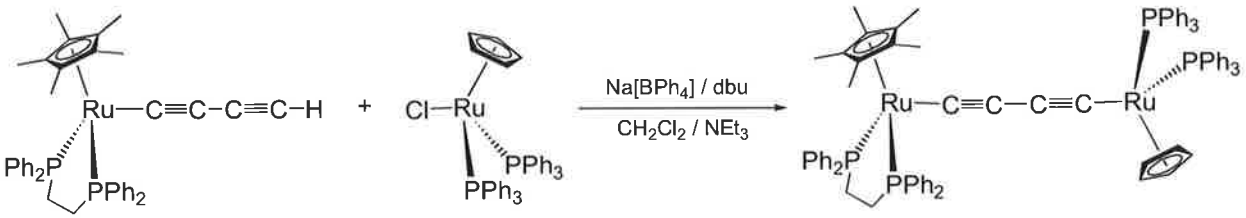

40 **50**

Scheme 4.17

A single ν(C≡C) band was observed in the IR spectrum of **50** at 1960 cm^{-1}, close to values found for both **25b** (1973 cm^{-1}) and **13** (1974 cm^{-1}). The ^1H NMR spectrum contained two different Cp signals at δ 1.72 (Cp*) and at 4.31 (Cp), while in the ^{31}P NMR spectrum, two equal intensity resonances were observed at δ 81.99 and 51.47, corresponding to the dppe and PPh_3 ligands, respectively. The complex was poorly soluble in all solvents, so the only resonances observable in the ^{13}C NMR spectrum were those of the Cp, Cp* and aromatic carbons; the acetylenic carbon resonances could not be detected, despite several attempts. The ES-mass spectrum contained a strong $[M]^+$ ion at *m/z* 1342, together with the fragment ion $[M - PPh_3]^+$ at *m/z* 1112. The cyclic voltammogram of **50** is reported below (Section 4.3.8).

4.3.6. Synthesis of Ru{C≡CC≡C[Au(PR$_3$)]}(dppe)Cp [R = Ph (51), tol (52)]*

Asymmetric diyndiyl complexes that possess a redox-active terminal at one end and a non-redox-active centre at the other may show some interesting electronic properties. Gold(I) phosphine centres coordinated to an alkynyl ligand generally cannot be oxidised or reduced themselves,[145] but may influence the electronic properties of the redox-active centre. Therefore, the syntheses of complexes that feature the electron-rich fragment Ru(dppe)Cp* together with a redox inactive Au(PR$_3$) end-group bridged by a butadiynyl ligand are of interest.

The reaction of **40** with the chloro-gold precursors AuCl(PR$_3$) gave new asymmetric diyndiyls Ru{C≡CC≡C[Au(PR$_3$)]}(dppe)Cp* [R = Ph (**51**), tol (**52**)]. A THF solution containing equimolar quantities of **40** and the gold chloride precursor was treated with a 1.0 M solution of KN(TMS)$_2$ in toluene. The solution was stirred at room temperature for four hours to give the mixed ruthenium-gold diyndiyls as bright yellow solids in reasonable yields [70% (**51**), 76% (**52**)] (Scheme 4.18). If Bu^{n}Li was used as the base in the reaction, yields were substantially reduced (*ca* 40%). This can be attributed to the deprotonated anion of **40** being a strong base itself, requiring an even stronger base to ensure the efficient formation of the diyne anion, which is then expected to attack the gold-chloride precursor to form **51** or **52**.

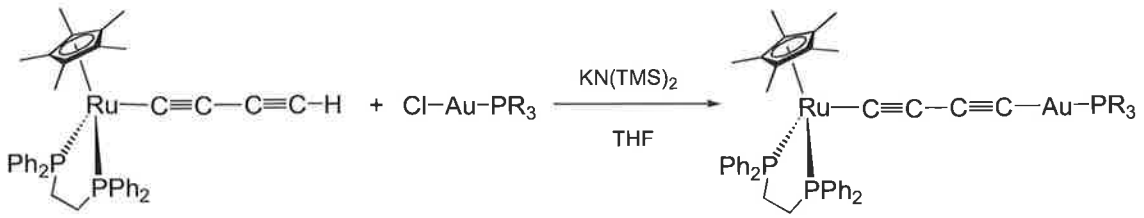

51 : R = Ph
52 : R = tol

Scheme 4.18

As with TMS-protected diynyl **39**, three ν(C≡C) bands were observed in the IR spectra for both **51** and **52**. The NMR interpretation was straightforward with the ^{31}P NMR spectra of both complexes revealing two resonances in a 2:1 ratio, one at

ca δ 80 corresponding to dppe and the second at *ca* δ 42 due to the phosphine attached to the gold centre.

The ^{13}C NMR spectra revealed all expected resonances for the Ru(dppe)Cp* and $Au(PR_3)$ fragments (see Section 4.5). Of interest were the resonances for the carbon chain, which in both complexes were virtually identical at δ *ca* 118, 92, 94 and 111, and assigned to $C_{1\text{-}4}$, respectively. Atom C_1 directly attached to ruthenium appeared as a characteristic triplet due to coupling with the two equivalent phosphorus nuclei of dppe, while in **52** the carbon directly attached to gold appeared as a broad doublet. In **51**, this resonance was fully resolved with $^2J(CP) = 75$ Hz.

In the ES-mass spectra of these complexes, molecular ions were observed at *m/z* 1142 and 1184, for **51** and **52**, respectively. However in both cases, ions at higher mass numbers were also observed, suggesting that aggregation was occurring. In **51**, ions at *m/z* 1601 and 1863 correspond to the correct mass and isotope pattern for the aggregates $[M + AuPPh_3]^+$ and $[M + Au(PPh_3)_2]^+$, respectively. Similar ions were also observed in the ES-mass spectrum of **52** and these are summarised in Section 4.5. Such aggregation processes have been observed with many organometallic compounds.[164]

Crystals of **51** grown from CH_2Cl_2/hexane and **52** from CH_2Cl_2 suitable for X-ray diffraction studies were obtained and their ORTEP plots are shown in Figure 4.8, while selected structural parameters are given in Table 4.5. As expected, the structures of the two complexes are closely related with similar bond angles and distances found throughout. Angles along the Ru-C_4-Au chain are close to linear between 172.1(1) and 179.6(2)°. Comparisons with related diynyls **39** and **40** show that the structure of the gold derivatives most closely resembles the TMS-protected diynyl **39**. Thus, substitution of H by a $Au(PR_3)$ group has enhanced the σ-donor ability of the diynyl ligand and as a consequence shorter Ru-C(1) and longer C(1)-C(2) distances are observed relative to **40**. This enhanced σ-donor ability is also reflected in a decrease in the formal oxidation potential of **51** and **52** relative to **40** (Section 4.3.8).

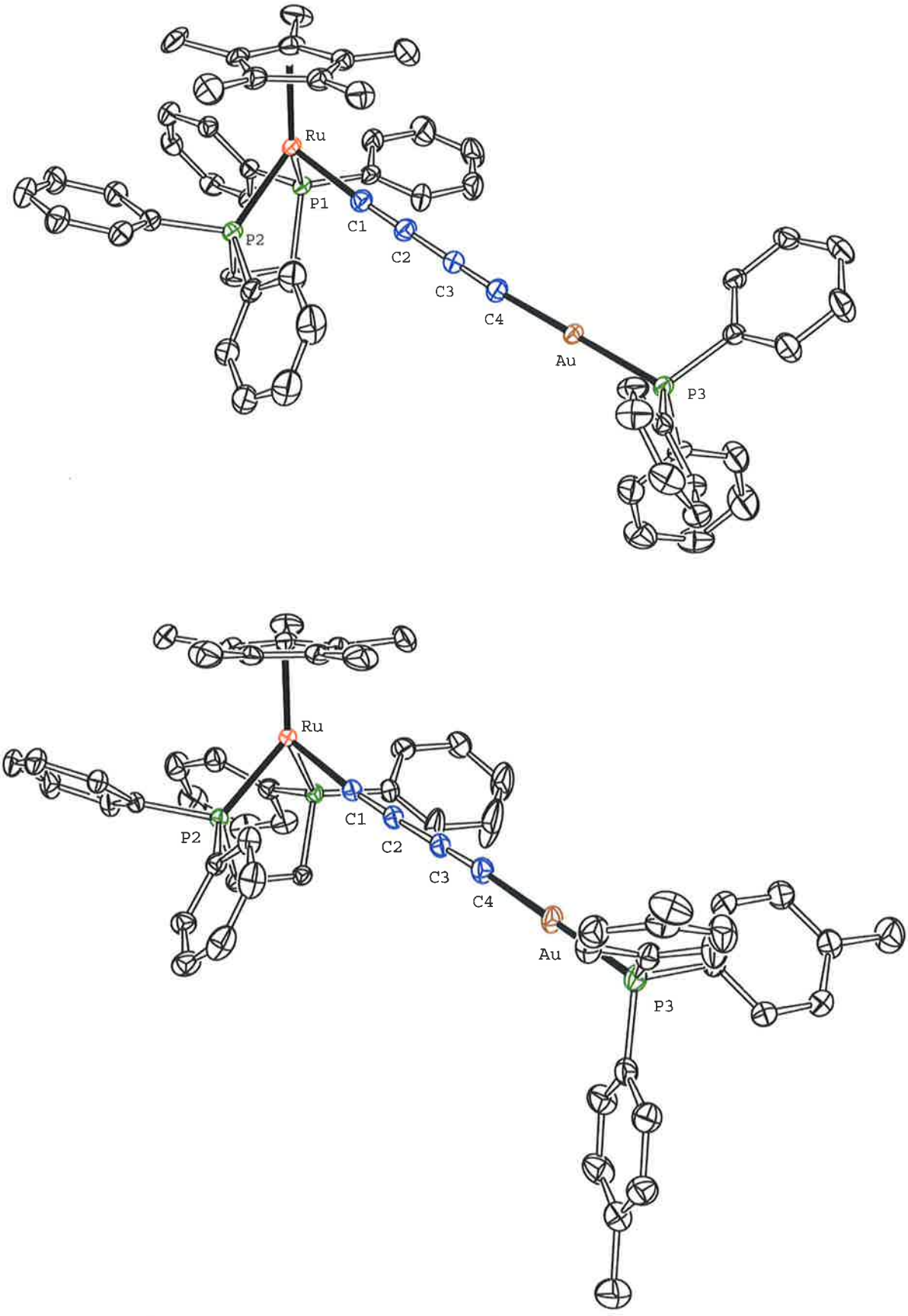

Figure 4.8: *ORTEP views of* ***51*** *(top) and* ***52*** *(bottom).*

	51	**52**
Bond Distances (Å)		
Ru-P(1)	2.2616(9)	2.2571(4)
Ru-P(2)	2.2777(9)	2.2778(4)
Ru-C(Cp*)	2.220-2.284(3)	2.230-2.273(2)
(av.)	2.25(2)	2.25(5)
Ru-C(1)	1.992(3)	1.995(2)
C(1)-C(2)	1.221(5)	1.225(2)
C(2)-C(3)	1.378(5)	1.380(2)
C(3)-C(4)	1.205(5)	1.211(2)
C(4)-Au	1.992(3)	1.988(2)
Au-P(3)	2.2666(8)	2.2677(5)
Bond Angles (°)		
P(1)-Ru-P(2)	83.62(3)	82.77(1)
P(1)-Ru-C(1)	85.6(1)	84.01(5)
P(2)-Ru-C(1)	86.6(1)	87.50(4)
Ru-C(1)-C(2)	172.2(3)	172.1(1)
C(1)-C(2)-C(3)	174.0(4)	175.7(2)
C(2)-C(3)-C(4)	179.0(3)	179.6(2)
C(3)-C(4)-Au	176.5(3)	175.9(2)

Table 4.5: *Selected structural parameters for* ***51*** *and* ***52****.*

4.3.7. Reactions of Ru(C≡CC≡CH)(dppe)Cp (40) with [Cu₂(μ-dppm)₂(NCMe)₂][PF₆]₂*

Trinuclear copper(I) alkynyls of the type $[Cu_3(\mu\text{-dppm})_3(\mu_3\text{-}\eta^1\text{-}C{\equiv}CAr)_2]^+$ show luminescence properties both in the solid state and in solution and have been suggested as ideal building blocks in the design of luminescent rigid-rod oligomers.[165,166] A large number of trinuclear copper(I) alkynyl complexes have been prepared and while the majority of these have been synthesised with purely organic acetylide fragments capping the trinuclear cluster,[166-170] two examples feature the organometallic fragments, $Re(CO)_3(bpy)$[165] or the redox-active ferrocenyl group (Figure 4.9).[171]

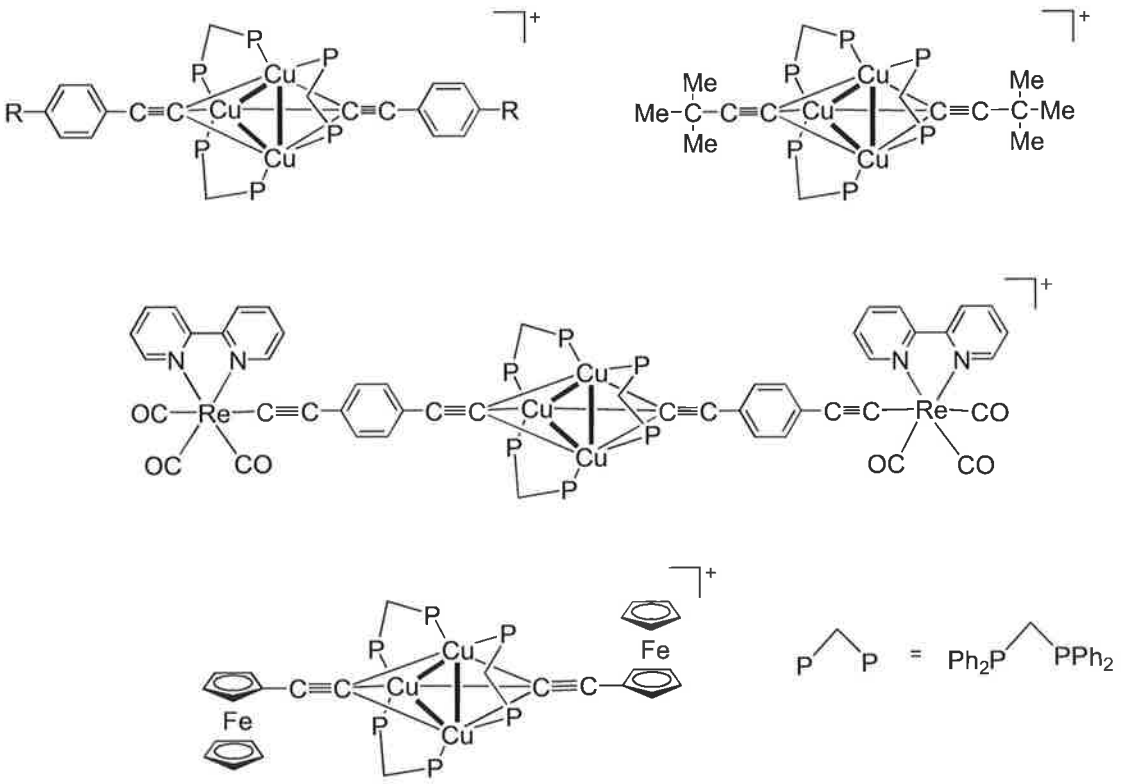

Figure 4.9: *Some examples of trinuclear copper(I) alkynyl complexes.*

The precursor for the trinuclear cluster is the binuclear copper(I) complex $[Cu_2(\mu\text{-dppm})_2(NCMe)_2]^{2+}$. Depending on the stoichiometric ratio used, this complex reacts with alkynes under a variety of conditions to give either mono- or bis-alkynyl

tricopper cluster complexes and in some cases can also react with the alkynes to form bi- or tetranuclear copper clusters.[172]

Accordingly, a solution of **40** and 1.5 equivalents of $[Cu_2(\mu\text{-dppm})_2(NCMe)_2][PF_6]_2$ was heated to reflux point in a THF/NEt_3 mixture for one hour (Scheme 4.19). Upon cooling, a bright orange crystalline solid was collected and identified as the mono-ruthenium complex $[\{Cp^*(dppe)Ru\}(C{\equiv}CC{\equiv}C)\{Cu_3(\mu\text{-dppm})_3\}][PF_6]_2$ (**53**). ^{31}P NMR spectroscopy proved very useful in this case, revealing that a single ruthenium diynyl fragment was capping the trinuclear copper cluster with the dppe (δ 78.85) and dppm (δ -7.83) resonances present in a 1:3 ratio.

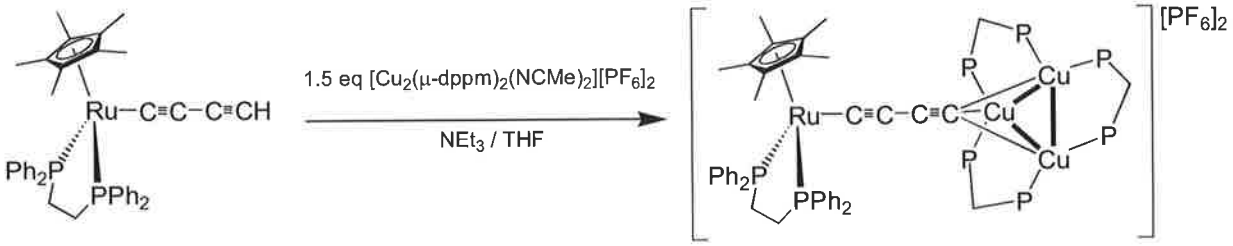

40 **53**

Scheme 4.19

Attempts to add a second ruthenium diynyl fragment under similar conditions failed with only the mono-ruthenium complex formed, even when a large excess of **40** was used. It proved necessary to use a stronger base (dbu) in order to obtain the bis-ruthenium complex **54**, however a small quantity of **53** was always formed and this could easily be separated from **54** by chromatography (Scheme 4.20).

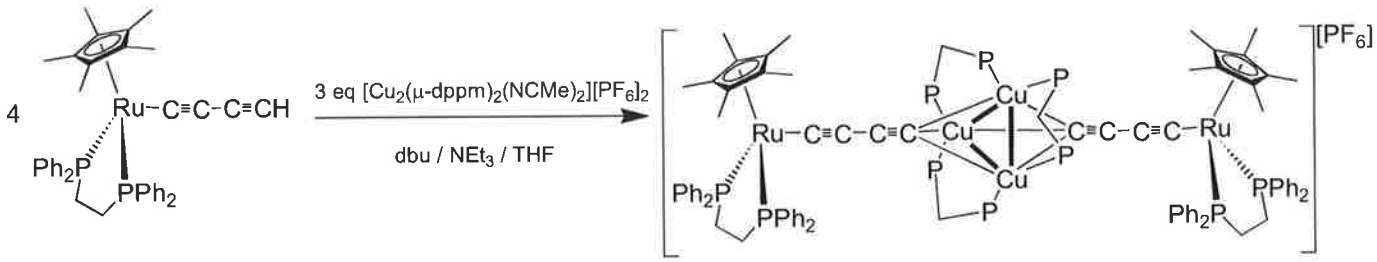

40 **54**

Scheme 4.20

The NMR spectra of **53** and **54** were very similar, the major difference being found in the relative ratios of dppe and dppm ^{31}P signals. Previously, no ^{13}C NMR data for any trinuclear copper alkynyl complexes have been reported, so the ^{13}C NMR of **53** and **54** were of interest. These spectra, recorded in acetone-d_6, revealed all expected resonances for the Ru(dppe)Cp* fragment and dppm ligands of the Cu_3 cluster. The resonances for the carbon chains in **53** and **54** were also observed and these are summarised in Figure 4.10. In both cases the C_1 resonance was observed as a triplet, with $^2J(CP) = 21$ Hz. Resonances for C_2, C_3 and C_4 were then assigned based upon decreased chemical shift. This trend was confirmed with the C_4 resonance in **53** appearing as a well-resolved septet as a consequence of coupling to the six equivalent phosphorus nuclei attached to the copper cluster. In **54** this resonance was observed as a broadened singlet.

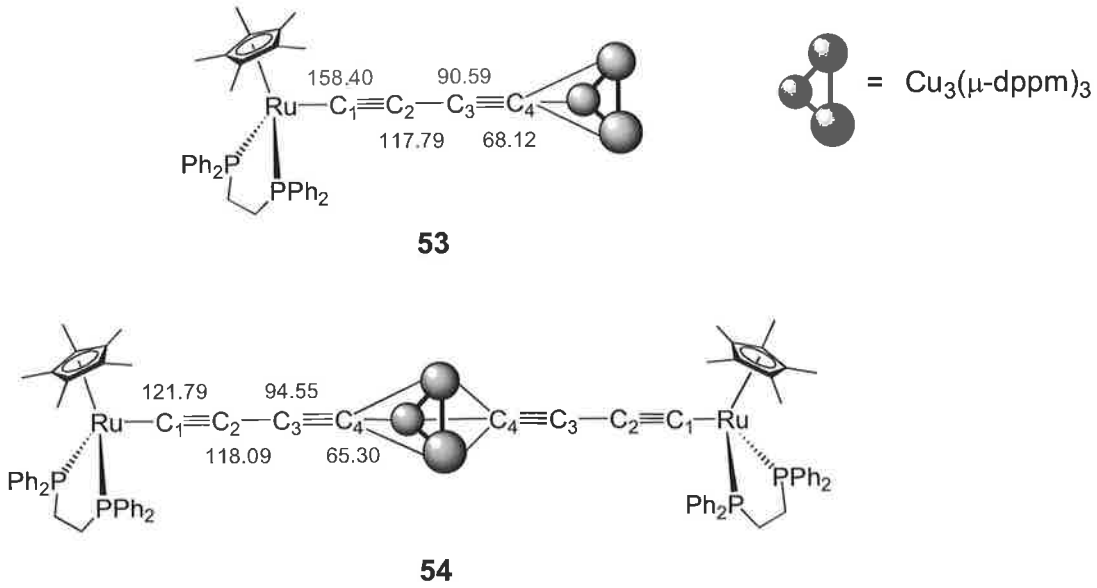

Figure 4.10: *^{13}C NMR data (ppm) for the carbon atoms of the C_4 chains, in **53** and **54**.*

4.3.8. Electrochemistry

The redox potentials for the isolated complexes **39-54** are given in Table 4.6. For the diynyl complexes **39** and **40**, single irreversible processes were observed at *ca* +0.4 V. The irreversibility of these processes may be due to rapid homo-coupling, as found with **23a/b**, although no further evidence for this process was obtained.

Comparison with the analogous iron complex **38** ($E_{½}$ = 0.00 V) shows that the oxidation process at iron is thermodynamically easier and in this case reversible.[147] Substitution of the terminal H or TMS group with a gold-phosphine moiety to give **51** or **52**, decreased the oxidation potential by *ca* 0.30 V. The tolyl derivative **52** is thermodynamically easier to oxidise by 0.07 V, consistent with the improved electron-donating ability of this phosphine.

For the mono-ruthenium complexes **41** and **43**, a single reversible oxidation wave, followed by an irreversible process at higher potentials were observed. As expected, the redox potentials for the neutral acetylethynyl **43** were lower than those for the cationic complex **41**.

For the bis-ruthenium cation **44**, in addition to a single reversible reduction at $E_{½}$ = -1.31 V, two oxidation waves at $E_{½}$ = +0.53 V (reversible) and at $E_{½}$ = 1.06 V (irreversible) were found. This electrochemical behaviour is in accord with that of related complexes recently reported.[173] The initial oxidation of **44** is presumably metal-centred and thought to involve a Ru(II)/Ru(III) process, while the second irreversible wave is consistent with the higher oxidised species undergoing further chemical reactions. The well-defined single reduction process in **44** was attributed to the reduction of the unsaturated C_7 ligand.

For the bis-ruthenium complex **50**, four redox processes were observed within the solvent imposed limits. The first three oxidation waves were all well defined and fully reversible while E_4 was irreversible as found with diyndiyl **13**. Figure 4.8 shows a plot of the redox potentials of the individual processes for **13**, **25b** and **50**. As can be seen, the potentials for **50** lie between those of **13** and **25b**. Noteworthy is that the position of the E_3 process appears to be independent of electronic influences of the ligands, and currently not understood.

The high thermodynamic stabilities of the oxidised species $[\mathbf{50}]^{n+}$ is evidenced by the large separations of each of the redox processes, which give rise to large comproportionation constants: n = 1, $K_c = 2.09 \times 10^{11}$; n = 2, $K_c = 4.57 \times 10^{11}$; n = 3, $K_c = 9.04 \times 10^{8}$.

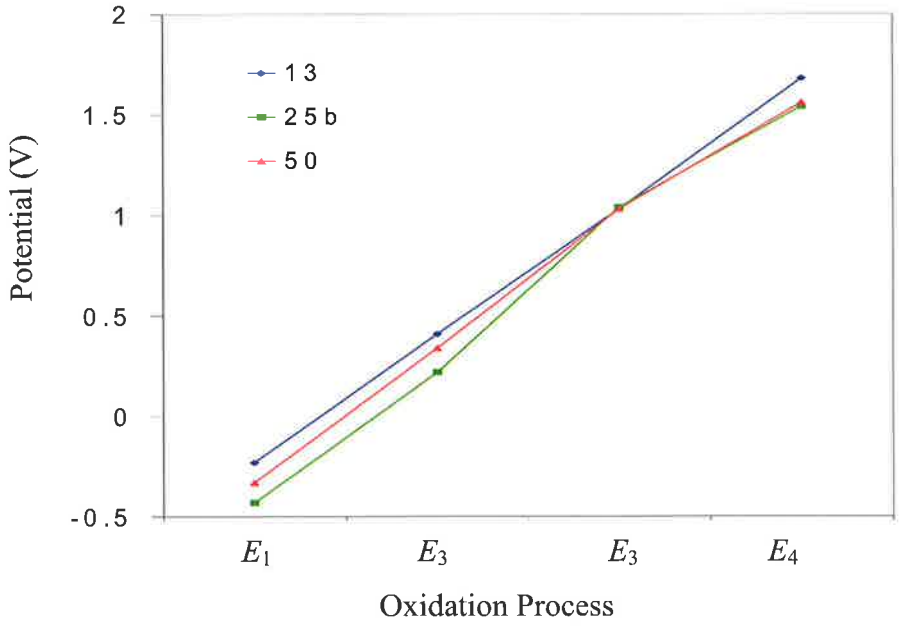

Figure 4.8: *Plot of the oxidation potential for each of the redox processes in* ***13***, ***25b*** *and* ***50***.

For **53**, a single reversible oxidation wave was observed, attributed to the Ru(II)/Ru(III) couple, while an irreversible process found at higher potentials was assigned to oxidation at the copper(I) centres as found in related systems.[167,171] For the bis-ruthenium derivative **54**, two well-defined reversible oxidation waves were observed, together with a single irreversible process at higher potentials. The peak separation between the first two processes, assigned to the successive oxidation of both ruthenium centres, is reasonably large (ΔE = 0.20 V, $K_c = 2.39 \times 10^3$), lying on the limit between Robin and Day Class II/III classification.[52] This suggests that despite the disruption of the π-conjugation between the two diynyl fragments, the trinuclear copper(I) cluster can still mediate reasonably strong interactions between the two ruthenium centres over an extended distance. No reduction of the copper(I) cluster was observed within the solvent-imposed limits.

Complex		E_1	E_2	E_3	E_4
39	Ru(C≡CC≡CTMS)(dppe)Cp*	+0.43 [a]			
40	Ru(C≡CC≡CH)(dppe)Cp*	+0.44 [a]			
41	[Ru{C≡CC(=NH_2)Me}(dppe)Cp*][PF_6]	+0.97	+1.50 [a]		
43	Ru{C≡CC(=O)Me}(dppe)Cp*	+0.43	+1.16 [a]		
44	[{Cp*(dppe)Ru}(C≡CC(OMe)=CHCMe=C=C=){Ru(dppe)Cp*}][PF_6]	-1.31	+0.53	+1.06 [a]	
50	{Cp*(dppe)Ru}(C≡CC≡C){Ru(PPh_3)$_2$Cp}	-0.33	+0.34	+1.03	+1.56 [a]
51	Ru{C≡CC≡C[Au(PPh_3)]}(dppe)Cp*	+0.15 [a]			
52	Ru{C≡CC≡C[AuP(tol)$_3$]}(dppe)Cp*	+0.08 [a]			
53	[{Cp*(dppe)Ru}(C≡CC≡C){Cu_3(μ-dppm)$_3$}][PF_6]	+0.65	+1.34 [a]		
54	[{Cp*(dppe)Ru}(C≡C)$_2${Cu_3(μ-dppm)$_3$}(C≡C)$_2${Ru(dppe)Cp*}][PF_6]	+0.13	+0.36	+1.21 [a]	

Table 4.6: *Redox potentials (V) for isolated ruthenium complexes* ***39-54****, recorded in CH_2Cl_2, 0.1 M [$Bu^n{}_4N$][PF_6]. [a] Peak potential of an irreversible process.*

4.4. Conclusions

Reliable, high-yielding preparations of the diynyls **39** and **40** have been developed. The synthesis of complex **39** probably proceeds *via* a butatrienylidene intermediate. In the absence of base and in the presence of a fluoride source, butatrienylidene **42** undergoes attack at C_3 by various nucleophiles (NH_3, H_2O or MeOH) to give the adducts **41**, **43** and **44**, respectively. The unprecedented [2 + 2] cycloaddition reaction between a molecule of **39** at the C(3)-C(4) bond with **42** generates the bis-ruthenium derivative **45**, which contains a cyclobutenylidene ring. While a logical synthesis of this complex has yet to be developed, deprotonation at the C_4 position might lead to the formation of a cyclobutadiene, a system that is not stable in purely organic compounds, and therefore worthy of further investigation.

The syntheses of diynyls **39** and **40** have allowed the preparation of new asymmetric diyndiyls **50-52**. The redox potentials of **50** were shown to lie between the values found in the symmetric diyndiyls **13** and **25b**. The presence of the gold-phosphine groups in **51** and **52** lowered the oxidation potentials relative to **40**, however there appears to be no difference in the stability of the oxidised forms, with these processes still being irreversible.

The syntheses of **53** and **54** have demonstrated the ability of the trinuclear copper(I) cluster to maintain reasonably strong electronic interactions between the two ruthenium centres. The separation between the first two oxidation processes in **54** confirms this complex lies on the boundary of a Class II/III system for MV complexes.

4.5. Experimental

General experimental conditions are detailed on page ix.

Reagents. The compounds TMSC≡CC≡CTMS,[97] TMSC≡CC≡CH,[174] $RuCl(PPh_3)_2Cp$,[175] $AuCl(PPh_3)$,[176] $AuCl[P(tol)_3]$[177] and $[Cu_2(dppm)_2(NCMe)_2][PF_6]_2$[169] were all prepared by standard literature methods.

Ru(C≡CC≡CTMS)(dppe)Cp* (39)

To a suspension of **19b** (2000 mg, 2.98 mmol) and $Na[BPh_4]$ (1025 mg, 2.98 mmol) in 1:1 THF/NEt_3 (80 mL) was added TMSC≡CC≡CH (1090 mg, 8.94 mmol). The suspension was stirred at 50°C in a sealed flask for 48 h. The orange suspension was evaporated to dryness and a bright yellow complex extracted in hexane and filtered *via* cannula into a second Schlenk flask. Extraction was continued until the hexane extracts were no longer coloured. The yellow solution was then concentrated under vacuum (*ca* 10 mL) and the resulting bright yellow solid was collected and dried on a sintered glass funnel to give **39** (1600 mg, 71%). Anal. Calcd ($C_{43}H_{48}P_2RuSi$): C, 68.32; H, 6.40. Found: C, 68.12; H, 6.72. IR (Nujol, cm^{-1}): ν(C≡C) 2171 w, 2095 m, 1990 w. ^1H NMR: δ 0.23 (s, 9H, TMS), 1.53 [t, ^3J(HP) 2 Hz, 15H, Cp*], 1.78, 2.49 (2m, 2 x 2H, CH_2CH_2), 6.89-7.86 (m. 20H, Ph). ^{13}C NMR: δ 1.17 (s, TMS), 10.17 (s, $C_5\underline{Me}_5$), 29.66 (m, CH_2CH_2), 67.00 (s, C_4), 93.40 [t, ^2J(CP) 2 Hz, $\underline{C}_5Me_5$], 96.59 (s, C_3), 115.84 (s, C_2), 120.06 (s, C_1), 129.16-138.88 (m, Ph). ^{31}P NMR: δ 81.30 (s, dppe). ES-mass spectrum (*m/z*): 757, $[M + H]^+$; 716, $[Ru\{C{\equiv}CC(OMe)CH_2\}(dppe)Cp^*]^+$; 635, $[Ru(dppe)Cp^*]^+$.

Ru(C≡CC≡CH)(dppe)Cp* (40)

To a solution of **39** (2000 mg, 2.65 mmol) in THF (30 mL) was added a 1.0 M solution of $[Bu^n{}_4N]F$ in THF (0.4 mL, 0.4 mmol). The solution was stirred at r.t. for 3 h and then evaporated to dryness. Extraction with hot hexane gave a bright yellow solution that was filtered *via* cannula into a second Schlenk flask. Extraction was continued until the hexane extracts were no longer coloured. The yellow solution

was concentrated under vacuum (*ca* 10 mL) and the bright yellow crystalline solid was collected and dried on a sintered glass funnel under a stream of nitrogen to give **40** (1750 mg, 97%). Anal. Calcd ($C_{40}H_{40}P_2Ru$): C, 70.26; H, 5.89. Found: C, 69.97; H, 5.63. IR (Nujol, cm^{-1}): ν(≡CH) 3299 w; ν(C≡C) 2109 m, 1971 w. ^1H NMR: δ 1.44 (s, 1H, ≡CH), 1.55 (s, 15H, Cp*), 1.79, 2.54 (2m, 2 x 2H, CH_2CH_2), 7.09-7.87 (m. 20H, Ph). ^{13}C NMR: δ 10.77 (s, $C_5\underline{Me}_5$), 29.64 (m, CH_2CH_2), 52.47 (s, C_4), 75.33 (s, C_3), 91.73 (s, C_2), 93.29 (s, $\underline{C}_5Me_5$), 124.90 [t, ^2J(CP) 24 Hz, C_1], 127.50-138.99 (m, Ph). ^{31}P NMR: δ 81.32 (s, dppe). ES-mass spectrum (*m/z*): 684, $[M]^+$; 635, $[Ru(dppe)Cp^*]^+$.

[Ru{C≡CC(=NH₂)Me}(dppe)Cp*][PF₆] (41)

Complex **19b** (290 mg, 0.43 mmol), TMSC≡CC≡CTMS (84 mg, 0.43 mmol), KF (25 mg, 0.43 mmol) and NH_4PF_6 (141 mg, 0.86 mmol) were dried under vacuum. MeOH (30 mL) was added and the solution was heated at reflux point for 1 h, after which the solvent was removed and the residue extracted in CH_2Cl_2 and loaded onto preparative TLC plates. Development with 1:1 acetone/hexane gave a bright yellow band (R_f= 0.6) that was crystallised from CH_2Cl_2/hexane to give **41** (245 mg, 81%). Anal. Calcd ($C_{40}H_{44}F_6NP_3Ru$): C, 56.73; H, 5.24; N, 1.65. Found: C, 56.60; H, 5.21; N, 1.58. IR (Nujol, cm^{-1}): ν(NH) 3449 w, 3357 w, 3271 w; ν(CCC) 1982 br; ν(CN) 1651 m; ν(PF) 837 s. ^1H NMR: δ 1.54 [t, ^3J(HP) 2 Hz, 15H, Cp*], 1.77 (s, 3H, Me), 2.24, 2.64 (2m, 2 x 2H, CH_2CH_2), 7.39-7.47 (m, 20H, Ph). ^{13}C NMR: δ 9.76 (s, $C_5\underline{Me}_5$), 26.15 (s, Me), 29.11 (m, PCH_2), 96.22 (s, $\underline{C}_5Me_5$), 121.72 (s, C_2), 127.96-135.69 (m, Ph), 156.74 [s, $C(=NH_2)$], 216.37 [t, ^2J(CP) 20 Hz, C_1]. ^{31}P NMR: δ -143.5 (septet, PF_6^-), 80.30 (s, dppe). ES-mass spectrum (*m/z*): 702, $[M]^+$; 635, $[Cp^*(dppe)Ru]^+$.

Ru{C≡CC(=O)Me}(dppe)Cp* (43)

A suspension of **19b** (200 mg, 0.30 mmol), NH_4PF_6 (98 mg, 0.60 mmol) and TMSC≡CC≡CH (73 mg, 0.60 mmol) in MeOH (10 mL) was stirred at r.t. for 3 h. The solvent was removed and the residue extracted in CH_2Cl_2 and loaded onto a basic alumina column (20 cm). Elution with diethyl ether gave a light yellow band

that was collected and identified as **43** (106 mg, 50%). Anal. Calcd ($C_{40}H_{42}OP_2Ru$): C, 68.46; H, 6.03. Found: C, 68.57; H, 6.08. IR (Nujol, cm^{-1}): ν(CC) 2024 s, 2006 s; ν(C=O) 1605 s. ^1H NMR: δ 1.59 (s, 15H, Cp*), 1.89 (s, 3H, Me), 2.18, 2.78 (2m, 2 x 2H, CH_2CH_2), 7.20-7.71 (m, 20H, Ph). ^{13}C NMR: δ 9.78 (s, $C_5\underline{Me}_5$), 29.11 (m, CH_2CH_2), 32.37 (s, Me), 93.71 (s, $\underline{C}_5Me_5$), 118.88 (s, C_2), 127.07-137.85 (m, Ph), 159.24 [t, ^2J(CP) 23 Hz, C_1], 180.89 (s, CO). ^{31}P NMR: δ 80.81 (s, dppe). ES-mass spectrum (*m/z*): 703, $[M + H]^+$; 635, $[Ru(dppe)Cp^*]^+$.

[{Cp*(dppe)Ru}(-C≡CC(OMe)=CHCMe=C=C=){Ru(dppe)Cp*}][PF_6] (44)
Elution with 1:9 acetone/diethyl ether gave a bright blue band that was further purified by a second column followed by crystallisation from acetone/hexane to give bright blue crystals identified as **44** (57 mg, 12%). Anal. Calcd ($C_{81}H_{85}F_6OP_5Ru_2$): C, 62.95; H, 5.54. Found: C, 63.49; H, 5.27. IR (Nujol, cm^{-1}): ν(CCC) 1959 s; ν(PF) 841 s. ES-mass spectrum (*m/z*): 1401, $[M]^+$; 635, $[Ru(dppe)Cp^*]^+$.

The NMR spectra contained peaks assigned to the two isomers present in a 56:44 ratio. Major *E* isomer in CD_2Cl_2: ^1H NMR: δ 1.69 (s, 3H, Me), 3.24 (s, 3H, OMe), 5.44 (s, 1H, CH). ^{13}C NMR: δ 10.18 (s, $C_5\underline{Me}_5$), 26.17 (s, Me), 58.03 (s, OMe), 96.31, 97.04 (2s, $\underline{C}_5Me_5$), 122.42 (s, C_4), 127.81 (s, C_2), 142.50 (s, C_5), 150.21 (s, C_6), 155.50 (s, C_3). ^{31}P NMR: δ 80.83 (s, dppe), 81.10 (s, dppe). Minor *Z* isomer: ^1H NMR: δ 1.47 (s, 3H, Me), 2.87 (s, 3H, OMe), 5.14 (s, 1H, CH). ^{13}C NMR: δ 10.14 (s, $C_5\underline{Me}_5$), 31.81 (s, Me), 58.11 (s, OMe), 96.21, 96.84 (2s, $\underline{C}_5Me_5$), 119.56 (s, C_4), 126.40 (s, C_2), 141.61 (s, C_5), 146.28 (s, C_6), 154.83 (s, C_3). ^{31}P NMR: δ 80.41 (s, dppe), 81.29 (s, dppe).

Peaks that could not be individually assigned; ^1H NMR: δ 1.58-1.62 (m, 4 x 15H, Cp*), 2.29, 2.66 (br, 16H, CH_2CH_2), 7.21-7.68 (m, 80H, Ph). ^{13}C NMR: δ 29.66 (m, CH_2CH_2), 127.38-137.11 (m, Ph), 203.40 [t, ^2J(CP) 22 Hz], 207.42 [t, ^2J(CP) 20 Hz], 208.83 [t, ^2J(CP) 21 Hz], 209.76 [t, ^2J(CP) 22 Hz]. ^{31}P NMR: δ -143.38 (septet, PF_6^-)

{Cp*(dppe)Ru}(C≡CC≡C){Ru(PPh$_3$)$_2$Cp} (50)

RuCl(PPh$_3$)$_2$Cp (106 mg, 0.14 mmol), Na[BPh$_4$] (48 mg, 0.14 mmol) and **40** (100 mg, 0.14 mmol) were dried under vacuum. A degassed solution of dbu (90 mg, 0.59 mmol) in 1:1 CH_2Cl_2/NEt_3 (50 mL) was added *via* cannula and the solution heated at reflux point for 24 h. The solvent was removed and the residue extracted in hot hexane until no further yellow fractions were extracted. The solvent was removed to give an orange residue that crystallised upon the addition of a small quantity of acetone giving **50** (68 mg, 35%). Anal. Calcd ($C_{81}H_{74}P_4Ru_2$): C, 70.83; H, 5.43. Found: C, 70.74; H, 5.46. IR (Nujol, cm^{-1}): ν(C≡C) 1960 w. ^{1}H NMR: δ 1.72 (s, 15H, Cp*), 2.02, 2.89 (2m, 2 x 2H, CH_2CH_2), 4.31 (s, 5H, Cp), 6.99-8.12 (m. 50H, Ph). ^{13}C NMR: δ 10.04 (s, $C_5\underline{Me}_5$), 29.52 (m, CH_2CH_2), 85.27 (s, C_5H_5), 92.38 (s, $\underline{C}_5Me_5$), 127.00-139.63 (m, Ph). ^{31}P NMR: δ 51.47 (s, PPh$_3$), 81.99 (s, dppe). ES-mass spectrum (*m/z*): 1374, [M]$^+$; 1112, [M - PPh$_3$]$^+$.

Ru{C≡CC≡C[Au(PPh$_3$)]}(dppe)Cp* (51)

Complex **40** (200 mg, 0.29 mmol) and AuCl(PPh$_3$) (146 mg, 0.29 mmol) were dried under vacuum before THF (10 mL) was added followed by the addition of a 0.5 M solution of KN(TMS)$_2$ in toluene (1.16 mL, 0.58 mmol). After the yellow solution was stirred at r.t. for 4 h, it was evaporated to dryness and acetone (5 mL) was added to initiate crystallisation. The flask was left in the freezer for 1 h, and the yellow crystalline solid was collected and washed with a further portion of acetone (5 mL) to give **51** (231 mg, 67%). Anal. Calcd ($C_{58}H_{54}AuP_3Ru$): C, 61.00; H, 4.77. Found: C: 61.02, H; 4.71. IR (Nujol, cm^{-1}): ν(C≡C) 2119 m, 2072 m, 1981 w. ^{1}H NMR: δ 1.52 (s, 15H, Cp*), 2.15, 2.77 (2m, 2 x 2H, CH_2CH_2), 7.04-7.76 (m. 35H, Ph). ^{13}C NMR (CD_2Cl_2): δ 10.26 (s, $C_5\underline{Me}_5$), 29.79 (m, CH_2CH_2), 92.20 (s, Ru-C≡$\underline{C}$, C_2), 93.29 (s, $\underline{C}_5Me_5$), 94.61 (s br, Au-C≡$\underline{C}$, C_3), 110.00 [d, ^2J(CP) 75 Hz, Au-$\underline{C}$≡, C_4], 118.65 [t, ^2J(CP) 23 Hz, Ru-$\underline{C}$≡, C_1], 127.51-139.13 (m, Ph). ^{31}P NMR: δ 42.48 (s, PPh$_3$), 80.84 (s, dppe). ES-mass spectrum (*m/z*): 721, [Au(PPh$_3$)$_2$]$^+$; 1142, [M]$^+$; 1601, [M + AuPPh$_3$]$^+$; 1863, [M + Au(PPh$_3$)$_2$]$^+$.

Ru{C≡CC≡C[AuP(tol)$_3$]}(dppe)Cp* (52)

Complex **40** (200 mg, 0.29 mmol) and AuCl[P(tol)$_3$] (158 mg, 0.29 mmol) were dried under vacuum before THF (10 mL) was added followed by the addition of a 0.5 M solution of KN(TMS)$_2$ in toluene (1.16 mL, 0.58 mmol). The yellow solution was left stirred at r.t. for 4 h after which the solvent was removed and the solid extracted in the minimum amount of CH_2Cl_2 and filtered into rapidly stirred hexane to precipitate a bright yellow solid identified as **52** (260 mg, 76%). Anal. Calcd ($C_{61}H_{60}AuP_3Ru$): C, 61.88; H, 5.11. Found: C, 61.74; H, 5.04. IR (Nujol, cm^{-1}): ν(C≡C) 2124 w, 2073 w, 1987 w. ^{1}H NMR: δ 1.56 (s, 15H, Cp*), 2.19, 2.81 (2m, 2 x H, CH_2CH_2), 2.40 (s, 9H, Me), 7.08-7.79 (m. 32H, Ph). ^{13}C NMR (CD_2Cl_2): δ 10.16 (s, $C_5\underline{Me}_5$), 21.54 (s, Me), 29.71 (m, CH_2CH_2), 92.32 (s, Ru-C≡$\underline{C}$-, C_2), 93.28 (s, $\underline{C}_5Me_5$), 94.57 (s br, Au-C≡$\underline{C}$-, C_3), 111.40 (br, Au-$\underline{C}$≡, C_4), 118.12 [t, ^2J(CP) 24 Hz, Ru-$\underline{C}$≡, C_1], 127.47-142.11 (m, Ph). ^{31}P NMR: δ 40.44 [s, P(tol)$_3$], 80.86 (s, dppe). ES-mass spectrum (*m/z*): 805, [Au{P(tol)$_3$}$_2$]$^+$; 1184, [M]$^+$; 1685, [M + Au{P(tol)$_3$}]$^+$; 1989, [M + Au{P(tol)$_3$}$_2$]$^+$.

[{Cp*(dppe)Ru}(C≡CC≡C){Cu$_3$(μ-dppm)$_3$}][PF$_6$]$_2$ (53)

[Cu$_2$(μ-dppm)$_2$(NCMe)$_2$][PF$_6$]$_2$ (100 mg, 0.078 mmol) and **40** (36 mg, 0.052 mmol) were dried under vacuum before 8:2 THF/NEt$_3$ (10 mL) was added and the solution heated to reflux for 1 h. The resulting suspension was left to cool to r.t. and the bright orange crystalline product was filtered and washed with diethyl ether to give **53** (85 mg, 70%). Anal. Calcd ($C_{115}H_{105}Cu_3F_{12}P_{10}Ru$): C, 59.63; H, 4.57. Found: C, 59.69; H, 4.63. IR (Nujol, cm^{-1}): ν(C≡C) 1983 m, ν(PF) 839 s. ^{1}H NMR (acetone-d_6): δ 1.77 (s, 15H, Cp*), 2.89, 2.57 (2m, 2 x 2H, dppe), 3.50 (m, 6H, dppm), 7.89-7.09 (m, 80H, Ph). ^{13}C NMR (acetone-d_6): 10.90 (s, $C_5\underline{Me}_5$), 28.60 (m, CH_2CH_2), 68.12 [septet, ^2J(CP) 17 Hz, C_4], 90.59 (s, C_3), 95.65 (s, $\underline{C}_5Me_5$), 117.79 (s, C_2), 137.87-128.98 (m, Ph), 158.40 [t, ^2J(CP) 21 Hz, C_1]. ^{31}P NMR (acetone-d_6): -142.35 (septet, PF_6^-), -7.83 (s, 6P, dppm), 78.85 (s, 2P, dppe). ES-mass spectrum (*m/z*): 1013, [M]$^{2+}$.

[{Cp*(dppe)Ru}(C≡C)$_2${Cu$_3$(μ-dppm)$_3$}(C≡C)$_2${Ru(dppe)Cp*}][PF$_6$] (54)

To a solution of **40** (70 mg, 0.10 mmol) in 8:2 THF/NEt$_3$ (10 mL) was added dbu (45 mg, 0.30 mmol) followed by [Cu$_2$(μ-dppm)$_2$(NCMe)$_2$][PF$_6$]$_2$ (100 mg, 0.078 mmol). After the solution was heated to reflux for 1 h the solvent was removed and the product extracted in CH_2Cl_2 and loaded onto a basic alumina column (20 cm). A yellow band was eluted with 4:6 acetone/hexane and the solvent removed. Crystallisation from CH_2Cl_2/hexane gave a bright yellow crystalline solid that was collected and washed with diethyl ether giving **54** (102 mg, 70%). Anal. Calcd ($C_{155}H_{144}Cu_3F_6P_{11}Ru_2$): C, 65.22; H, 5.08. Found: C, 65.27; H, 4.97. IR (Nujol, cm^{-1}): ν(C≡C) 2018 w; ν(PF) 838 s. ^{1}H NMR (acetone-d_6): δ 1.86 (s, 30H, Cp*), 2.58, 3.02 (2m, 2 x 4H, dppe), 3.14 (m, 6H, dppm), 6.76-7.97 (m, 100H, Ph). ^{13}C NMR spectrum (acetone-d_6): δ 11.53 (s, $C_5\underline{Me}_5$), 28.25 (m, CH_2CH_2), 65.30 (br, C_4), 94.21 (s, $\underline{C}_5Me_5$), 94.55 (s, C_3), 118.09 (s, C_2), 121.79 [t, ^2J(CP) 21 Hz, C_1], 128.35-138.84 (m, Ph). ^{31}P NMR (acetone-d_6): δ -142.33 (septet, PF_6^-), -7.49 (s, 6P, dppm), 79.09 (s, 4P, dppe). ES-mass spectrum: (*m/z*) 1355, $[M + H]^{2+}$.

CHAPTER FIVE

Syntheses, Structures and Electronic Properties of Mixed Iron-Ruthenium Diyndiyl Complexes

5.1. Introduction

While most symmetric diyndiyl complexes can be prepared in a single step reaction, those featuring inequivalent metal-ligand fragments require multi-step syntheses. Consequently, only a limited number of asymmetric diyndiyl complexes have been reported and even fewer of these have been structurally characterised.

Despite the synthetic challenges, the physical properties of these materials make them of significant interest. Electron transfer within molecules containing electron-rich and electron-poor metal-ligand fragments is expected to be more favourable in one direction and such materials can be regarded as prototypes for polarised molecular wires.[147] Furthermore, the chemistry of the bridging ligand may show selectivity as a consequence of steric or electronic influences imposed by the two different metal-ligand fragments.

5.1.1. Syntheses of Asymmetric Diyndiyl Complexes

The syntheses of asymmetric diyndiyl complexes typically involve the initial preparation of a diynyl complex of the general formula [M](C≡CC≡CR) (R = H, TMS or Li). Substitution with a second metal-ligand fragment can be achieved under a variety of different reaction conditions.

The tungsten diynyl W(C≡CC≡CH)(CO)$_3$Cp (**55**) has been used to prepare a number of asymmetric diyndiyl complexes.[150] Complex **55** can be coupled with a range of metal-halide precursors using Cadiot-Chodkiewicz coupling conditions (CuI/NHEt$_2$) (Scheme 5.1). These reactions proceed very quickly, often in less than 15 minutes, with yields between 51-97%.

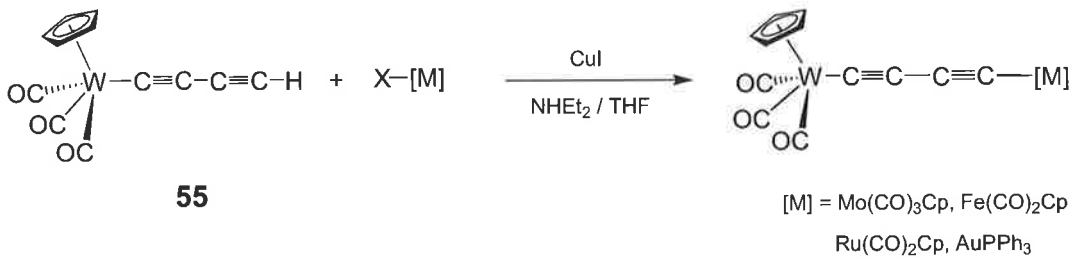

Scheme 5.1

The chemistry of **55** was further demonstrated upon its reaction with the Group 9 metal triflates $M(OTf)(CO)(PPh_3)_2$.[178] The use of the metal triflates in this reaction, rather than the usual metal halides, allowed the coupling reaction to proceed in the absence of a copper catalyst, resulting in a much cleaner reaction that gave the corresponding diyndiyls $\{Cp(OC)_3W\}(C{\equiv}CC{\equiv}C)\{M(CO)(PPh_3)_2\}$ [M = Rh (**56**), Ir (**57**)] in high yields (Scheme 5.2). The metal triflates were prepared *in situ* from the corresponding metal chloride and AgOTf in a non-coordinating solvent such as CH_2Cl_2.[178] Diethylamine was required to neutralise the strong acid (HOTf) that was formed upon coupling.

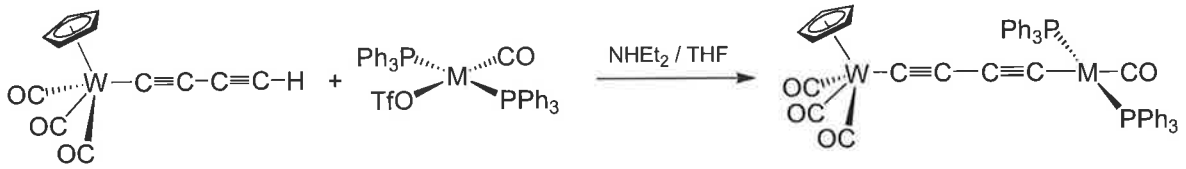

55

56 : M = Rh

57 : M = Ir

Scheme 5.2

Treatment of **55** with $LiNPr^i_2$ (LDA) in THF at low temperatures generated the lithiated derivative $W(C{\equiv}CC{\equiv}CLi)(CO)_3Cp$. Reaction of this nucleophilic species with $MnI(CO)_5$ gave $\{Cp(OC)_3W\}(C{\equiv}CC{\equiv}C)\{Mn(CO)_5\}$ (**58**) as an extremely light sensitive yellow solid in a relatively low yield (18%) (Scheme 5.3).[150]

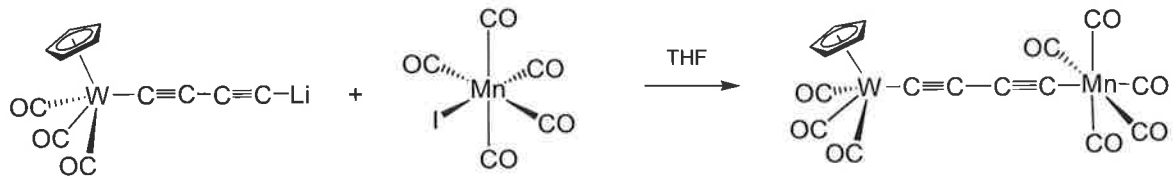

58

Scheme 5.3

The TMS-protected derivative $W(C{\equiv}CC{\equiv}CTMS)(CO)_3Cp$ (**59**) was used in the synthesis of $\{Cp(OC)_3W\}(C{\equiv}CC{\equiv}C)\{Ru(PPh_3)_2Cp\}$ (**60**) (Scheme 5.4).[179] Addition of $RuCl(PPh_3)_2Cp$ to a solution of the diynyl complex in the presence of KF and dbu

gave **60** in 61% yield. This complex features electron-poor (W) and electron-rich (Ru) metal-ligand fragments and would most likely show some interesting electron transfer properties arising from this polarisation.

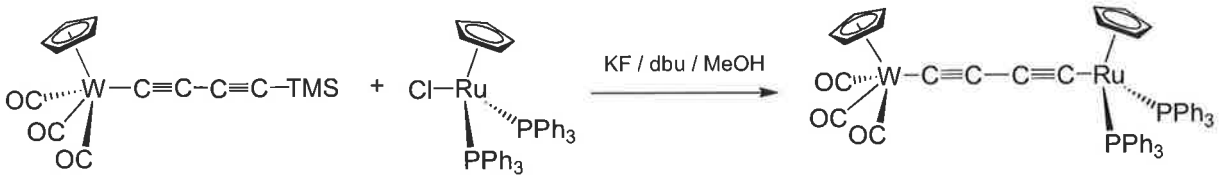

59 **60**

Scheme 5.4

The TMS-protected rhenium diynyl **36** has been used to synthesise several asymmetric diyndiyl complexes. Desilylation followed by deprotonation with Bu^{n}Li generated the lithiated derivative Re(C≡CC≡CLi)(NO)(PPh_3)Cp* which could be isolated as an air- and moisture-sensitive orange solid but was generally used *in situ*.[180] The reaction of the lithiated diynyl with one equivalent of *trans*-$PdCl_2(PEt_3)_2$ gave a 24:58:18 mixture of the starting palladium complex along with the mono- and bis-rhenium complexes **61** and **62**, respectively (Scheme 5.5). Isolation of pure **61** was achieved after several crystallisations.

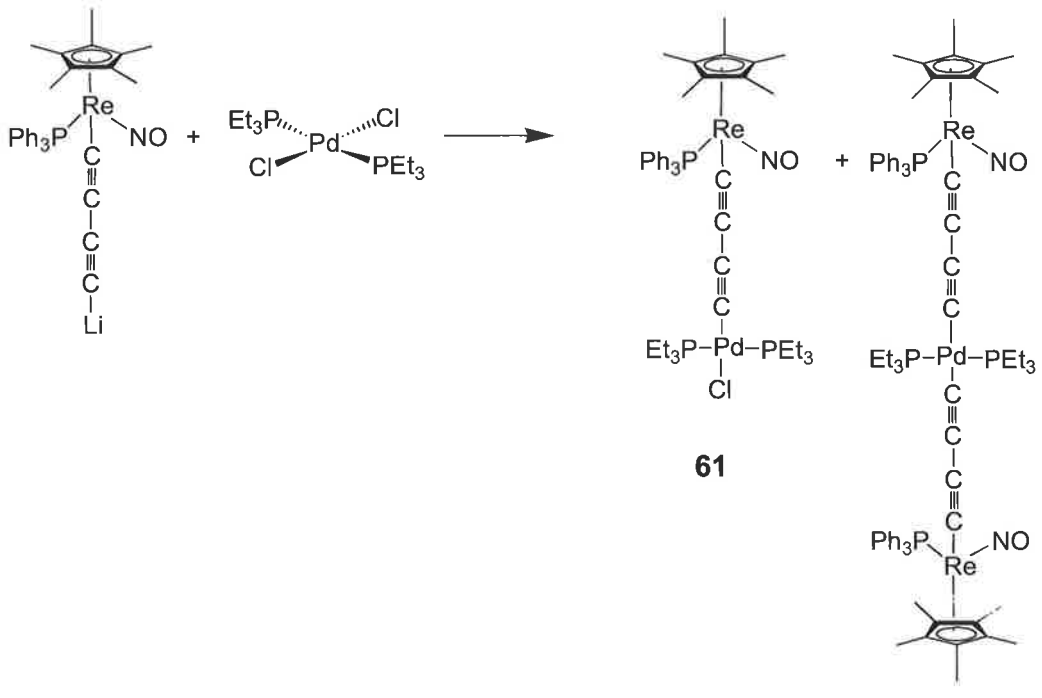

Scheme 5.5

Coupling of **36** with FeCl(dppe)Cp* in the presence of KF, KPF_6 and 18-crown-6 in MeOH/THF gave the mixed-metal {Cp*(Ph_3P)(ON)Re}(C≡CC≡C){Fe(dppe)Cp*} (**63**) in 65% yield (Scheme 5.6).[181] The role of 18-crown-6 in this reaction was to assist the solubility of KF by encapsulating the potassium cation, leaving the fluoride anion in solution. The synthesis of **63** allowed direct comparisons to be made with the related symmetric diyndiyls **4** and **5**.

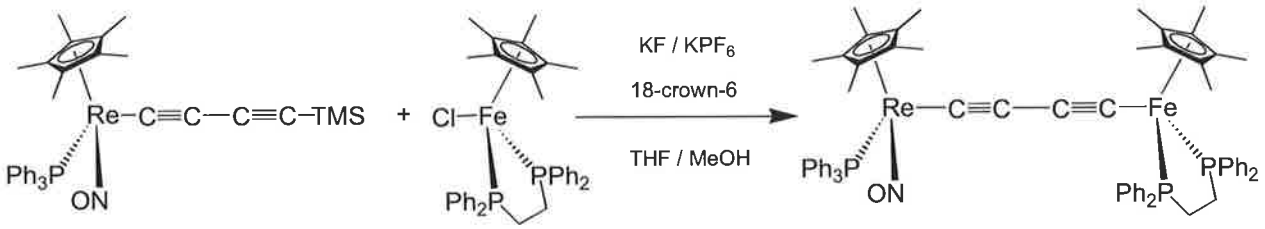

36 **63**

Scheme 5.6

The electron-deficient iron diynyl **37** was coupled with the electron-rich fragment FeCl(dppe)Cp* in the presence of $KOBu^t$ and KPF_6 in methanol to give {Cp*$(OC)_2$Fe}(C≡CC≡C){Fe(dppe)Cp*} (**64**) in 50% yield (Scheme 5.7).[147] In this reaction, the TMS group of **37** was removed by treatment with KF prior to the addition of the FeCl(dppe)Cp*.

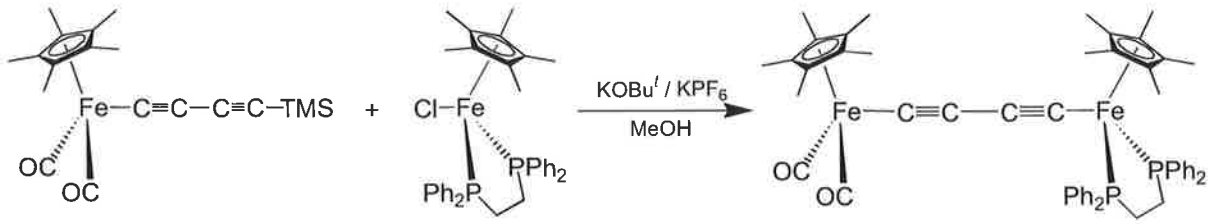

37 **64**

Scheme 5.7

5.1.2. Properties of Asymmetric Diyndiyl Complexes

While the chemistry of asymmetric diyndiyl complexes is relatively well understood, in most cases the physical properties, especially the electrochemical response, have not been investigated. Exceptions to this are **63** and **64**, which contain the electron-rich fragment Fe(dppe)Cp*.

In the cyclic voltammogram of **64**, two one-electron oxidation waves at $E_{½}$ = -0.36 and +0.74 V were observed, with the former being fully reversible and the latter only partially reversible (i_a/i_c = 0.9).[147] Chemical oxidation with one equivalent of $[FeCp_2][PF_6]$ gave the monocation **[64]**$[PF_6]$. Oxidation occurs at the more electron-rich Fe(dppe)Cp* fragment, as confirmed by Mössbauer spectroscopy, with the isomeric shift and quadrupole splitting of the $Fe(CO)_2Cp^*$ fragment being typical of a Fe(II) centre. Cation **[64]**$[PF_6]$ is best described as a Class II MV complex and the presence of a weak IVCT band in the NIR resulted from electronic interactions between the electron-rich and electron-poor sites (V_{ab} = 0.021 eV).[147]

The iron-rhenium diyndiyl complex **63** undergoes two reversible oxidation processes at $E_{½}$ = -0.50 and +0.23 V followed by an irreversible oxidation at a higher potential ($E_{½}$ = +1.33 V). Chemical oxidation with $[FeCp_2][PF_6]$ gave the monocation **[63]**$[PF_6]$, which was shown by IR, cyclic voltammetry and Mössbauer spectroscopy to exist predominantly as an iron-centred radical (Structure **5a**, Scheme 5.8). A contribution from the rhenium-centred radical (Structure **5b**) was confirmed by ESR spectroscopy that revealed coupling of the unpaired electron to rhenium, which has a nuclear spin of 5/2. The NIR spectrum of **[63]**$[PF_6]$ contained a weak IVCT band, from which the electronic coupling parameter was determined (V_{ab} = 0.019 eV).[181]

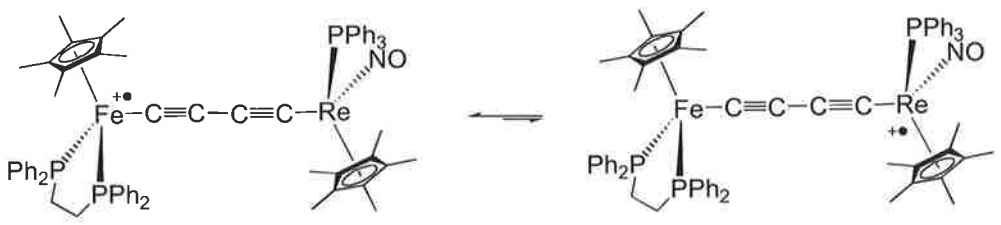

5a **5b**

Scheme 5.8

Treatment of [**63**][PF_6] with a second equivalent of [$FeCp_2$][PF_6] gave the dication [**63**][PF_6]$_2$, which exists in a temperature-dependent spin-equilibrium between interconverting singlet and triplet states (Scheme 5.9). Structures **5d** and **5e** are limiting resonance forms of the singlet state, while structure **5c** represents the triplet state. Although the dication [**63**][PF_6]$_2$ was found to have a singlet ground state, the singlet triplet energy gap (ΔG_{ST}) is sufficiently small that at room temperature the triplet state was found to be significantly populated.[181]

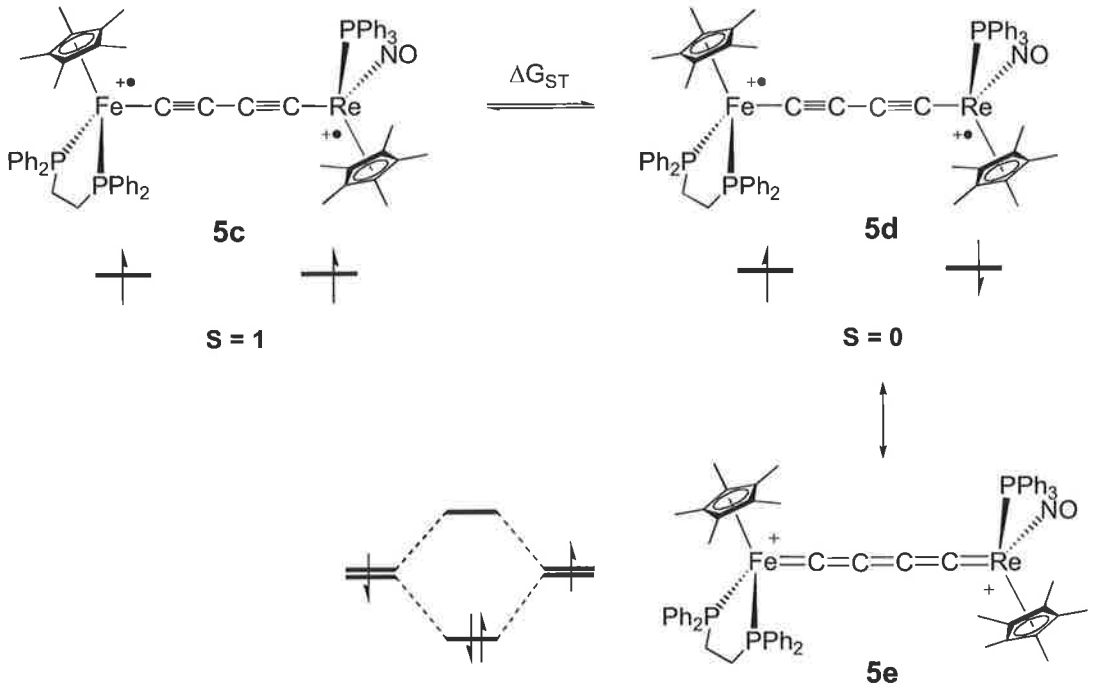

Scheme 5.9

5.2. Aims

As described in Chapter 2, the bridging C_4 ligand in **25b** exists in the 1,3-butadiynyl form, however upon oxidation significant changes were observed. In particular, structural characterisation of the dication [**25b**][PF_6]$_2$ confirmed the unique cumulenic nature of the bridging ligand (Figure 5.1). Furthermore, the observation of the relatively sharp spectral profiles of [**25b**][PF_6]$_2$, together with the fact that it is ESR silent, suggest that [**25b**][PF_6]$_2$ is a diamagnetic complex, with no detectable contributions from any triplet state.

This is in contrast to the analogous iron complex **5**, which upon oxidation gave the paramagnetic dication [**5**][PF_6]$_2$. Although [**5**][PF_6]$_2$ was shown to have a singlet ground state, ΔG_{ST} is sufficiently small that even at liquid nitrogen temperature the paramagnetic triplet state is still significantly populated.[181]

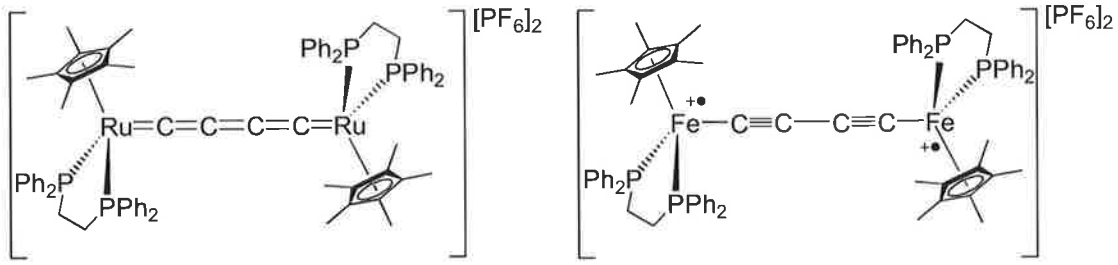

[25b][PF_6]$_2$ **[5][PF_6]$_2$**

Figure 5.1: *Electronic structures of the dications [25b][PF_6]$_2$ and [5][PF_6]$_2$.*

As the ligand environments are identical in the case of [**25b**][PF_6]$_2$ and [**5**][PF_6]$_2$, the observed differences must be a consequence of the two different metals. This leads to the obvious question of what properties a mixed iron-ruthenium dication would have; would it exist predominantly in the singlet or triplet state? Furthermore, the synthesis of the MV species is of interest as the observation of an IVCT band in the NIR should enable the calculation of V_{ab}, allowing direct comparisons to be made with other Class II complexes such as [**63**][PF_6] and [**64**][PF_6].

5.3. Results and Discussion

5.3.1. Synthesis of {Cp(dppe)Ru}(C≡CC≡C){Fe(PP)Cp*} [PP = dppe (65), dppp (66)]*

As outlined in Scheme 5.10, the mixed ruthenium-iron diyndiyls **65** and **66** were prepared in one-pot reactions of **40** with one equivalent of the chloro-iron precursor FeCl(PP)Cp* in NEt_3. The reaction was stirred at room temperature for 24 hours before the solvent was removed and extraction with diethyl ether gave a red solution that was evaporated and washed with methanol to give either **65** (73%) or **66** (71%). The tetraphenylborate salt was present to assist with the ionisation of the Fe-Cl bond. Analytically pure samples were obtained after crystallisation from CH_2Cl_2/hexane, toluene/hexane or benzene/hexane solvent mixtures.

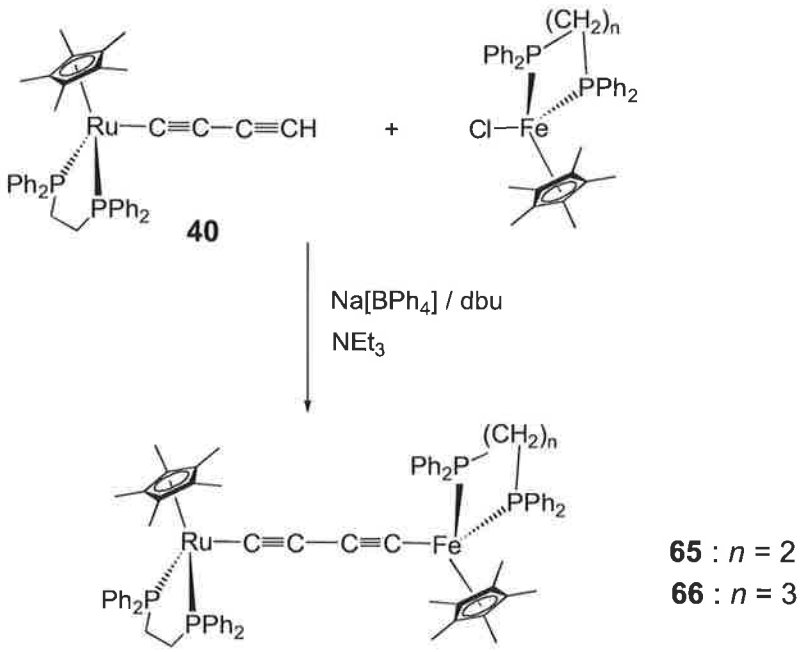

Scheme 5.10

It is assumed that the reaction of **40** with the chloro-iron complexes proceeds *via* an initial 1,2- or 1,4-hydrogen shift to give either an ethynylvinylidene (**5f**) or butatrienylidene (**5g**) intermediate (Scheme 5.11). Both of these species are expected to be susceptible to nucleophilic attack and must be deprotonated immediately upon formation to prevent significant losses. In the absence of dbu, yields were significantly reduced (*ca* 50%). A possible explanation for the lower

yields is the relatively low acidity of the proton attached to the C_4 chain in **5f** or **5g** due to the presence of strongly electron-donating end-groups. This results in an equilibrium between intermediates **5f** and **5g** and the deprotonated diyndiyl **65** or **66** (Scheme 5.11). Once formed, the neutral complexes **65** and **66** can also be protonated by $[NHEt_3]Cl$, a by-product in the reaction, resulting in the regeneration of the reactive intermediates **5f** and **5g**, consequently lowering the yields. Addition of dbu, a stronger base than NEt_3, forces the equilibrium to the right-hand side.

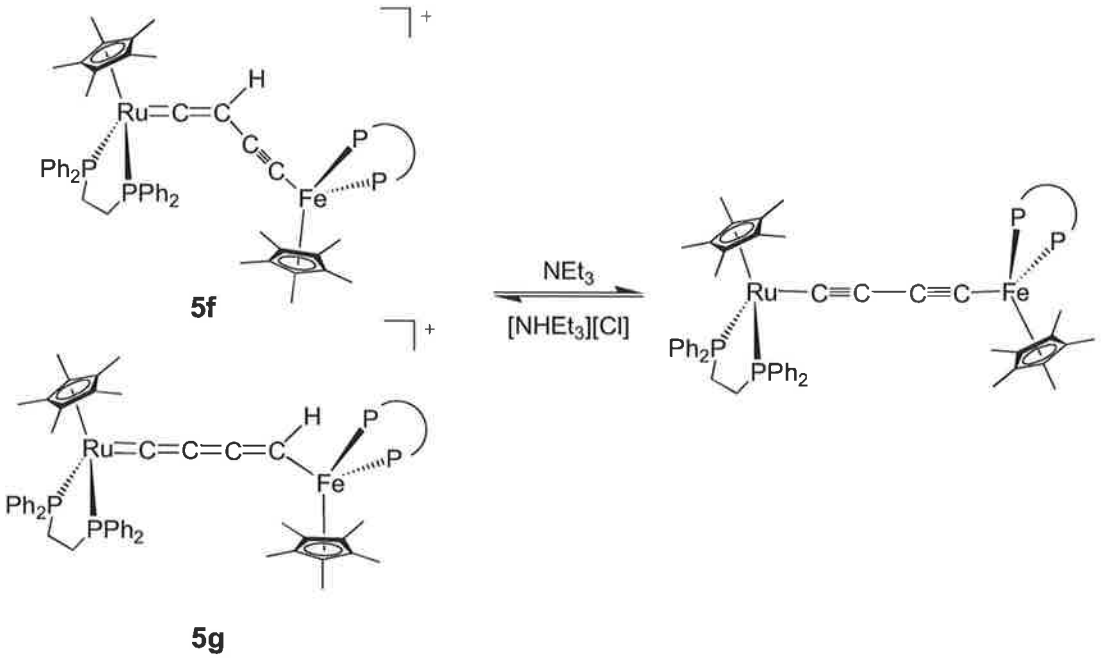

Scheme 5.11

5.3.2. Spectroscopic Characterisation of 65 and 66

As expected, **65** and **66** display similar spectroscopic features, both containing a weak ν(C≡C) band in their IR spectra at *ca* 1965 cm^{-1}, consistent with the anticipated diyndiyl nature of the C_4 chain. In the ^1H NMR spectra, two individual resonances for the Cp* ligands were observed at δ 1.82 and 1.59 for **65** and at δ 1.68 and 2.02 for **66**. In both complexes the upfield resonances were broadened and these were assigned to the iron-bound ligand based on comparison with NMR data for **5** and **25b**. Characteristic resonances for both the CH_2CH_2 and aromatic protons of dppe were observed and these are summarised in Section 5.5. Significant differences between the phosphorus resonances for the iron- and ruthenium-bound

dppe ligands were found. In the case of **65**, the ^{31}P NMR spectrum contained two broadened resonances at δ 101.90 and 82.55 in a 1:1 ratio, with the former assigned to the iron-bound ligand. This iron-bound dppe resonance shifted upfield to δ 60.92 in the dppp complex **66**. As shown in Figure 5.2, the phosphorus resonances in the ^{31}P NMR spectrum of **66** sharpened at lower temperatures. A similar result was found in the ^{31}P NMR spectrum of **65**. This broadening at higher temperatures was attributed to the rapid relaxation of the phosphorus nuclei in the presence of a small quantity of paramagnetic impurity, most likely $[\mathbf{65}]^+$ or $[\mathbf{66}]^+$ from oxidation in aerobic solutions.

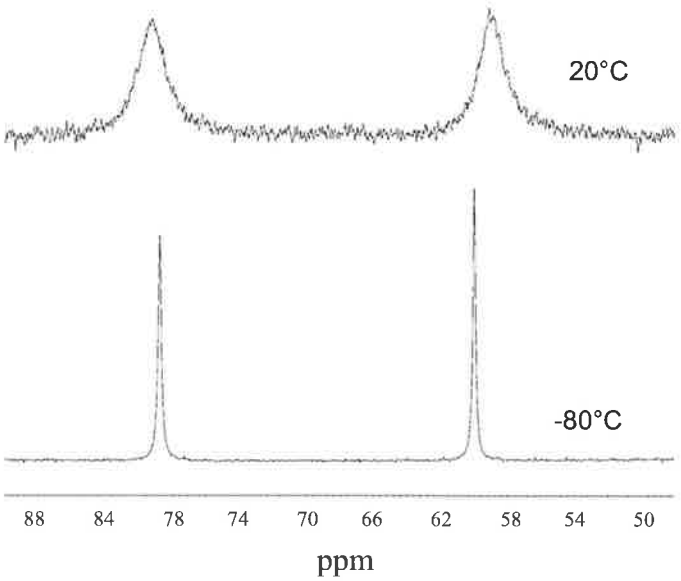

Figure 5.2: *^{31}P NMR spectra of **66** recorded in toluene-d_8 at 20°C (top) and at -80°C (bottom).*

The ^{13}C NMR spectrum of **65** in benzene-d_6 at 20°C revealed all the expected resonances for the Cp* and dppe ligands. However, resonances for the C_4 chain were not observed, even with concentrated solutions and extended acquisition times. Upon lowering the temperature to -80°C, the resonances for the C_4 chain could be seen in toluene-d_8, and these are summarised in Figure 5.3. The positions of these signals correlate well with those found in the related symmetric diyndiyls **25b** and **5**.

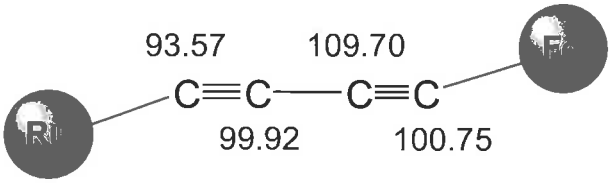

Figure 5.3: *^{13}C NMR data (ppm) for the carbon atoms of the C_4 chain in **65**.*

5.3.3. Molecular Structures of 65 and 66

In the CH_2Cl_2, benzene and toluene solvates of **65**, the two metal sites are completely disordered. In hindsight this result is not surprising considering that the ligand environments around the two metal centres are identical. Substitution of dppe at the iron centre with dppp to give **66** was not sufficient to enable a distinction to be made between the Ru and Fe centres. Consequently the bond parameters are averages of the individual bond lengths and bond angles for the Ru and Fe centres. Table 5.1 collects important structural parameters along the C_4 chain, while the ORTEP plot of a single molecule of **65** is given in Figure 5.3, together with the space-filling model in Figure 5.4 that illustrates the complete encapsulation of the two metals by their associated ligands.

The diyndiyl nature of both **65** and **66** is apparent from the short C(1)-C(2) and long C(2)-C(3) bonds. The M-C bond lengths are close to the average values found in related symmetric complexes [1.884(3) (**5**)[182] and 2.003(3) Å (**25b**)]. Angles at the individual carbon atoms C(1-4) are close to linear [in the range 174.8 to 178.1(7)°].

	65	**66**
Bond lengths (Å)		
M(1)-C(1)	1.939(4)	1.974(9)
C(1)-C(2)	1.223(6)	1.25(1)
C(2)-C(3)	1.374(6)	1.39(1)
C(3)-C(4)	1.233(6)	1.24(1)
C(4)-M(2)	1.957(4)	1.950(9)
Bond angles (°)		
M(1)-C(1)-C(2)	177.3(4)	178.1(7)
C(1)-C(2)-C(3)	176.6(4)	177.4(8)
C(2)-C(3)-C(4)	177.7(4)	177.5(8)
C(3)-C(4)-M(2)	177.3(4)	174.8(7)
Σ (total bend)	11.1	12.2

Table 5.1: *Selected structural data for **65** and **66**.*

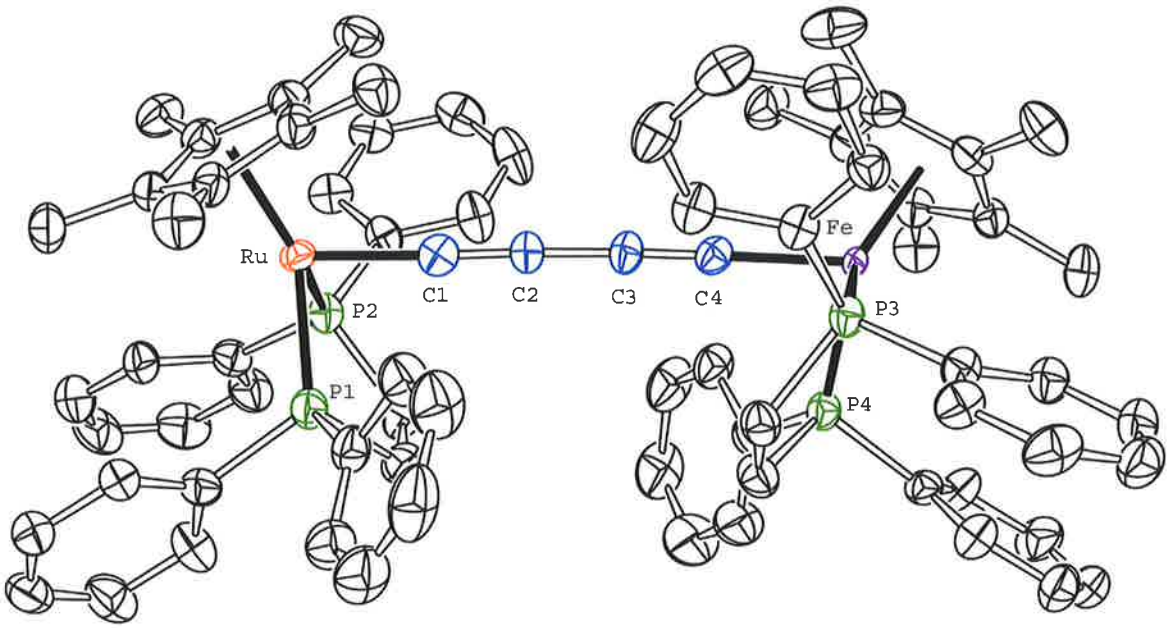

Figure 5.4: *ORTEP view of* ***65****.*

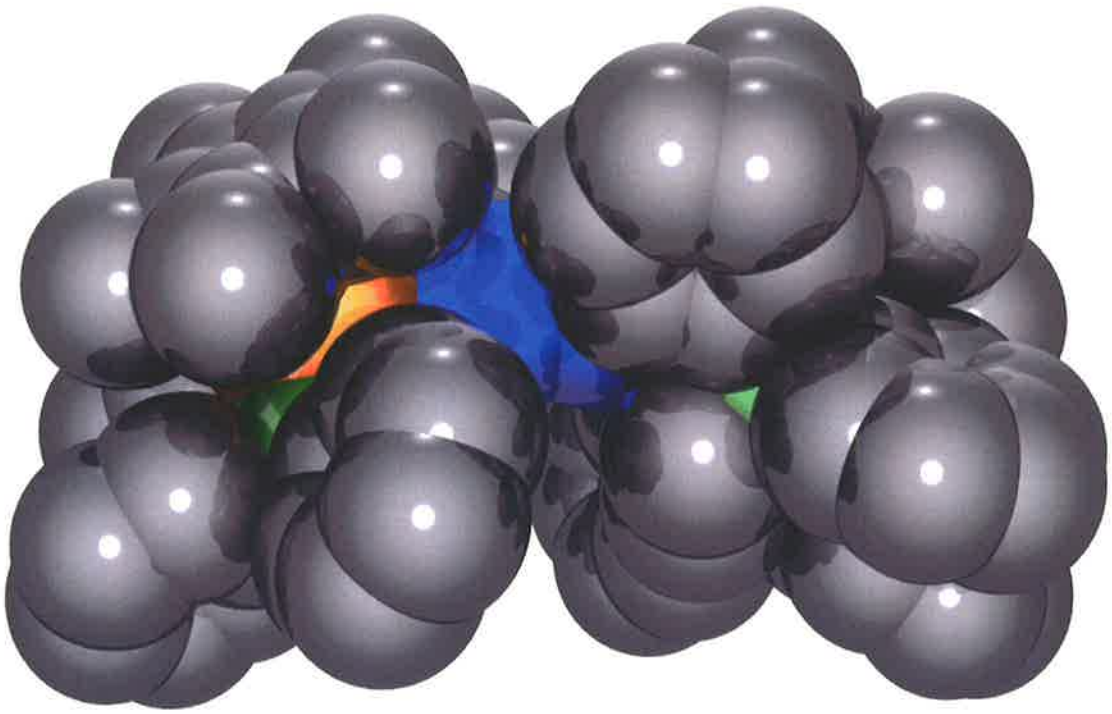

Figure 5.5: *Space-filling model of* ***65*** *shown in the same orientation as in Figure 5.4. Generated using ORTEP for Windows (Version 3.0) and POV-Ray (Version 3.5) with hydrogen atoms omitted for clarity (Grey = carbon; Orange = ruthenium; Green = phosphorus; Blue = carbon atoms of the* C_4 *Chain).*

5.3.4. Redox Chemistry

The cyclic voltammograms of **65** and **66** each contained three well-separated, fully reversible oxidation waves (Figure 5.6). Table 5.2 contains electrochemical data for **65**, **66** and the related complexes **5**, **25b**, **38** and **39** measured under similar conditions.

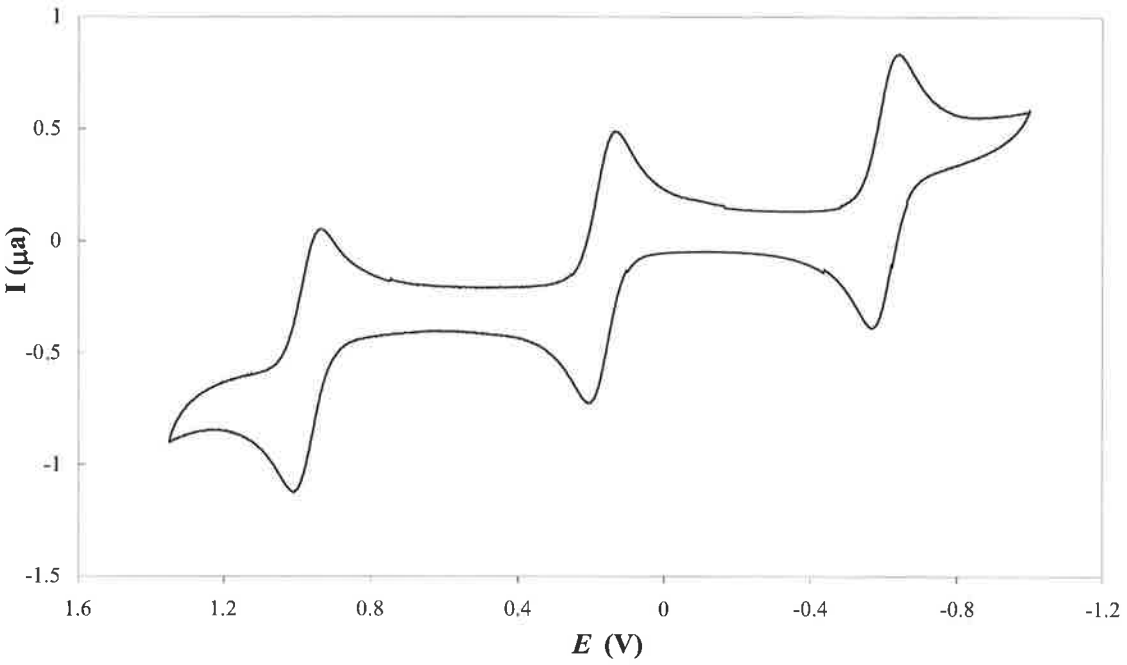

Figure 5.6: *Cyclic voltammogram of* ***65****, recorded in* CH_2Cl_2*, 0.1 M* $[Bu^n_4N][PF_6]$.

Inspection of the $E_{½}$ values confirms that strong interactions exist between ruthenium and iron centres in **65** and **66** across the C_4 ligand. Substitution of the TMS group in the iron diynyl **38** with Ru(dppe)Cp* to give complex **65**, renders the first oxidation 0.59 V more favourable. The electrochemical data suggests that the E_1 process in **65** and **66** is largely iron-centred, while E_2 is more ruthenium-centred. The latter process is 0.26 V more favourable than in the mononuclear ruthenium diynyl complex **39** and is now reversible. Assuming that there is no significant change in the solvation energies between these complexes, this stabilisation of the radical cation is evidence for electronic interaction along the all-carbon bridge and also reveals that even when oxidised, the Fe(III)(dppe)Cp* fragment is still more electron releasing than a TMS group.

Complex		E_1	E_2	E_3	E_4	Ref
5	{Fe(dppe)Cp*}$_2$(C≡CC≡C)	-0.67	+0.04	+0.95		[44]
25b	{Ru(dppe)Cp*}$_2$(C≡CC≡C)	-0.43	+0.22	+1.04	+1.54 [a]	this work
38	Fe(C≡CC≡CTMS)(dppe)Cp*	0.00				[149]
39	Ru(C≡CC≡CTMS)(dppe)Cp*	+0.44 [b]				this work
65	Cp*(dppe)Ru-C$_4$-Fe(dppe)Cp*	-0.59	+0.18	+0.99		this work
66	Cp*(dppe)Ru-C$_4$-Fe(dppp)Cp*	-0.58	+0.19	+0.99		this work

Table 5.2: *Electrochemical data for **65** and **66** and related complexes recorded under similar conditions.* [a] *partially reversible.* [b] *peak potential of an irreversible process.*

Comparisons of the redox potentials for **65** with those of **5** and **25b** show that oxidation of the iron centre is *ca* 0.1 V more difficult than in **5**. This suggests that replacement of one of the iron atoms by ruthenium has decreased the electron density at the iron centre, resulting in the increased oxidation potential. Similarly the second oxidation in **65** is 0.04 V more favourable than the corresponding oxidation in **25b**, further supporting the suggestion that the iron fragment is more electron-releasing than ruthenium.

In the case of the third wave, the oxidation potential for **65** is very close to the values found for **25b** and **5**. The potentials for these oxidations are far from the values obtained for the mononuclear derivatives and are possibly characteristic of the metal-metal interaction through the carbon bridge. The fourth oxidation process found in **25b** has not been observed in the iron complex **5**,[44] and could not be observed in either **65** or **66**.

5.3.5. Synthesis and Characterisation of [65]$^{n+}$ (n = 1, 2)

Considering the redox potentials, chemical oxidation of **65** was achieved by addition of a slight deficiency of $[FeCp_2][PF_6]$ to give the brown monocation **[65][PF$_6$]** (91%). Similarly, the reaction of **[65][PF$_6$]** with one equivalent of $[FeCp_2][PF_6]$ or the addition of two equivalents of the oxidising agent to **65** afforded the bright blue salt **[65][PF$_6$]$_2$** (98%). Both salts were purified by crystallisation, all manipulations being performed in the absence of air to prevent decomposition. A mixture of CH_2Cl_2/diethyl ether gave small black crystals of **[65][PF$_6$]**, while CH_2Cl_2/hexane gave large blue cubic crystals of **[65][PF$_6$]$_2$**.

Possible resonance formulations for the monocation **[65][PF$_6$]** are given in Scheme 5.12. Structures **5h-j** represent the monocation with dominant ruthenium radical character, while structures **5k-m** contain valence forms with dominant iron radical character.

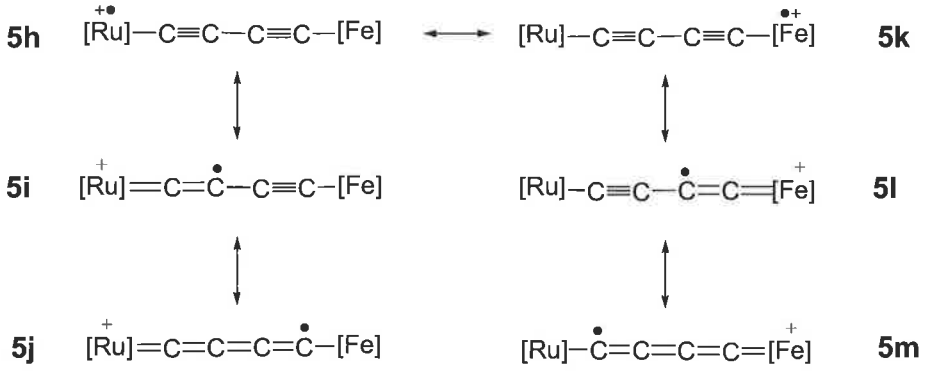

Scheme 5.12

In the case of the dication **[65][PF$_6$]$_2$** (Scheme 5.13), a singlet-triplet equilibrium exists as a consequence of the two unpaired electrons being spin-opposed (**5n**, singlet, S = 0) or spin-aligned (**5p**, triplet, S = 1). Structures **5n** and **5o** both contribute to the singlet state, the electron delocalisation assisting with its stabilisation.

In order to determine the major resonance contributors to the overall bonding in the cations **[65][PF$_6$]** and **[65][PF$_6$]$_2$**, a detailed spectroscopic investigation was

necessary. The use of IR, Mössbauer and ESR spectroscopies all provided details of the bonding within the cations. Furthermore, structural characterisation of the oxidised complexes further served to support these findings.

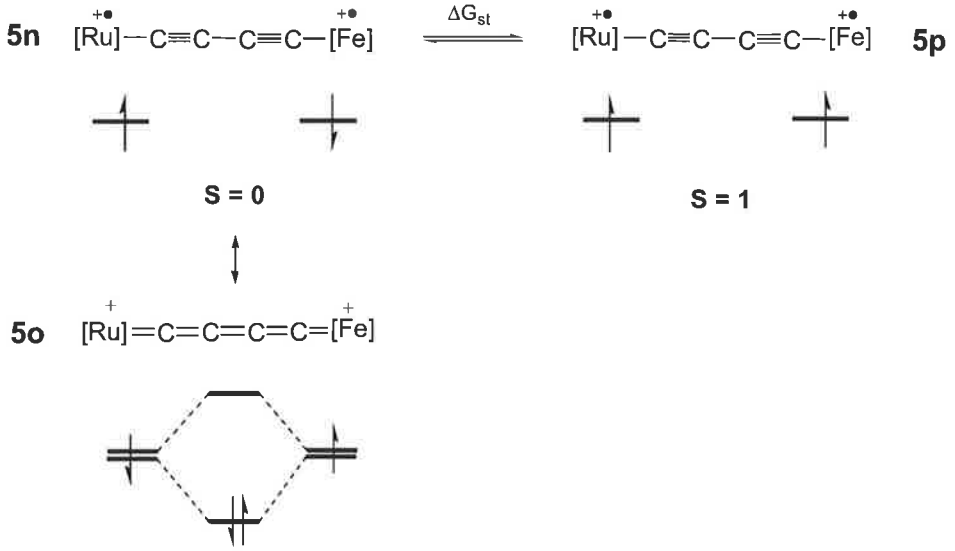

Scheme 5.13

5.3.6. IR Spectroscopy

IR spectra of $[\mathbf{65}]^{n+}$ (n = 0, 1, 2) were recorded in a range of different media and the data are summarised in Table 5.3. For simplicity, the discussion below refers to measurements made in KBr discs (Figure 5.7). In the neutral complex **65**, a weak band at 1960 cm^{-1} is fully consistent with the diyndiyl nature of the carbon chain. Upon oxidation, the monocation **[65]**[PF_6] revealed two ν(CC) bands, one of slightly higher (1986 cm^{-1}) and the other of slightly lower (1946 cm^{-1}) energy than in **65**. These relatively minor changes between **65** and **[65]**[PF_6] compared to the changes observed in the bis-ruthenium series between **25b** and **[25b]**[PF_6] (1973 vs. 1859 cm^{-1}) suggests that minimal structural rearrangement has occurred upon oxidation and the diyndiyl nature of the carbon chain in **[65]**[PF_6] is most likely retained. Therefore, IR data suggest that the resonance structures **5h** and **5k** seem to be the most likely contributors to the overall bonding in the monocation **[65]**[PF_6].

Upon removal of a second electron, far more drastic changes were observed. In **[65]**$[PF_6]_2$, two bands at 1879 and 1787 cm^{-1} are much closer to the value found in the pure cumulenic system **[25b]**$[PF_6]_2$ (1769 cm^{-1}) than for the diyndiyl complex **[5]**$[PF_6]_2$ (2160, 1950 cm^{-1}).[44] Therefore this data suggests that in the dication **[65]**$[PF_6]_2$, the diyndiyl nature of the carbon chain is no longer present and it is better described by the cumulenic form **5o**.

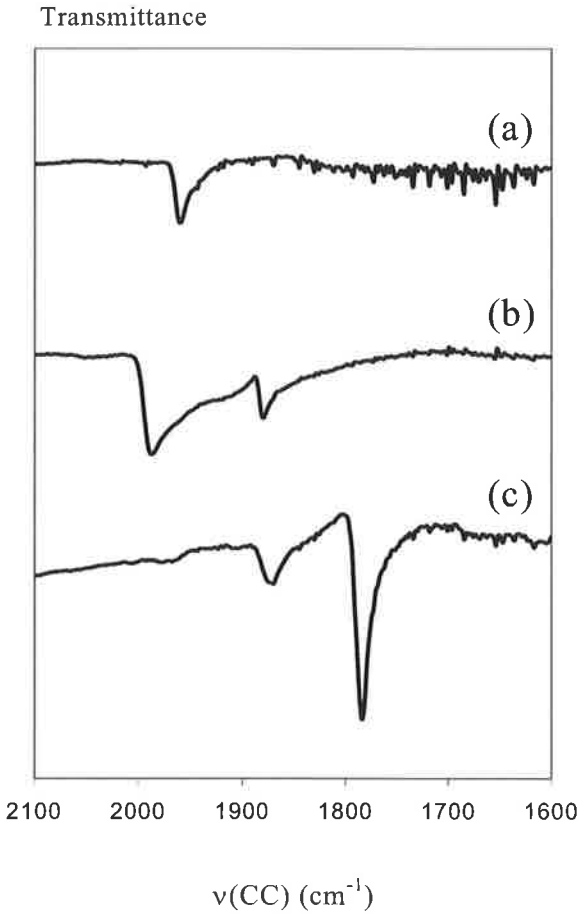

Figure 5.7: *IR spectra (20°C, KBr) for (a)* ***65****; (b)* ***[65][PF6]****; (c)* ***[65][PF6]2****.*

	KBr	**Nujol**	**CH_2Cl_2**
65	1960	1966	1966, 1951
[65]$[PF_6]$	1986, 1946	1986, 1877	1972, 1882
[65]$[PF_6]_2$	1879, 1787	1870, 1783	1850, 1785, 1711

Table 5.3: *IR ν(CC) bond stretching modes for* ***65*** *and its oxidised complexes (cm^{-1}).*

5.3.7. ^{57}Fe Mössbauer Spectroscopy

Invented by Rudolf Ludwig Mössbauer who received the 1961 Nobel Prize in Physics for his discovery, Mössbauer spectroscopy deals with transitions between energy levels within a given nucleus. These transitions (≤ 100 pm) result from the absorption of high-energy γ-radiation. Mössbauer spectroscopy is particularly useful for complexes containing iron, although many other transition elements including ruthenium (^{99}Ru and to a lesser extent ^{101}Ru) show a Mössbauer effect.[183] A brief explanation of Mössbauer spectroscopy is given below; in-depth explanations are available elsewhere.[183,184]

The first requirement of Mössbauer spectroscopy is a suitable source of γ-rays. In the case of iron, radioactive ^{57}Co is used as a source of iron nuclei in an excited energy state (^{57}Fe*), which rapidly decay with the emission of high-energy γ-rays (Figure 5.8). Radioactive ^{57}Co is used because the half-life for the ^{57}Co→^{57}Fe* transition ($t_{½}$) is 270 days, thus avoiding the continual replacement of the source.[184]

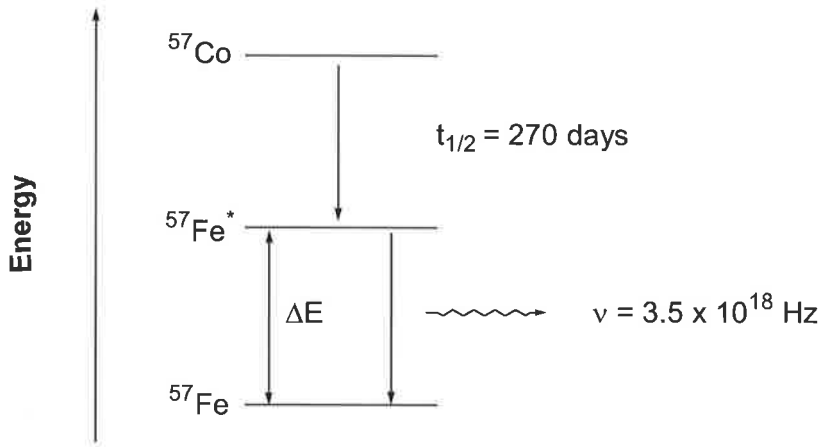

Figure 5.8: *Energy levels used in ^{57}Fe Mössbauer spectroscopy.*

The energy difference (ΔE) for the ^{57}Fe*→^{57}Fe transition is 2.3 x 10^{15} J. Using Planck's equation (Equation 5.1) gives an emission frequency of 3.5 x 10^{18} Hz.

$$\nu = \frac{\Delta E}{h} \qquad \textit{Equation 5.1}$$

If an iron nucleus, initially in its ground state, absorbs this γ-radiation, this would result in the Fe→Fe* transition. However, ΔE will differ for metallic iron present in the source and in the sample, which is in a different chemical state and as a result no absorption will occur. Therefore, in order for absorption of the high-energy radiation, the ability to scan through a series of frequencies is required.

Considering the width of the γ-ray emission, the half-life for the Fe*→Fe transition is $t_{½} = 1.5 \times 10^{-7}$ s. Substitution of this value into Equation 5.2 embodying the Heisenberg Uncertainty Principle gives the uncertainty in energy $\delta E \approx 10^{-27}$ J s.

$$\delta E \times \delta t \approx \frac{h}{2\pi} \approx 10^{-34} \text{ J s} \qquad \textit{Equation 5.2}$$

$$\delta E \approx \frac{10^{-34}}{10^{-7}} \approx 10^{-27} \text{ J s}$$

Using Equation 5.3, the uncertainty in the emission (δν) is approximately equal to 10^6 Hz. This value is small in comparison with the actual frequency ($\nu = 3.5 \times 10^{18}$ Hz). In fact, the relative line width (δν/ν) is approximately equal to 10^{-12} and is much smaller than those of other spectroscopic techniques (NMR 10^{-8}, IR 10^{-5}).[184]

$$\delta\nu = \frac{\delta E}{h} \approx \frac{1}{2\pi\delta t} \qquad \textit{Equation 5.3}$$

To enable a suitably wide range of frequencies to be scanned, the well-understood principle known as the Doppler shift is utilised. The frequency observed (or heard) from a moving body emitting radiation (or sound) by a stationary observer is shifted by an amount Δν, where

$$\Delta\nu = \frac{\nu\upsilon}{c} \text{ Hz} \qquad \textit{Equation 5.4}$$

Equation 5.4 describes the Doppler effect, where ν is the frequency of the emitted radiation, υ is the relative velocity of the source with respect to the observer and c is the speed of light. Using Equation 5.4, a shift of the source relative to the sample of 1 cm s^{-1} (10^{-2} m s^{-1}) will give a shift of ≈ 10^8 Hz. This is 100 times the line width

calculated using Equation 5.3 and gives a suitable range of frequencies to scan the sample.

In order to achieve this shift, a number of different methods are available, the simplest being to mount the source on a screw thread that when twisted will give a steady velocity either towards or away from the sample (Figure 5.9).

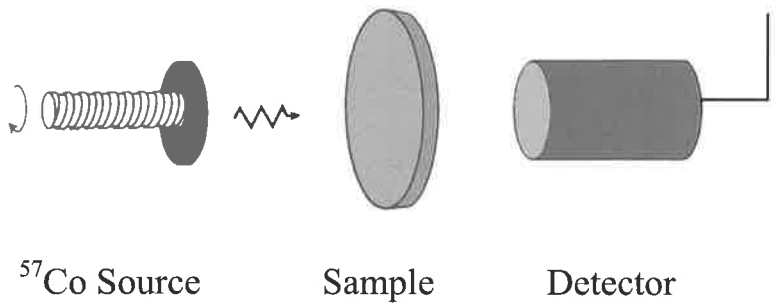

Figure 5.9: *Schematic illustration of an experimental arrangement suitable for Mössbauer spectroscopy.*[184]

Analysis of an iron Mössbauer spectrum reveals two key parameters. Firstly, the position of the absorption known as the isomeric shift (IS), reported in mm s^{-1}, is a measure of the difference in energy of the Fe→Fe* transition in a sample compared to that in the source. Secondly, the absorption is often split into a doublet due to separation of the energy levels within the excited Fe* nucleus. This splitting is the result of an internal nuclear quadrupole moment and is termed the quadrupole splitting (QS) and is also reported with the units of mm s^{-1}. The IS and QS are both influenced by the electron density at the iron nucleus and analyses of these parameters provide information concerning the oxidation state and bonding at the Mössbauer-active nucleus.[6,185]

In the Fe(R)(dppe)Cp* series, variations in IS and QS with the oxidation state and bond order have been established by studying a range of complexes with Fe(II) and Fe(III) centres bearing R groups that include σ-bound alkynyl or hydrocarbyl ligands, π-bound carbene, vinylidene or allenylidene type ligands.[185]

Generally, the IS varies with the R group and provides an indication of the electronic density at the iron centre, with values for Fe(CH_2OMe)(dppe)Cp* (IS = 0.13 mm s^{-1}) and Fe(C≡CH)(dppe)Cp* (IS = 0.27 mm s^{-1}) reflecting the effects of different electron donating abilities of the R ligands (i.e. C≡CH is greater than CH_2OMe).[185] The IS is also dependent on the oxidation state of the metal and in the iron-alkynyl series (i.e. R = alkynyl) as oxidation proceeds, values for the IS generally decrease.[6]

Figure 5.10 summarises the expected QS values in the Fe(R)(dppe)Cp* series.[185] Typically, the QS reflects the electron density at the iron nucleus and for Fe(II) complexes with Fe-C single bonds, the QS is usually close to 2.0 mm s^{-1}. In the case of the 17-electron Fe(III) cations bearing σ-bound ligands, the QS is always less than 1.0 mm s^{-1}. The third class of compounds are those with Fe=C double bonds. The QS for these Fe(II) derivatives are different from those described above, and are generally in the range of 1.0-1.4 mm s^{-1}.

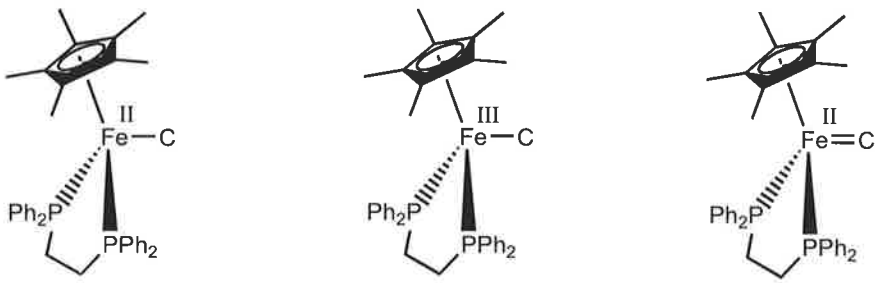

QS = 2.0 **QS = < 1.0** **QS = 1.0-1.4**

Figure 5.10: *Expected QS values (mm s^{-1}) in the Fe(R)(dppe)Cp* series.*

By comparing the IS and QS parameters measured for **[65]**$[PF_6]_n$ (n = 0, 1, 2) with others in the Fe(R)(dppe)Cp* series, information regarding the bonding of the R ligand to the iron nucleus can be gathered and conclusions regarding the nature of the bridging C_4 ligand can be made.

The zero-field ^{57}Fe Mössbauer spectra of the complexes [**65**][PF_6]$_n$ (n = 0, 1, 2) were recorded at 80 K. Each of these compounds shows the characteristic doublet pattern (Figure 5.11) and the corresponding fitting parameters are given in Table 5.4. The presence of a unique doublet in each of the spectra also confirms the purity of the samples.

In the case of the monocation [**65**][PF_6], the IS is significantly reduced relative to the neutral **65**, suggesting that electron density at the iron centre has been reduced upon oxidation. A similar reduction in the IS value is found for the dication [**65**][PF_6]$_2$, revealing the second oxidation process has contributed to a similar extent to the reduction of electron density centred at the iron.

	Temp (K)	IS (mm s^{-1})	QS (mm s^{-1})	Ref
5	80	0.27	2.07	[44]
[**5**][PF_6]	80	0.21	1.32	[44]
[**5**][PF_6]$_2$	80	0.18	1.05	[44]
63	80	0.255	1.983	[181]
[**63**][PF_6]	80	0.191	0.995	[181]
[**63**][PF_6]$_2$	80	0.138	0.957	[181]
65	80	0.252	2.006	this work
[**65**][PF_6]	80	0.211	1.147	this work
[**65**][PF_6]$_2$	80	0.155	1.118	this work
[**65**][PF_6]$_2$	293	0.177	1.069	this work
[**65**][PF_6]$_2$	4	0.151	1.113	this work
66	80	0.293	2.066	this work

Table 5.4: *^{57}Fe Mössbauer parameters for [**65**][PF_6]$_n$ (n = 0, 1, 2) and related compounds.*

In both **65** and **66**, the QS values are close to 2.0 mm s^{-1}, typical of Fe(II) centres with a Fe-C single bond, further supporting the diyndiyl nature of the C_4 ligands. Upon oxidation, the QS for [**65**][PF_6] (1.147 mm s^{-1}) lies within the range expected for a Fe(II) centre with a Fe=C double bond suggesting contributions from resonance structures **5l** and **5m**. However, this value is also between the values expected for valence-trapped structures **5h** (2.0 mm s^{-1}) and **5k** (<1.0 mm s^{-1}),

therefore contributions from these two forms cannot be ruled out. Assuming that the exchange between structure **5h** and **5k** is fast on the Mössbauer time scale (*ca* 10^{-8} s), an averaged value would be observed. This seems to be more a more plausible situation, complementing the IR data and suggesting the diyndiyl nature of the C_4 chain is retained with the unpaired electron delocalised between iron and ruthenium. As a consequence, the iron nucleus has an intermediate oxidation state between +2 and +3. This result is similar to that found for [**5**][PF_6], a typical Class III MV complex.[44] In this case, the two iron centres possess a formal Fe(2.5) oxidation state with the QS close to the average of the values found in the related neutral and dicationic species (Table 5.4).

The spin state of the dication [**65**][PF_6]$_2$ can exist in an equilibrium between two spin isomers, a triplet state with a diyndiyl structure and a singlet state in which the carbon chain adopts a cumulene structure (Scheme 5.12). The QS value measured at 80 K for [**65**][PF_6]$_2$ (1.118 mm s^{-1}) is inside the range expected for a Fe(II) centre with a Fe=C double bond. This suggests that at 80 K, strong contributions are made from the singlet cumulene state (Structure **5o**). Furthermore, variable temperature experiments revealed that when the temperature was raised to 298 K the value of QS decreased, closer to the value expected for a Fe(III)-C single bond, suggesting increased contributions from the triplet state **5p**. Upon cooling to 4 K, the QS was found to remain unchanged relative to the measurement made at 80 K, suggesting that at 80 K and certainly at 4 K, [**65**][PF_6]$_2$ exists purely in the singlet state.

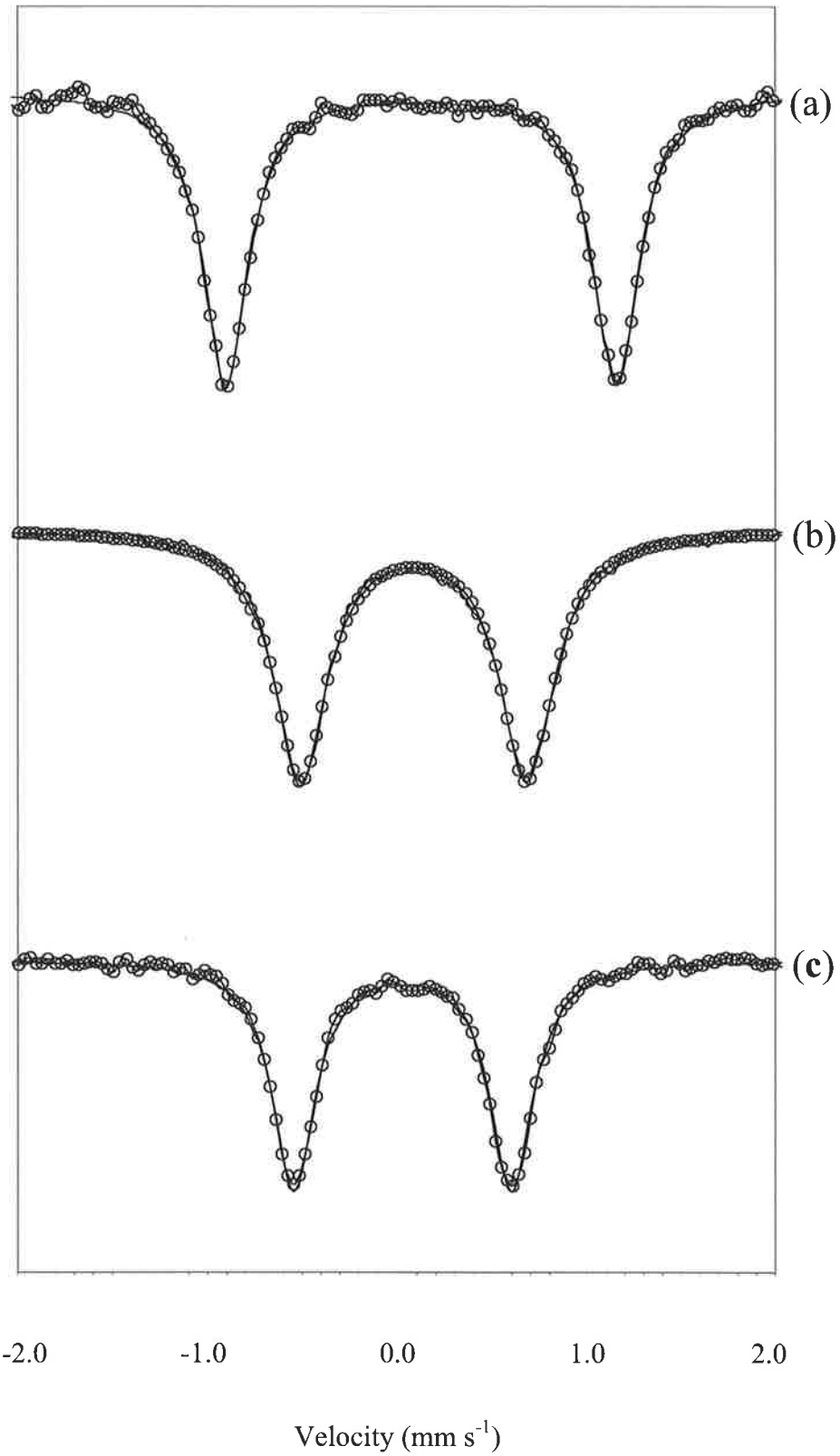

Figure 5.11: *^{57}Fe Mössbauer spectra (80 K) for **[65]**$[PF_6]_n$ (a) n = 0; (b) n = 1; (c) n = 2.*

5.3.8. ESR Spectroscopy

The X-band ESR spectrum of **[65]**[PF_6] recorded at 80 K in a CH_2Cl_2/$ClCH_2CH_2Cl$ (1:1 v/v) glass is shown in Figure 5.12. The spectrum resembles that of related Ru/Fe(III) piano-stool complexes, displaying three features corresponding to the three components of the *g*-tensor as expected for d^5 low-spin Ru/Fe(III) complexes in a pseudo-octahedral geometry.[120] The values for *g* are collected in Table 5.5, together with those of some related complexes.

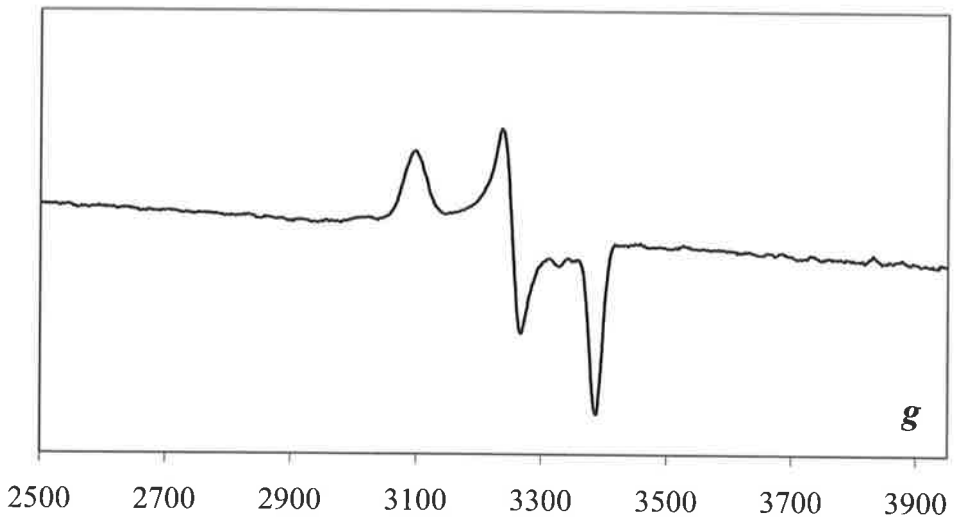

Figure 5.12: *ESR spectrum of [65][PF_6] recorded in CH_2Cl_2/$ClCH_2CH_2Cl$ at 80 K.*

In an homogeneous series of MV compounds, the anisotropy of the ESR signal ($\Delta g = g_1 - g_3$) decreases as the rate of the intramolecular electron transfer increases.[186-188] This has been demonstrated in a series of dinuclear iron complexes featuring the electron-rich fragment Fe(dppe)Cp*. The anisotropy of the signal in the Class II complex [{Cp*(dppe)Fe}(C≡C-1,3-C_6H_4-C≡C){Fe(dppe)Cp*}][PF_6] (Δg = 0.530)[189] is much larger than in the borderline Class II/III MV complex [{Cp*(dppe)Fe}(C≡C-1,4-C_6H_4-C≡C){Fe(dppe)Cp*}][PF_6] (Δg = 0.168).[190] The anisotropy of the signal is further reduced in the highly delocalised Class III complex **[5]**[PF_6] (Δg = 0.060).[44] Therefore, by comparing Δg values, the relative rates of electron transfer between redox sites in related complexes can be estimated. For **[65]**[PF_6], Δg = 0.187 and is quite low compared with other Class II complexes **[63]**[PF_6] (0.315) and **[64]**[PF_6] (0.361). This suggests that the rate of electron

transfer in **[65]**[PF_6] is faster, relative to **[63]**[PF_6] and **[64]**[PF_6]. This result is in agreement with the values of the electronic coupling (V_{ab}) found for these compounds (Section 5.3.11).

Complex	n	g_1	g_2	g_3	Δg [a]	g_{iso} [b]	Ref
[5]$^{n+}$	1	2.139	2.089	2.079	0.060	2.102	[44]
	2	ESR silent					[44]
[25b]$^{n+}$	1	2.2284	2.0697	1.9910	0.232	2.096	this work
	2	ESR silent					this work
[63]$^{n+}$	1	2.2356	2.0075	1.9202	0.315	2.054	[181]
	2	2.04	2.10	2.15			[181]
[64]$^{n+}$	1	2.3474	2.0214	1.9867	0.361	2.123	[147]
[65]$^{n+}$	1	2.1865	2.0820	1.9995	0.187	2.089	this work
	2	ESR silent					this work

Table 5.5: *ESR parameters [80 K, $CH_2Cl_2/C_2H_4Cl_2$ (1:1) glass] for [**65**][PF_6] and related complexes.* [a] $\Delta g = g_1 - g_3$. [b] $g_{iso} = (g_1+g_2+g_3)/3$.

The X-band ESR spectrum of the dication **[65]**[PF_6]$_2$ was also recorded at various temperatures in the range 4-298 K in a $CH_2Cl_2/ClCH_2CH_2Cl$ (1:1 v/v) glass as well as using powdered samples. However, in no case could the $\Delta m_s = 2$ transition, characteristic of the triplet state be observed, as in the related iron-rhenium dication **[63]**[PF_6]$_2$.[181] Although the dication is ESR silent at room temperature, at which Mössbauer data suggests that there should be some detectable contribution from the triplet state, this may be due to spin-spin relaxation, a process that allows for efficient relaxation giving very broad signals that cannot be distinguished from the base line.[184]

Magnetic susceptibility measurements were also carried out with crystalline samples of **[65]**[PF_6]$_2$ between 2 and 300 K. However, traces of paramagnetic impurities formed during crystallisation precluded determination of the singlet-triplet energy gap by the variation of the magnetic susceptibility with temperature.[191]

5.3.9. Paramagnetic NMR Study of [65][PF$_6$]$_2$

The strong antiferromagnetic interactions in **[65]**[PF$_6$]$_2$ that prevent the observation of an ESR signal, enabled the observation of well resolved NMR spectra. The ^{31}P NMR spectrum of **[65]**[PF$_6$]$_2$ contained two broadened resonances at δ -51.2 and 289.8, together with a characteristic septet due to the PF$_6^-$ anion (Figure 5.13). The half-height line widths of these two resonances were measured to be 82 and 214 times that of the PF$_6^-$ anion, respectively. Assuming the line broadening follows the same trend observed with other ^{1}H and ^{13}C NMR resonances, the signal at δ -51.2 was tentatively assigned to the dppe ligand bound to the ruthenium, whereas the broader signal at δ 289.8 was assigned to the dppe ligand coordinated to iron.

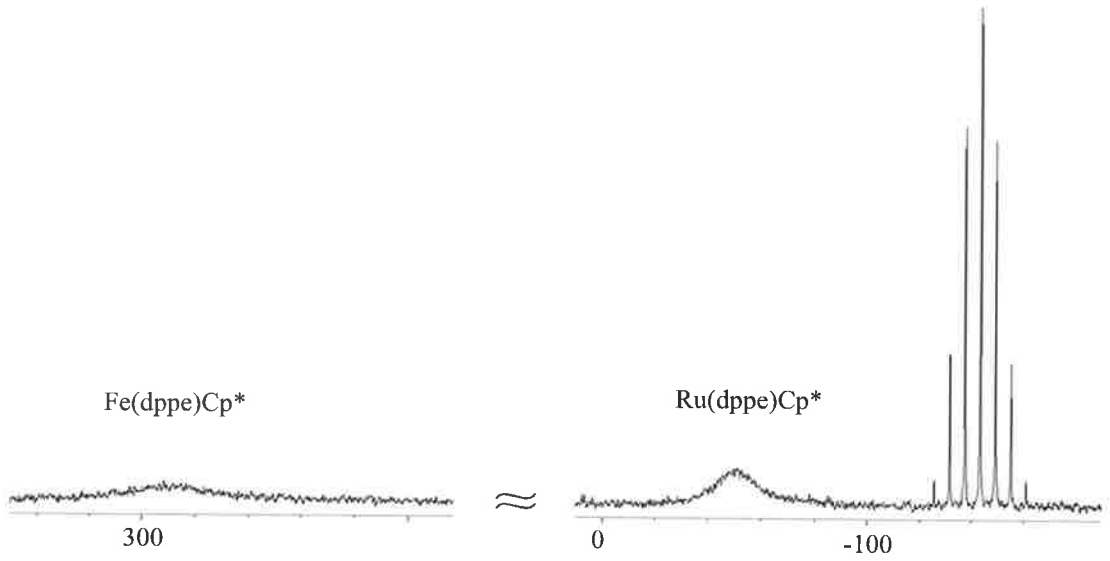

Figure 5.13: *^{31}P NMR spectrum of [65][PF$_6$]$_2$ recorded at -80°C in acetone-d_6 (ppm).*

The ^{1}H NMR spectrum of **[65]**[PF$_6$]$_2$ recorded in acetone-d_6 is shown in Figure 5.14. The most upfield resonance in the spectrum at δ -3.83 was assigned to the methyl protons of the Cp* bound to iron, while the corresponding resonance for the ruthenium-bound Cp* ligand was observed downfield at δ 5.46. Four broadened resonances between δ -0.22 and 4.26 were assigned to the methylene protons of the two dppe ligands. The aromatic protons were significantly spread, with the majority found in the region δ 6.80-9.40, while the upfield resonance at δ 2.88 was assigned to the *ortho* protons of the iron-bound dppe ligand based on comparisons with related Fe(III)(dppe)Cp* complexes. The upfield position of this resonance was due to the close proximity of the *ortho* protons to the paramagnetic Fe(III) centre.[192]

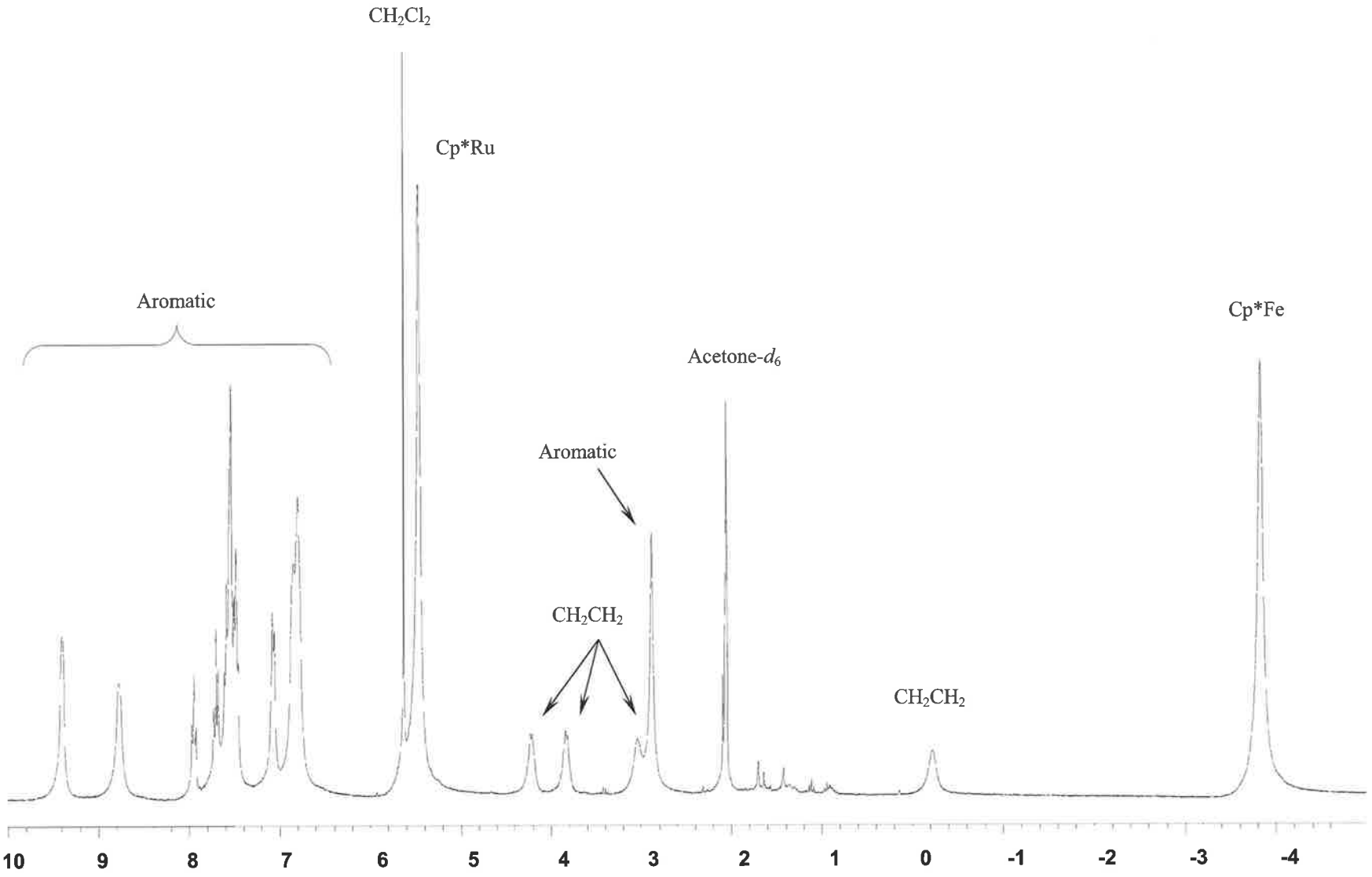

Figure 5.14: *^{1}H NMR spectrum (298 K) of **[65]**$[PF_6]_2$ recorded in acetone-d_6 (ppm), 300 MHz.*

In the situation where singlet and triplet states rapidly interconvert on the NMR time scale, the observed chemical shift results from a combination of both the singlet (δ_S) and triplet states (δ_T) as defined by Equation 5.5 where α and (1-α) represent the molar fractions of the triplet and singlet states, respectively. The variation of α with absolute temperature can be described using the modified Boltzmann thermal population law (Equation 5.6), where ΔG_{ST} represents the singlet-triplet energy gap, *k* is the Boltzmann constant and T is the temperature in Kelvins. Similar analyses have successfully allowed determinations of the singlet-triplet energy gap in related systems.[122,193]

$$\delta_{obs} = \alpha\delta_T + (1-\alpha)\delta_S \qquad \textit{Equation 5.5}$$

$$\alpha = \frac{3}{3 + \exp^{-\Delta G_{ST}/kT}} \qquad \textit{Equation 5.6}$$

The resonance contribution from the singlet-state (δ_S) will largely be independent of temperature, however δ_T should obey the Curie Law and can be approximated by Equation 5.7.

$$\delta_T = \frac{\delta_{293} \times 293}{T} \qquad \textit{Equation 5.7}$$

The presence of the unpaired electron in the 17-electron [Fe(Me)(dppe)Cp*][PF_6] and [Fe(CH_2OMe)(dppe)Cp*][PF_6] complexes significantly influences the chemical shifts of the Cp* ligands in the ^{1}H NMR spectra.[192] For this reason, the chemical shifts of the Cp* ligands at the iron (δ_{Cp^*Fe}) and ruthenium (δ_{Cp^*Ru}) centres in [**65**][PF_6]$_2$ were measured over a variable temperature range of 288-218 K (Figure 5.15).

The spectra show that δ_{Cp^*Fe} increased from δ -3.63 to -1.25 as the temperature decreased, whereas the signal for δ_{Cp^*Ru} decreased from δ 5.46 to 3.69. These shifts at lower temperatures towards the regions expected for a purely diamagnetic complex (i.e. **5** and **25b**) suggest a singlet ground state in [**65**][PF_6]$_2$. The same experiment carried out with a solution of the bis-ruthenium complex [**25b**][PF_6]$_2$ showed a downfield shielding of the Cp* resonance from δ 1.93 to 1.52, while a variable temperature ^{31}P NMR experiment showed a broadened ^{31}P signal that moved from δ 117.8 to 77.7. Using Equations 5.5-5.7, a value for the singlet-triplet

energy gap was obtained from each of the measured resonances in **[25b]**$[PF_6]_2$ and **[65]**$[PF_6]_2$. Starting at the expected value for a purely diamagnetic complex (δ_S), the three parameters δ_S, δ_T and ΔG_{ST} were varied to yield the closest fit to the experimentally measured behaviour. The plots are shown in Figure 5.16 with the observed frequencies represented by the blue line, while the red lines show the theoretical curves. In the case of the mixed ruthenium-iron complex **[65]**$[PF_6]_2$, the fit of both Ru- and Fe-bound Cp* ligands gave the same value (ΔG_{ST} = -718 cm^{-1}).

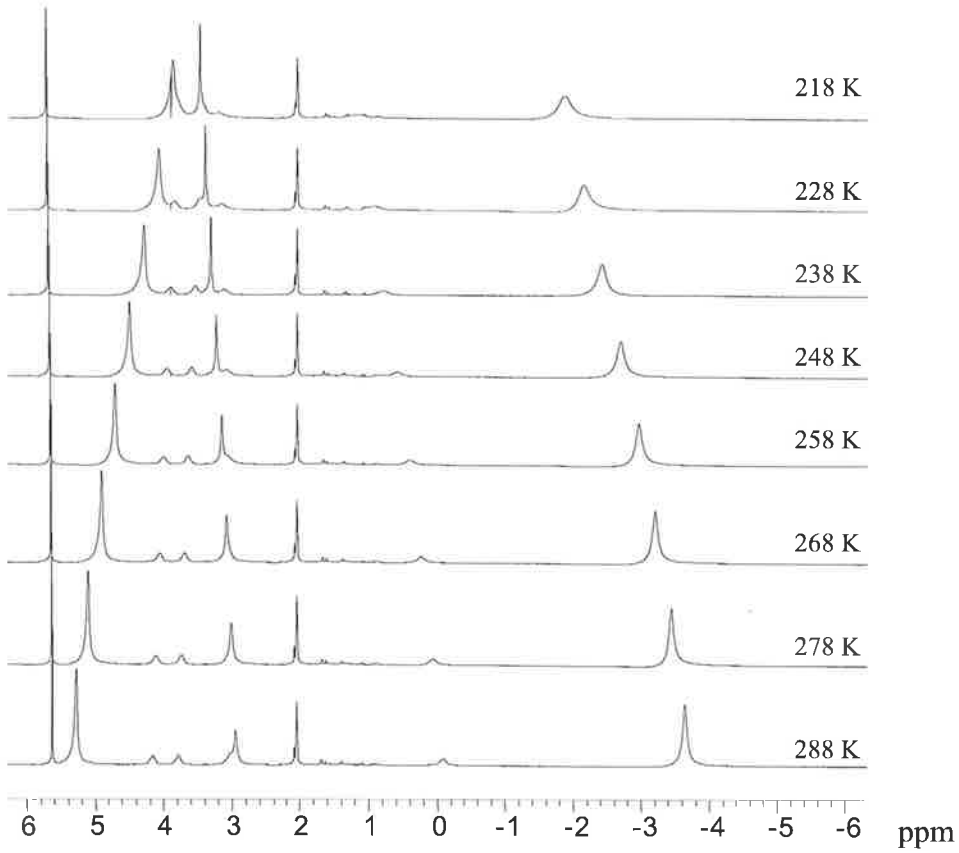

Figure 5.15: *Variable temperature ^1H NMR spectra of [65]$[PF_6]_2$, recorded in acetone-d_6.*

For **[25b]**$[PF_6]_2$, using the same analysis, the fits of the ^1H and ^{31}P chemical shifts vs. 1000/T gave the singlet-triplet energy gap (ΔG_{ST} = -980 cm^{-1}). The negative signs for **[65]**$[PF_6]_2$ and **[25b]**$[PF_6]_2$ confirm that both have singlet ground states, as previously found for the bis-iron dication **[5]**$[PF_6]_2$. However, in **[5]**$[PF_6]_2$, the triplet state lies only 18 cm^{-1} above the singlet state. Therefore, substitution of Ru for one Fe has increased the gap by 700 cm^{-1}, while substitution of Ru atoms for both irons atoms has increased the gap by *ca* 960 cm^{-1}. These results emphasize the ability of ruthenium to stabilise the singlet versus the triplet state.

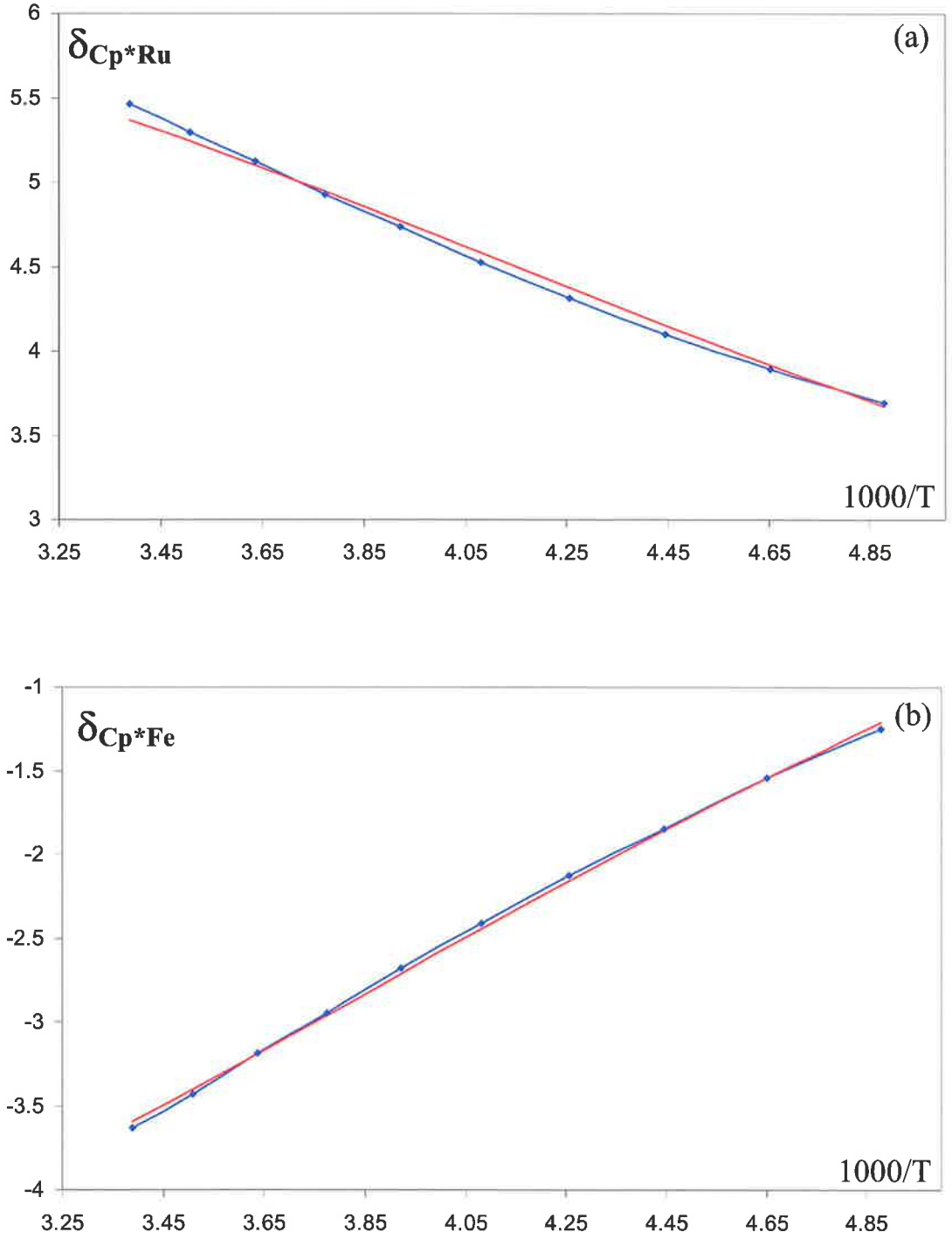

Figure 5.16: *Plots of the temperature dependence of* ***[65]*** *$[PF_6]_2$ for the Cp*Ru (a) and Cp*Fe (b) bound ligands. Blue lines indicate observed values, while red lines are theoretical curves calculated from Equations 5.5-5.7.*

5.3.10. Molecular Structures of Oxidised Complexes

In an effort to probe further the nature of the bridging C_4 ligand in the oxidised species, X-ray crystal structures of [**65**][PF_6] and [**65**][PF_6]$_2$ were obtained. The cations [**65**]$^{n+}$ (n = 1, 2) were completely disordered, rendering the metal centres indistinguishable, as found in **65** and **66**. As a result, only average values for the M-P and M-C distances were found (Figure 5.18, Table 5.6). Nevertheless, as oxidation proceeds, the average values for the M-P separations increase from 2.200(1) Å for n = 0 to 2.252(6) and 2.296(9) Å for n = 1 and 2, respectively, reflecting the decrease in M-P back-bonding. Corresponding values for the M-C(1,4) bonds are 1.948(4), 1.886(2) and 1.83(1) Å. The C≡C triple bonds lengthen from 1.23 to 1.24 and 1.26 Å, while the central C(2)-C(3) bonds shorten from 1.374(6) to 1.349(3) and finally to 1.325(5) Å in the dication. All of these values are consistent with increased contributions from the cumulene resonance form **5o** as oxidation proceeds. In the crystal structure of the neutral complex **65** (Figure 5.4), the RuC_4Fe linkage is essentially linear with angles at individual carbons being in the range 174.8-178.1(7)°. The total bending (Σ) in the carbon chain is 11.1° for **65** with the chain adopting a *transoid* conformation. Upon oxidation, deformation of the chain occurs, with Σ = 32.8 and 34.7° for n = 1 and 2, respectively.

In an effort to overcome the disorder between the two metal centres, significant structural changes were required. Related research in the Bruce group by M. E. Smith involved the synthesis of {$Cp(PPh_3)_2Ru$}(C≡CC≡C){Fe(dppe)Cp*} (**67**).[145] Confirmation of the diyndiyl nature of the C_4 chain in **67** was obtained by the solid-state structure, with Ru-C(1) and Fe-C(4) distances of 2.019 and 1.898(5) Å, respectively.[145] These values are typical for M-C(*sp*) single bonds, reflecting the difference in atomic radii (Fe = 1.26, Ru = 1.34 Å),[153] and similar to those found in the symmetric derivatives M-C 1.889, 1.885(3) (Fe),[182] 2.001(1) (Ru)[98]. While the mono- and dications of **67** were isolated,[145] crystals suitable for X-ray structure determinations were not obtained. As part of this work, crystallisation of the oxidised species [**67**][PF_6] and [**67**][PF_6]$_2$ afforded large crystals by layering CH_2Cl_2 solutions of the salts with hexane in the absence of air (Figure 5.18, Table 5.7). In this case, substitution of Cp for Cp* and the bidentate phosphine dppe or dppp with $(PPh_3)_2$ enabled the two metal atoms to be distinguished.

The unit cell in the structure of the supposed dication [**67**][PF_6]$_2$, was found to contain three PF_6^- anions and two cations, attributed to the presence of disordered mono- and dications. This was confirmed when the IR spectrum of a single crystal was measured in a CH_2Cl_2 solution (Figure 5.17). The large band at 1973 cm^{-1} is characteristic of the monocation [**67**][PF_6] and disappeared after the addition of a small quantity of [$FeCp_2$][PF_6], confirming the presence of both the mono- and dications in the lattice. Therefore, bond distances for the dication were calculated by extrapolating from the data found for [**67**][PF_6] and [**67**]$_2$[PF_6]$_3$ (Table 5.7).

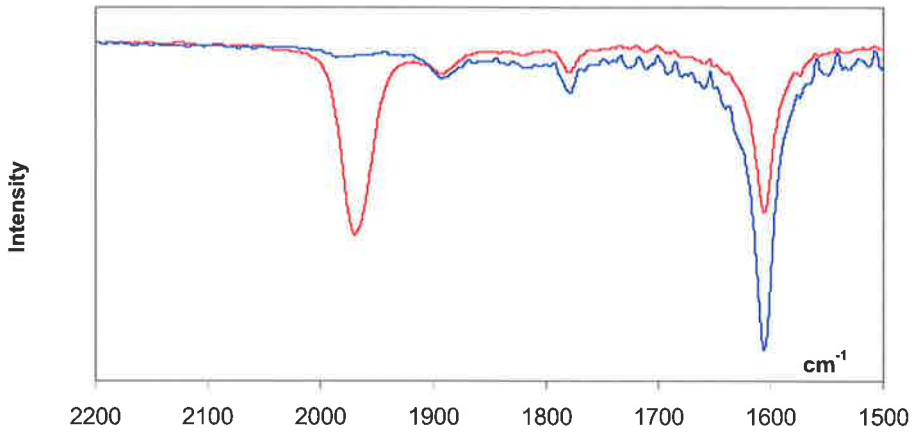

Figure 5.17: *IR solution spectra (CH_2Cl_2) of a single crystal of the supposed dication [**67**][PF_6]$_2$ (red line) and after the addition of [$FeCp_2$][PF_6] (blue line).*

In the monocation [**67**][PF_6], shortening of the M-C bonds relative to **67** to 1.953(5) (Ru) and 1.830(5) Å (Fe) occurred, while in the dication, these values were calculated to be 1.873 and 1.776(6) Å, respectively. Both are consistent with a considerable increase in bond order resulting from the oxidation. For the C(1)-C(2) and C(3)-C(4) separations, lengthening to 1.240(8) and 1.242(9) Å (in the monocation) and 1.244(8) and 1.280(9) Å (in the dication) was found, while the C(2)-C(3) bonds shorten to 1.362(7) and 1.314(8) Å, respectively. The somewhat longer C≡C and shorter C-C bonds can be rationalised by contributions of the cumulenic tautomer **5o**. In general, all these results are consistent with changes in the electronic structure of the M-C_4-M bridge occurring upon oxidation, which result in less electron density at the metal centres (with less back-bonding to phosphorus) and increases in the M-C and central C-C bond orders with concomitant decreases in the C≡C triple bond orders.

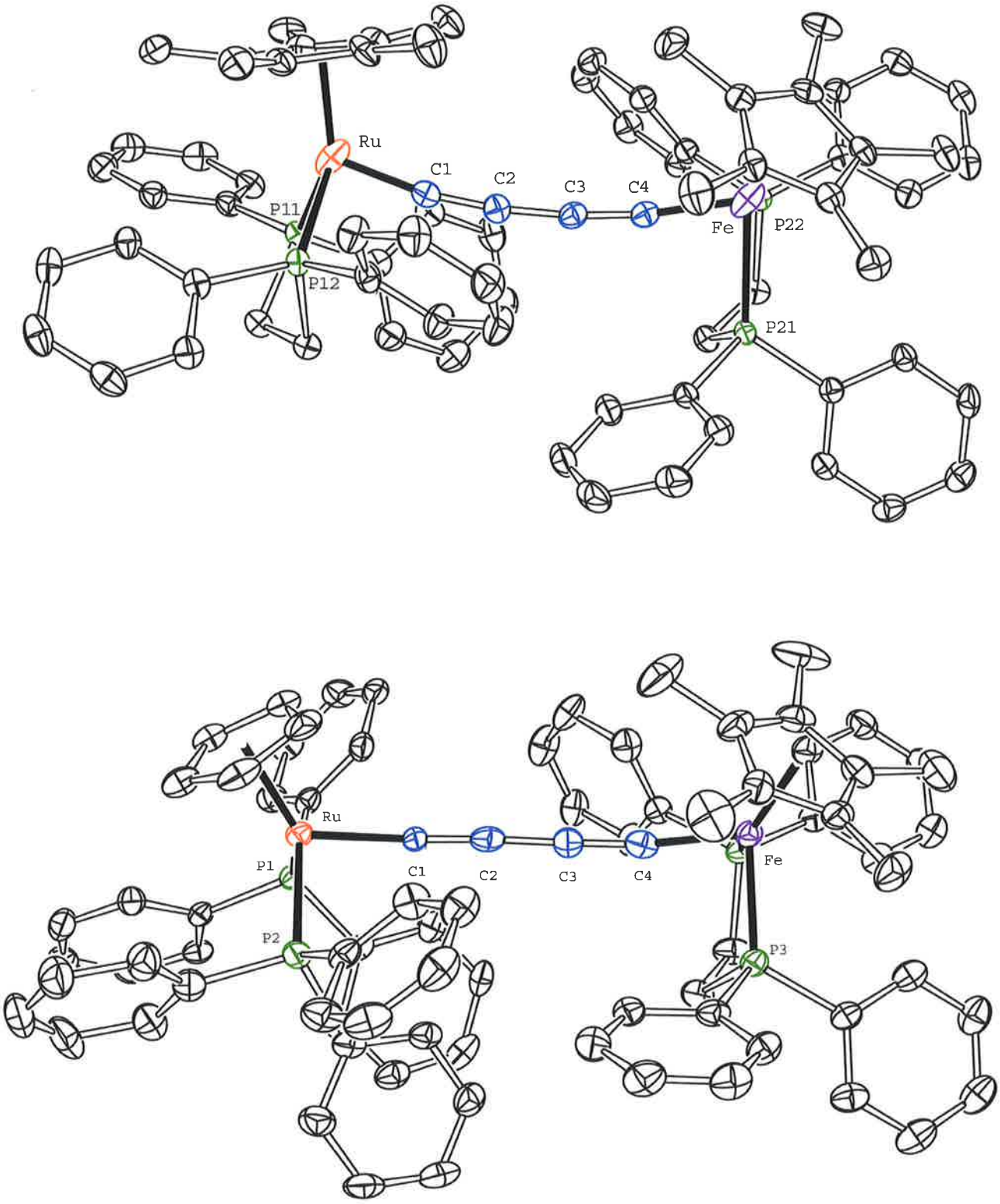

Figure 5.18: *ORTEP views of the cations* $[\mathbf{65}]^{2+}$ *(top) and* $[\mathbf{67}]^{+}$ *(bottom).*

	65	[**65**][PF_6] [a]	[**65**][PF_6]$_2$
Bond lengths (Å)			
M(1)-P(11)	2.190(1)	2.2360(6)	2.303(9)
M(1)-P(12)	2.201(1)	2.2680(6)	2.334(9)
M(2)-P(21)	2.215(1)		2.276(9)
M(2)-P(22)	2.197(1)		2.270(9)
M(1)-C(Cp*)	2.141-2.201(4)	2.172-2.227(2)	2.081-2.235(7)
(av.)	2.179(4)	2.200(2)	2.224(11)
M(2)-C(Cp*)	2.155-2.214(4)		2.090-2.305(10)
(av.)	2.192(4)		2.293(9)
M(1)-C(1)	1.939(4)	1.886(2)	1.845(9)
C(1)-C(2)	1.223(6)	1.240(3)	1.261(5)
C(2)-C(3)	1.374(6)	1.349(3)	1.325(5)
C(3)-C(4)	1.233(6)		1.260(5)
C(4)-M(2)	1.957(4)		1.820(10)
Bond angles (°)			
P(11)-M(1)-P(12)	83.05(4)	83.21(2)	82.4(3)
P(11)-M(1)-C(1)	85.1(1)	84.11(7)	82.0(3)
P(12)-M(1)-C(1)	82.3(1)	93.66(7)	94.1(4)
P(21)-M(2)-P(22)	84.04(4)		84.3(3)
P(21)-M(2)-C(4)	81.6(1)		89.3(4)
P(22)-M(2)-C(4)	82.5(1)		86.2(4)
M(1)-C(1)-C(2)	177.3(4)	166.1(2)	168.0(5)
C(1)-C(2)-C(3)	176.6(4)	177.5(3)	174.0(4)
C(2)-C(3)-C(4)	177.7(4)		173.3(4)
C(3)-C(4)-M(2)	177.3(4)		170.0(4)
Σ (total bend)	11.1	32.8	34.7

Table 5.6: *Selected structural data for [**65**][PF_6]$_n$ (n = 0, 1, 2).* [a] *centrosymmetric structure.*

	67	[**67**][PF_6] [a]	[**67**]$_2$[PF_6]$_3$ [a]	[**67**][PF_6]$_2$ [a,b]
Bond lengths				
Ru-P(1)	2.289(2)	2.304(1)	2.321(1)	2.338(1)
Ru-P(2)	2.288(2)	2.295(1)	2.324(1)	2.353(1)
Fe-P(3)	2.168(2)	2.209(1)	2.219(2)	2.229(2)
Fe-P(4)	2.175(2)	2.228(2)	2.221(2)	2.214(2)
Ru-C(Cp)	2.224-2.254(7)	2.231-2.263(6)	2.246-2.271(6)	
(av.)	2.24(3)	2.264(6)	2.251(5)	
Fe-C(Cp*)	2.100-2.144(5)	2.130-2.159(5)	2.121-2.171(6)	
(av.)	2.12(3)	2.140(6)	2.142(6)	
Ru-C(1)	2.019(5)	1.953(5)	1.913(6)	1.873(6)
C(1)-C(2)	1.226(7)	1.240(8)	1.242(8)	1.244(8)
C(2)-C(3)	1.392(7)	1.362(7)	1.338(8)	1.314(8)
C(3)-C(4)	1.238(7)	1.242(8)	1.261(9)	1.280(9)
C(4)-Fe	1.898(5)	1.830(5)	1.803(6)	1.776(6)
Bond angles (°)				
P(11)-Ru-P(12)	101.49(6)	99.82(5)	98.40(5)	
P(11)-Ru-C(1)	87.6(2)	88.1(2)	90.8(2)	
P(12)-Ru-C(1)	85.5(2)	91.3(1)	91.8(1)	
P(21)-Fe-P(22)	85.77(7)	85.12(5)	84.17(6)	
P(21)-Fe-C(4)	84.1(2)	86.8(2)	87.3(2)	
P(22)-Fe-C(4)	84.6(2)	87.0(2)	86.6(2)	
Ru-C(1)-C(2)	187.3(5)	175.9(5)	173.7(5)	
C(1)-C(2)-C(3)	177.4(7)	176.1(5)	176.4(5)	
C(2)-C(3)-C(4)	177.3(6)	177.4(6)	178.8(5)	
C(3)-C(4)-Fe	179.4(5)	172.7(5)	176.2(4)	
Σ (total bend)	7.6	17.9	14.9	11.9

Table 5.7: *Selected structural data for [**67**][PF_6]$_n$ (n = 0, 1, 2).* [a] *This work.* [b] *Values calculated by extrapolation from [**67**][PF_6] and [**67**]$_2$[PF_6]$_3$ structural data.

5.3.11. UV/Vis/NIR Spectroscopy

The UV/Vis spectrum of **65** shows high-energy bands at 232 and 268 nm in CH_2Cl_2 at 20°C (Figure 5.19, Table 5.8), assigned to intraligand (IL) transitions (Cp* and dppe). The low-energy absorption of **65** is tentatively assigned to a combination of dπFe→π*(C≡C) and dπRu→π*(C≡C) metal-to-ligand charge transfer (MLCT) transitions after comparison with the electronic absorption spectra of the iron and ruthenium related precursors, Fe(C≡CPh)(dppe)Cp* (**68**)[194] and diynyls **38** and **39,** which show low-energy absorptions at 348, 371, and 345 nm, respectively,

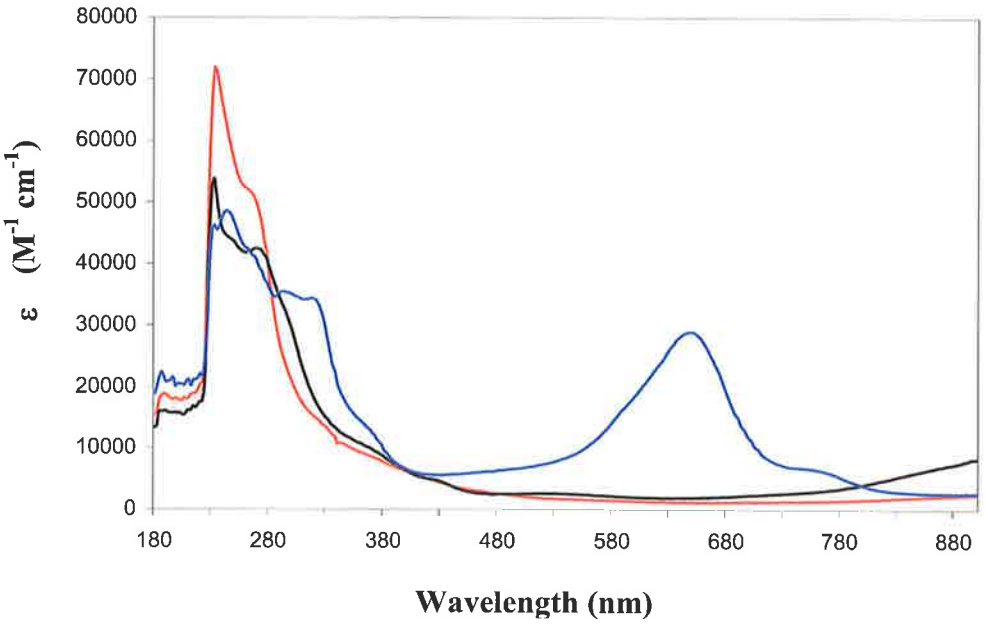

Figure 5.19: *UV/Vis spectra of* ***65*** *(—), [**65**][PF_6] (—) and [**65**][PF_6]$_2$ (—) in CH_2Cl_2 at 20°C.*

The intense bands observed at 232-268 nm in **65** are shifted slightly (6 nm) in the radical-cation [**65**][PF_6] and are less intense, with the appearance of a shoulder at 326 nm. It is likely that upon oxidation of Fe(II) to Fe(III), the band due to the dπFe→π*(C≡C) transition would vanish leaving the band due to dπRu→π*(C≡C). A similar loss of the dπFe→π*(C≡C) band has been reported upon oxidation of the related compound **68** to [**68**][PF_6].[194] In addition, the radical cation [**65**][PF_6] exhibits a low-energy absorption at *ca* 1028 nm with a shoulder at *ca* 750 nm. These absorption bands are assigned to ligand-to-metal charge transfer (LMCT) bands derived from the Fe(C≡CC≡C)(dppe)Cp* moiety. Similar LMCT absorption bands have also been observed in the related complexes [**5**][PF_6] (619 and 845

nm),[194] [**63**][PF_6] (829 nm),[147] [**64**][PF_6] (868 nm)[181] and in [**25b**][PF_6] (714 and 816 nm).

Intense red-shifted bands at *ca* 295, 322, and 370 nm were observed in the spectrum of the dication [**65**][PF_6]$_2$. Considering the energies of these bands, they can be assigned to a mixture of dπFe→π*(C≡C) and dπRu→π*(C≡C) MLCT transitions. In addition, the spectrum of [**65**][PF_6]$_2$ shows two low-energy absorption bands at 650 and 760 nm. Similar transitions have been observed in the complexes [**5**][PF_6]$_2$ (621, 828 nm),[44] [**4**][PF_6]$_2$ (348 and 454 nm) and in [**25b**][PF_6]$_2$ (465 and 580 nm).[45] These transitions are assigned to LMCT transitions derived from the Fe(C≡CC≡C)(dppe)Cp* and Ru(C≡CC≡C)(dppe)Cp* moieties.

	ν_{max} (nm)	ν_{max} (cm^{-1})	ε (M^{-1} cm^{-1})
65	232	43,100	72,000
	266	37,590	51,000
[**65**][PF_6]	232	43,100	54,000
	272	36,765	42,000
	360	27,780	10,600
	850	11,765	4,300
	1028	9,730	18,000
[**65**][PF_6]$_2$	246	40,650	48,000
	268	37,310	41,000
	295	33,900	35,000
	322	31,055	34,000
	370	27,030	13,000
	650	15,385	29,000
	760	13,160	6,500

Table 5.8: *UV/Vis/NIR spectral data for [65]$^{n+}$ (n = 0, 1, 2) in CH_2Cl_2, 300-3000 nm.*

The Vis/NIR absorption spectra of the cations are shown in Figure 5.20, together with an expansion of the region between 1100-2000 nm. The trace of the monocation shows a shoulder on the band centred at 1028 nm. This lower-energy

band was assigned to the Ru(II)→Fe(III) IVCT. As the insert shows, this feature is absent in the spectrum of the dication [**65**][PF_6]$_2$. Assuming that the absorption bands have Gaussian profiles, the NIR spectrum was deconvoluted. The band shape analysis of the NIR spectra of [**65**][PF_6] revealed the following key parameters for the IVCT band: ν_{max} = 7310 cm^{-1} (1368 nm); ε = 980 M^{-1} cm^{-1}; $\Delta\nu_{½}$ = 2120 cm^{-1}.

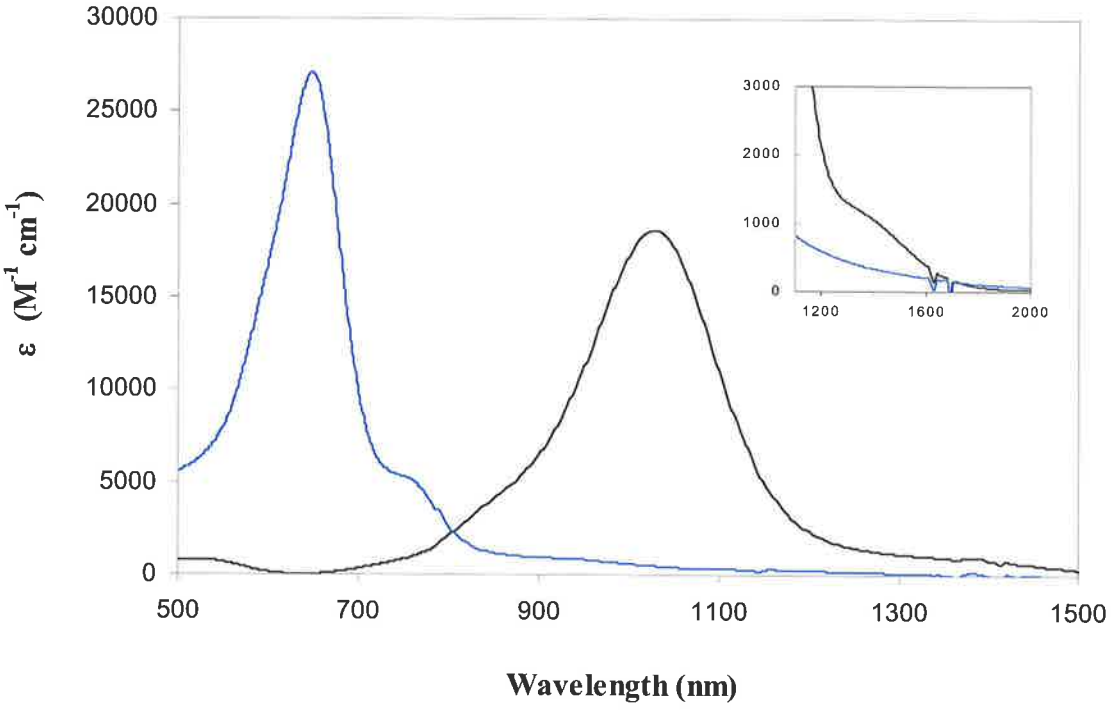

Figure 5.20: *Vis/NIR spectra of [65][PF_6] (—) and [65][PF_6]$_2$ (—) in CH_2Cl_2 at 20°C.*

Physically, the IVCT band corresponds to the photo-induced electron transfer of a ruthenium centred electron to the iron site. In the case of asymmetric MV systems the redox centres are weakly coupled and the Hush model applies.[195] From the experimental data, the electronic coupling parameter can be computed. For these calculations the Fe-Ru distance was estimated to be the average of the Fe-Ru distances determined by the X-ray diffraction study of [**65**][PF_6] ($d_{Fe\text{-}Ru}$ = 7.61 Å). Therefore using Equation 1.6 the electronic coupling parameter, V_{ab} = 390 cm^{-1} (0.048 eV). This value is much higher than those found in [**63**][PF_6] (152 cm^{-1}, 0.019 eV) and [**64**][PF_6] (169 cm^{-1}, 0.021 eV), suggesting that despite being a Class II MV complex, strong interactions between iron and ruthenium are present in [**65**][PF_6].

5.4. Conclusions

In summary, this work has demonstrated a new synthetic procedure for the syntheses of asymmetric diyndiyl complexes with Ru(dppe)Cp* and Fe(PP)Cp* fragments. Cyclic voltammetry has shown that strong interactions exist between the two metal centres. The mono- and dications of **65** were prepared by one- and two-electron oxidations of the neutral complex using the ferrocenium cation. Attempts to isolate the tricationic derivative were unsuccessful.

Single crystal X-ray structures of [**65**][PF_6]$_n$ (n = 0, 1, 2) were obtained, but the metal sites are completely disordered as a result of their identical ligand environments. A combination of various spectroscopic techniques including IR, Mössbauer, ESR, NMR and UV/Vis/NIR spectroscopies all provided an insight into the bonding in these cationic derivatives.

The monocation [**65**][PF_6] was shown by IR and Mössbauer spectroscopy to exist predominantly in the diyndiyl form as an iron-centred radical-cation. Upon further oxidation, the dication [**65**][PF_6]$_2$ exists in a singlet-triplet equilibrium between the cumulenic (**5o**) and diyndiyl (**5p**) forms. In this case, variable temperature Mössbauer and NMR spectroscopies confirmed that at low temperatures (< 80 K) the singlet form dominates. As the temperature was raised, increased contributions from the triplet state could be detected.

For the MV cation [**65**][PF_6], calculation of the electronic coupling parameter (0.048 eV) confirmed the strong interaction observed by cyclic voltammetry. Although V_{ab} lies well below those found in the symmetric diyndiyls **5** (0.43 eV) and **25b** (0.63 eV), it is at the upper limit of Class II MV complexes reported.

5.5. Experimental

General experimental conditions are detailed on page ix.

Reagents: The compounds FeCl(dppe)Cp*,[192] FeCl(dppp)Cp*[196] and $[FeCp_2][PF_6]$[121] were prepared by standard literature methods.

{Cp*(dppe)Ru}(C≡CC≡C){Fe(dppe)Cp*} (65)

In a Schlenk flask, **40** (250 mg, 0.36 mmol), FeCl(dppe)Cp* (228 mg, 0.36 mmol) and $Na[BPh_4]$ (125 mg, 0.36 mmol) were dried under vacuum. A solution of NEt_3 (30 mL) and dbu (109 mg, 0.72 mmol) was added *via* cannula and the mixture was stirred at r.t. for 24 h. The light brown suspension was evaporated to dryness and the resulting solid extracted in diethyl ether (2 x 20 mL) and the extract was filtered *via* cannula into a second Schlenk flask. The solvent was removed and the solid washed with methanol (2 x 10 mL) and dried under vacuum to give **65** as a brick red powder (335 mg, 73%). Anal. Calcd ($C_{76}H_{78}FeP_4Ru$): C, 71.74; H, 6.18. Found: C, 71.64; H, 6.23. IR (Nujol, cm^{-1}): ν(CC) 1966 w. ^{1}H NMR (benzene-d_6): δ 1.59 (s, 15H, *Cp**Fe), 1.82 (s, 15H, *Cp**Ru), 2.06, 2.85 (2m, 2 x 4H, CH_2CH_2), 7.14-8.26 (m, 40H, Ph). ^{13}C NMR (benzene-d_6, -80°C): δ 10.50 (s, $C_5\underline{Me}_5Ru$), 10.56 (s, $C_5\underline{Me}_5Fe$), 30.05 (m, Ru$\underline{C}H_2$), 31.52 (m, Fe$\underline{C}H_2$), 87.43 (s, $\underline{C}_5Me_5Fe$), 92.53 (s, $\underline{C}_5Me_5Ru$), 93.57 (s, Ru-$\underline{C}$≡C), 99.92 (s, Ru-C≡$\underline{C}$), 100.75 (br, C≡$\underline{C}$-Fe), 109.70 (s, $\underline{C}$≡C-Fe), 124.80-140.68 (m, Ph). ^{31}P NMR (benzene-d_6): δ 82.55 (br, *dppe*Ru), 101.90 (br, *dppe*Fe). FAB-mass spectrum (*m/z*): 1272, $[M]^+$; 1195, $[M - Ph]^+$; 874, $[M - dppe]^+$; 635, $[Ru(dppe)Cp^*]^+$; 589, $[Fe(dppe)Cp^*]^+$.

[{Cp*(dppe)Ru}(C_4){Fe(dppe)Cp*}][PF_6] ([65][PF_6])

To a solution of **65** (500 mg, 0.39 mmol) in CH_2Cl_2 (20 mL) was added solid $[FeCp_2][PF_6]$ (123 mg, 0.37 mmol). The solution quickly changed colour from orange to brown and the mixture was stirred at r.t. for 2 h. Toluene (20 mL) was added and the solution was filtered *via* cannula into a second Schlenk flask. Crystallisation began upon concentration under vacuum and the resulting black solid was collected on a sintered glass funnel and washed with toluene (2 x 10 mL)

followed by pentane (2 x 10 mL) to give [**65**][PF_6] (475 mg, 91%). Anal. Calcd ($C_{76}H_{78}F_6FeP_5Ru$): C, 64.41; H, 5.55. Found: C, 64.43; H, 5.41. IR (Nujol, cm^{-1}): ν(CC) 1986 m, 1877 w; ν(PF) 839 s.

[{Cp*(dppe)Ru}(C_4){Fe(dppe)Cp*}][PF_6]$_2$ ([65][PF_6]$_2$)

To a solution of [**65**][PF_6] (400 mg, 0.28 mmol) in CH_2Cl_2 (20 mL) was added [$FeCp_2$][PF_6] (91.2 mg, 0.27 mmol). The brown solution quickly turned bright blue and the mixture was stirred at r.t. for 2 h. Toluene (20 mL) was added and the solution was filtered *via* cannula into another Schlenk flask before being concentrated under vacuum (20 mL) to initiate crystallisation. The dark blue crystalline solid was filtered on a sintered glass funnel and washed with toluene (2 x 10 mL) and pentane (2 x 10 mL) to give [**65**][PF_6]$_2$ (431 mg, 98%). Anal. Calcd ($C_{76}H_{78}F_{12}FeP_6Ru$): C, 58.43; H, 5.03. Found: C, 58.25; H, 4.89. IR (Nujol, cm^{-1}): ν(CC) 1869 w, 1783 m; ν(PF) 838 s. ^{1}H NMR (acetone-d_6): δ -3.83 (s, 15H, *Cp**Fe), -0.22 (br, 2H, CH_2), 2.88 (s, *ortho*-Ph), 3.04 (br, 2H, CH_2), 3.82 (br, 2H, CH_2), 4.26 (br, 2H, CH_2), 5.46 (s, 15H, *Cp**Ru), 6.80-9.40 (m, Ph). ^{31}P NMR (acetone-d_6): δ -143.60 (septet, PF_6^-), -51.24 (br, *dppe*Ru), 291.83 (br, *dppe*Fe).

{Cp*(dppe)Ru}(C≡CC≡C){Fe(dppp)Cp*} (66)

In a Schlenk flask, **40** (250 mg, 0.36 mmol), FeCl(dppp)Cp* (233 mg, 0.36 mmol) and Na[BPh_4] (125 mg, 0.36 mmol) were dried under vacuum. A solution of NEt_3 (30 mL) and dbu (109 mg, 0.72 mmol) was added *via* cannula and the reaction was stirred at r.t. for 24 h. The light brown suspension was evaporated to dryness and the resulting solid extracted in diethyl ether (2 x 20 mL) and filtered *via* cannula into a second Schlenk flask. The solvent was removed and the solid washed with methanol (2 x 10 mL) and dried under vacuum to give **66** as a brick red powder (335 mg, 71%). Anal. Calcd ($C_{77}H_{80}FeP_4Ru$): C, 71.89; H, 6.27. Found: C, 71.64; H, 6.23. IR (Nujol, cm^{-1}): ν(CC) 1965 w. ^{1}H NMR (benzene-d_6): δ 1.68 (s, 15H, *Cp**Fe), 2.02 (s, 15H, *Cp**Ru), 2.37 [m, 6H, $(CH_2)_3$], 3.36 (m, 4H, CH_2CH_2), 7.35-8.45 (m, 40H, Ph). ^{13}C NMR (benzene-d_6): δ 10.45 (s, $C_5\underline{Me}_5Ru$), 10.68 (s, $C_5\underline{Me}_5Fe$), 21.29 [t, ^2J(CP) 6 Hz, $PCH_2\underline{C}H_2CH_2P$], 29.94 (m, $FeP\underline{C}H_2$), 30.29 (m, $RuP\underline{C}H_2$), 87.74 (s, $\underline{C}_5Me_5Fe$), 92.67 (s, $\underline{C}_5Me_5Ru$), 124.78-140.86 (m, Ph). ^{31}P

NMR (benzene-d_6): δ 60.92 (br, *dppe*Fe), 81.17 (br, *dppe*Ru). FAB-mass spectrum (*m/z*): 1286, $[M]^+$; 1209, $[M - Ph]^+$; 888, $[M - dppp]^+$; 635, $[Ru(dppe)Cp^*]^+$; 593, $[Fe(dppp)Cp^*]^+$.

CHAPTER SIX

Ruthenium Yndiyl and Polyyndiyl Complexes: Syntheses and Characterisation of [Ru]-$(C\equiv C)_n$-[Ru] [Ru = Ru(dppe)Cp'; n = 1-11]

6.1. Introduction

While much of the work with [M]-$(C\equiv C)_n$-[M] complexes has been focussed around diyndiyl complexes (n = 2), higher analogues containing between three and ten acetylene units have gained considerable interest in recent times.[46,197] Two key points have driven this research. Firstly, to what point are the electronic interactions observed in the C_4 complexes maintained as the chain length is increased? Secondly, the syntheses of complexes with extended carbon chains ($n \geq 5$) offers a unique route towards the synthesis of the polymeric carbon allotrope 'carbyne'.[198]

At the time this work was commenced, the most detailed series of polyyndiyl complexes were those bearing the redox-active fragment Re(NO)(PPh_3)Cp*.[46] In this series, complexes containing between four and twenty carbon atoms in the all-carbon bridge were synthesised. The distinction between strongly and weakly interacting rhenium centres as determined by cyclic voltammetry was found to occur with the C_{10} complex (ΔE = 0.2 V). For complexes with longer bridging ligands, the separation between the two redox processes steadily decreased, until C_{20}, for which only a single irreversible wave was observed.[46] Similarly, the C_8 analogue of the iron complex **5** was found to maintain strong interactions between the two iron centres,[35] but this system has yet to be extended to longer chain lengths.

6.2. Aims

The aim of this work was to prepare a series of polyyndiyl complexes with Ru(dppe)Cp* end-groups allowing comparisons with related redox-active systems to be made. The use of cyclic voltammetry allows quantification of the 'electronic communication' between the two metals upon extension of the bridging carbon chain (Section 6.3.4).

The simplest subset of yndiyl complexes are those with bridging C_2 units. Previously considered too sterically hindered to be regarded as realistic synthetic targets, ethyndiyls that are structurally related to electron-rich C_4 analogues, such as those with Fe(dppe)Cp*, Re(NO)(PPh_3)Cp* end-groups, have not been reported. In

light of this (mis)conception together with the reported synthesis and structural characterisation of the related cyano-bridged complex $[\{Cp(PPh_3)_2Ru\}(CN)\{Ru(dppe)Cp\}]^+$,[199] the synthesis of $\{Ru(dppe)Cp\}_2(C\equiv C)$ will be investigated. In this case, Cp rather than the more electron-donating Cp* ligands are expected to minimise steric repulsions between the two end-groups.

6.3. Results and Discussion

6.3.1. C_2 Complexes

While a large number of [M]-C≡C-[M] complexes have been reported with metals possessing a range of different coordination spheres and electron counts, most are relatively unstable, resulting in limited spectroscopic characterisation.[200] A considerable quantity of this work has been focussed around the Group 11 metals Cu, Ag and Au, however their chemistry is often hindered by violent explosions associated with such extremely reactive species. By coordinating phosphines to the Group 11 metals these problems can be generally overcome and a number of complexes of the type $\{Au(PAr_3)\}_2(C\equiv C)$ have recently been reported.[201,202]

Group 8 ethyndiyls are limited to $\{Fe(CO)_2Cp^*\}_2(C\equiv C)$,[203] $\{Ru(CO)_2Cp\}_2(C\equiv C)$ and its Cp^{Me} analogue.[204] Both ruthenium complexes were prepared by the reaction of $Ru(C\equiv CMe)(CO)_2Cp'$ with $(Me_3CO)_3W\equiv W(OCMe_3)_3$, which proceeded *via* a metal-catalysed alkyne metathesis mechanism. The iron complex was prepared by the reaction of $Fe(C\equiv CH)(CO)_2Cp^*$ with $[Fe(THF)(CO)_2Cp^*]^+$, which gave the cationic bis-iron complex $[\{Fe(CO)_2Cp^*\}_2(C\equiv CH)]^+$. Deprotonation of this species (NaOMe) gave the neutral complex $\{Fe(CO)_2Cp^*\}_2(C\equiv C)$ as a brick-red solid in 41% yield.

The structure of $[\{Fe(CO)_2Cp^*\}_2(C\equiv CH)]^+$ has gained considerable attention due to the possibility of there being different geometric isomers. Spectroscopic and X-ray studies confirmed the π-bonded resonance forms to be the major contributors, with fluxional behaviour between structures **6a** and **6c**, which interconvert *via* an intermediate **6b**, in which the proton is attached to both carbon atoms of the C_2 ligand (Scheme 6.1).[203]

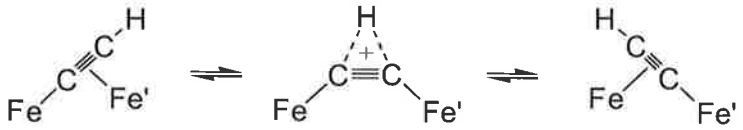

6a **6b** **6c**

Scheme 6.1

The corresponding ruthenium analogue $[\{Ru(CO)_2Cp\}_2(C{\equiv}CH)][BF_4]$ was prepared by treating $\{Ru(CO)_2Cp\}_2(C{\equiv}C)$ with $HBF_4.OEt_2$ at 0°C and also displayed similar fluxional behaviour.[205]

6.3.1.1. Synthesis of $\{Ru(dppe)Cp\}_2(C{\equiv}C)$ (69)

Scheme 6.2 outlines the synthesis of the ethyndiyl $\{Ru(dppe)Cp\}_2(C{\equiv}C)$ (**69**). Starting from RuCl(dppe)Cp (**70**), treatment with excess $TMSC{\equiv}CH$ and NH_4PF_6 in CH_2Cl_2 in a sealed Carius tube at 80°C afforded the vinylidene complex $[Ru(=C=CH_2)(dppe)Cp][PF_6]$ (**71**).[206] Addition of two equivalents of Bu^nLi to a solution of **71** in THF gave the lithio derivative **72**, which was treated *in situ* with $[Ru(THF)(dppe)Cp]^+$ (formed by reaction of **70** with AgOTf) to give **69** as a bright orange solid. However, even under strict Schlenk conditions it was found that **69** was readily converted to a bright green complex, later identified as $[\{Ru(dppe)Cp\}_2(C{\equiv}CH)]^+$ (**73**). In this case, the proton source could have possibly been the Si-OH groups on the glass surface, from the THF solvent or from trace quantities of water present in the solvents. As a consequence of this facile protonation, the mono-protonated complex **73** was regarded a more suitable synthetic target rather than the highly reactive neutral ethyndiyl.

Isolation of **73** was achieved by passing the orange THF solution of **69** down a silica gel column, eluting with acetone. This gave a bright green band that was concentrated and crystallised from CH_2Cl_2/hexane to give **73** (67%) as the PF_6^- salt. Complex **73** was very stable and could be stored as a solid indefinitely at room temperature. It was less stable in solution however, changing colour firstly to bright blue, followed by an intense pink. In light of the behaviour of the related diyndiyl complex **25b**, these transformations were anticipated to be caused by the sequential

formation of the mono- and dicationic forms of **69**, and this has since been proven through a combination of cyclic voltammetry and X-ray structure determination.[207]

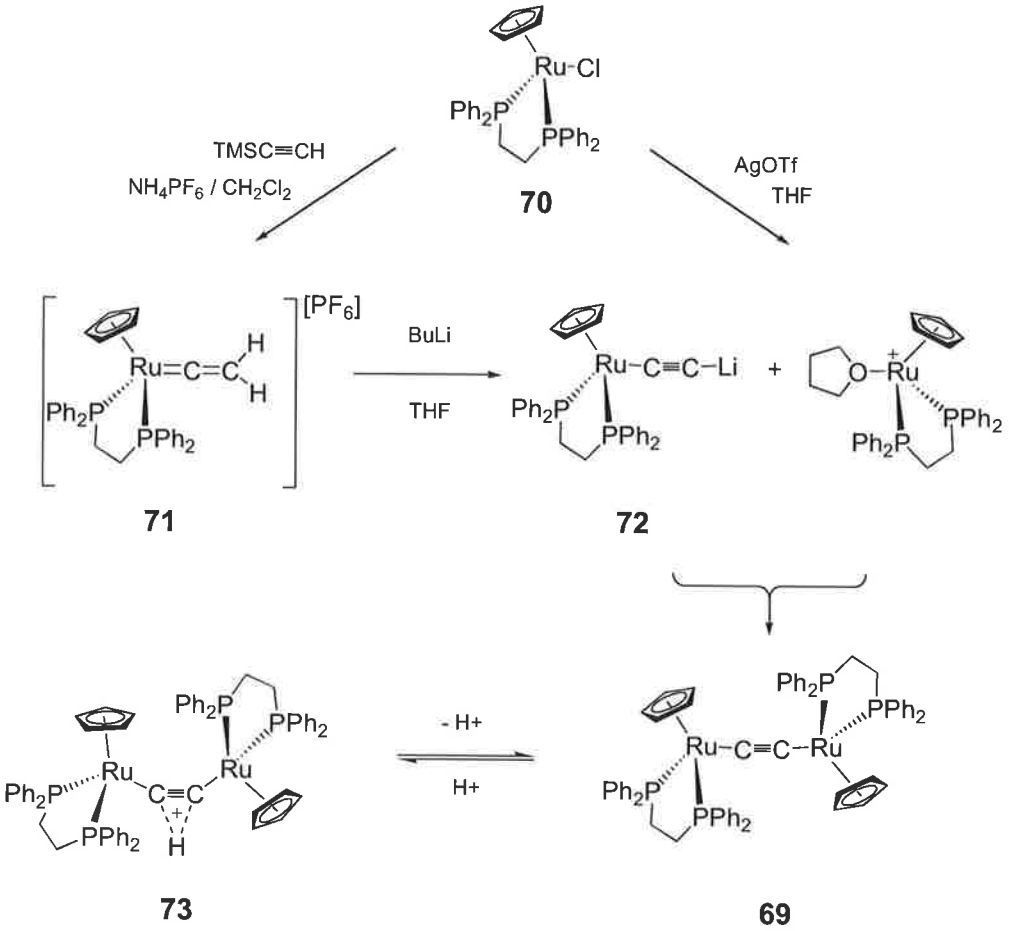

Scheme 6.2

For the protonated complex **73**, only a single resonance at δ 4.75 was observed in ^{1}H NMR spectrum in the expected region for Cp ligands, suggesting the equivalence of the two ruthenium fragments on the NMR timescale. A quintet at δ 2.51 was attributed to the proton attached to the C_2 ligand, showing coupling to the four equivalent phosphorus nuclei. In the ^{31}P NMR spectrum, a singlet at δ 81.66 together with a septet at δ -142.43, reaffirmed that the two ruthenium centres were equivalent and that the complex was a cation, stabilised as the PF_6^- salt. In the ES-mass spectrum, ions centred at *m/z* 1154 and 577 were attributed to $[M]^+$ and $[M]^{2+}$, respectively. No bands were observed between 2100-1600 cm^{-1} in the IR spectrum.

Unfortunately, crystals suitable for X-ray structure determination were not obtained. However, considering the similarities in the spectroscopic results to those of both the $Ru(CO)_2Cp'$ and $Fe(CO)_2Cp$ analogues, it is suggested that the structure of **73** is

similar to these systems, with one ruthenium coordinated *via* a σ-bond, while the second is π-bonded to the C≡C triple bond. The equivalence of the two ruthenium fragments by NMR suggests that this system is fluxional between two rapidly interconverting forms, such as that seen in Scheme 6.1.

Deprotonation of **73** was achieved by treatment with KOBu^t in THF, resulting in a rapid colour change from green to orange. Extraction into hexane and filtration gave a bright orange solution of **69** that was allowed to evaporate under a stream of nitrogen, resulting in the formation of large red cubic crystals (27%). The low yield in this case was due to reformation of considerable quantities of **73**, which could be extracted from the red crystals of **69** by washing with cold acetone.

For neutral **69**, a broad singlet in the ^{31}P NMR spectrum was found at δ 87.79, while in the ^{1}H NMR spectrum, a singlet at δ 4.59 was attributed to the two equivalent Cp ligands. Resonances for the C_2 ligand were not detected, due to the poor solubility of **69** in benzene-d_6 or toluene-d_8 and decomposition or protonation to give **73** occurring in polar protic solvents. ES-mass spectrometry in MeOH gave a spectrum identical to that of **73** with $[M + H]^+$ and $[M + H]^{2+}$ ions at *m/z* 1154 and 577, respectively, suggesting **69** is readily protonated to form **73** in MeOH. As expected for a symmetric complex, **69** did not show any ν(C≡C) bands in its IR spectrum.

Large red crystals of **69** suitable for X-ray analysis were grown by the slow evaporation of a CH_2Cl_2/hexane solution and the ORTEP plot of a single molecule is shown in Figure 6.1, while selected structural parameters are collected in Table 6.1. As expected, each ruthenium adopts a pseudo-octahedral geometry with the Ru-C_2-Ru chain approaching a *transoid* configuration, with the torsion angle Cp-Ru….C_2….Ru-Cp of 101.9(3)°. The Ru-C single and C≡C triple bond distances are close to the values found in **25b**. The angles at the carbons of the C_2 ligand are close to linear at 170.2 and 174.0(4)°. While the structure is unexceptional, it demonstrates that while the phenyl groups of both dppe ligands lie over atoms C_1 and C_2, arrangement of the two capping groups in a *transoid* configuration allows the two Ru(dppe)Cp fragments to be in close proximity, with interlocking of the phenyl groups.

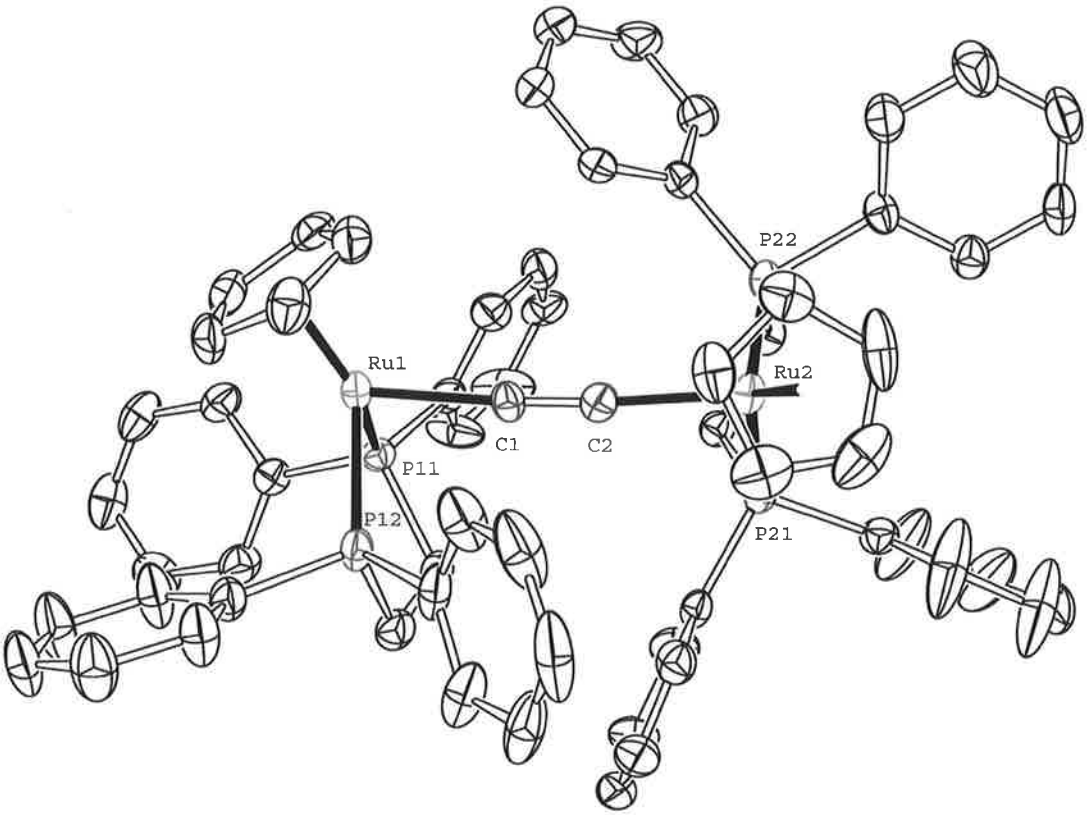

Figure 6.1: *ORTEP view of* ***69****.*

Bond distances (Å)		Bond angles (°)	
Ru(1)-P(11)	2.234(1)	P(11)-Ru(1)-P(12)	84.04(4)
Ru(1)-P(12)	2.234(1)	P(21)-Ru(1)-P(22)	83.43(4)
Ru(2)-P(21)	2.243(1)	P(11)-Ru(1)-C(1)	84.04(13)
Ru(2)-P(22)	2.239(1)	P(12)-Ru(1)-C(1)	84.99(13)
Ru(1)-C(Cp)	2.202-2.263(5)	P(21)-Ru(2)-C(2)	83.19(12)
(av.)	2.240(5)	P(22)-Ru(2)-C(2)	90.10(12)
Ru(2)-C(Cp)	2.232-2.266(5)	Ru(1)-C(1)-C(2)	174.0(4)
(av.)	2.241(6)	Ru(2)-C(2)-C(1)	170.2(4)
Ru-C(1)	2.046(5)		
C(1)-C(2)	1.230(7)		
C(2)-Ru(2)	2.051(5)		

Table 6.1: *Selected structural parameters for* ***69****.*

6.3.2. C_6 and C_8 Complexes

In recent times, a subset of polyyndiyl complexes containing C_6 and C_8 chains have attracted significant interest. Much of this work has been focussed on the influence that chain length has on the interactions between the two redox centres. Complexes featuring C_6 and C_8 chains bridging two metal centres [M]-$(C\equiv C)_n$-[M] (n = 3, 4) include [M] = $Re(NO)(PAr_3)Cp^*$,[46,86,208,209] $Fe(CO)_2Cp^*$,[146,210] $Fe(dppe)Cp^*$,[35] $Ru(PPh_3)_2Cp$,[98,211] $Ru_2(ap)_4$,[68] $Ru_2(dpf)_4$,[212] $Au(PR_3)$ (R = aryl / Cy),[213,214] $Pt(PAr_3)_2Ar$,[118,197,215,216] $W(CO)_3Cp$,[103] and $Pt(Bu^t_3\text{-trpy})$.[217]

Hexatriyndiyl (or C_6) complexes are generally prepared by metal couplings with Group 14 hexatriyne derivatives, such as TMS-$(C\equiv C)_3$-TMS. However, alternative methods, such as the cross-coupling of diynyl [M]$(C\equiv C)_2$H and ethynyl [M]C≡CH complexes or the reactions of hexatriynyl complexes [M]$(C\equiv C)_3$H with a second metal-ligand fragment, have also been used (Scheme 6.3).

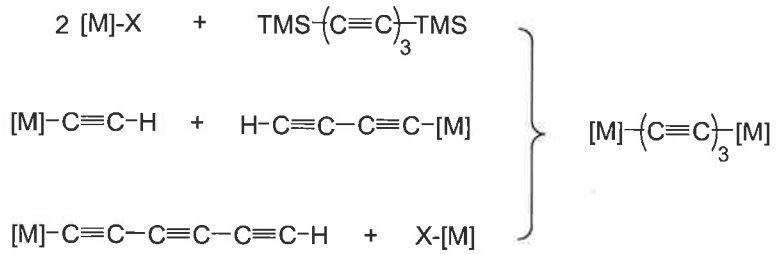

Scheme 6.3

Octatetrayndiyl (or C_8) complexes are generally prepared by two different synthetic methods. By far the majority of these complexes have been obtained by the oxidative coupling of diynyl complexes, under Glaser or Hay coupling conditions (Figure 6.4). Fewer have been formed by the use of the preformed C_8 unit TMS-$(C\equiv C)_4$-TMS, which can be treated with two equivalents of a metal-halide precursor in the presence of a desilylating agent (Figure 6.4).

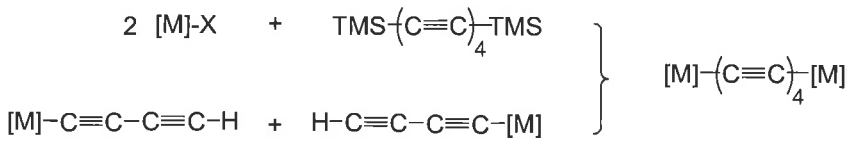

Scheme 6.4

6.3.2.1. Synthesis of {Ru(dppe)Cp}$_2$(C≡C)$_n$ [n = 3 (74), 4 (75)]*

As described in Chapters 2 and 4, the chloro-ruthenium complex **19b** does not react with TMS-(C≡C)$_2$-TMS to give the anticipated diyndiyl complex **25b**. This is a result of the reaction intermediate (most likely **40**), readily undergoing protonation in protic solvents to give the butatrienylidene **42**, which is susceptible to nucleophilic attack. In spite of this, treatment of **19b** with half an equivalent of TMS-(C≡C)$_n$-TMS in MeOH in the presence of KF gave {Ru(dppe)Cp*}$_2$(C≡C)$_n$ [*n* = 3 (**74**), 4 (**75**)] in 57 and 89% yields, respectively (Scheme 6.5).

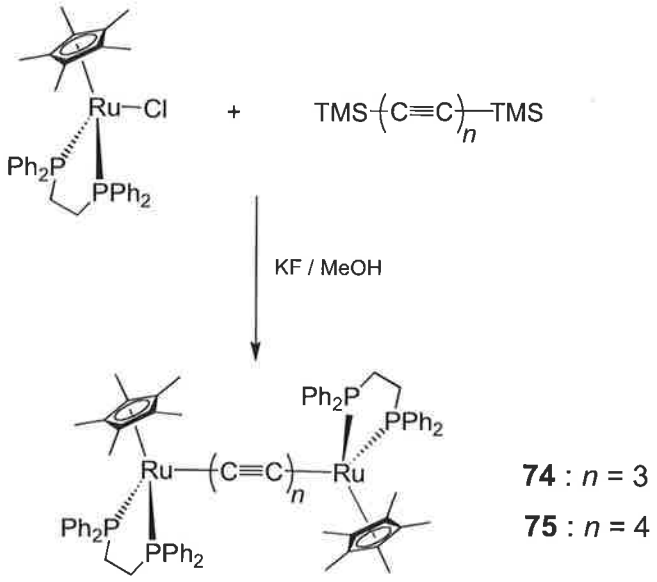

Scheme 6.5

Both **74** and **75** were characterised by elemental analysis along with various spectroscopic techniques. In the IR spectra, three ν(C≡C) bands were found between 1951 and 2129 cm^{-1} for **74**, while in **75**, two bands were found at 1951 and 2107 cm^{-1}. In the ^{1}H NMR spectra, singlets at δ 1.61 (**74**) and 1.49 (**75**) were assigned to the methylene protons of Cp*, while the dppe protons appeared as multiplets over the expected regions. In the ^{31}P NMR spectra of **74** and **75**, sharp singlets close to δ 79.00 were observed, characteristic of the Ru(dppe)Cp* fragment.

A well-resolved ^{13}C NMR spectrum of **74** was not obtained, due to the poor solubility of the complex in all available solvents. However, **75** was sufficiently soluble to allow all resonances, including those corresponding to the four types of

carbon atoms of the C_8 chain, to be observed. The resonance for C_1 was observed as a triplet at δ 94.58 [^2J(CP) 22 Hz], while atoms C_2, C_3 and C_4 gave singlet resonances at δ 92.54, 63.60 and 51.12, respectively. The ^{13}C resonances of the C_8 chain shift progressively upfield as the carbon atoms move further from ruthenium and approach the limiting values found in other extended polyyne systems.[218,219] Comparisons between **75** and **25b** show that there is little difference between the chemical shifts of atoms C_1, with both resonances appearing as triplets close to δ 94.00. This is in contrast to the C_4 and C_8 complexes in the related Fe(dppe)Cp* series, in which the C_1 carbons were observed at δ 99.7 and 143.2, respectively. This significant downfield shift in the C_8 complex was attributed to increased π-back-bonding from the metal centre as the chain length was increased.[220]

The ES-mass spectrum of **74** contained a strong $[M]^+$ ion at *m/z* 1342, while in **75**, a $[M + MeOH]^+$ ion was found at *m/z* 1398, together with a weaker $[M]^+$ ion at *m/z* 1366. Although both complexes were readily crystallised [**74** (CH_2Cl_2), **75** (CH_2Cl_2/MeCN)], crystals suitable for X-ray diffraction were not obtained.

6.3.2.2. Reaction of {Ru(dppe)Cp}$_2$(C≡C)$_3$ (74) with TCNE*

TCNE is a very useful reagent, which undergoes cycloaddition reactions with transition-metal alkynyl complexes.[221-229] Generally, the TCNE-derivatives are readily crystallised, allowing for structural characterisation that can unequivocally confirm the structure of the parent complex.[98,211]

Addition of one equivalent of TCNE to a suspension of **74** in CH_2Cl_2 resulted in an immediate colour change from yellow to a deep blue, followed by a change to red over a period of 30 minutes. After purification, red crystalline {Ru(dppe)Cp*}$_2${μ-C≡CC[=C(CN)$_2$]C[=C(CN)$_2$]C≡C} (**76**) was isolated as the major product (Scheme 6.6). The structure of **76** was determined from crystals obtained from CH_2Cl_2/hexane mixtures, and the ORTEP plot of a single molecule of **76** is given in Figure 6.2, while selected structural parameters are collected in Table 6.2. In accord with related systems, the reaction is anticipated to proceed *via* a paramagnetic intermediate, possibly the deep blue solution mentioned above, which then

undergoes a [2 + 2] cycloaddition to give a cyclobutenyl complex. Although this latter complex has been isolated in some systems,[230] ring opening usually occurs to relieve the strained four-membered ring to give the butadienyl **76** (Scheme 6.6).

The IR spectrum of **76** contained two ν(C≡N) bands at 2193 and 2208 cm^{-1} together with ν(C≡C) bands at 1959 and 1973 cm^{-1}. In the ^{1}H NMR spectrum, a triplet at δ 1.51 [^{4}J(HP) 2 Hz] was assigned to the two Cp* ligands while other resonances at δ 1.98 and 2.44 and between δ 6.77-7.71 were assigned to the protons of the dppe ligands. ^{13}C NMR spectroscopy revealed two CN groups at δ 115.61 and 116.97, while a resonance at δ 122.25 could not be individually assigned, possibly due to C_3 or $\underline{C}(CN)_2$. The remaining resonance was not observed and was possibly masked by the phenyl signals. Triplet resonances at δ 204.94 [t, ^{2}J(CP) 21 Hz] and 148.82 [t, ^{3}J(CP) 2 Hz] were assigned to atoms C_1 and C_2, based on the decreasing coupling to the phosphorus nuclei of dppe. In the ^{31}P NMR spectrum, two distinct doublets were observed at δ 76.04 and 79.88, due to the two magnetically inequivalent phosphorus nuclei of each dppe ligand.

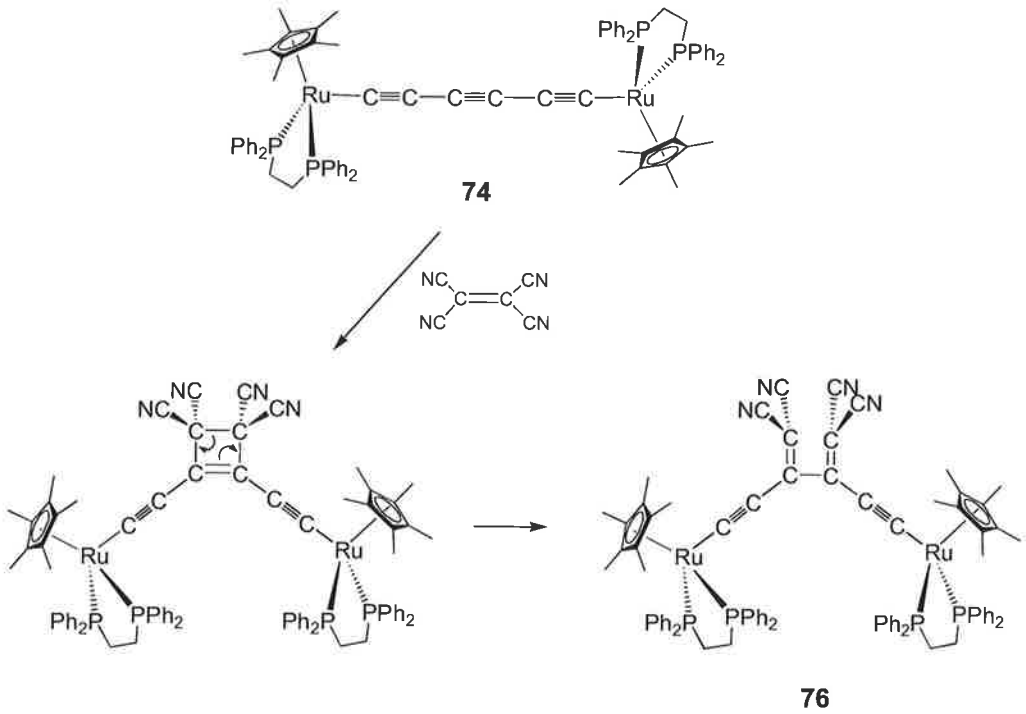

Scheme 6.6

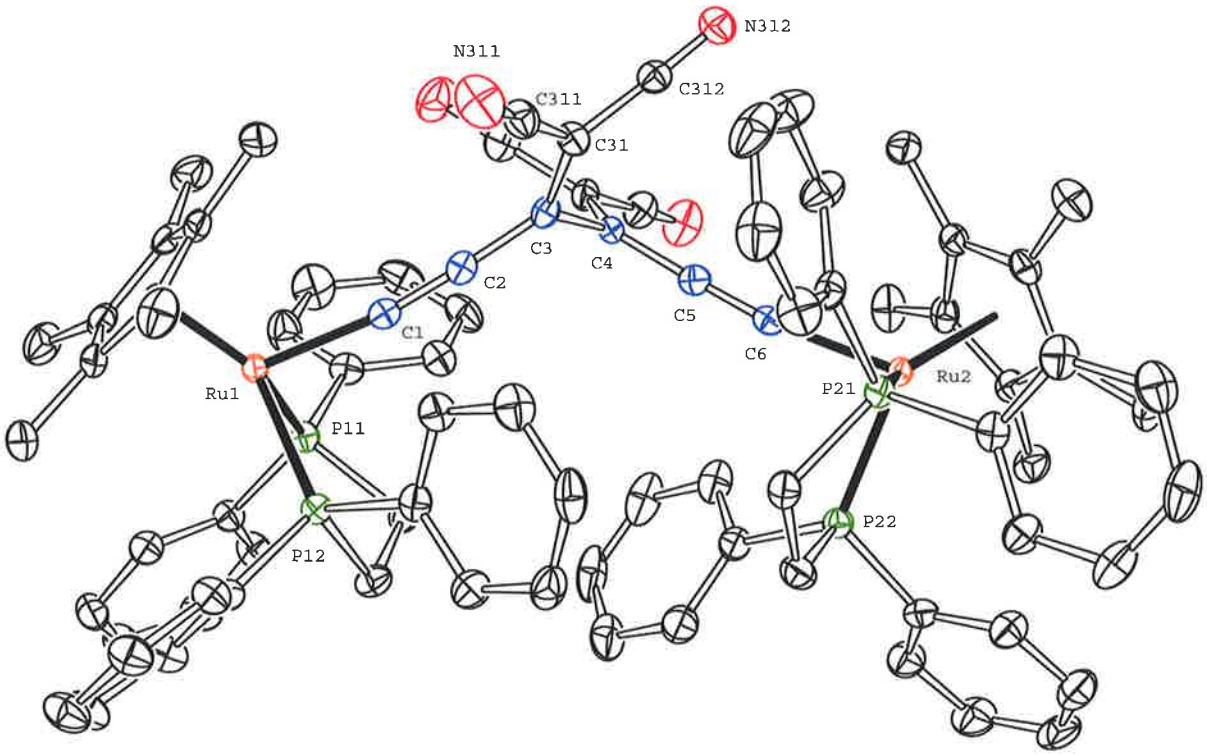

Figure 6.2: *ORTEP view of* ***76****.*

Bond distances (Å)		Bond angles (°)	
Ru(1,2)-P(11,12)	2.2729(8), 2.2808(7)	P(11,21)-Ru(1,2)-P(12,22)	83.02, 84.10(3)
Ru(1,2)-P(12,22)	2.3040, 2.2973(7)	P(11,21)-Ru(1,2)-C(1,6)	84.83, 89.00(8)
Ru(1,2)-C(Cp*)	2.234(3)-2.292(2),	P(12,22)-Ru(1,2)-C(1,6)	88.76, 89.49(8)
	2.247-2.283(3)	Ru(1,2)-C(1,6)-C(2,5)	171.5, 168.5(2)
(av.)	2.267, 2.266(3)	C(1,6)-C(2,5)-C(3,4)	175.3, 173.3(3)
Ru(1,2)-C(1,6)	1.938, 1.958(2)	C(2,5)-C(3,4)-C(4,3)	117.8, 116.4(2)
C(1,6)-C(2,5)	1.236, 1.230(3)	C(2,5)-C(3,4)-C(31,41)	125.7, 125.2(2)
C(2,5)-C(3,4)	1.389, 1.396(3)		
C(3)-C(4)	1.498(4)		
C(3,4)-C(31,41)	1.388, 1.376(4)		
C(31,41)-C(311,C411)	1.430, 1.433(4)		
C(31,41)-C(312,C412)	1.428, 1.427(4)		

Table 6.2: *Selected structural parameters for* ***76****.*

The X-ray crystal structure of **76** confirmed that TCNE has added to the central C≡C triple bond and the reaction has proceeded to the ring-opened product. It also confirmed the structure of the parent complex **74**, which could not be structurally characterised. Within the Ru-C≡C fragment, the Ru-C single bonds are relatively short [1.938 and 1.958(2) Å], while the C≡C triple bonds are slightly elongated [1.236 and 1.230(3) Å], relative to the values found in the diyndiyl complex **25b**. The long C(3)-C(4) bond [1.489(4) Å] confirms the presence of a C-C single bond, while the C(3)-C(31) and C(4)-C(41) bonds are typical C=C double bond lengths.

6.3.2.3. Reactions of 74 and 75 with $Fe_2(CO)_9$

It is well established that $Fe_2(CO)_9$ reacts with transition metal alkynes to cleave C≡C triple bonds, inserting the trinuclear iron species $Fe_3(CO)_9$.[231,232] While reactions of related C_6 and C_8 complexes with $Fe_2(CO)_9$ have previously been reported,[103,211] the redox behaviour of these compounds was never investigated and the influence of the trinuclear cluster on the 'electronic communication' between two redox-active end-groups remains unclear.

Treatment of the starting complexes **74** and **75** with $Fe_2(CO)_9$ afforded the bright red complexes **77** and **78**, respectively (Scheme 6.7). During the reaction, solutions gradually changed colour from yellow to a cherry red and purification by preparative TLC allowed isolation in low to moderate yields (7 and 30%, respectively).

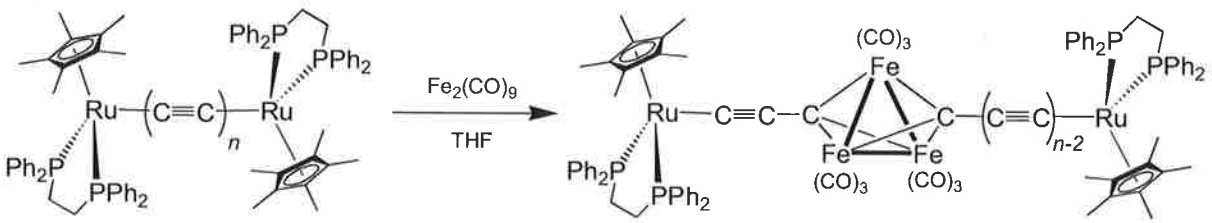

74 : *n* = 3
75 : *n* = 4

77 : *n* = 3
78 : *n* = 4

Scheme 6.7

While the mechanisms of such reactions are not completely understood, it is thought that upon interaction of $Fe_2(CO)_9$ with the C≡C triple bond, a tetrahedral Fe_2C_2 species is formed.[230] Addition of a third Fe atom results in C≡C triple bond cleavage and formation of the trinuclear cluster. It has been suggested that strongly electron-donating groups stabilise the intermediate formed prior to C≡C cleavage.[232]

For the symmetric complex **77**, a single Cp* resonance was observed in the ^1H NMR spectrum. In the ^{13}C NMR, resonances for the individual atoms of the carbon chain were found at δ 188.59, 145.59 and 263.18 and assigned to atoms C_1, C_2 and C_3 respectively. The highly deshielded resonance of C_3 is characteristic of a μ_3-alkylidyne group.[211,233] The resonance at δ 188.59 appears as a triplet and confirms the assignment to C_1, leaving the remaining signal at δ 145.59 to be assigned to C_2, which is reasonable for a C_2 atom in close proximity to an electron withdrawing group. The carbonyl groups on iron are fluxional appearing as a single resonance at δ 212.44.

In the ^1H NMR spectrum of **78**, the presence of two Cp* resonances, together with two dppe resonances in the ^{31}P NMR spectrum, confirmed the asymmetric nature of this complex. The carbon atoms directly attached to the iron cluster were found at δ 257.98 and 273.25, but they could not be individually assigned. Resonances at δ 161.65 and 171.84 were assigned to C_1 or C_8 based on comparisons with **73**, while four resonances at δ 53.65, 86.91, 96.77 and 149.23 were assigned to the remaining carbons of the chain.

Single crystals of **77** and **78** suitable for X-ray diffraction studies were grown from CH_2Cl_2/hexane solvent mixtures and the ORTEP plots are given in Figure 6.3 and 6.4, respectively, while selected structural parameters are compared in Table 6.3. The structures confirm that the geometries of the trinuclear Fe_3 clusters are close to an equilateral triangle with Fe-Fe distances in the range of 2.482(6) to 2.496(8) Å (**73**) and 2.516 to 2.534(2) Å (**74**). Each face of the cluster is capped with a single carbon atom to give a $(\mu_3\text{-}C)_2Fe_3(CO)_9$ unit with Fe-C distances in both complexes equal, within the 3σ range [1.93(2)-2.01(3) Å]. For the Ru-C≡C moiety, the Ru-C bonds are contracted, while the C≡C triple bonds are longer than those found in **25b**.

However, the low accuracies of the two structures prevent any definitive conclusions being drawn. Nevertheless, the polyyne nature of the chains is apparent from the alternating short and long C-C separations. Angles at the carbon atoms of the bridging ligand are close to linear, between 168(2) and 179(1)°.

Further supporting the NMR data, the structures confirm the cleavage of the central C≡C triple bond in **74** to give the symmetric adduct **77**. In the case of **75**, cleavage of one of the inner C≡C triple bonds has resulted in the formation of an asymmetric adduct with C_3 and C_5 fragments.

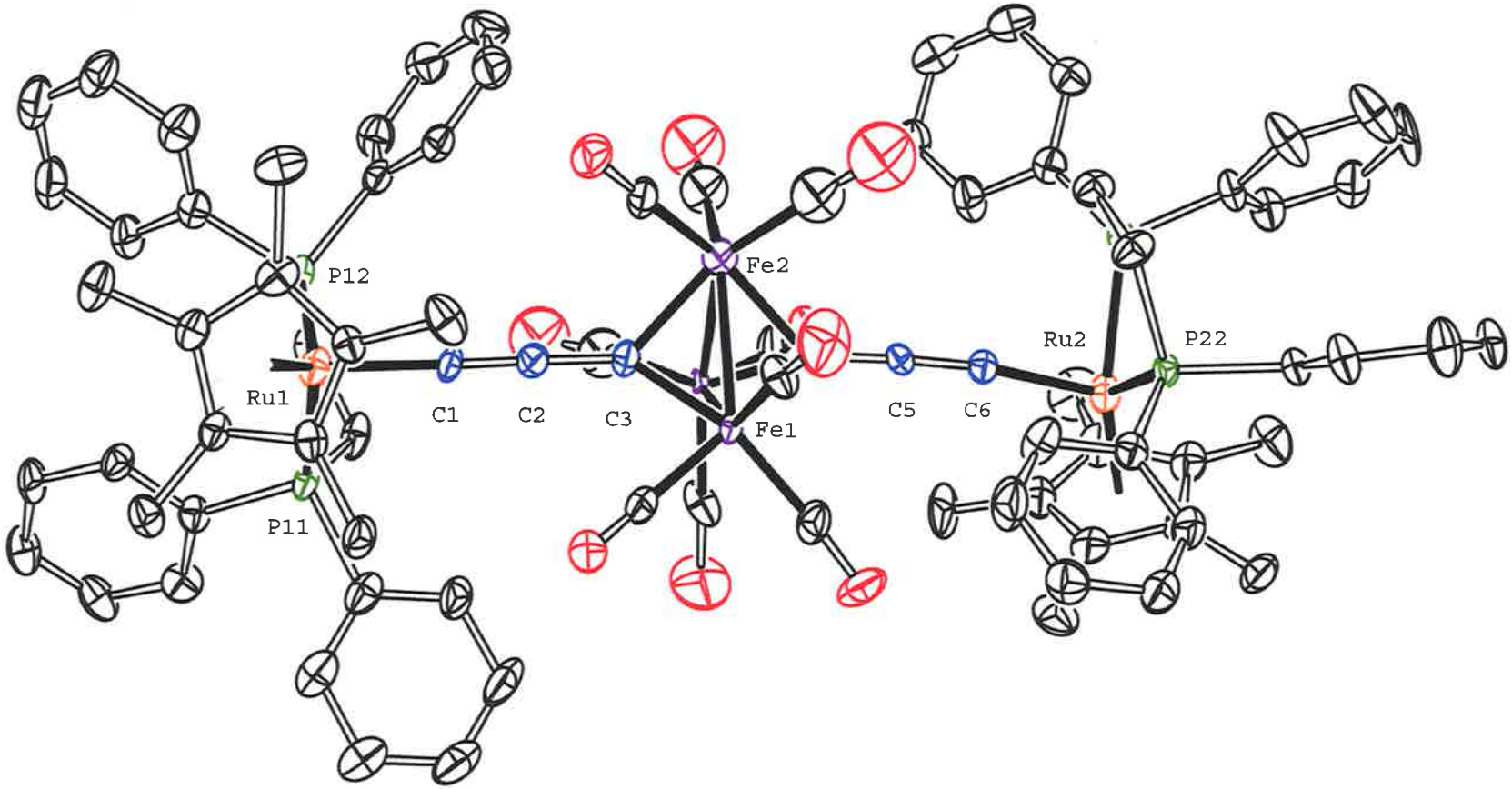

Figure 6.3: *ORTEP view of 77.*

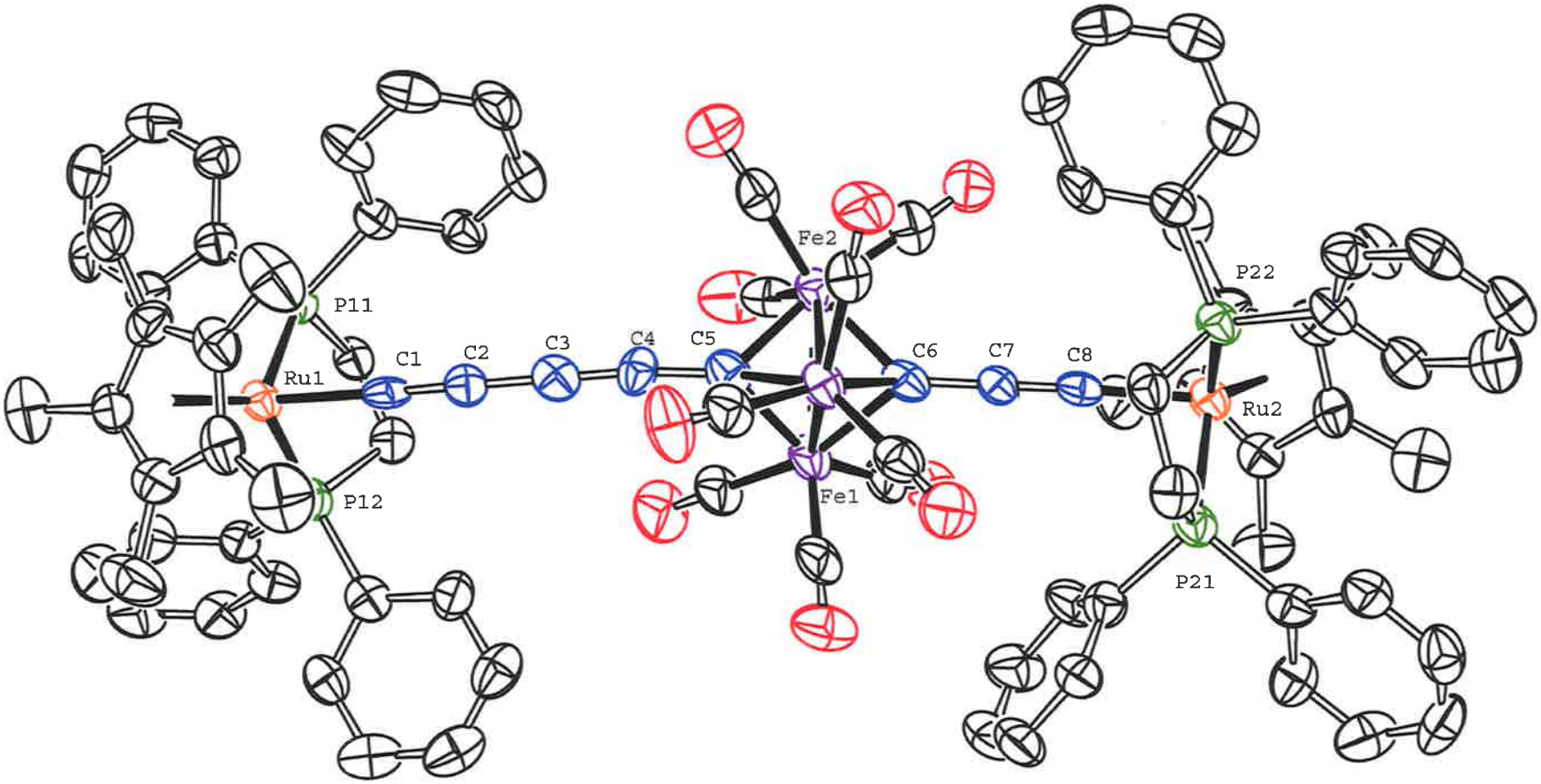

Figure 6.4: *ORTEP view of* ***78****.*

	77	**78**
Bond distances (Å)		
Ru(1,2)-P(11,21)	2.283(8), 2.294(9)	2.272, 2.272(3)
Ru(1,2)-P(12,22)	2.286(9), 2.270(8)	2.279, 2.263(3)
Ru(1,2)-C(Cp*)	2.17(3)-2.26(3),	2.21-2.28(1),
	2.20(2)-2.33(3)	2.23-2.27(1)
(av.)	2.23, 2.27(3)	2.25, 2.25(1)
Ru(1)-C(1)	1.93(3)	1.95(1)
C(1)-C(2)	1.28(4)	1.23(2)
C(2)-C(3)	1.44(4)	1.37(2)
C(3)-C(4)	[2.713]	1.23(2)
C(4)-C(5)	1.42(4)	1.37(2)
C(5)-C(6)	1.27(4)	[2.688]
C(6)-Ru(2)	1.92(3)	
C(6)-C(7)		1.39(2)
C(7)-C(8)		1.24(2)
C(8)-Ru(2)		1.98(1)
Fe(1)-C(3,4)/C(5,6)	1.98, 1.97(3)	1.99, 1.99(1)
Fe(2)-C(3,4)/C(5,6)	1.99, 2.01(3)	1.96, 2.00(1)
Fe(3)-C(3,4)/C(5,6)	1.93(2), 1.99(3)	1.98, 1.97(1)
Fe(1)-Fe(2)	2.496(8)	2.516(2)
Fe(1)-Fe(3)	2.485(7)	2.534(2)
Fe(2)-Fe(3)	2.482(6)	2.526(3)
Bond angles (°)		
P(11,12)-Ru(1)-C(1)	87.6(7), 85.3(8)	85.1(4), 83.7(3)
P(21,22)-Ru(2)-C(6)	85.7(9), 89.9(8)	
P(21,22)-Ru(2)-C(8)		84.1(4), 84.6(3)
Ru(1)-C(1)-C(2)	175(2)	178.2(9)
C(1)-C(2)-C(3)	179(3)	172(1)
C(4)-C(5)-C(6)	174(3)	
C(5)-C(6)-Ru(2)	168(2)	
C(2)-C(3)-C(4)		177(1)
C(3)-C(4)-C(5)		174(1)
C(6)-C(7)-C(8)		179(1)
C(7)-C(8)-Ru(2)		177(1)

Table 6.3: *Selected structural parameters for 77 and 78.*

6.3.2.4. Reaction of {Ru(dppe)Cp}$_2$(C≡C)$_3$ (74) with Co$_2$(μ-dppm)$_2$(CO)$_6$*

Another reaction that can be used to structurally characterise C_n chain complexes that resist crystallisation, involves the treatment with the cobalt clusters $Co_2(CO)_8$ and $Co_2(\mu\text{-dppm})(CO)_6$. These reactions generally proceed readily with the Co_2 cluster π-coordinated to the least sterically hindered triple bond (Scheme 6.8).[234]

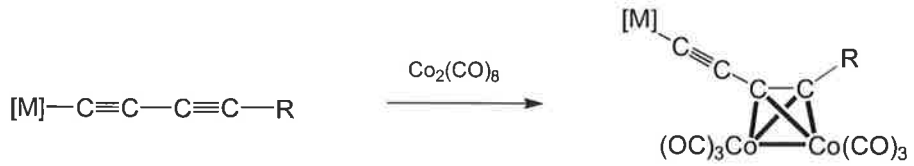

Scheme 6.8

Treatment of **74** with either $Co_2(CO)_8$ or $Co_2(\mu\text{-dppm})(CO)_6$ in benzene at room temperature did not result in the formation of any such adducts, with only starting complexes isolated. However, the reaction of **74** with $Co_2(\mu\text{-dppm})(CO)_6$ in refluxing benzene gave a mixture from which preparative TLC showed an olive green band (R_f = 0.4) was the major product. After purification, crystallisation from CH_2Cl_2/MeOH mixtures gave black crystals that were later identified as $Co_4(\mu\text{-dppm})_2(CO)_8$ (**79**) (Scheme 6.9).

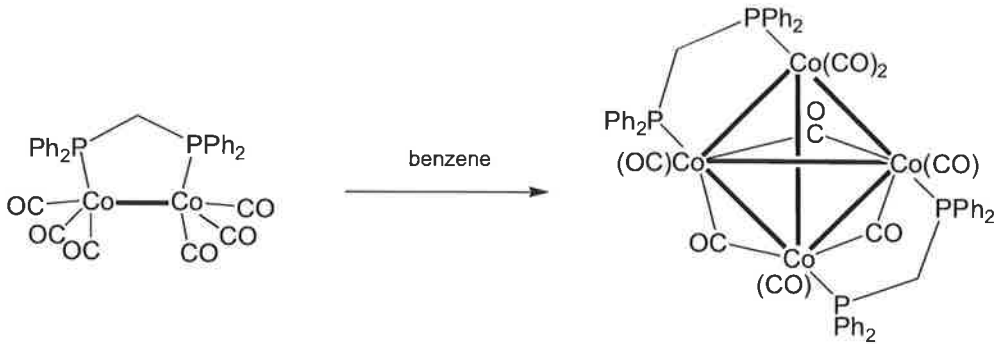

79

Scheme 6.9

In this case, rather than coordinating to a C≡C triple bond, thermolysis of $Co_2(\mu\text{-dppm})(CO)_6$ resulted in the formation of **79**. NMR characterisation of **79** was hindered by severe broadening, arising from unresolved coupling to the ^{59}Co nuclei (I = 7/2, natural abundance 100%). Despite this, a singlet at δ 24.67 could still be observed in the ^{31}P NMR spectrum due to the dppm ligands. ES-mass spectroscopy

confirmed the structure with a $[M]^+$ ion at *m/z* 1228, together with ions corresponding to the sequential loss of up to three carbonyl groups.

Suitable crystals for an X-ray diffraction study were grown by the slow diffusion of hexane into a CH_2Cl_2 solution of **79**. The ORTEP plot of a single molecule is given in Figure 6.5, together with key structural parameters around the Co_4 core. The structure contains a Co_4 tetrahedron, the basal face of which contains three bridging CO ligands. One of the dppm ligands is also coordinated to the base, while the second bridges a Co(basal) atom and the Co(apical) atom. The remaining coordination sites are occupied by five carbonyl ligands, one each on Co(1, 2 and 3), while Co(4) coordinates two. The Co-Co distances fall in the range 2.4302(4) to 2.5442(4) Å, the shortest of which, Co(1)-Co(2) is bridged by both dppm and CO ligands. The longest Co-Co distance between Co(3) and Co(4) is bridged by a single dppm ligand.

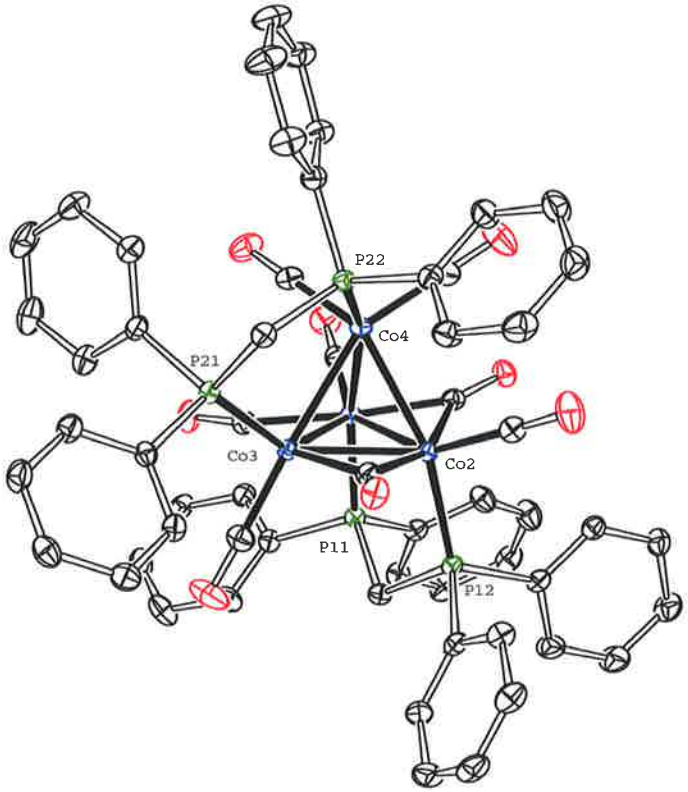

Figure 6.5: *ORTEP view of* ***79****. Selected bond distances (Å) and angles (°): Co(1)-C(11) 1.776(2); Co(2)-C(21) 1.752(3); Co(3)-C(31) 1.767(3); Co(4)-C(41) 1.782(2); Co(1)-C(12) 1.891(2); Co(1)-C(32) 1.983(2); Co(2)-C(22) 1.894(2); Co(2)-C(12) 1.942(2); Co(3)-C(22) 1.950(2); Co(3)-C(32) 1.914(2); Co(4)-C(42) 1.785(3); Co(1)-Co(2) 2.4302(4); Co(1)-Co(3) 2.4965(4); Co(1)-Co(4) 2.5136(4); Co(2)-Co(3) 2.4776(4); Co(3)-Co(4) 2.5442(4); Co(1)-P(11) 2.2009(7); Co(2)-P(12) 2.2029(7); Co(3)-P(21) 2.2049(7); Co(4)-P(22) 2.2184(7); Co(1)-Co(4)-Co(2) 57.89(1); Co(1)-Co(4)-Co(3) 59.13; Co(2)-Co(1)-Co(3) 60.38; Co(1)-Co(2)-Co(3) 61.12; Co(2)-Co(4)-Co(3) 58.73.*

6.3.3. Complexes with Extended Carbon Chains ($n \geq 5$)

At present, it is generally regarded that C_{10} complexes represent the distinction between short and long *sp* carbon chains spanning two transition metals. Unlike their lower analogues, bimetallic complexes bridged by $(C{\equiv}C)_n$ chains where $n \geq 5$ are rare and many lack full characterisation. This is due to the synthetic challenges involved in their preparation, together with the decreased stability of these complexes at longer chain lengths. At the time this work was commenced, only three series of these complexes were reported, the longest examples of which are shown in Figure 6.6.

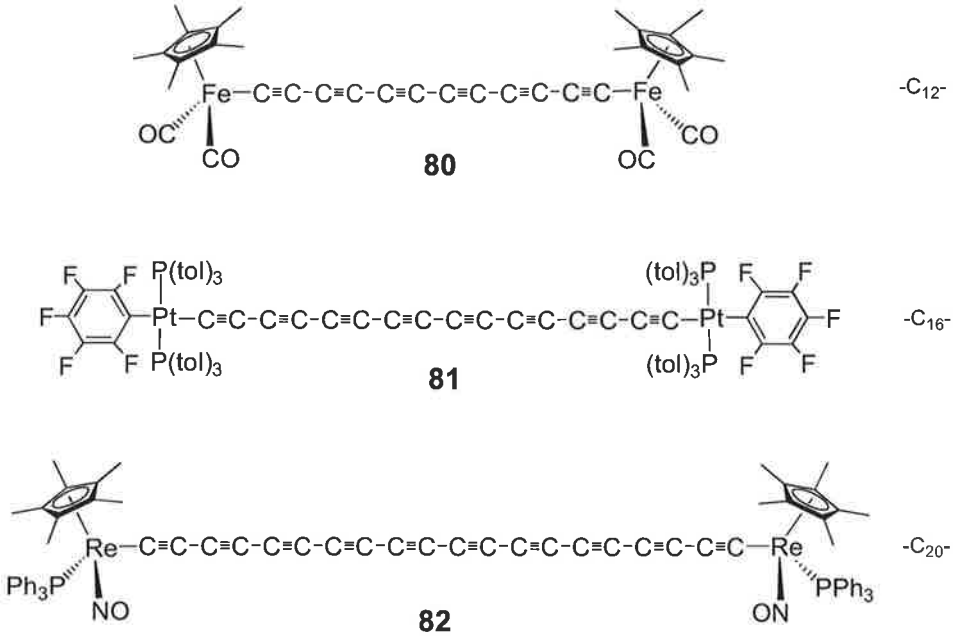

Figure 6.6: *Complexes with extended carbon chains spanning two transition metals.*

The iron C_{12} complex **80** was the longest structurally characterised polyyndiyl complex at the time of publication (1999).[210] It was prepared by the homo-coupling between two mononuclear $[Fe](C{\equiv}C)_3H$ units under Hay conditions, which after purification afforded **80** in an excellent yield (73%). This complex was fully characterised by IR and ^1H and ^{13}C NMR spectroscopic data, which were further supported by elemental microanalysis.

In the bis-platinum series (**81**), complexes with C_8, C_{12} and C_{16} chains have been synthesised, the latter two being structurally characterised.[119] These complexes were analysed by ^{13}C NMR spectroscopy, with chemical shifts of the C_1 and C_2

atoms at *ca* δ 105.0 and 95.0, respectively, while resonances for the inner *sp* carbons were observed between δ 55.9 and 66.7. Further characterisation included IR, UV/Vis absorption, elemental microanalysis and electrochemistry. The cyclic voltammogram of the C_8 complex contained a partially reversible oxidation wave at $E_{½}$ = +0.74, which became thermodynamically more difficult and less reversible as the chain length was increased.

These complexes were synthesised in excellent yields (89-97%) by the homo-coupling (Hay conditions) between two [Pt](C≡C)$_n$H units. More recently the same methodology has been used to prepare trace quantities of the C_{24} complex isolated within a mixture.[197] Related C_{12} complexes featuring the platinum centres Pt(PAr$_3$)$_2$(tol) (Ar = Ph, tol) have also been reported.[118]

The bis-rhenium C_{20} complex **82** completes the largest series of [M]-(C≡C)$_n$-[M] complexes reported, with n = 2, 3, 4, 5, 6, 8 and 10.[46] The stabilities of these compounds decrease significantly upon extension of the bridging carbon chain. While the lower analogues were sufficiently stable to provide correct microanalyses, the C_{20} complex was not as stable and did not give an acceptable analysis. In this case, characterisation data was obtained using IR, Raman, UV/Vis and NMR spectroscopies. The cyclic voltammograms contained two well-separated reversible oxidation waves for the lower analogues ($n \leq 4$), which became thermodynamically more difficult and less reversible as the chain length was extended.

More recently, two examples of C_{12} complexes containing *trans*-RuCl(dppe)$_2$[235] and Ru$_2$(ap)$_4$[68] end-groups have been reported, with the former being structurally characterised. For an up to date account of structurally characterised polyynes, a review has recently been published.[236]

6.3.3.1. Synthesis of {Ru(dppe)Cp}$_2$(C≡C)$_n$ [n = 7 (83), 11 (86)]*

Recently a reaction involving the treatment of gold acetylides {Au[P(tol)$_3$]}$_2$(C≡C)$_n$ (n = 2-4) with two equivalents of the bromocarbyne Co$_3$(μ$_3$-CBr)(μ-dppm)(CO)$_7$ in the presence of Pd(PPh$_3$)$_4$ and CuI gave {Co$_3$(μ-dppm)(CO)$_7$}{μ$_3$:μ$_3$-C(C≡C)$_n$C} (n

= 2, 3, 4) in excellent yields (Scheme 6.10).[213] This reaction shows great potential as an alternative method for the syntheses of complexes with extended carbons chains.

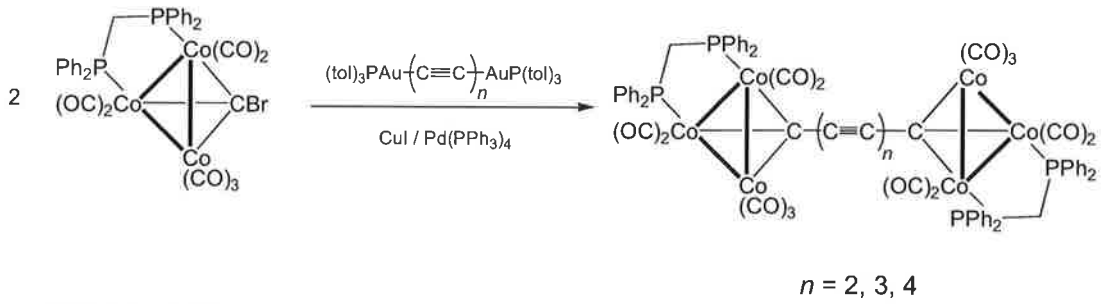

Scheme 6.10

In a procedure related to that just demonstrated, which uses the gold polyyne as the source of the $(C{\equiv}C)_n$ framework, the reaction between a polyyne capped by a gold-phosphine group with a diiodopolyyne in the presence of the palladium/copper catalyst also resulted in a new C(*sp*)-C(*sp*) coupling reaction. As the mixed ruthenium-gold diyndiyl **51** was already prepared (Chapter 4), it was anticipated that the reaction of this complex with various diiodopolyynes would result in double couplings to give a new series of extended chain complexes.

The synthesis of 1,6-diiodohexatriyne $I(C{\equiv}C)_3I$ has recently been reported and can be prepared by the treatment of TMS-$(C{\equiv}C)_3$-TMS with *N*-iodosuccinimide and $AgNO_3$ in DMF to give the diiodo product in 65% yield.[237] **CAUTION**: this compound is quite unstable and must stored in the freezer to prevent decomposition. It is also thermally unstable, exploding above 100°C. On two occasions, rapid decomposition occurred with violent detonations when the compound was scratched as a dry solid.

Treatment of **51** with half an equivalent of $I(C{\equiv}C)_3I$ in the presence of $Pd(PPh_3)_4$ and CuI in a NEt_3/benzene mixture at 0°C gave $\{Ru(dppe)Cp^*\}_2(C{\equiv}C)_7$ (**83**) in 36% yield (Scheme 6.11). Coupling of the hexatriyne with two C_4 fragments has allowed access to a C_{14} system, a chain length that previously has not been reported. This is because all earlier reported extended chain complexes were synthesised from the homo-coupling between two $[M](C{\equiv}C)_nH$ units where $2n$ can only give complexes with 4, 8, 12, 16 or 20 carbon atoms in the chain.

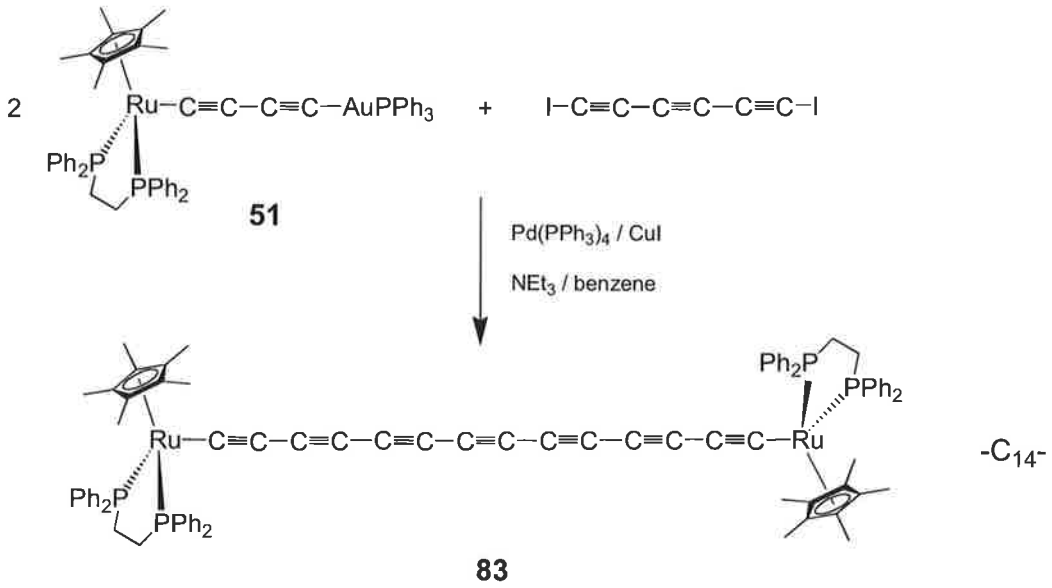

Scheme 6.11

Spectroscopic characterisation of **83** was similar to the related C_4, C_6 and C_8 complexes, with a single resonance at δ 78.96 in the ^{31}P NMR spectrum confirming the equivalence of all four phosphorus nuclei. In the ^{1}H NMR spectrum, a triplet at δ 1.45 [^{2}J(HP) 2 Hz] was assigned to the Cp* ligands, while multiplets at δ 1.70 and 2.36 and between δ 6.99-7.68 were due to dppe. Complex **83** was soluble in most solvents including hexane, CH_2Cl_2 and MeOH, and readily crystallised in the NMR tube to give very thin needles, thereby preventing a well-resolved ^{13}C NMR spectrum to be obtained. The ES-mass spectrum of **83** contained a very weak $[M + H]^+$ ion centred at *m/z* 1438 together with the usual fragment ion at *m/z* 635 due to $[Ru(dppe)Cp^*]^+$. In the IR spectrum, two ν(C≡C) bands were observed at 2058 and 1947 cm^{-1}.

Two independent crystals suitable for X-ray diffraction were grown from separate benzene/MeOH and benzene/hexane solvent mixtures. The X-ray study confirms the identity of **83**, revealing the presence of the linear C_{14} chain capped at both ends by a Ru(dppe)Cp* fragment. Both structures contain benzene molecules in the lattice, with the crystals grown from benzene/MeOH containing four benzene molecules and those grown from benzene/hexane containing seven benzene molecules. The ORTEP plots of **83**·7(C_6H_6) and **83**·4(C_6H_6) are shown in Figures 6.7 and 6.8, respectively, together with selected structural parameters.

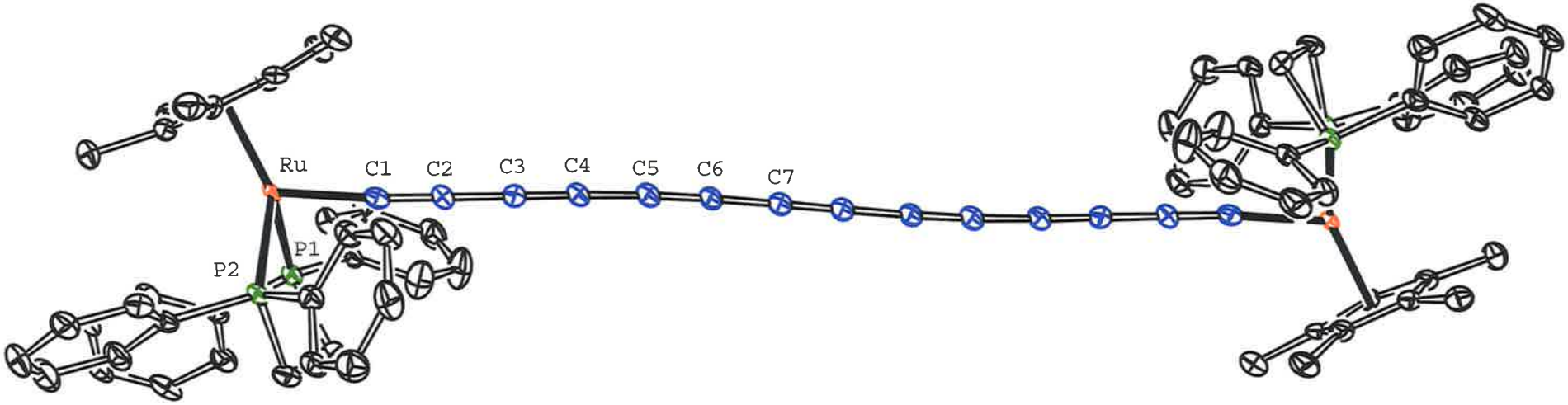

Figure 6.7: *ORTEP plot of* ***83***$\cdot 7(C_6H_6)$. *Selected bond distances (Å) and angles (°): Ru-P(1) 2.282(1); Ru-P(2) 2.289(1); Ru-C(Cp*) 2.231(5)-2.286(3) av. 2.274(5); Ru-C(1) 1.957(4); C(1)-C(2) 1.236(7); C(2)-C(3) 1.353(7); C(3)-C(4) 1.226(7); C(4)-C(5) 1.350(7); C(5)-C(6) 1.217(7); C(6)-C(7) 1.357(7); C(7)-C(7') 1.222(6); P(1)-Ru-P(2) 82.49(5); P(1)-Ru-C(1) 80.7(1); P(2)-Ru-C(1) 91.0(2); Ru-C(1)-C(2) 173.8(4); C(1)-C(2)-C(3) 176.0(5); C(2)-C(3)-C(4) 178.6(5); C(3)-C(4)-C(5) 178.5(5); C(4)-C(5)-C(6) 177.4(6); C(5)-C(6)-C(7) 178.0(6); C(6)-C(7)-C(7') 178.6(5).*

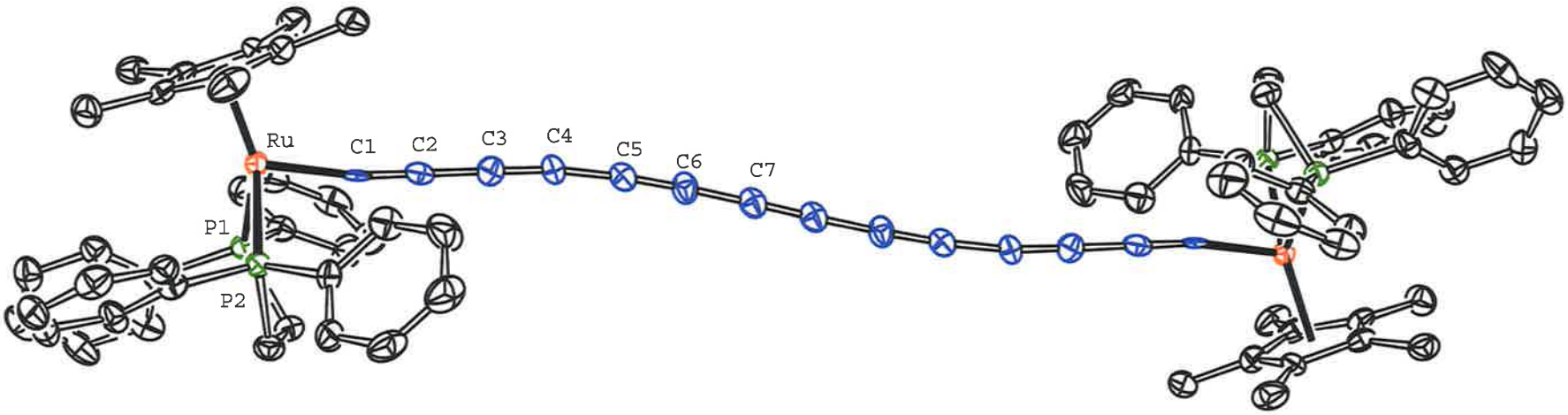

Figure 6.8: *ORTEP plot of **83**·4(C_6H_6). Selected bond distances (Å) and angles (°): Ru-P(1) 2.251(1); Ru-P(2) 2.253(1); Ru-C(Cp*) 2.208-2.262(6) av. 2.234(6); Ru-C(1) 1.917(5); C(1)-C(2) 1.202(8); C(2)-C(3) 1.360(8); C(3)-C(4) 1.200(8); C(4)-C(5) 1.340(8); C(5)-C(6) 1.204(8); C(6)-C(7) 1.330(8); C(7)-C(7') 1.202(8); P(1)-Ru-P(2) 83.01(6); P(1)-Ru-C(1) 82.9(1); P(2)-Ru-C(1) 91.1(2); Ru-C(1)-C(2) 171.7(5); C(1)-C(2)-C(3) 175.6(6); C(2)-C(3)-C(4) 177.8(6); C(3)-C(4)-C(5) 172.0(6); C(4)-C(5)-C(6) 175.6(7); C(5)-C(6)-C(7) 177.0(7); C(6)-C(7)-C(7') 178.9(6).*

Both structures contain a centre of inversion, with the two Cp* ligands arranged *transoid* to each other. The structures also reveal the expected pseudo-octahedral geometry around ruthenium. Selected bond distances are within the expected range with average Ru-P distances for the two structures being 2.286(1) and 2.252(1) Å, while the average Ru-C(Cp*) distances are 2.274(5) and 2.234(6) Å, respectively. For the C_{14} chains, the alternating short and long C-C bonds confirm their polyyne nature.

An interesting feature in both structures is the slight sigmoidal-shape of the C_{14} chain, which is more pronounced in **83**·4(C_6H_6). The average bond angles at the carbon atoms for the two structures are closer to linear in **83**·7(C_6H_6) (177.6°) than in **83**·4(C_6H_6) (175.5°) with the through space Ru-Ru separations of 20.56 and 20.14 Å, respectively, being only 0.2 and 0.8% shorter than the sum of the individual bond lengths along the chain.

As found in related polyyndiyl complexes, this distortion is due to the facile bending modes at the *sp* carbons that result from crystal packing forces.[117,119,174] Two common bending modes are possible and these are represented in Figure 6.9. The most frequently observed situation is **6d** in which a sigmoidal chain is observed. Such structures usually contain a crystallographic centre of inversion bisecting the central C-C single or triple bond. Although less common, several examples of the concave form **6e** have recently been reported in platinum polyyndiyls.[119,197,215] As the angles at the carbon atoms are cumulative, only small deviations from linearity are necessary to produce such effects.

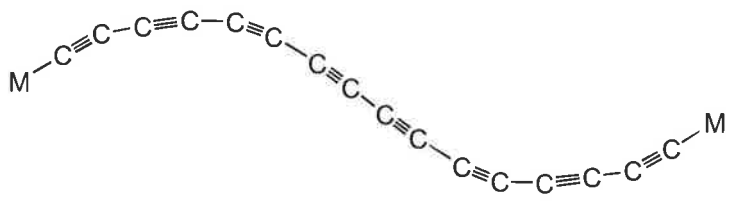

6d

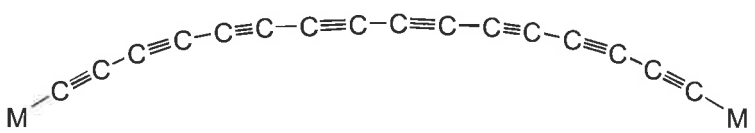

6e

Figure 6.9: *Bending modes in polyyndiyl complexes. (**6d**) sigmoidal and (**6e**) concave.*

Once the C_{14} complex **83** was successfully synthesised, the question remained as to how far this coupling reaction could be extended. The next aim was to synthesise a mixed ruthenium-gold complex with a C_8 bridging ligand to further react with $I(C{\equiv}C)_3I$ and determine if the same coupling reaction would proceed.

In order to make the new mixed octatetrayne complex, the TMS-protected complex Ru(C≡CC≡CC≡CC≡CTMS)(dppe)Cp* (**84**) was firstly prepared. In a similar reaction to the synthesis of **83**, complex **51** was treated with 1,4-diiodobutadiyne IC≡CC≡CTMS in a toluene/NEt_3 mixture in the presence of $Pd(PPh_3)_4$ and CuI (Scheme 6.12). After three hours, hexane was added to precipitate the remaining catalyst, which was removed by filtration. The resulting bright orange solution was purified on a basic alumina column to give a bright yellow band, which was eluted with 1:1 diethyl ether/hexane. ^{31}P NMR spectroscopy revealed two resonances, one at *ca* 79.0 due to the Ru(dppe)Cp* fragment and a second at *ca* 33.0 assigned to $AuI(PPh_3)$, a by-product of the coupling reaction. Separation of the two components was achieved by fractional crystallisation from hexane which gave white crystals of $AuI(PPh_3)$, while **84** remained in solution and could be isolated after a second basic alumina column as a yellow crystalline solid. Yields for this reaction were quite reasonable, ranging between 60-70%.

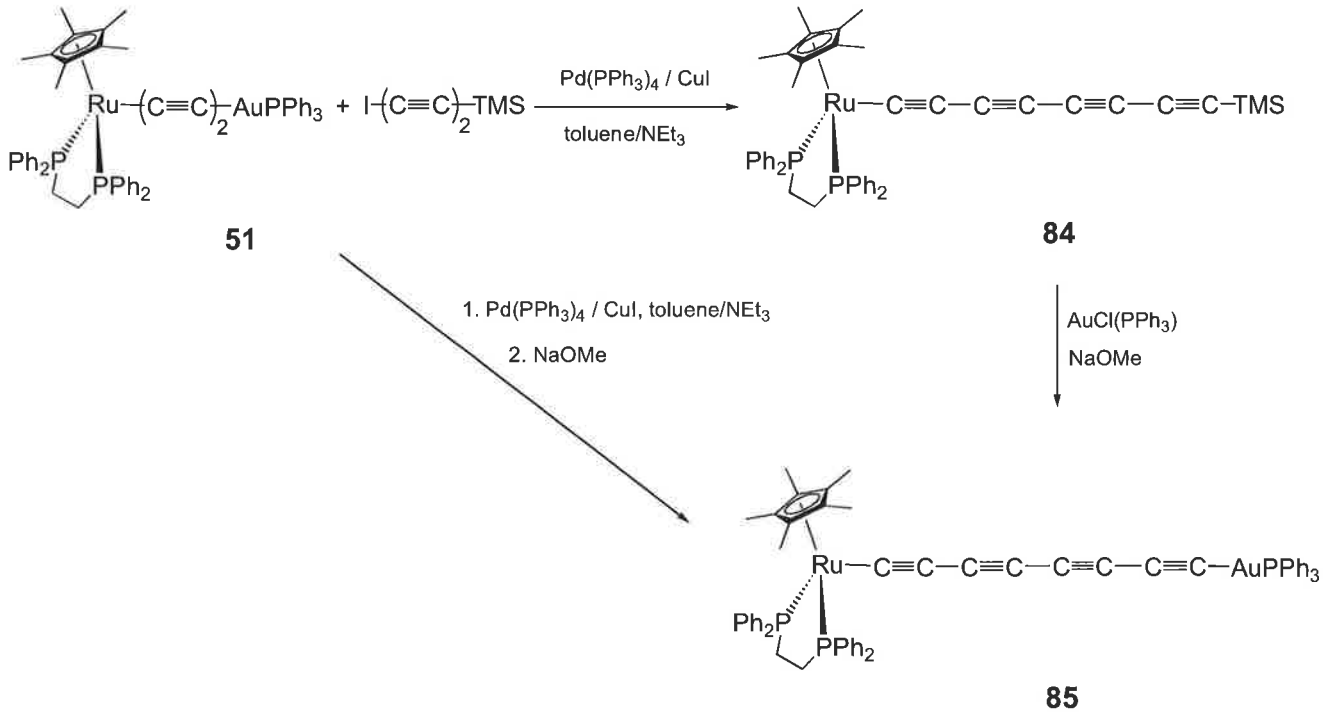

Scheme 6.12

Substitution of the TMS group by a $Au(PPh_3)$ fragment was achieved by treating **84** with $AuCl(PPh_3)$ in the presence of NaOMe (Scheme 6.12). When MeOH was used as the solvent a bright orange product precipitated from solution in 74% yield, which was identified as $Ru\{C{\equiv}CC{\equiv}CC{\equiv}CC{\equiv}C[Au(PPh_3)]\}(dppe)Cp^*$ (**85**). Alternatively, **85** could be prepared by adding NaOMe to a MeOH solution containing **84** and $AuI(PPh_3)$ that was obtained from the initial column (Scheme 6.12).

As expected, the spectroscopic features of **84** and **85** were similar. In the IR spectra, five $\nu(C{\equiv}C)$ bands were found between 2143 and 1957 cm^{-1} in **84**, and four $\nu(C{\equiv}C)$ bands were found between 2129 and 1960 cm^{-1} in **85**. In the ES-mass spectra, a $[M + H]^+$ ion was found at *m/z* 805 for **84**, while in **85** a $[M]^+$ ion was found at *m/z* 1190. In **85**, the aggregate ion $[M + AuPPh_3]^+$ was found at *m/z* 1649, similar to the observation of its C_4 analogue **51**.

In the ^1H NMR spectra of **84**, singlets at δ 1.45 and 0.02 were assigned to the Cp* and TMS groups, respectively, while multiplets at δ 1.74 and 2.37 and between δ 6.86 and 7.69 were due to the dppe ligand. In **85**, the spectrum was somewhat simpler with a single Cp* resonance at δ 1.54, together with resonances for the dppe protons. Both complexes displayed a singlet for the Ru(dppe)Cp* fragment close to δ 79.0 in the ^{31}P NMR spectrum, while in the gold-capped complex **85**, an additional broadened resonance of half intensity assigned to the $Au(PPh_3)$ group was observed at δ 41.40.

In the ^{13}C NMR spectra of both complexes, resonances for the eight quaternary carbon atoms of the C_8 chain were observed and these are summarised in Figure 6.10. In both complexes, triplets close to δ 140.0 were assigned to C_1 based on the large $^2J(CP)$ coupling constants, typical of these systems. The remaining resonances were tentatively assigned to the individual carbon atoms $C_{2\text{-}8}$ based on comparisons with related C_4 complexes **39** and **51**. In **85**, the two carbon atoms closest to the gold phosphine moiety were assigned based upon the broadness of these peaks, a similar feature being found in **51**. In **84**, the C_7 and C_8 carbons were assigned to the only two resonances that did not show coupling to the phosphorus of dppe, at δ 82.09 and 92.57, respectively.

Interestingly, while the coupling constants steadily decrease as the carbons move further from dppe, the C_2 resonances in both complexes showed little if any coupling to the phosphorus nuclei. This phenomenon was also observed in the rhenium complex $Re(C{\equiv}CC{\equiv}CC{\equiv}CC{\equiv}CTMS)(NO)(PPh_3)Cp^*$, which showed strong coupling to phosphorus with C_1 and C_3, but not to C_2.[174]

Ru—C_1—C_2—C_3—C_4—C_5—C_6—C_7—C_8—R

144.04 (24 Hz)	92.29 (1 Hz)	70.44 (3 Hz)	49.91 (2 Hz)	68.59 (2 Hz)	57.27 (1 Hz)	82.09 (s)	92.57 (s)	**84**: R = TMS
141.80 (24 Hz)	91.20 (s)	66.75 (3 Hz)	49.11 (2 Hz)	60.61 (2 Hz)	58.05 (s)	94.06 (br)	88.88 (br)	**85**: R = $AuPPh_3$

Figure 6.10: *^{13}C NMR resonances for the C_8 chain in **84** and **85**.*

Crystals of the TMS-protected complex **84** were grown by the slow evaporation of a CH_2Cl_2/hexane solution. The ORTEP plot of a single molecule is shown in Figure 6.11, while selected structural parameters are collected in Table 6.4.

The most obvious feature of the structure is the sigmoidal bend in the *sp* carbon chain, similar to that observed in **83**·4(C_6H_6). This feature results from bending at the carbon atoms between 169.6(3) and 178.7(4)°, which average to 175.0(4)°. The Ru-C distance is typical for a ruthenium-carbon single bond and the C≡C triple bonds are between 1.206-1.235(6) Å, with the shortest distances found furthest away from ruthenium. Similarly the C-C single bond distances gradually lengthen from 1.345(6) Å between C(2)-C(3) to 1.376(6) Å between C(6)-C(7). This feature is consistent with increased contributions from the cumulene resonance form (Scheme 6.13), as found in related systems.[210] This effect appears to fall off as the carbons extend out from the ruthenium and is the reason why these bond lengths approach the typical values found in 1,3-butadiyne [C≡C, 1.217(1); C-C, 1.384(2) Å].[238]

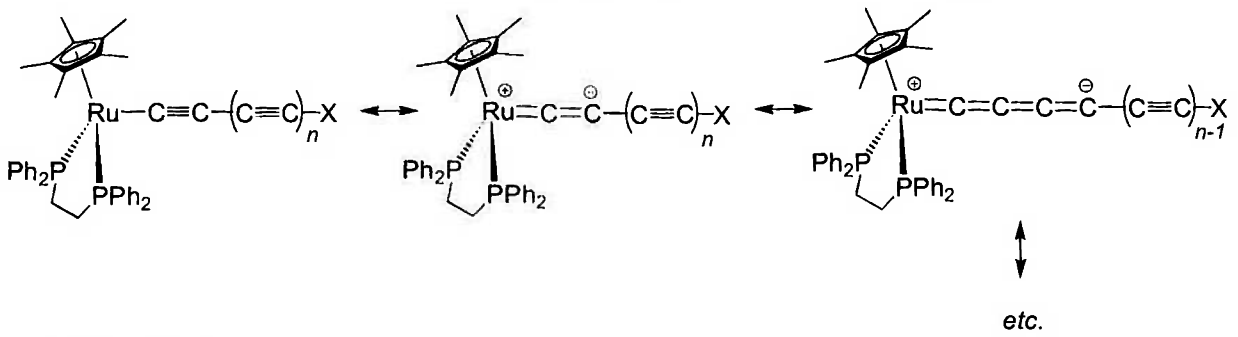

Scheme 6.13

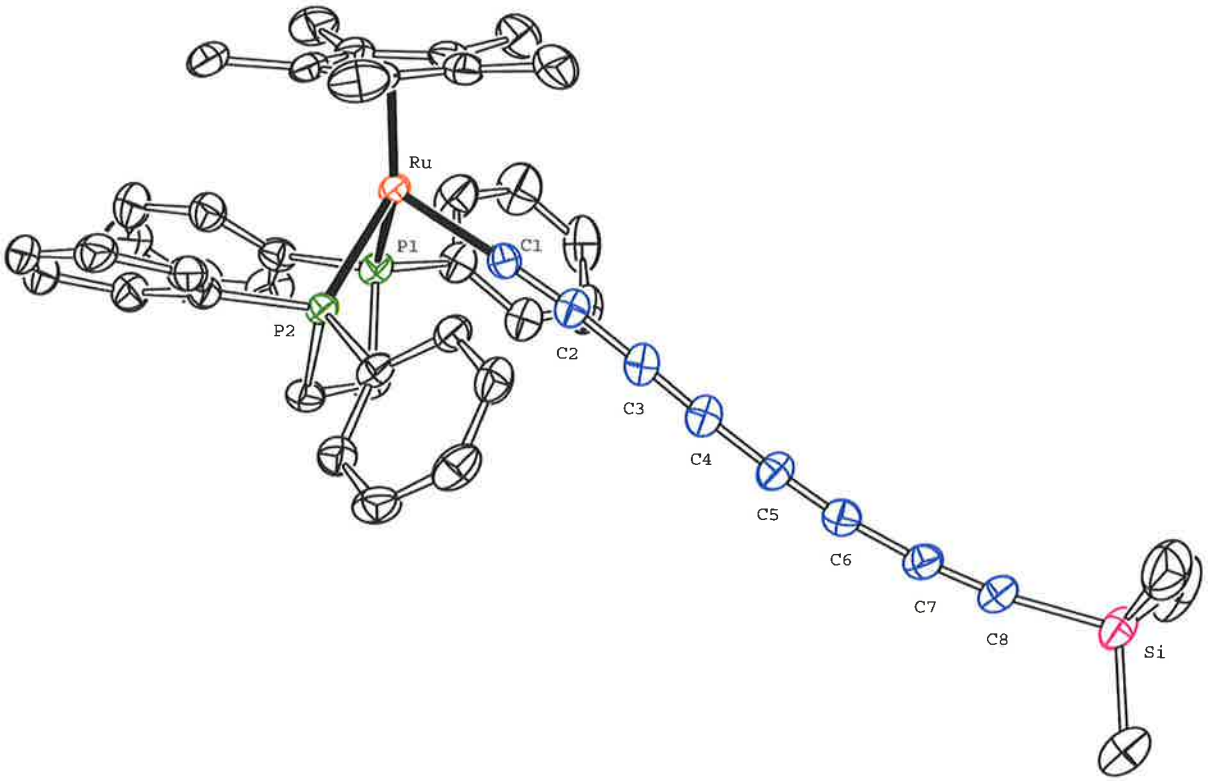

Figure 6.11: *ORTEP view of* ***84****.*

Bond Distances (Å)		**Bond Angles (°)**	
Ru-P(1)	2.2723(9)	P(1)-Ru-P(2)	83.18(3)
Ru-P(2)	2.2856(9)	P(1)-Ru-C(1)	81.3(1)
Ru-C(Cp*)	2.232-2.271(4)	P(2)-Ru-C(1)	86.5(1)
(av.)	2.253(8)	Ru-C(1)-C(2)	177.1(3)
Ru-C(1)	1.963(4)	C(1)-C(2)-C(3)	175.7(4)
C(1)-C(2)	1.235(6)	C(2)-C(3)-C(4)	178.7(4)
C(2)-C(3)	1.345(6)	C(3)-C(4)-C(5)	175.9(4)
C(3)-C(4)	1.220(6)	C(4)-C(5)-C(6)	176.4(4)
C(4)-C(5)	1.357(6)	C(5)-C(6)-C(7)	172.3(4)
C(5)-C(6)	1.211(6)	C(6)-C(7)-C(8)	174.5(4)
C(6)-C(7)	1.376(6)	C(7)-C(8)-Si	169.6(3)
C(7)-C(8)	1.206(6)		
C(8)-Si	1.844(5)		

Table 6.4: *Selected structural parameters for* ***84****.*

With **85** successfully synthesised, it was anticipated that its reaction with $I(C{\equiv}C)_3I$ would result in a double coupling to give the corresponding C_{22} complex. Treatment of **85** with half an equivalent of the diiodopolyyne in the presence of $Pd(PPh_3)_4$ and CuI gave $\{Ru(dppe)Cp^*\}_2(C{\equiv}C)_{11}$ (**86**) as a red solid in 12% yield (Scheme 6.14). In this case, the reaction was hampered by the formation of an intensely purple coloured complex, which was the major product from the reaction and at this stage remains unidentified.

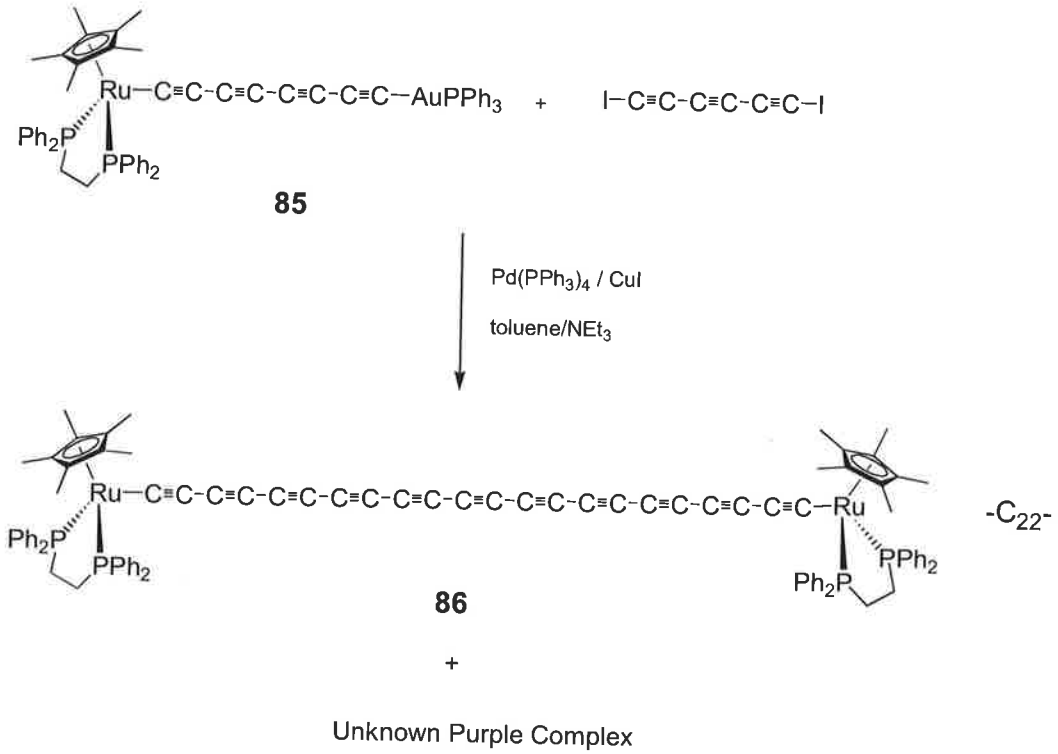

Scheme 6.14

Complex **86** could be isolated from the reaction after purification on a Florisil column and was crystallised from CH_2Cl_2/diethyl ether to give very small microanalytically pure crystals. Despite only being formed in a low yield, **86** was completely characterised except for ^{13}C NMR, which was not obtained due to poor solubility. IR spectroscopy revealed four $\nu(C{\equiv}C)$ bands between 2137 and 1916 cm^{-1}. In the ^{31}P NMR spectrum, a singlet at δ 78.79 was found, while in the ^1H NMR spectrum a triplet resonance for Cp* was observed at δ 1.44. Other resonances for dppe were found as multiplets at δ1.74 and 2.36 and between δ 6.81-7.66. At this stage, crystals suitable for X-ray diffraction have not been obtained.

The unidentified purple product, which prevented the efficient formation of **86** remains unidentified. Small amounts of similar bright purple products were also observed with the syntheses of the C_8 and C_{14} complexes **75** and **83**, respectively. A bright purple complex also formed if the TMS-protected **84** was desilylated with $[Bu^n_4N]F$ in THF. No such products were observed upon thermolysis of **75**, **83** or **86**, suggesting that mono-ruthenium intermediates are the source of these products.

The stability of polyynes has been demonstrated to be strongly dependent on the end-groups. For example, a C_{20} chain capped with two $Re(NO)(PPh_3)Cp^*$ fragments is stable as a solid at room temperature.[46] However, a solid sample of the dicyanopolyyne $NC(C{\equiv}C)_9CN$ decomposes under these conditions.[239] This trend was attributed to the bulky organometallic fragments forcing the carbon chains apart from each other in the crystal lattice, preventing the facile polymerisation.

The stability of the mono-ruthenium complexes $[Ru](C{\equiv}C)_nH$ decreases with increasing chain length, with purple complexes formed when $n > 3$. It is likely that the lack of a bulky end-group at one end of the carbon chain is the source of this decomposition. The formation of the bright purple complex in the reaction of **85** with $I(C{\equiv}C)_3I$ was also found to be concentration dependent. When concentrated reaction mixtures were used, little if any of the desired product **86** was obtained, while dilute solutions kept at low temperatures gave the best yields.

6.3.4. Electrochemistry

The aim of this work was to investigate the electronic interactions between two ruthenium centres across carbon chains of varying lengths. All cyclic voltammograms were recorded in CH_2Cl_2 under standard conditions, provided in the General Experimental Conditions. Electrochemical data are summarised in Table 6.5.

For the C_2 complex **69**, four oxidation waves were observed with the first three being fully reversible [$i_a/i_c = 1$; current proportional to (scan rate)$^{1/2}$], while the E_4 process was only partially reversible ($i_a/i_c = 0.9$) (Figure 6.12).

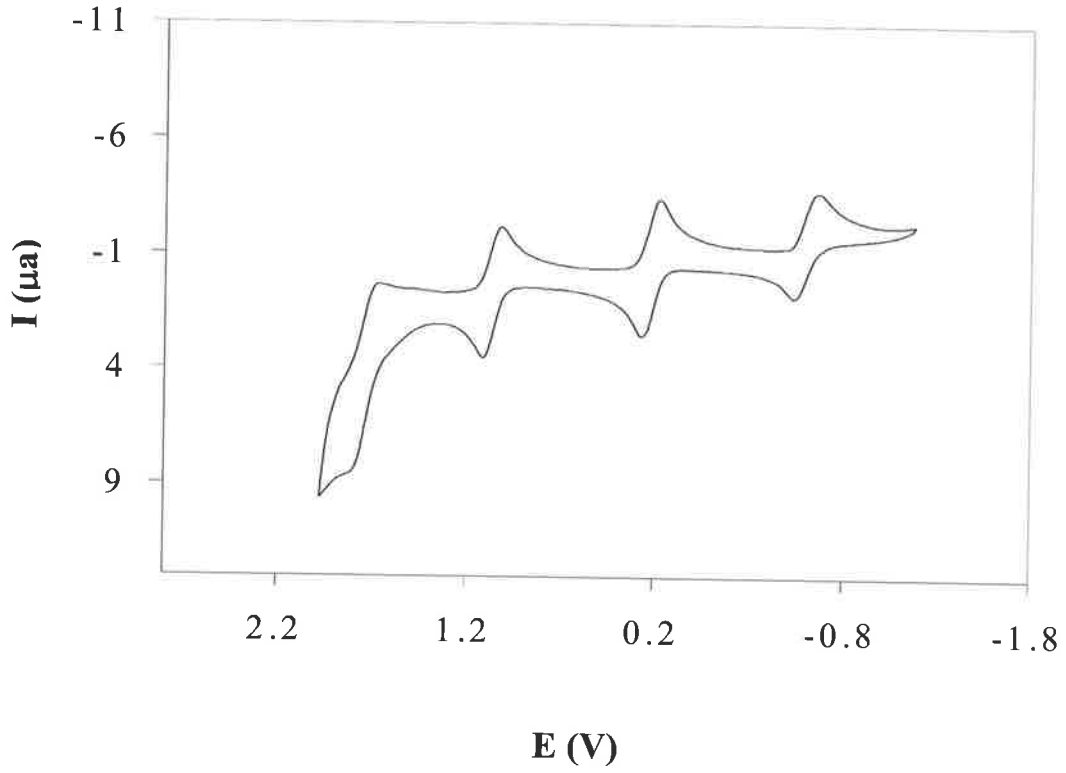

Figure 6.12: *Cyclic voltammogram of* ***69****, recorded in* CH_2Cl_2*, 0.1 M* $[Bu^n_4N][PF_6]$.

In the case of the protonated complex **73**, a single reversible oxidation wave at $E_{½}$ = +0.33 V was followed by an irreversible process at $E_{½}$ = +1.31 V. The relatively high potential of the first process compared with the corresponding wave in the neutral **69** is consistent with **73** existing as a monocation. The second irreversible process suggests that this species undergoes a further chemical reaction at the electrode surface and therefore cannot be regarded as a viable synthetic target.

The cyclic voltammograms of the C_6 and C_8 complexes **74** and **75** confirm that strong interactions exist between the two metal centres across the all-carbon ligand (Figure 6.13). As found for the C_4 complex **25b**, both complexes displayed four redox processes with the first three waves being fully reversible, while the fourth wave was only partially reversible. Despite the large peak separation indicating the stability of the oxidised forms towards disproportionation, chemical oxidation of **74** or **75** did not proceed cleanly. Addition of a slight deficiency of $[FeCp_2][PF_6]$ to a solution of **75** in CH_2Cl_2 resulted in an immediate colour change from yellow to green. However, upon the addition of diethyl ether or hexane, a deep blue solid

precipitated that when analysed by cyclic voltammetry gave a different trace from that of the neutral complex, indicating that a further chemical reaction had occurred after oxidation or isolation. A similar result was found for the C_8 complex $\{Re(NO)(PPh_3)Cp^*\}_2(C{\equiv}C)_4$, for which the mono- and dication could not be isolated.[86] To date, the only C_8 complex that has been chemically oxidised to form an isolable product is the iron complex $\{Fe(dppe)Cp^*\}_2(C{\equiv}C)_4$.[35]

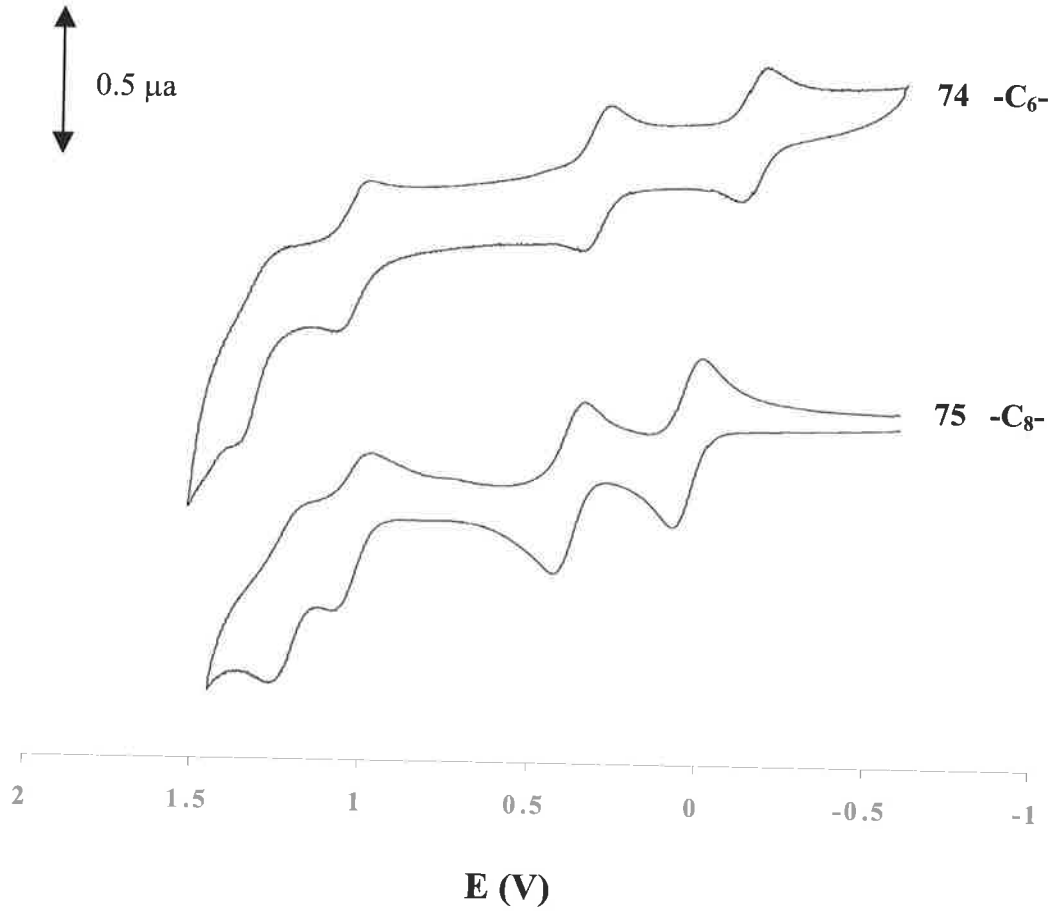

Figure 6.13: *Cyclic voltammograms of 74 and 75, recorded in CH_2Cl_2, 0.1 M $[NBu^n_4][PF_6]$.*

In the cyclic voltammogram of the C_{14} complex **83**, only two waves were observed between -1.0 V and +2.0 V. When the trace was run over this entire range, these two waves were completely irreversible. However, if the switching potential was set at +0.8 V, the second wave became partially reversible while the first wave remained irreversible (Figure 6.14). At low temperatures (-78°C) there was no noticeable difference in the reversibility of these processes. These findings indicate the high chemical reactivity of these species after oxidation.

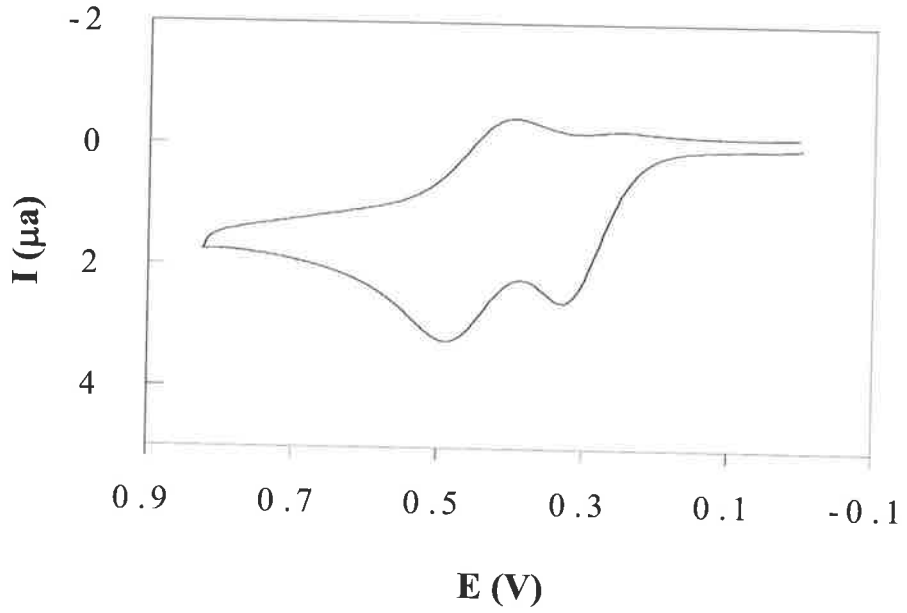

Figure 6.14: *Cyclic voltammogram of* ***83****, recorded in* CH_2Cl_2*, 0.1 M* $[Bu^n_4N][PF_6]$.

Other complexes that have been analysed by cyclic voltammetry included the TCNE derivative **76** and the iron carbonyl adduct **78**. In the case of **76**, two fully reversible waves were observed at $E_{½}$ = +0.64 and +0.84 V, while no reduction waves, usually observed with TCNE adducts, were observed within the solvent imposed limits. In **78**, four oxidations waves were observed, with the first two processes being fully reversible while the third and fourth processes were irreversible.

To gauge the effect on electronic interactions upon addition of TCNE or insertion of a $Fe_3(CO)_9$ unit, comparisons were made with the parent complexes **74** and **75**. Upon reaction of TCNE with **74**, the separation between the first two waves decreased [ΔE = 0.48 (**74**), 0.20 V (**76**)], suggesting that the strong interaction between the two metal centres was significantly reduced. In the case of the C_8 complex, it appears that cleavage of one of the inner C≡C triple bonds and insertion of a $Fe_3(CO)_9$ fragment has reduced the electronic interaction between the two ruthenium fragments [ΔE = 0.35 (**75**), 0.21 V (**78**)], however this effect is not as pronounced as that in the transformation of **74** to **76**. Thus, while the $Fe_3(CO)_9$ fragment has disrupted the π-conjugation, the trinuclear iron cluster can still mediate reasonably strong interactions between the two ruthenium centres.

Complex		E_1	E_2	$\Delta E_{1/2}$	K_c (0/+1/+2) [a]	E_3	E_4
25b	$\{Ru(dppe)Cp^*\}_2(C{\equiv}C)_2$	-0.43	+0.22	0.65	1.27×10^{11}	+1.04	+1.54 [b]
69	$\{Ru(dppe)Cp\}_2(C{\equiv}C)$	-0.61	+0.21	0.82	1.02×10^{14}	+1.06	+1.74 [b]
73	$[\{Ru(dppe)Cp\}_2(C{\equiv}CH)][PF_6]$	+0.33	+1.31 [c]				
74	$\{Ru(dppe)Cp^*\}_2(C{\equiv}C)_3$	-0.15	+0.33	0.48	1.58×10^{8}	+1.05	+1.33 [b]
75	$\{Ru(dppe)Cp^*\}_2(C{\equiv}C)_4$	+0.08	+0.43	0.35	9.5×10^{5}	+1.07	+1.27 [b]
76	$\{Ru(dppe)Cp^*\}_2\{C{\equiv}CC[{=}C(CN)_2]C[{=}C(CN)_2]C{\equiv}C\}$	+0.64	+0.84	0.20	2.6×10^{3}		
78	$Fe_3\{CC{\equiv}C[Ru(dppe)Cp^*]\}\{C(C{\equiv}C)_2[Ru(dppe)Cp^*]\}(CO)_9$	+0.16	+0.37	0.21	3.9×10^{3}	+1.14 [c]	+1.30 [c]
83	$\{Ru(dppe)Cp^*\}_2(C{\equiv}C)_7$	+0.42 [c]	+0.55 [b]	0.17 [d]	8.0×10^{2}		

Table 6.5: *Electrochemical data (V), measured in CH_2Cl_2 with $[Bu^n_4N][PF_6]$ supporting electrolyte, values referenced to $[FeCp_2]/[FeCp_2]^+$ = 0.46 V.* [a] *All values calculated from ΔE and Equation 1.5.* [b] *Partially reversible.* [c] *Peak potential of an irreversible process.* [d] *ΔE was measured as the separation between the two anodic waves.*

With a series of [Ru]-(C≡C)$_n$-[Ru] complexes prepared and their cyclic voltammograms recorded, the influence of chain length on the electronic interactions can be examined. For these comparisons, the separation of the first two waves was considered the best indication of the extent of interactions between the two redox centres. As previously noted in Chapter 2, comparisons between all four ruthenium complexes given in Table 2.3 suggested that subtle changes in the coordinated ligands have little effect on ΔE and for this reason **69** [featuring the Ru(dppe)Cp fragment] is included in comparisons between C_4, C_6, C_8 and C_{14} complexes with the more electron-rich Ru(dppe)Cp* metal centres. The data in Table 6.5 confirm that as the chain length is increased, the interactions between the two ruthenium centres decreases at a steady rate. This trend is represented graphically in Figure 6.15, which is a plot of ΔE for the first two waves as a function of chain length.

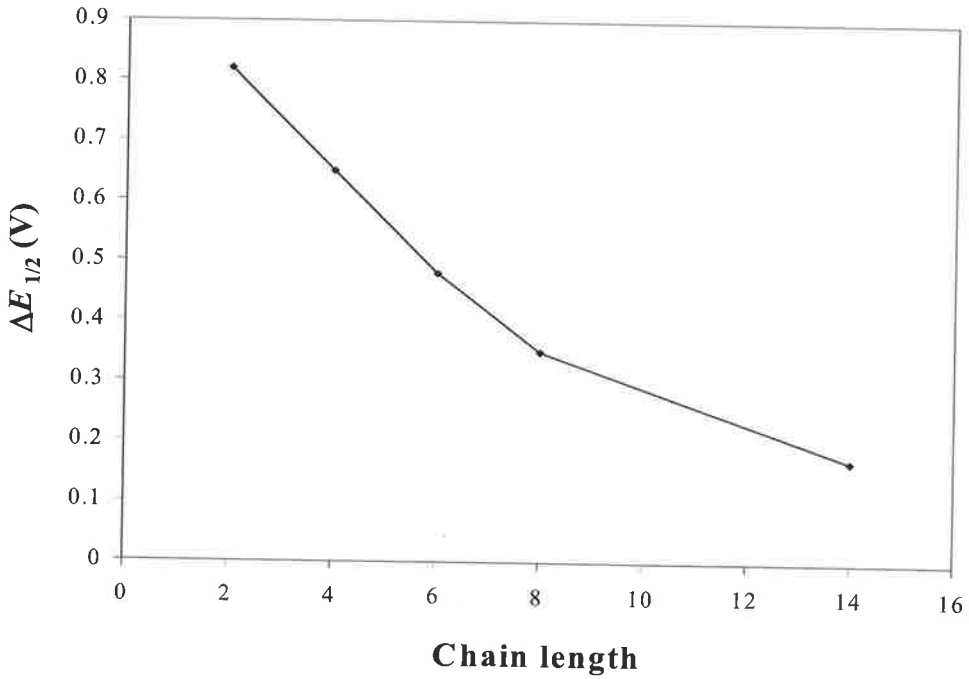

Figure 6.15: *Chain length effect on ΔE in the [Ru]-(C≡C)$_n$-[Ru] series.*

Comparisons of the data contained within Table 6.5 show that as the chain length is extended, E_1 becomes thermodynamically more difficult while the E_4 process becomes easier. In other words, when the chain length is short, the four waves are spread out over a larger range of potentials, while those with higher chain lengths have a narrower range of potentials. The E_2 processes are less affected by chain

length (range +0.21 to +0.51 V), while E_3 are almost completely unaffected by chain length (range +1.04 to +1.07 V). Taking 0.2 V as an indication between Class II and Class III systems, it appears from Figure 6.15 that this value would be reached in the C_{12} complex. While this complex has not been prepared to date, its synthesis would be of considerable interest, as this complex would lie on the boundary of a Class II/III MV complex. Such systems have attracted considerable interest in recent times, displaying properties normally associated with both localised and delocalised electronic states.[74,240]

Similar trends were also observed in the $Re(NO)(PPh_3)Cp^*$ and $Fe(dppe)Cp^*$ series. In these cases, ΔE for the C_8 complexes were 0.29[46] and 0.43 V,[35] respectively. Therefore it can be concluded that the strength of electronic interactions across polyyndiyl ligands is also influenced by the metals and follows the trend Fe > Ru > Re.

6.4. Conclusions

In summary, this work has demonstrated several different methodologies that can be used to synthesise yndiyl and polyyndiyl complexes. Of significant interest were the syntheses of the bis-ruthenium complexes **69** and **86**, which represent the shortest and longest yndiyl and polyyndiyl complexes reported to date with electron-rich metal end-groups. The C_{14} complex **83** represents the second longest polyyndiyl of any type that has been structurally characterised to date, with the two structures having different solvates, displaying the slight bending modes at the *sp* carbons due to crystal packing forces.

Previously regarded as being too sterically hindered to be considered as a viable synthetic target, the ethyndiyl **69** is the first C_2 complex in the M(PP)Cp series (M = Fe, Ru, Os) to be isolated. In this case, cyclic voltammetry confirmed that strong interactions exist between the two ruthenium centres with a large separation in the oxidation waves. This results in a very high value for the comproportionation constant (K_c = 1.02 x 10^{14}), indicating the high thermodynamic stability of the oxidised forms.

While the C_6 and C_8 complexes could not be structurally characterised, reactions with TCNE or $Fe_2(CO)_9$ have afforded adducts which were more readily crystallised, therefore allowing for structural characterisation. In both cases, addition of TCNE to one of the C≡C triple bonds or insertion of a $Fe_3(CO)_9$ fragment, decreased the electronic communication between the two ruthenium centres.

The new coupling reactions of **51** or **85** with iodopolyynes have provided a new and very useful route to complexes with extended carbon chains. Syntheses of the C_{14} and C_{22} complexes have been achieved by the double coupling of $Ru\{(C{\equiv}C)_n[Au(PPh_3)]\}(dppe)Cp^*$ with $I(C{\equiv}C)_3I$ in the presence of Pd(0)/Cu(I) catalyst. Although in the case of **85** the yield was quite low, isolation in an analytically pure form is a significant achievement. As discussed above, polyynes generally decrease in stability with increasing chain length and with sterically less demanding end-groups. Using $Au(PPh_3)$ fragments in these reactions rather than H (usually used in palladium-catalysed cross coupling reactions) has enabled access to higher chain-lengths that would not be possible using conventional methodology. In contrast to the present work, reaction of $Re(C{\equiv}CC{\equiv}CCu)(NO)(PPh_3)Cp^*$ with $Br(C{\equiv}C)_4Br$ was complicated with violent explosions and in no case was the desired C_{16} complex detected,[46] further highlighting the significance of this reaction.

Cyclic voltammetry has confirmed that electronic interactions decrease with increasing chain length. The anticipated change-over point between Class II and Class III MV complex is expected to be the C_{12} complex in the Ru(dppe)Cp* series, a target for future work.

6.5. Experimental

General experimental conditions are detailed on page ix.

Reagents: The compounds RuCl(dppe)Cp,[241] $[Ru(=C=CH_2)(dppe)Cp][PF_6]$[206] $I(C{\equiv}C)_3I$,[237] $Co_2(\mu\text{-dppm})(CO)_6$,[242] IC≡CC≡CTMS,[243] $Pd(PPh_3)_4$[244] and $AuCl(PPh_3)$[176] were all prepared by standard literature methods.

{Cp(dppe)Ru}(C≡C){Ru(dppe)Cp} (69)

To a suspension of **73** (100 mg, 0.08 mmol) in THF (5 mL) was added $KOBu^t$ (35 mg, 0.31 mmol). The colour quickly changed from green to orange and after 5 min, hexane (50 mL) was added and the suspension was concentrated (*ca* 20 mL) on a hot plate before being filtered through a sintered glass funnel. CH_2Cl_2 (1 mL) was added and the orange solution was left to crystallise slowly under a gentle stream of nitrogen. After 24 h, the mother liquor was removed and the red crystals were washed with acetone and diethyl ether to give **69** (24 mg, 27%). Anal. Calcd ($C_{64}H_{58}P_4Ru_2$): C, 66.66; H, 5.07. Found: C, 66.70; H, 5.06. ^{1}H NMR (benzene-d_6): δ 1.92, 2.11 (2m, 2 x 4H, CH_2CH_2), 4.59 (s, 10H, Cp), 6.85-7.93 (m. 40H, Ph). ^{13}C NMR (benzene-d_6): δ 29.09 (m, CH_2CH_2), 82.84 (s, C_5H_5), 129.18-145.90 (m, Ph). ^{31}P NMR (benzene-d_6): δ 87.79 (br, dppe). ES-mass spectrum (*m/z*): 1154, $[M + H]^+$; 577 $[M + H]^{2+}$.

[{Ru(dppe)Cp*}$_2$(C≡CH)][PF$_6$] (73)

To a solution of RuCl(dppe)Cp (350 mg, 0.58 mmol) in THF (20 mL) was added AgOTf (144 mg, 0.56 mmol, 0.97 eq) and the suspension was left to stir in the dark for 30 min. In a separate flask $[Ru(=C=CH_2)(dppe)Cp][PF_6]$ (429 mg, 0.58 mmol) in THF (20 mL) was treated with a 2.5 M solution of Bu^nLi in hexane (0.48 mL, 1.20 mmol, 2.1 eq) and the solution was left to stir at r.t. for 30 min. The suspension of [Ru(THF)(dppe)Cp][OTf] was filtered through a pad of Celite into the solution of Ru(C≡CLi)(dppe)Cp. Stirring was continued at r.t. for 12 h after which the orange solution was passed down a silica column (20 cm) eluting a bright green band with acetone. The solvent was removed and the residue was extracted in a minimum quantity of CH_2Cl_2 and filtered into rapidly stirred diethyl ether (300 mL) to give a

green powder identified as **73** (508 mg, 67%). An analytically pure sample was prepared by crystallisation from CH_2Cl_2/hexane. Anal. Calcd ($C_{64}H_{59}F_6P_5Ru_2$): C, 59.17; H, 4.57. Found: C, 59.07; H, 4.45. ^{1}H NMR (CD_2Cl_2): δ 1.91, 2.08 (2m, 2 x 4H, CH_2CH_2), 2.51 [quintet, ^3J(HP) 6 Hz, C≡CH], 4.75 (s, 10H, Cp), 6.52-8.02 (m. 40H, Ph). ^{31}P NMR (CD_2Cl_2): δ -142.43 (septet, PF_6), 81.66 (s, dppe). ES-mass spectrum (*m/z*): 1154, $[M]^+$; 577 $[M]^{2+}$.

{Cp*(dppe)Ru}(C≡CC≡CC≡C){Ru(dppe)Cp*} (74)

To a suspension of **19b** (321 mg, 0.48 mmol) and KF (28 mg, 0.48 mmol) in MeOH (25 mL) was added TMS-$(C\equiv C)_3$-TMS (50 mg, 0.23 mmol). The reaction was stirred at r.t. for 12 h. The yellow suspension was then filtered on a sintered glass funnel and washed with acetone (2 x 10 mL) followed by pentane (5 x 10 mL) to give **74** as a crude solid (250 mg, 81%). An analytically pure sample was obtained by dissolving the crude solid in CH_2Cl_2 and passing it through a basic alumina squat column (5 cm), eluting with CH_2Cl_2. The solution was concentrated under vacuum (*ca* 5 mL) resulting in a yellow crystalline solid precipitating. The suspension was centrifuged and the bright yellow solid washed several times with diethyl ether (175 mg, 57%). Anal. Calcd ($C_{78}H_{78}P_4Ru\cdot\frac{1}{2}CH_2Cl_2$): C, 68.12; H, 5.75. Found: C, 68.51; H, 5.17. IR (Nujol, cm^{-1}): ν(C≡C) 2129 w, 2057 s, 1959 m. ^{1}H NMR: δ 1.61 (s, 30H, Cp*), 2.16, 2.81 (2m, 2 x 4H, CH_2CH_2), 7.20-7.88 (m, 40H, Ph). ^{31}P NMR: δ 79.41 (s, dppe). ES-mass spectrum (*m/z*): 1342, $[M]^+$; 635, $[Ru(dppe)Cp^*]^+$.

{Cp*(dppe)Ru}(C≡CC≡CC≡CC≡C){Ru(dppe)Cp*} (75)

To a cooled (0°C) suspension of **19b** (250 mg, 0.37 mmol) and KF (22 mg, 0.37 mmol) in MeOH (25 mL) was added TMS-$(C\equiv C)_4$-TMS (45 mg, 0.18 mmol). The suspension was allowed to warm to r.t. and continued to stir in the dark for 3 h. The brick red suspension was filtered on a sintered glass funnel and washed with MeOH (10 mL) followed by pentane (2 x 10 mL) to give **75** (226 mg, 89%). Anal. Calcd ($C_{80}H_{78}P_4Ru$): C, 70.37; H, 5.75. Found: C, 70.40; H, 5.87. IR (Nujol, cm^{-1}): ν(C≡C) 2107 m, 1951 m. ^{1}H NMR: δ 1.49 (s, 30H, Cp*), 2.09, 2.67 (2m, 2 x 4H, CH_2CH_2), 7.09-7.66 (m, 40H, Ph). ^{13}C NMR: δ 10.23 (s, $C_5\underline{Me}_5$), 29.79 (s,

CH_2CH_2), 51.12 (s, C_4), 63.60 (s, C_3), 92.54 (s, C_2), 93.79 (s, $\underline{C}_5Me_5$), 94.58 [t, ^2J(CP) 22 Hz, C_1], 127.69-138.62 (m, Ph). ^{31}P NMR: δ 79.99 (s, dppe). ES-mass spectrum (*m/z*): 1398, $[M + MeOH]^+$; 1366, $[M]^+$; 635, $[Ru(dppe)Cp^*]^+$.

{Ru(dppe)Cp*}$_2${μ-C≡CC[=C(CN)$_2$]C[=C(CN)$_2$]C≡C} (76)

To a suspension of **74** (50 mg, 0.037 mmol) in CH_2Cl_2 (20 mL) was added TCNE (9.5 mg, 0.074 mmol) resulting in an immediate colour change from yellow to blue. The mixture was stirred at r.t. for 1 h, gradually changing to a deep red solution. The solvent was removed and the residue extracted in minimum CH_2Cl_2 and purified using preparative TLC 1:3 acetone/hexane (R_f = 0.5) to give a red band identified as **76** (30 mg, 55%). Anal. Calcd ($C_{84}H_{78}N_4P_4Ru_2{\cdot}½CH_2Cl_2$): C, 67.12; H, 5.26; N, 3.70. Found: C, 66.88; H, 5.30; N, 3.74. IR (Nujol, cm^{-1}): ν(CN) 2208 w, 2193 w; ν(C≡C) 1973 sh, 1959 m. ^{1}H NMR: δ 1.51 [t, ^4J(HP) 2 Hz, 30H, Cp*], 1.98, 2.44 (2m, 2 x 4H, CH_2Cl_2), 6.77-7.71 (m, 40H, Ph). ^{13}C NMR: δ 10.23 (s, $C_5\underline{Me}_5$), 29.26 (s, CH_2CH_2), 96.07 [t, ^2J(CP) 2 Hz, $\underline{C}_5Me_5$], 115.61, 116.97 (2s, CN), 122.25 [s, C_3 or $\underline{C}(CN)_2$], 127.42-138.28 (m, Ph) 148.82 [t, ^3J(CP) 2 Hz, C_2], 204.94 [t, ^2J(CP) 21 Hz, C_1]. ^{31}P NMR: δ 76.04 [d, ^3J(PP) 13 Hz, dppe], 79.88 [d, ^3J(PP) 13 Hz, dppe]. ES-mass spectrum (*m/z*): 1493, $[M + Na]^+$.

Fe_3{μ$_3$-CC≡C[Ru(dppe)Cp*]}$_2$(CO)$_9$ (77)

A suspension of **74** (200 mg, 0.15 mmol) and $Fe_2(CO)_9$ (327 mg, 0.9 mmol) in THF (100 mL) was heated to reflux for 2 h, gradually changing colour from orange to cherry red. The solvent was removed and the residue extracted in CH_2Cl_2 and passed down a silica gel column (10 cm) eluting a bright red band with 1:1 acetone/hexane. The complex was further purified by preparative TLC using a 1:3 acetone/hexane solvent system (R_f = 0.6) to give the cherry red complex **77** (18 mg, 7%). Anal. Calcd ($C_{87}H_{78}O_9P_4Ru_2Fe_3{\cdot}½CH_2Cl_2$): C, 58.27; H, 4.41. Found: C, 58.52; H, 4.75. IR (Cyclohexane, cm^{-1}): ν(CC) 2078 w; ν(CO) 2018 m, 2012 m, 1988 m, 1948 sh, 1934 br. ^{1}H NMR: δ 1.59 (s, 30H, Cp*), 2.05, 2.70 (2m, 2 x 4H, CH_2CH_2), 7.15-7.71 (m, 40H, Ph). ^{13}C NMR: δ 10.33 (s, $C_5\underline{Me}_5$), 29.22 (s, CH_2CH_2), 94.33 (s, $\underline{C}_5Me_5$), 126.84-138.23 (m, Ph), 145.59 (s, RuC≡$\underline{C}$), 188.59 [t,

^{2}J(CP) 24 Hz, Ru$\underline{C}$≡C], 212.44 (s, CO), 263.18 (S, ≡C$\underline{C}$Fe$_3$). ^{31}P NMR: δ 78.45 (s, dppe).

Fe$_3${μ$_3$-CC≡C[Ru(dppe)Cp*]}{μ$_3$-CC≡CC≡C[Ru(dppe)Cp*]}(CO)$_9$ (78)

A solution of **75** (100 mg, 0.07 mmol) and $Fe_2(CO)_9$ (107 mg, 0.29 mmol) in THF (25 mL) was heated to reflux for 2 h, gradually changing colour from orange to cherry red. The solvent was removed and the red residue extracted in minimum CH_2Cl_2 and loaded onto a silica column (10 cm). Elution with 1:1 acetone/hexane gave a cherry red band that was collected and the solvent removed. The complex was further purified by preparative TLC using 1:3 acetone/hexane to give a cherry red band (R_f = 0.6) identified as **78** (38 mg, 30%). Anal. Calcd ($C_{89}H_{78}Fe_3O_9P_4Ru_2$): C, 59.88; H, 4.40. Found: C, 60.04; H, 4.44. IR (Nujol, cm^{-1}): ν(C≡C) 2078 w; ν(CO) 2042 m, 2025 s, 2021 s, 1998 m, 1993 m, 1964 w, 1959 w, 1933 w, 1930 w. ^{1}H NMR: δ 1.48 (s, 15H, Cp*), 1.55 (s, 15H, Cp*), 2.01, 2.66 (2m, 2 x 4H, CH_2CH_2), 7.09-7.65 (m, 40H, Ph). ^{13}C NMR: δ 10.21, 10.57 (2s, $C_5\underline{Me}_5$), 29.96 (m, CH_2C_2), 53.65, 86.91, 96.77, 149.23 (4s, C≡$\underline{C}\underline{C}$≡$\underline{C}CFe_3C\underline{C}$≡C), 94.29, 95.47 (2s, $\underline{C}_5Me_5$), 127.72-138.37 (m, Ph), 161.65, 171.84 (2s, Ru$\underline{C}$≡C), 211.92 (s, CO), 257.98, 273.25 (2s, ≡C$\underline{C}$Fe$_3$$\underline{C}$C≡). ^{31}P NMR: δ 78.04 (s, dppe), 79.04 (s, dppe).

Co$_4$(μ-dppm)$_2$(CO)$_8$ (79)

A solution of Co_2(μ-dppm)$(CO)_6$ (50 mg, 0.074 mmol) and **74** (98 mg, 0.074 mmol) in benzene (20 mL) was heated at reflux for 1 h. Solvent was removed under vacuum and the residue purified by preparative TLC (3:7 acetone/hexane). Black crystals ($CHCl_3$/MeOH) of **79** (36 mg, 71%) were obtained from the olive-green band (R_f = 0.4). Anal. Calcd ($C_{58}H_{44}Co_4O_8P_4$): C, 56.7; H, 3.6. Found: C, 56.0; H, 3.7. IR (Cyclohexane, cm^{-1}): ν(CO) 2012 s, 1980 s, 1969 w, 1953 m, 1828 w, 1787 m, 1766 m. ^{1}H NMR (benzene-d_6): δ 3.59 (m br, 4H, CH_2); 6.92-7.54 (m, 40H, Ph). ^{31}P NMR (benzene-d_6): δ 24.67 (br, dppm). ES-mass spectrum (*m/z*): 1228, $[M]^+$; 1200, $[M - CO]^+$; 1172, $[M - 2CO]^+$; 1144, $[M - 3CO]^+$.

{Cp*(dppe)Ru}(C≡CC≡CC≡CC≡CC≡CC≡CC≡C){Ru(dppe)Cp*} (83)

To a solution of **51** (200 mg, 0.17 mmol) in 1:1 NEt_3/benzene (30 mL) was added $I(C{\equiv}C)_3I$ (28.5 mg, 0.09 mmol) followed by $Pd(PPh_3)_4$ (20 mg, 0.02 mmol) and CuI (2 mg, 0.01 mmol). The solution was stirred at r.t. for 3 h, before being loaded directly onto an alumina column (30 cm). Elution with diethyl ether removed any free $AuI(PPh_3)$. Elution with 3:7 NEt_3/benzene gave a yellow band that was evaporated to give **83** (45 mg, 36%). A microanalytically pure sample was prepared by crystallisation from CH_2Cl_2/hexane. Anal. Calcd ($C_{86}H_{78}P_4Ru_2{\cdot}CH_2Cl_2$): C, 68.63; H, 5.29. Found: C, 68.92; H, 5.19%. IR (Nujol, cm^{-1}): ν(C≡C) 2058 m, 1947 br. ^1H NMR (benzene-d_6): δ 1.45 [t, ^3J(HP) 2 Hz, 30H, Cp*], 1.70, 2.36 (2m, 2 x 4H, CH_2CH_2), 6.99-7.68 (m, 40H, Ph). ^{13}C NMR (benzene-d_6): δ 10.39 (s, $C_5\underline{Me}_5$), 30.01 (s, CH_2CH_2), 94.75 (s, $\underline{C}_5Me_5$), 129.43-133.95 (m, Ph). ^{31}P NMR (benzene-d_6): δ 78.96 (s, dppe). ES-mass spectrum (*m/z*): 1438, $[M + H]^+$; 635, $[Ru(dppe)Cp^*]^+$.

Ru(C≡CC≡CC≡CC≡CTMS)(dppe)Cp* (84)

To a suspension of **51** (400 mg, 0.35 mmol) and IC≡CC≡CTMS (104 mg, 0.42 mmol) in 2:1 toluene/NEt_3 (30 mL) at 0°C was added $Pd(PPh_3)_4$ (40 mg, 0.04 mmol) and CuI (6.4 mg, 0.0035 mmol). The suspension was slowly warmed to r.t. over a period of 3 h. The resulting orange solution was diluted with hexane (100 mL) precipitating any excess catalyst. The filtrate was loaded directly onto a basic alumina column (20 cm). Elution with hexane removed any excess organic starting material. Elution with 1:1 diethyl ether/hexane gave a bright yellow band that was evaporated to dryness. The residue was extracted in hexane (300 mL) and left in the freezer overnight to crystallise any remaining $AuI(PPh_3)$. The next day the suspension was filtered and the yellow solution loaded directly onto a basic alumina column. Elution with 1:1 diethyl ether/hexane gave a bright yellow band that was evaporated to dryness to give **84** (180 mg, 64%). Anal. Calcd ($C_{47}H_{48}P_2RuSi$): C, 70.21; H, 6.02. Found: C, 70.18; H, 5.94. IR (Nujol, cm^{-1}): ν(C≡C) 2143 w, 2105 w, 2064 sh, 2034 m, 1957 m. ^1H NMR (benzene-d_6): δ 0.02 (s, 9H, TMS), 1.45 (s, 15H, Cp*), 1.74, 2.37 (2m, 2 x 2H, CH_2CH_2), 6.86-7.69 (m, 20H, Ph). ^{13}C NMR (benzene-d_6): δ 0.15 (s, TMS), 10.42 (s, $C_5\underline{Me}_5$), 30.04 (s, CH_2CH_2), 49.91 [t, ^5J(CP)

2 Hz, C_4], 57.27 [t, ^7J(CP) 1 Hz, C_6], 68.59 [t, ^6J(CP) 2 Hz, C_5], 70.44 [t, ^4J(CP) 3 Hz, C_3], 82.09 (s, C_7), 92.29 [t, ^3J(CP) 1 Hz, C_2] 92.57 (s, C_8), 94.68 [t, ^2J(CP) 2 Hz, $\underline{C}_5Me_5$], 127.93-138.47 (m, Ph), 144.04 [t, ^2J(CP) 24 Hz, C_1]. ^{31}P NMR (benzene-d_6): δ 79.35 (s, dppe). ES-mass spectrum (*m/z*): 805, $[M + H]^+$; 635, $[Ru(dppe)Cp^*]^+$.

Ru{C≡CC≡CC≡CC≡C[Au(PPh$_3$)]}(dppe)Cp* (85)

To a solution of **84** (200 mg, 0.24 mmol) and AuCl(PPh$_3$) (122 mg, 0.24 mmol) in MeOH (20 mL) was added a solution of NaOMe (2.4 mmol) made from 57 mg of Na in 1 mL of MeOH. The reaction was stirred at r.t. for 30 min before being concentrated (*ca* 2 mL). The resulting precipitate was filtered and washed with MeOH to give **85** (218 mg, 74%). Anal. Calcd ($C_{62}H_{54}AuP_3Ru$): C, 62.57; H, 4.57. Found: C, 62.50; H, 4.62. IR (Nujol, cm^{-1}): ν(C≡C) 2129 w, 2103 m, 2028 m, 1960 m. ^{1}H NMR: δ 1.54 (s, 15H, Cp*), 2.14, 2.70 (2m, 2 x 2H, CH_2CH_2), 7.16-7.64 (m, 20H, Ph). ^{13}C NMR (CD_2Cl_2): δ 10.26 (s, $C_5\underline{Me}_5$), 29.87 (s, CH_2CH_2), 49.11 [t, ^5J(CP) 2 Hz, C_4], 58.05 (s, C_6), 60.61 [t, ^6J(CP) 2 Hz, C_5], 66.75 [t, ^4J(CP) 3 Hz, C_3], 88.88 (br, C_8), 91.20 (s, C_2) 94.06 (br, C_7), 94.60 [t, ^2J(CP) 2 Hz, $\underline{C}_5Me_5$], 127.91-138.20 (m, Ph), 141.80 [t, ^2J(CP) 24 Hz, C_1]. ^{31}P NMR (benzene-d_6): δ 41.40 (s, 1P, PPh$_3$), 79.30 (s, 2P, dppe). ES-mass spectrum (*m/z*): 1649, $[M + AuPPh_3]^+$; 1190, $[M]^+$.

{Cp*(dppe)Ru}(C≡C)$_{11}${Ru(dppe)Cp*} (86)

To a solution of **85** (50 mg, 0.042 mmol) in 3:7 NEt$_3$/toluene (200 mL) at -60°C ($CHCl_3/CO_2$) was added I(C≡C)$_3$I (7 mg, 0.021 mmol) followed by Pd(PPh$_3$)$_4$ (5 mg, 0.0042 mmol) and CuI (0.8 mg, 0.0042 mmol). The solution was stirred at -60°C for 4 h before being warmed to r.t. over a period of 1 h. The solvent was removed and the residue was extracted with 1:3 benzene/hexane until no further colour was removed. The extracts were loaded onto a Florisil column (20 cm) and a bright orange band was eluted with 1:9 hexane/diethyl ether to give **86** (4 mg, 12%). Anal. Calcd ($C_{94}H_{78}P_4Ru_2$): C, 73.61; H, 5.12. Found: C, 73.50; H, 5.20%. IR (Nujol, cm^{-1}): ν(C≡C) 2137 w, 2065 w, 1998 m 1916 m. ^{1}H NMR (benzene-d_6):

δ 1.44 [t, ^{3}J(HP) 2 Hz, 30H, Cp*], 1.74, 2.36 (2m, 2 x 4H, CH_2CH_2), 6.81-7.66 (m, 40H, Ph). ^{31}P NMR (benzene-d_6): δ 78.79 (s, dppe). Elution with CH_2Cl_2 gave a bright purple band that was evaporated to give an unidentified complex (5 mg).

General Conclusions

In summary, this Thesis presents the study of a novel family of bimetallic complexes, $\{Ru(dppe)Cp'\}_2(C{\equiv}C)_n$ (Cp' = Cp*, Cp), which serve to increase the overall understanding of ruthenium alkynyl chemistry. The incorporation of the electron-rich organo-ruthenium synthon, Ru(dppe)Cp*, has provided complexes that are redox-active, enabling the use of cyclic voltammetry to evaluate the through-bridge interactions in these binuclear systems. The bulky Cp* and dppe ligands also provided complexes that were readily crystallised, enabling the structural characterisation of almost all complexes reported to be achieved.

Within the $\{Ru(dppe)Cp'\}_2(C{\equiv}C)_n$ series, complexes with n = 1, 2, 3, 4, 7 and 11 have been prepared. Cyclic voltammetry has revealed that within the bis-ruthenium C_2, C_4, C_6 and C_8 complexes, very strong to strong interactions exist between the two ruthenium end-groups, highlighting the potential of these complexes to be used as one-dimensional molecular wires. Although yet to be synthesised, the C_{12} complex in this series is expected to lie on the boundary of a Class II/III system, a target for future work.

As described in Chapter 6, the coupling reaction between the mixed ruthenium-gold complexes $Ru\{(C{\equiv}C)_n[Au(PPh_3)]\}(dppe)Cp^*$ (n = 2, 4) with the diiodopolyyne $I(C{\equiv}C)_3I$ presents a very useful route into the syntheses of complexes with extended carbon chains. The use of the gold-phosphine protecting group in this reaction is very important as it prevents the isolation of the terminal acetylide complex $Ru\{(C{\equiv}C)_nH\}(dppe)Cp^*$, a compound that has only moderate stability when n = 2 and is unstable when n = 4.

This work has also resolved the previously unknown influence that the trinuclear clusters $Fe_3(CO)_9$ and $Cu_3(\mu\text{-dppm})_3$ have on electronic interactions in binuclear systems. In these cases, it was found that while there were some decrease in the electronic interaction between the ruthenium end-groups, the separation between the first two redox processes in the cyclic voltammograms confirm strong interactions are still present. Not surprisingly, addition of the electron-deficient alkene TCNE to

the unsaturated carbon chain reduced the interactions considerably, however some separation in the first two redox processes remained.

Only a limited number of oxidised complexes of the general formula $[M\text{-}C_4\text{-}M]^{n+}$ have been isolated. Such complexes are generally regarded as being difficult to purify and are even more difficult to obtain crystals suitable for structural characterisation, with the structures of only five complexes of this type reported in the literature. This work reports the X-ray structural data for an additional six complexes in this series, increasing the understanding of how oxidation influences the nature of the bridging C_4 ligand in these systems. Also a significant result is the X-ray structures of the complete series containing the neutral, mono- and dication of the diyndiyl complex $\{Ru(dppe)Cp^*\}_2(C{\equiv}CC{\equiv}C)$, confirming the expected decrease in the C≡C bond order as oxidation proceeds, with a concomitant increase in the Ru-C and C-C bond orders. While spectroscopic and structural data for the C_4 oxidised derivatives were obtained, the highly reactive nature of the C_6 and C_8 derivatives prevented their isolation on a preparative or semi-preparative scale.

The syntheses of ruthenium-iron diyndiyls $\{Cp^*(dppe)Ru\}(C{\equiv}CC{\equiv}C)\{Fe(PP)Cp^*\}$ (PP = dppe, dppp) have enabled comparisons between the related homometallic derivatives to be made. Cyclic voltammetry revealed that these complexes undergo the sequential loss of three electrons to give the mono-, di- and trications. Chemical oxidation enabled the isolation of the mono- and dications, however the trication was not stable towards isolation. Interesting results were found in connection with the electronic structures of the dications. In the bis-ruthenium dication, X-ray and IR data suggested the nature of the carbon chain was best described as a cumulene, while in the bis-iron dication, the carbon chain was found to retain the diyndiyl form as found in the neutral complex. In the mixed ruthenium-iron dication, X-ray and spectroscopic data confirm that the nature of the carbon chain lies closer to a cumulene system rather that a diyndiyl, suggesting that ruthenium has a greater influence on the nature of the carbon chain than iron.

References

[1] J. M. Tour, *Acc. Chem. Res.*, **2000**, *33*, 791.

[2] G. E. Moore, *Electronics,* **1965**, *38*, 114.

[3] N. Robertson, C. A. McGowan, *Chem. Soc. Rev.*, **2003**, *32*, 96.

[4] A. Aviram, M. A. Ratner, *Chem. Phys. Lett.*, **1974**, *29*, 277.

[5] M. D. Ward, *Chem. Ind.*, **1996**, 568.

[6] F. Paul, C. Lapinte, *Coord. Chem. Rev.*, **1998**, *178-180*, 431.

[7] J. M. Tour, A. M. Rawlett, M. Kozaki, Y. Yao, R. C. Jagessar, S. M. Dirk, D. W. Price, M. A. Reed, C.-W. Zhou, J. Chen, W. Wang, I. Campbell, *Chem. Eur. J.*, **2001**, *7*, 5118.

[8] M. D. Ward, *Chem. Ind.*, **1997**, 640.

[9] Z. J. Donhauser, B. A. Mantooth, K. F. Kelly, L. A. Bumm, J. D. Monnell, J. J. Stapleton, D. W. Price, Jr., A. M. Rawlett, D. L. Allara, J. M. Tour, P. S. Weiss, *Science,* **2001**, *292*, 2303.

[10] S. Fraysse, C. Coudret, J.-P. Launay, *Eur. J. Inorg. Chem.*, **2000**, 1581.

[11] J. Chen, M. A. Reed, A. M. Rawlett, J. M. Tour, *Science,* **1999**, *286*, 1550.

[12] K. M. Roth, N. Dontha, R. B. Dabke, D. T. Gryko, C. Clausen, J. S. Lindsey, D. F. Bocian, W. G. Kuhr, *J. Vac. Sci. Technol. B,* **2000**, *18*, 2359.

[13] R. M. Metzger, *Chem. Rev.*, **2003**, *103*, 3803.

[14] R. M. Metzger, B. Chen, U. Hoepfner, M. V. Lakshmikantham, D. Vuillaume, T. Kawai, X. Wu, H. Tachibana, T. V. Hughes, H. Sakurai, J. W. Baldwin, C. Hosch, M. P. Cava, L. Brehmer, G. J. Ashwell, *J. Am. Chem. Soc.*, **1997**, *119*, 10455.

[15] H. L. Anderson, *J. Chem. Soc., Chem. Commun.*, **1999**, 2323.

[16] H.-W. Fink, C. Schönenberger, *Nature,* **1999**, *398*, 407.

[17] A. G. MacDiarmid, *Rev. Mod. Phys.*, **2001**, *73*, 701.

[18] S. Ijima, *Nature,* **1991**, *354*, 56.

[19] P. G. Collins, P. Avouris, *Sci. Am.*, **2000**, *283*, 62.

[20] S. J. Tans, M. H. Devoret, H. Dal, A. Thess, R. E. Smalley, L. J. Geerligs, C. Dekker, *Nature,* **1997**, *386*, 474.

[21] H. Dai, E. W. Wong, C. M. Lieber, *Science,* **1996**, *272*, 523.

[22] J. E. Fischer, H. Dai, A. Thess, R. Lee, N. M. Hanjani, D. L. Dehaas, R. E. Smalley, *Phys. Rev. B,* **1997**, *55*, 4921.

[23] S. J. Tans, A. R. M. Verschueren, C. Dekker, *Nature,* **1998**, *393*, 49.

[24] R. Martel, T. Schmidt, H. R. Shea, T. Hertel, P. Avouris, *Appl. Phys. Lett.,* **1998**, *73*, 2447.

[25] M. A. Reed, C. Zhou, C. J. Muller, T. P. Burgin, J. M. Tour, *Science,* **1997**, *278*, 252.

[26] M. T. Cygan, T. D. Dunbar, J. J. Arnold, L. A. Bumm, N. F. Shedlock, T. P. Burgin, L. Jones II, D. L. Allara, J. M. Tour, P. S. Weiss, *J. Am. Chem. Soc.,* **1998**, *120*, 2721.

[27] C. Zhou, M. R. Deshpande, M. A. Reed, K. Jones, II, J. M. Tour, *Appl. Phys. Lett.,* **1997**, *71*, 611.

[28] F.-R. F. Fan, J. Yang, L. Cai, D. W. Price, Jr., S. M. Dirk, D. V. Kosynkin, Y. Yao, A. M. Rawlett, J. M. Tour, A. J. Bard, *J. Am. Chem. Soc.,* **2002**, *124*, 5550.

[29] J. J. Stapleton, P. Harder, T. A. Daniel, M. D. Reinard, Y. Yao, D. W. Price, J. M. Tour, D. L. Allara, *Langmuir,* **2003**, *19*, 8245.

[30] J. M. Tour, *Chem. Rev.,* **1996**, *96*, 537.

[31] L. Jones, II, J. S. Schumm, J. M. Tour, *J. Org. Chem.,* **1997**, *62*, 1388.

[32] J. Chen, W. Wang, M. A. Reed, A. M. Rawlett, D. W. Price, J. M. Tour, *Appl. Phys. Lett.,* **2000**, *77*, 1224.

[33] J. M. Seminario, A. G. Zacarias, J. M. Tour, *J. Am. Chem. Soc.,* **2000**, *122*, 3015.

[34] L. A. Bumm, J. J. Arnold, M. T. Cygan, T. D. Dunbar, T. P. Burgin, L. Jones II, D. L. Allara, J. M. Tour, P. S. Weiss, *Science,* **1996**, *271*, 1705.

[35] F. Coat, C. Lapinte, *Organometallics,* **1996**, *15*, 477.

[36] C. Creutz, H. Taube, *J. Am. Chem. Soc.,* **1973**, *95*, 1086.

[37] C. Creutz, H. Taube, *J. Am. Chem. Soc.,* **1969**, *91*, 3988.

[38] J. P. Launay, M. Tourrel-Pagis, J. F. Lipskier, V. Marvaud, C. Joachim, *Inorg. Chem.,* **1991**, *30*, 1033.

[39] J. E. Sutton, P. M. Sutton, H. Taube, *Inorg. Chem.,* **1979**, *18*, 1017.

[40] I. de Sousa Moreira, D. W. Franco, *J. Chem. Soc., Chem Commun.,* **1992**, 450.

[41] M.-C. Chung, X. Gu, B. A. Etzenhouser, A. M. Spuches, P. T. Rye, S. K. Seetharaman, D. J. Rose, J. Zubieta, M. B. Sponsler, *Organometallics,* **2003**, *22*, 3485.

[42] B. A. Etzenhouser, M. D. Cavanaugh, H. N. Spurgeon, M. B. Sponsler, *J. Am. Chem. Soc.*, **1994**, *116*, 2221.

[43] M. I. Bruce, P. J. Low, K. Costuas, J.-F. Halet, S. P. Best, G. A. Heath, *J. Am. Chem. Soc.*, **2000**, *122*, 1949.

[44] N. Le Narvor, L. Toupet, C. Lapinte, *J. Am. Chem. Soc.*, **1995**, *117*, 7129.

[45] M. Brady, W. Weng, Y. Zhou, J. W. Seyler, A. J. Amoroso, A. M. Arif, M. Boehme, G. Frenking, J. A. Gladysz, *J. Am. Chem. Soc.*, **1997**, *119*, 775.

[46] R. Dembinski, T. Bartik, B. Bartik, M. Jaeger, J. A. Gladysz, *J. Am. Chem. Soc.*, **2000**, *122*, 810.

[47] R. Chukwu, A. D. Hunter, B. D. Santarsiero, S. G. Bott, J. L. Atwood, J. Chassaignac, *Organometallics,* **1992**, *11*, 589.

[48] A. D. Hunter, A. B. Szigety, *Organometallics,* **1989**, *8*, 2670.

[49] M. Beley, J. P. Collin, R. Louis, B. Metz, J. P. Sauvage, *J. Am. Chem. Soc.*, **1991**, *113*, 8521.

[50] M. Beley, J. P. Collin, J. P. Sauvage, *Inorg. Chem.*, **1993**, *32*, 4539.

[51] D. Astruc, *Acc. Chem. Res.*, **1997**, *30*, 383.

[52] M. B. Robin, P. Day, *Adv. Inorg. Chem. Radiochem.*, **1967**, *10*, 247.

[53] J. A. McCleverty, M. D. Ward, *Acc. Chem. Res.*, **1998**, *31*, 842.

[54] W. Kaim, A. Klein, M. Gloeckle, *Acc. Chem. Res.*, **2000**, *33*, 755.

[55] C. M. Fischer, M. Burghard, S. Roth, K. von Klitzing, *Appl. Phys. Lett.*, **1995**, *66*, 3331.

[56] S. Datta, W. Tian, S. Hong, R. Reifenberger, J. I. Henderson, C. P. Kubiak, *Phys. Rev. Lett.*, **1997**, *79*, 2530.

[57] C. Joachim, J. K. Gimzewski, R. R. Schlittler, C. Chavy, *Phys. Rev. Lett.*, **1995**, *74*, 2102.

[58] J. Reichert, R. Ochs, D. Beckmann, H. B. Weber, M. Mayor, H. von Löhneysen, *Phys. Rev. Lett.*, **2002**, *88*, 176804.

[59] C. Kergueris, J. P. Bourgoin, S. Palacin, D. Esteve, C. Urbina, M. Magoga, C. Joachim, *Phys. Rev. B,* **1999**, *59*, 12505.

[60] M. Mayor, C. von Hänisch, H. B. Weber, J. Reichert, D. Beckmann, *Angew. Chem. Int. Ed.*, **2002**, *41*, 1183.

[61] A. Bolognesi, M. Catellani, S. Destri, *Comprehensive Polymer Science, Vol. 4*, Pergamon, Oxford, **1989**, p. 143.

[62] N. N. Greenwood, A. Earnshaw, *Chemistry of the Elements*, Pergamon, Oxford, **1984**, p. 307.

[63] P. T. Kissinger, W. R. Heineman, *J. Chem. Educ.*, **1983**, *60*, 702.

[64] D. H. Evans, K. M. O'Connell, R. A. Petersen, M. J. Kelly, *J. Chem. Educ.*, **1983**, *60*, 290.

[65] D. B. Hibbert, *Introduction to Electrochemistry*, Macmillan, London, **1993**, p. 158.

[66] F. Barrière, N. Camire, W. E. Geiger, U. T. Mueller-Westerhoff, R. Sanders, *J. Am. Chem. Soc.*, **2002**, *124*, 7262.

[67] J. B. Flanagan, S. Margel, A. J. Bard, F. C. Anson, *J. Am. Chem. Soc.*, **1978**, *100*, 4248.

[68] G.-L. Xu, G. Zou, Y.-H. Ni, M. C. DeRosa, R. J. Crutchley, T. Ren, *J. Am. Chem. Soc.*, **2003**, *125*, 10057.

[69] D. E. Richardson, H. Taube, *Inorg. Chem.*, **1981**, *20*, 1278.

[70] G. A. Neyhart, J. T. Hupp, J. C. Curtis, C. J. Timpson, T. J. Meyer, *J. Am. Chem. Soc.*, **1996**, *118*, 3724.

[71] R. J. LeSuer, W. E. Geiger, *Angew. Chem. Int. Ed.*, **2000**, *39*, 248.

[72] D. E. Richardson, H. Taube, *J. Am. Chem. Soc.*, **1983**, *105*, 40.

[73] J.-P. Launay, *Chem. Soc. Rev.*, **2001**, *30*, 386.

[74] B. S. Brunschwig, C. Creutz, N. Sutin, *Chem. Soc. Rev.*, **2002**, *31*, 168.

[75] C. Creutz, *Prog. Inorg. Chem.*, **1983**, *30*, 1.

[76] N. S. Hush, *Coord. Chem. Rev.*, **1985**, *64*, 135.

[77] C. G. Atwood, W. E. Geiger, A. L. Rheingold, *J. Am. Chem. Soc.*, **1993**, *115*, 5310.

[78] K. D. Demadis, C. M. Hartshorn, T. J. Meyer, *Chem. Rev.*, **2001**, *101*, 2655.

[79] J. M. Lehn, *Supramolecular Chemistry: Concepts and Perspectives*, VCH, New York, **1995**, p. 106.

[80] J. C. W. Chien, *Polyacetylene: Chemistry, Physics, and Material Science*, Academic, Orlando, **1984**.

[81] T. Masuda, T. Higashimura, *Acc. Chem. Res.*, **1984**, *17*, 51.

[82] J. L. Foley, L. Li, D. J. Sandman, *Chem. Mater.*, **1998**, *10*, 3984.

[83] Y. Zhao, K. Campbell, R. R. Tykwinski, *J. Org. Chem.*, **2002**, *67*, 336.

[84] K. Hayamizu, W. S. Price, H. Matsuda, S. Okada, H. Nakanishi, *J. Mol. Struct.*, **1998**, *441*, 205.

[85] J. Xiao, M. Yang, J. W. Lauher, F. W. Fowler, *Angew. Chem. Int. Ed.,* **2000**, *39*, 2132.

[86] W. E. Meyer, A. J. Amoroso, C. R. Horn, M. Jaeger, J. A. Gladysz, *Organometallics,* **2001**, *20*, 1115.

[87] F. J. Fernandez, O. Blacque, M. Alfonso, H. Berke, *J. Chem. Soc., Chem. Commun.,* **2001**, 1266.

[88] L. Brandsma, *Preparative Acetylenic Chemistry*, 2nd ed., Elsevier, Amsterdam, **1988**, p. 81.

[89] H. Werner, R. W. Lass, O. Gevert, J. Wolf, *Organometallics,* **1997**, *16*, 4077.

[90] T. Rappert, O. Nuernberg, H. Werner, *Organometallics,* **1993**, *12*, 1359.

[91] M. F. Shostakovskii, A. V. Bogdanova, *The Chemistry of Diacetylenes*, Wiley, New York, **1974**.

[92] G. Zweifel, S. Rajagopalan, *J. Am. Chem. Soc.,* **1985**, *107*, 700.

[93] A. B. Holmes, C. L. D. Jennings-White, A. H. Schulthess, B. Akinde, D. R. M. Walton, *J. Chem. Soc., Chem Commun.,* **1979**, 840.

[94] A. Wong, P. C. W. Kang, C. D. Tagge, D. R. Leon, *Organometallics,* **1990**, *9*, 1992.

[95] P. J. Kim, H. Masai, K. Sonogashira, N. Hagihara, *Inorg. Nucl. Chem. Lett.,* **1970**, *6*, 181.

[96] R. Crescenzi, C. L. Sterzo, *Organometallics,* **1992**, *11*, 4301.

[97] G. E. Jones, D. A. Kendrick, A. B. Holmes, *Org. Synth.,* **1987**, *65*, 52.

[98] M. I. Bruce, B. C. Hall, B. D. Kelly, P. J. Low, B. W. Skelton, A. H. White, *J. Chem. Soc., Dalton Trans.,* **1999**, 3719.

[99] C.-M. Che, H.-Y. Chao, V. M. Miskowski, Y. Li, K.-K. Cheung, *J. Am. Chem. Soc.,* **2001**, *123*, 4985.

[100] O. Gevert, J. Wolf, H. Werner, *Organometallics,* **1996**, *15*, 2806.

[101] S. Kheradmandan, K. Heinze, H. W. Schmalle, H. Berke, *Angew. Chem. Int. Ed.,* **1999**, *38*, 2270.

[102] M. Guillemot, L. Toupet, C. Lapinte, *Organometallics,* **1998**, *17*, 1928.

[103] M. I. Bruce, M. Ke, P. J. Low, B. W. Skelton, A. H. White, *Organometallics,* **1998**, *17*, 3539.

[104] M. I. Bruce, M. Ke, P. J. Low, *J. Chem. Soc., Chem. Commun.,* **1996**, 2405.

[105] R. L. Roberts, H. Puschmann, J. A. K. Howard, J. H. Yamamoto, A. J. Carty, P. J. Low, *J. Chem. Soc., Dalton Trans.*, **2003**, 1099.

[106] G. Jia, R. J. Puddephatt, J. J. Vittal, N. C. Payne, *Organometallics,* **1993**, *12*, 263.

[107] N. J. Long, *Angew. Chem. Int. Ed. Engl.*, **1995**, *34*, 21.

[108] F. Morandini, A. Dondana, I. Munari, G. Pilloni, G. Consiglio, A. Sironi, M. Moret, *Inorg. Chim. Acta,* **1998**, *282*, 163.

[109] M. I. Bruce, C. Hameister, A. G. Swincer, R. C. Wallis, *Inorg. Synth.*, **1982**, *21*, 78.

[110] P. S. Hallman, T. A. Stephenson, G. Wilkinson, *Inorg. Synth.*, **1970**, *12*, 237.

[111] T. D. Tilley, R. H. Grubbs, J. E. Bercaw, *Organometallics,* **1984**, *3*, 274.

[112] N. Oshima, H. Suzuki, Y. Morooka, *Chem. Lett.*, **1984**, 1161.

[113] L. Luo, N. Zhu, N.-J. Zhu, E. D. Stevens, S. P. Nolan, *Organometallics,* **1994**, *13*, 669.

[114] M. I. Bruce, *Chem. Rev.*, **1991**, *91*, 197.

[115] P. T. Czech, X.-Q. Ye, R. F. Fenske, *Organometallics,* **1990**, *9*, 2016.

[116] M. I. Bruce, K. Costuas, J.-F. Halet, B. C. Hall, P. J. Low, B. K. Nicholson, B. W. Skelton, A. H. White, *J. Chem. Soc., Dalton Trans.*, **2002**, 383.

[117] R. Dembinski, T. Lis, S. Szafert, C. L. Mayne, T. Bartik, J. A. Gladysz, *J. Organomet. Chem.*, **1999**, *578*, 229.

[118] T. B. Peters, J. C. Bohling, A. M. Arif, J. A. Gladysz, *Organometallics,* **1999**, *18*, 3261.

[119] W. Mohr, J. Stahl, F. Hampel, J. A. Gladysz, *Inorg. Chem.*, **2001**, *40*, 3263.

[120] P. H. Rieger, *Coord. Chem. Rev.*, **1994**, *135-136*, 203.

[121] N. G. Connelly, W. E. Geiger, *Chem. Rev.*, **1996**, *96*, 877.

[122] V. Guillaume, V. Mahias, A. Mari, C. Lapinte, *Organometallics,* **2000**, *19*, 1422.

[123] A. B. Holmes, C. N. Sporikou, *Org. Synth.*, **1987**, *65*, 61.

[124] M. I. Bruce, A. G. Swincer, *Adv. Organomet. Chem.*, **1983**, *22*, 59.

[125] N. M. Kostic, R. F. Fenske, *Organometallics,* **1982**, *1*, 974.

[126] M. I. Bruce, D. N. Duffy, M. G. Humphrey, A. G. Swincer, *J. Organomet. Chem.*, **1985**, *282*, 383.

[127] S. G. Davies, A. J. Smallridge, *J. Organomet. Chem.*, **1990**, *395*, C39.

[128] M. P. Gamasa, J. Gimeno, E. Lastra, B. M. Martin, A. Aguirre, S. Garcia-Granda, P. Pertierra, *J. Organomet. Chem.*, **1992**, *429*, C19.

[129] V. Cadierno, M. P. Gamasa, J. Gimeno, B. M. Martin-Vaca, *J. Organomet. Chem.*, **2001**, *617-618*, 261.

[130] K. A. Kramarczuk, *Osmium: The New Element In Molecular Wires*, B.Sc. Honours Thesis. University of Adelaide, **2001**.

[131] C. Lapinte, *personal communication*, **2002**.

[132] M. I. Bruce, A. G. Swincer, R. C. Wallis, *J. Organomet. Chem.*, **1979**, *171*, C5.

[133] L. A. Oro, M. A. Ciriano, M. Campo, C. Foces-Foces, F. H. Cano, *J. Organomet. Chem.*, **1985**, *289*, 117.

[134] A. Mezzetti, G. Consiglio, F. Morandini, *J. Organomet. Chem.*, **1992**, *430*, C15.

[135] R. Le Lagadec, E. Roman, L. Toupet, U. Mueller, P. H. Dixneuf, *Organometallics,* **1994**, *13*, 5030.

[136] C. Bianchini, P. Innocenti, M. Peruzzini, A. Romerosa, F. Zanobini, *Organometallics,* **1996**, *15*, 272.

[137] M. I. Bruce, P. J. Low, *Adv. Organomet. Chem.*, **2001**, *48*, 71.

[138] P. J. Stang, B. Olenyuk, *Acc. Chem. Res.*, **1997**, *30*, 502.

[139] S. Leininger, B. Olenyuk, P. J. Stang, *Chem. Rev.*, **2000**, *100*, 853.

[140] K. Sonogashira, T. Yatake, Y. Tohda, S. Takahashi, N. Hagihara, *J. Chem. Soc., Chem Commun.*, **1977**, 291.

[141] K. Sonogashira, Y. Fujikura, T. Yatake, N. Toyoshima, S. Takahashi, N. Hagihara, *J. Organomet. Chem.*, **1978**, *145*, 101.

[142] H. Lang, K. Koehler, S. Blau, *Coord. Chem. Rev.*, **1995**, *143*, 113.

[143] H. Lang, D. S. A. George, G. Rheinwald, *Coord. Chem. Rev.*, **2000**, *206-207*, 101.

[144] H. Lang, A. del Villar, *J. Organomet. Chem.*, **2003**, *670*, 45.

[145] M. E. Smith, *Molecular Wires: Syntheses, Electrochemistry and Properties of Metal Complexes Containing Carbon Chains*, Ph.D. Thesis. University of Adelaide, **2002**.

[146] M. Akita, M.-C. Chung, A. Sakurai, S. Sugimoto, M. Terada, M. Tanaka, Y. Moro-oka, *Organometallics,* **1997**, *16*, 4882.

[147] F. Coat, M.-A. Guillevic, L. Toupet, F. Paul, C. Lapinte, *Organometallics,* **1997**, *16*, 5988.

[148] Y. Sun, N. J. Taylor, A. J. Carty, *J. Organomet. Chem.,* **1992**, *423*, C43.

[149] F. Coat, P. Thominot, C. Lapinte, *J. Organomet. Chem.,* **2001**, *629*, 39.

[150] M. I. Bruce, B. C. Hall, P. J. Low, M. E. Smith, B. W. Skelton, A. H. White, *Inorg. Chim. Acta,* **2000**, *300-302*, 633.

[151] V. W.-W. Yam, S. H.-F. Chong, K.-K. Cheung, *J. Chem. Soc., Chem. Commun.,* **1998**, 2121.

[152] W. Weng, T. Bartik, M. Brady, B. Bartik, J. A. Ramsden, A. M. Arif, J. A. Gladysz, *J. Am. Chem. Soc.,* **1995**, *117*, 11922.

[153] D. F. Shriver, P. W. Atkins, C. H. Langford, *Inorganic Chemistry*, Oxford University Press, Oxford, **1994**, p. 35.

[154] M. I. Bruce, *Coord. Chem. Rev.,* **1997**, *166*, 91.

[155] R. F. Winter, K.-W. Klinkhammer, S. Zalis, *Organometallics,* **2001**, *20*, 1317.

[156] R. F. Winter, *Eur. J. Inorg. Chem.,* **1999**, 2121.

[157] R. Fernández-Galán, B. R. Manzano, A. Otero, M. Lanfranchi, M. A. Pellinghelli, *Inorg. Chem.,* **1994**, *33*, 2309.

[158] N. E. Kolobova, V. V. Skripkin, G. G. Aleksandrov, Y. T. Struchkov, *J. Organomet. Chem.,* **1979**, *169*, 293.

[159] B. E. Boland-Lussier, R. P. Hughes, *Organometallics,* **1982**, *1*, 635.

[160] W. Weng, T. Bartik, M. T. Johnson, A. M. Arif, J. A. Gladysz, *Organometallics,* **1995**, *14*, 889.

[161] H. Fischer, F. Leroux, G. Roth, R. Stumpf, *Organometallics,* **1996**, *15*, 3723.

[162] F. Leroux, R. Stumpf, H. Fischer, *Eur. J. Inorg. Chem.,* **1998**, 1225.

[163] S. Rigaut, L. Le Pichon, D. Touchard, P. H. Dixneuf, J.-C. Daran, *J. Chem. Soc., Chem. Commun.,* **2001**, 1206.

[164] M. I. Bruce, M. J. Liddell, *J. Organomet. Chem.,* **1992**, *427*, 263.

[165] V. W.-W. Yam, W. K.-M. Fung, K. M.-C. Wong, V. C.-Y. Lau, K.-K. Cheung, *J. Chem. Soc., Chem. Commun.,* **1998**, 777.

[166] V. W.-W. Yam, W. K.-M. Fung, K.-K. Cheung, *Organometallics,* **1998**, *17*, 3293.

[167] V. W.-W. Yam, W. K.-M. Fung, M.-T. Wong, *Organometallics,* **1997**, *16*, 1772.

[168] E. Lastra, M. P. Gamasa, J. Gimeno, M. Lanfranchi, A. Tiripicchio, *J. Chem. Soc., Dalton Trans.*, **1989**, 1499.

[169] J. Diez, M. P. Gamasa, J. Gimeno, A. Aguirre, S. García-Granda, *Organometallics,* **1991**, *10*, 380.

[170] J. Diez, M. P. Gamasa, J. Gimeno, E. Lastra, A. Aguirre, S. García-Granda, *Organometallics,* **1993**, *12*, 2213.

[171] J. H. K. Yip, J. Wu, K.-Y. Wong, K.-W. Yeung, J. J. Vittal, *Organometallics,* **2002**, *21*, 1612.

[172] M. P. Gamasa, J. Gimeno, E. Lastra, X. Solans, *J. Organomet. Chem.*, **1988**, *346*, 277.

[173] S. Rigaut, J. Massue, D. Touchard, J.-L. Fillaut, S. Golhen, P. H. Dixneuf, *Angew. Chem. Int. Ed.*, **2002**, *41*, 4513.

[174] B. Bartik, R. Dembinski, T. Bartik, A. M. Arif, J. A. Gladysz, *New J. Chem.*, **1997**, *21*, 739.

[175] M. I. Bruce, C. Hameister, A. G. Swincer, R. C. Wallis, *Inorg. Synth.*, **1990**, *28*, 270.

[176] M. I. Bruce, B. K. Nicholson, O. bin Shawkataly, *Inorg. Synth.*, **1989**, *26*, 324.

[177] R. Uson, A. Laguna, *Inorg. Synth.*, **1982**, *21*, 71.

[178] M. I. Bruce, B. G. Ellis, B. W. Skelton, A. H. White, *J. Organomet. Chem.*, **2000**, *607*, 137.

[179] M. I. Bruce, P. J. Low, M. Ke, B. D. Kelly, B. W. Skelton, M. E. Smith, A. H. White, N. B. Witton, *Aust. J. Chem.*, **2001**, *54*, 453.

[180] T. J. Johnson, L. J. Alvey, M. Brady, C. L. Mayne, A. M. Arif, J. A. Gladysz, *Chem. Eur. J.*, **1995**, *1*, 294.

[181] F. Paul, W. E. Meyer, L. Toupet, H. Jiao, J. A. Gladysz, C. Lapinte, *J. Am. Chem. Soc.*, **2000**, *122*, 9405.

[182] H. Jiao, K. Costuas, J. A. Gladysz, J.-F. Halet, M. Guillemot, L. Toupet, F. Paul, C. Lapinte, *J. Am. Chem. Soc.*, **2003**, *125*, 9511.

[183] P. Gütlich, R. Link, A. Trautwein, *Inorganic Chemistry Concepts, Vol. 3: Mössbauer Spectroscopy and Transition Metal Chemistry*, Springer-Verlag, New York, **1978**.

[184] C. N. Banwell, E. M. McCash, *Fundamentals of Molecular Spectroscopy. 4th ed*, McGraw-Hill, London, **1997**, pp. 283-291.

[185] V. Guillaume, P. Thominot, F. Coat, A. Mari, C. Lapinte, *J. Organomet. Chem.*, **1998**, *565*, 75.

[186] S. Le Stang, F. Paul, C. Lapinte, *Organometallics,* **2000**, *19*, 1035.

[187] T. Y. Dong, D. N. Hendrickson, C. G. Pierpont, M. F. Moore, *J. Am. Chem. Soc.*, **1986**, *108*, 963.

[188] T. Y. Dong, C. C. Schei, M. Y. Hwang, T. Y. Lee, S. K. Yeh, Y. S. Wen, *Organometallics,* **1992**, *11*, 573.

[189] T. Weyland, K. Costuas, L. Toupet, J.-F. Halet, C. Lapinte, *Organometallics,* **2000**, *19*, 4228.

[190] N. Le Narvor, C. Lapinte, *Organometallics,* **1995**, *14*, 634.

[191] R. E. Carlin, *Magnetochemistry*, Springer-Verlag, New York, **1986**, p. 75.

[192] C. Roger, P. Hamon, L. Toupet, H. Rabaa, J. Y. Saillard, J. R. Hamon, C. Lapinte, *Organometallics,* **1991**, *10*, 1045.

[193] S. Roue, S. Le Stang, L. Toupet, C. Lapinte, *C. R. Chimie,* **2003**, *6*, 353.

[194] R. Denis, L. Toupet, F. Paul, C. Lapinte, *Organometallics,* **2000**, *19*, 4240.

[195] N. S. Hush, *Prog. Inorg. Chem.*, **1967**, *8*, 391.

[196] G. Argouarch, P. Hamon, L. Toupet, J.-R. Hamon, C. Lapinte, *Organometallics,* **2002**, *21*, 1341.

[197] W. Mohr, J. Stahl, F. Hampel, J. A. Gladysz, *Chem. Eur. J.,* **2003**, *9*, 3324.

[198] F. Diederich, Y. Rubin, *Angew. Chem. Int. Ed.,* **1992**, *31*, 1101.

[199] G. J. Baird, S. G. Davies, S. D. Moon, S. J. Simpson, R. H. Jones, *J. Chem. Soc., Dalton Trans.,* **1985**, 1479.

[200] M. I. Bruce, P. J. Low, *Adv. Organomet. Chem.,* **2004**, *50*, 231.

[201] T. E. Mueller, S. W.-K. Choi, D. M. P. Mingos, D. Murphy, D. J. Williams, V. W.-W. Yam, *J. Organomet. Chem.,* **1994**, *484*, 209.

[202] H. Lang, S. Koecher, S. Back, G. Rheinwald, G. van Koten, *Organometallics,* **2001**, *20*, 1968.

[203] M. Akita, M. Terada, S. Oyama, Y. Moro-oka, *Organometallics,* **1990**, *9*, 816.

[204] G. A. Koutsantonis, J. P. Selegue, *J. Am. Chem. Soc.,* **1991**, *113*, 2316.

[205] C. S. Griffith, G. A. Koutsantonis, B. W. Skelton, A. H. White, *J. Organomet. Chem.,* **2003**, *670*, 198.

[206] M. I. Bruce, G. A. Koutsantonis, *Aust. J. Chem.,* **1991**, *44*, 207.

[207] B. G. Ellis, G. J. Perkins, *unpublished results,* **2003**.

[208] M. Brady, W. Weng, J. A. Gladysz, *J. Chem. Soc., Chem Commun.*, **1994**, 2655.

[209] C. R. Horn, J. M. Martin-Alvarez, J. A. Gladysz, *Organometallics,* **2002**, *21*, 5386.

[210] A. Sakurai, M. Akita, Y. Moro-oka, *Organometallics,* **1999**, *18*, 3241.

[211] M. I. Bruce, B. D. Kelly, B. W. Skelton, A. H. White, *J. Organomet. Chem.*, **2000**, *604*, 150.

[212] K.-T. Wong, J.-M. Lehn, S.-M. Peng, G.-H. Lee, *J. Chem. Soc., Chem. Commun.*, **2000**, 2259.

[213] M. I. Bruce, M. E. Smith, N. N. Zaitseva, B. W. Skelton, A. H. White, *J. Organomet. Chem.*, **2003**, *670*, 170.

[214] W. Lu, H.-F. Xiang, N. Zhu, C.-M. Che, *Organometallics,* **2002**, *21*, 2343.

[215] J. Stahl, J. C. Bohling, E. B. Bauer, T. B. Peters, W. Mohr, J. M. Martin-Alvarez, F. Hampel, J. A. Gladysz, *Angew. Chem. Int. Ed.*, **2002**, *41*, 1871.

[216] W.-Y. Wong, C.-K. Wong, G.-L. Lu, K.-W. Cheah, J.-X. Shi, Z. Lin, *J. Chem. Soc., Dalton Trans.*, **2002**, 4587.

[217] V. W.-W. Yam, K. M.-C. Wong, N. Zhu, *Angew. Chem. Int. Ed.*, **2003**, *42*, 1400.

[218] T. Gibtner, F. Hampel, J.-P. Gisselbrecht, A. Hirsch, *Chem. Eur. J.*, **2002**, *8*, 408.

[219] G. Schermann, T. Grösser, F. Hampel, A. Hirsch, *Chem. Eur. J.*, **1997**, *3*, 1105.

[220] F. Coat, F. Paul, C. Lapinte, L. Toupet, K. Costuas, J.-F. Halet, *J. Organomet. Chem.*, **2003**, *683*, 368.

[221] A. Davison, J. P. Solar, *J. Organomet. Chem.*, **1979**, *166*, C13.

[222] M. I. Bruce, T. W. Hambley, M. R. Snow, A. G. Swincer, *Organometallics,* **1985**, *4*, 494.

[223] M. I. Bruce, P. A. Humphrey, M. R. Snow, E. R. T. Tiekink, *J. Organomet. Chem.*, **1986**, *303*, 417.

[224] M. I. Bruce, D. N. Duffy, M. J. Liddell, M. R. Snow, E. R. T. Tiekink, *J. Organomet. Chem.*, **1987**, *335*, 365.

[225] M. I. Bruce, M. J. Liddell, M. R. Snow, E. R. T. Tiekink, *Organometallics,* **1988**, *7*, 343.

[226] M. I. Bruce, M. P. Cifuentes, M. R. Snow, E. R. T. Tiekink, *J. Organomet. Chem.,* **1989**, *359*, 379.

[227] M. I. Bruce, T. W. Hambley, M. J. Liddell, A. G. Swincer, E. R. T. Tiekink, *Organometallics,* **1990**, *9*, 2886.

[228] M. I. Bruce, P. J. Low, B. W. Skelton, A. H. White, *New J. Chem.,* **1998**, *22*, 419.

[229] M. I. Bruce, M. E. Smith, B. W. Skelton, A. H. White, *J. Organomet. Chem.,* **2001**, *637-639*, 484.

[230] D. Nuel, F. Dahan, R. Mathieu, *Organometallics,* **1985**, *4*, 1436.

[231] J. A. Hriljac, D. F. Shriver, *J. Am. Chem. Soc.,* **1987**, *109*, 6010.

[232] M. Akita, A. Sakurai, Y. Moro-oka, *J. Chem. Soc., Chem. Commun.,* **1999**, 101.

[233] D. Seyferth, M. O. Nestle, A. T. Wehman, *J. Am. Chem. Soc.,* **1975**, *97*, 7417.

[234] M. I. Bruce, B. D. Kelly, B. W. Skelton, A. H. White, *J. Chem. Soc., Dalton Trans.,* **1999**, 847.

[235] S. Rigaut, J. Perruchon, L. Le Pichon, D. Touchard, P. H. Dixneuf, *J. Organomet. Chem.,* **2003**, *670*, 37.

[236] S. Szafert, J. A. Gladysz, *Chem. Rev.,* **2003**, *103*, 4175.

[237] K. Gao, N. S. Goroff, *J. Am. Chem. Soc.,* **2000**, *122*, 9320.

[238] M. Tanimoto, K. Kuchitsu, Y. Morino, *Bull. Chem. Soc. Jpn,* **1971**, *44*, 386.

[239] G. Schermann, T. Grosser, F. Hampel, A. Hirsch, *Chem. Eur. J.,* **1997**, *3*, 1105.

[240] K. D. Demadis, C. M. Hartshorn, T. J. Meyer, *Chem. Rev.,* **2001**, *101*, 2655.

[241] A. Gutiérrez Alonso, L. Ballester Reventós, *J. Organomet. Chem.,* **1988**, *338*, 249.

[242] L. S. Chia, W. R. Cullen, *Inorg. Chem.,* **1975**, *14*, 482.

[243] W. De Graaf, A. Smits, J. Boersma, G. van Koten, W. P. M. Hoekstra, *Tetrahedron,* **1988**, *44*, 6699.

[244] D. R. Coulson, *Inorg. Synth.,* **1990**, *28*, 107.